Search for Magnetic Monopoles and Other Highly Ionizing Particles in 13 TeV Centre-of-Mass Energy Proton–Proton Collisions with the ATLAS Detector at the LHC

ANA MARÍA RODRÍGUEZ VERA

A DISSERTATION SUBMITTED TO
THE FACULTY OF GRADUATE STUDIES
IN PARTIAL FULFILLMENT OF THE REQUIREMENTS
FOR THE DEGREE OF

DOCTOR OF PHILOSOPHY

GRADUATE PROGRAM IN PHYSICS AND ASTRONOMY
YORK UNIVERSITY
TORONTO, ONTARIO

SEPTEMBER 2023

CERN-THESIS-2023-190
28/08/2023

Search for Magnetic Monopoles and Other Highly Ionizing Particles in 13 TeV Centre-of-Mass Energy Proton–Proton Collisions with the ATLAS Detector at the LHC

Abstract

Among the outstanding questions of particle physics, proof of the existence of a magnetic monopole is still one of great interest. One compelling argument that motivates the search for magnetic monopoles is Paul Dirac's finding that the seemingly inexplicable quantized nature of the electric charge can be explained through the existence of magnetic monopoles. TeV-mass Dirac magnetic monopoles could potentially be produced by the $\sqrt{s} = 13\,\text{TeV}$ proton-proton collisions at the LHC. This thesis documents a search for magnetic monopoles using a $138\,\text{fb}^{-1}$ dataset of Run 2 proton-proton collisions at the LHC collected by the ATLAS experiment. Due to the highly ionizing nature of the interaction of magnetic monopoles with matter, the search is extended to include other highly ionizing particles known as high electric charge objects. Two production mechanisms are considered as benchmark models to interpret the results, Drell-Yan and photon fusion. No spin constraints are imposed by Dirac's theory, and therefore both spin-0 and spin-½ are modeled. The collision conditions allow for masses between 0.2 and 4 TeV to be studied. Theoretical considerations and experimental constraints motivate studying magnetic charges $|g| = 1$ and 2 g_D for magnetic monopoles and the range of $|z| = 20$ through $|z| = 100$ for high electric charge objects. Detection is based on the particle's characteristic high ionization of matter, penetration distance in the detector and lack of calorimeter shower. A data driven method is used to estimate the background contamination. No excess events are found in the signal region. Cross-section limits are computed through the CLs method with 95% confidence level. The highest mass limits to date for particle collider highly ionizing particle searches are presented.

Susana, Juan: ank u. Por escucharme, reirse conmigo, correr conmigo, alimentarme, explicarme Git, cuidarme y cuidar a Tomate. Gracias por estar conmigo cuando se fue la luz. **Momita**, algún día estudiaré diseño. Gracias por hacer tanto por mi, todos los colores en esta tesis son para ti. **Babuelito**: gracias por transmitirme el cariño que sientes por la ciencia y por enseñarme a correr.

I am glad I checked my spam mail 8 years ago. Thank you Wendy for having faith in my abilities and pushing me to be better.

Sampa, Scott and Randy: I am grateful for your questions, feedback and advice. Miriam: thank you for your careful reading of this thesis.

Gracias a quienes se aseguraron de cuidarme en Toronto: Susy, Elder y Paola.

To those who made my time at York better: Melissa, Travis, Brian, Priyanka, Darij, Mario, Anirudh, Rohith and Emmanuel, thank you.

Big thank you to everyone from ATLAS who made this possible including but not limited to: Louie, Philip M., Anthoni and Wen Yi. A Gabriel Palacino, gracias por las sugerencias y conversaciones que tuvimos. To Rebeca, Katarina and the rest of ATLAS Outreach.

Sioux, Filipo, Mario, Sergio, Diego, Hugo, Laura, Juan Manuel, Sebastian T., Aroosha y Mauro Mendivelso: gracias porque en su momento cada uno me animó a intentarlo.

Giovanny: gracias por todos los kilometros compartidos.

Gracias a los Rodriguez y Vera que estuvieron siempre pendientes, especialmente Jaky, Karen, Erika, Naspun, Con, Caro, Martin, Diana L., Diana C., Juan, Pau, Auris, Pao Pixeles, Patry.

Bailey, thank you for being there. Danilo, gracias por ser parte de mi familia y consentir a Tomate.

Nemanja: Thank you for fixing the washing machine, for helping me debug my code, for the Git masterclass, for sharing your family with me and for making sure I always have a smile on my face. Hvala ti puno.

A Tutti y a las goticas,

Contents

List of Tables

List of Figures

CHAPTER 1

Highly Ionizing Particles

The field known as particle physics, which studies the building blocks of nature and their interactions, began with the discovery of the electron and was developed extensively during the twentieth century. In 1894, Pierre Curie discussed the possibility of observing magnetic monopoles[1] in nature [1]. There have been many methods developed to search for both naturally occurring and collider-produced magnetic monopoles. So far, no particle with magnetic charge has been detected. With the construction of the Large Hadron Collider (LHC) at Centre Europeen de Recherche Nucléaire (CERN), it is possible to probe the highest-ever mass range (O(TeV)) of collider-produced magnetic monopoles.

In this chapter, I briefly introduce the current theory of particle physics and where the monopole fits in it. Then I discuss theories of magnetic monopoles. Some of the most relevant searches and their results are listed. Finally, an outline of this thesis is presented.

[1] "Magnetic monopole" or simply "monopole" will be used interchangeably throughout this thesis.

1.1 Standard Model

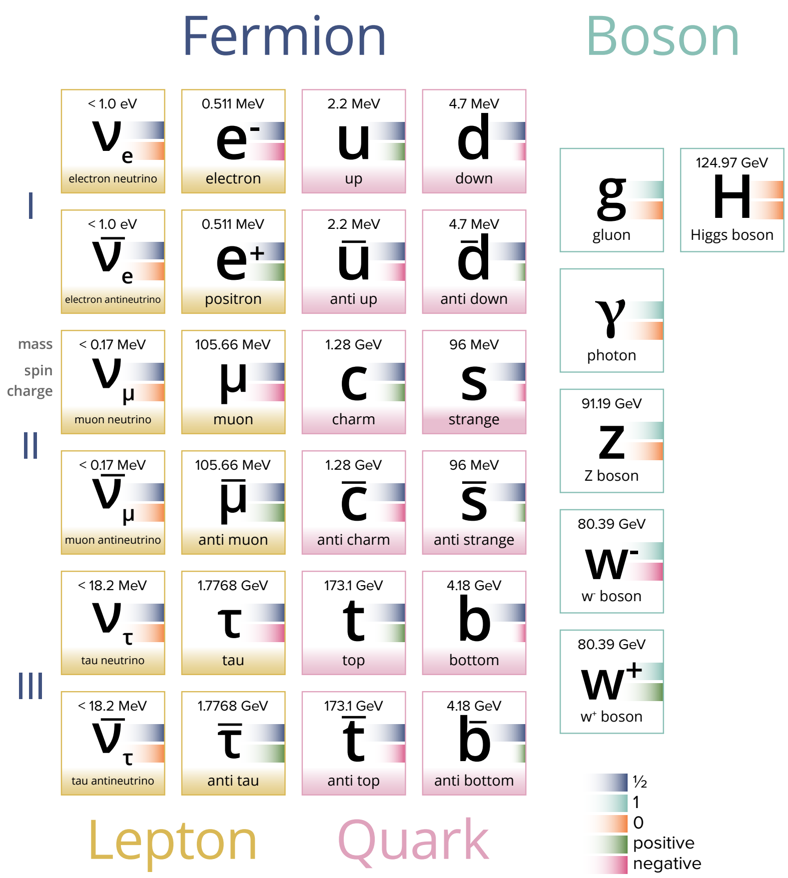

Figure 1.1: Particle content of the Standard Model of particle physics and their main characteristics.

The Standard Model (SM) of Particle Physics is the theory which has successfully described three of the four fundamental forces of nature. The work done by Glashow [2], Weinberg [3] and Salam [4] describes the weak and electromagnetic interactions. The Standard Model successfully predicted the existence of the particles responsible for mediating the weak interactions as well as the Higgs Boson. The fundamental particles that make up the universe are classified into fermions and bosons. Figure 1.1 summarizes the particle content of the Standard Model, their properties and the way they are classified based on these.

Despite the robustness of the Standard Model, there are known physical phenomena that are not described within it. Some examples include neutrino masses, dark energy/matter and matter-antimatter asymmetry. Formalisms that include these phenomena are known as physics Beyond Standard Model (BSM). Many BSM theories predict the existence of a magnetic monopole; therefore, evidence of their existence may help confirm a BSM theory.

1.2 Magnetic monopoles

A magnetic monopole is a hypothetical physical object with intrinsic positive or negative magnetic charge. Because of this magnetic charge, a magnetic monopole is a source of a positive or negative magnetic field, as illustrated in Figure 1.2.

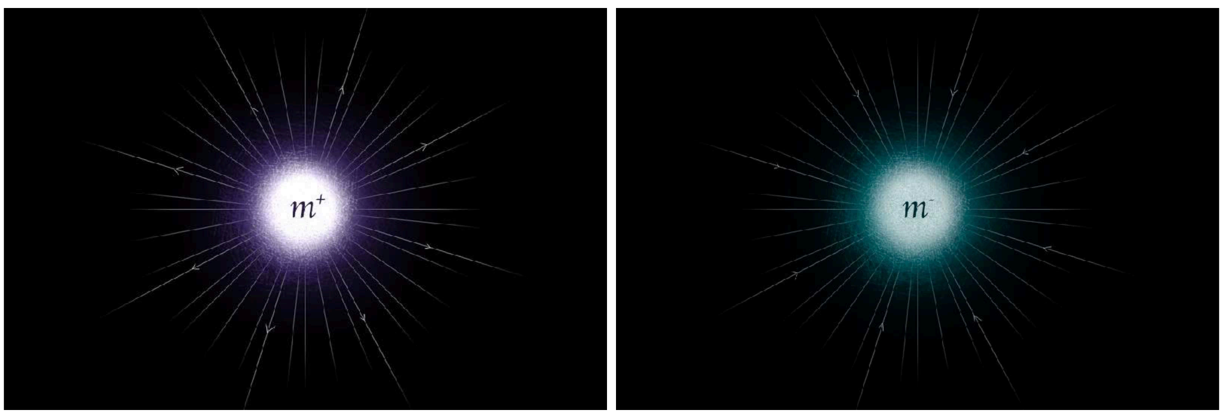

Figure 1.2: Illustration of positively (left) and negatively (right) charged magnetic monopoles with magnetic field lines radiating from/towards them. The colors in the image have no meaning.

Since magnetic monopoles were first formally theorized to be consistent with quantum mechanics by Paul Dirac in 1931 [5], new theories predicting magnetic monopoles and their properties have arisen. In this section, I will summarize Dirac's theory of magnetic monopoles and list a few of the other most relevant theories. Finally, I will describe some of the methods used to search for magnetic monopoles.

1.2.1 Generalized Maxwell's equations

In the absence of a magnetic monopole, Maxwell's equations are written as Eqs. 1.1–1.4,

$$\text{Gauss's law for electricity:} \quad \nabla \cdot \vec{E} = \frac{\rho}{\epsilon_0} \tag{1.1}$$

$$\text{Gauss's law for magnetism:} \quad \nabla \cdot \vec{B} = 0 \tag{1.2}$$

$$\text{Faraday's law:} \quad \nabla \times \vec{E} = -\frac{\partial \vec{B}}{\partial t} \tag{1.3}$$

$$\text{Ampère's law:} \quad \nabla \times \vec{B} = \mu_0 \vec{J} + \mu_0 \epsilon_0 \frac{\partial \vec{E}}{\partial t} \tag{1.4}$$

where ρ is the electric charge density, ϵ_0 is the permittivity of free space, μ_0 is the permeability of free space, $\vec{J}$ is the electric current density, $\vec{E}$ the electric field and $\vec{B}$ the magnetic field. The consequences of an observation of a magnetic monopole would introduce a magnetic charge density ρ_m, as well as a magnetic current density, $\vec{J}_m$, which restores symmetry in Maxwell's equations:

$$\text{Gauss's law for electricity:} \quad \nabla \cdot \vec{E} = \frac{\rho}{\epsilon_0} \tag{1.5}$$

$$\text{Gauss's law with magnetic charge:} \quad \nabla \cdot \vec{B} = \mu_0 \rho_m \tag{1.6}$$

$$\text{Faraday's law with magnetic current:} \quad \nabla \times \vec{E} = -\frac{\partial \vec{B}}{\partial t} - \mu_0 \vec{J}_m \tag{1.7}$$

$$\text{Ampère's law:} \quad \nabla \times \vec{B} = \mu_0 \vec{J} + \mu_0 \epsilon_0 \frac{\partial \vec{E}}{\partial t} \tag{1.8}$$

In addition, the discovery of even one magnetic monopole would explain electric charge quantization, as described in the following section.

1.2.2 Dirac magnetic monopole

In 1931, Paul Dirac wrote a paper [6] where he addressed the question of whether the theory of quantum mechanics prohibited magnetic monopoles. His approach led him to describe the physics of an electric charge q in the vicinity of a magnetic charge g, and concluded that electric charge quantization can be explained in theory by the presence of magnetic monopoles.

In classical electrodynamics, the electric force of an electric charge q is described by the electric field $\vec{E}$ as

$$\vec{E}(\vec{r}) = \frac{1}{4\pi\epsilon_0}\frac{q}{r^2}\hat{r}, \tag{1.9}$$

where r is the distance from the source charge q. Similarly, the magnetic field $\vec{B}(\vec{r})$ of a magnetic charge g is described as

$$\vec{B}(\vec{r}) = \frac{\mu_0 g}{4\pi r^2}\hat{r}. \tag{1.10}$$

In quantum mechanics, nonetheless, electromagnetic forces are described by scalar and vector potentials. In particular, the magnetic field is associated with the vector potential, $\vec{A}$, as stated in equation Eq. 1.11

$$\vec{B}(\vec{r}) = \nabla \times \vec{A}. \tag{1.11}$$

Thus, a magnetic monopole of charge g requires the definition of an electromagnetic vector potential from which the magnetic field in Eq. 1.10 can be obtained, as described in Eq. 1.12.

$$\vec{B}(\vec{r}) = \nabla \times \vec{A} = \frac{\mu_0 g}{4\pi r^2}\hat{r}. \tag{1.12}$$

One possible solution is the magnetic vector potential,

$$\vec{A}(\vec{r}) = \frac{\mu_0 g(1-\cos\theta)}{4\pi r\sin\theta}\hat{\phi}, \tag{1.13}$$

where θ and ϕ are the polar and azimuthal angular coordinates. This vector potential describes the magnetic field of a point source of magnetic charge overlaid on the field of an infinitely-long thin solenoid extending from $z = -\infty$ to the origin, where the magnetic monopole is located, as illustrated in Figure 1.3.

This potential in Eq. 1.13 is undefined at $\theta = \pi$. This singularity is known as the Dirac string, a hypothetical one-dimensional topological defect that represents a line of magnetic flux. From the classical electrodynamics perspective, this singularity poses no problem since the observable is the magnetic field and not the vector potential. If the Dirac string is infinitely long and thin, then the Dirac string is invisible in any electrodynamic interaction. In quantum mechanics, however, the Dirac

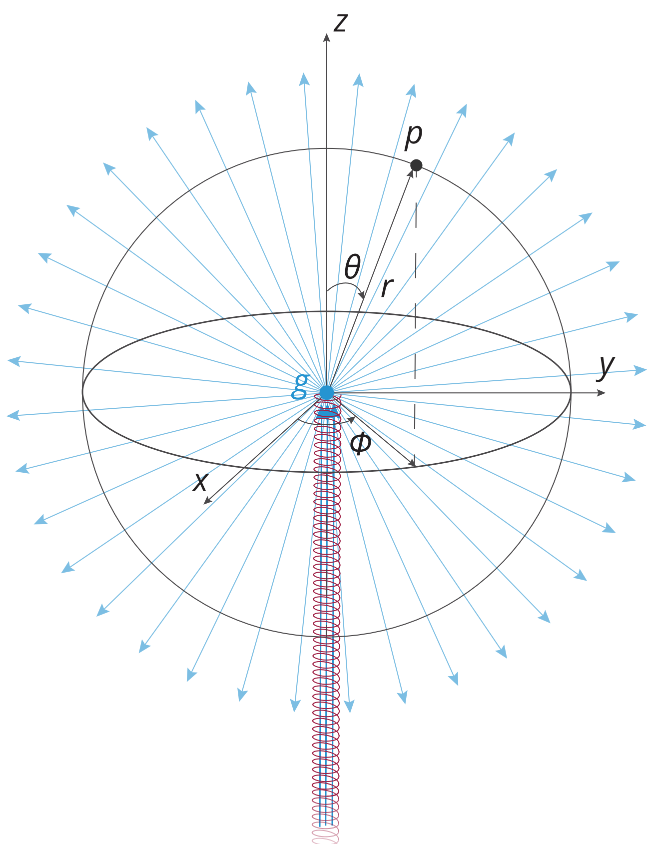

Figure 1.3: Schematic representation of the magnetic monopole of charge g, at the origin, with magnetic field lines (blue) and the polar coordinates for a position p inside the magnetic field. The Dirac string (red) is represented at $\theta = \pi$.

string has observable consequences because a point particle with charge q in the presence of the vector potential, defined by Eq. 1.13, will experience a change in the complex phase of its wave equation ψ, $\psi \rightarrow \psi^{-i\Delta\Phi}$ when moving along a path. The phase shift, $\Delta\Phi$, when the electric charge makes an infinitesimally small loop around the string, is

$$\begin{aligned}
\Delta\Phi &= \frac{q}{\hbar}\int_s \vec{A}\cdot\delta\vec{l} \\
&= \frac{q}{\hbar}\int_0^{2\pi} \frac{\mu_0 g(1-\cos\theta)}{4\pi r\sin\theta} r\sin\theta\delta\phi \\
&= \frac{\mu_0 g q}{4\pi\hbar}\lim_{\theta\rightarrow\pi}(1-\cos\theta)\int_0^{2\pi}\delta\phi \\
&= \frac{\mu_0 g q}{\hbar}. \qquad (1.14)
\end{aligned}$$

For the electric charge to remain unaffected by the string, i.e., for the string to be invisible, the phase shift, Eq. 1.14, should be a non-negative integer multiple, n, of 2π:

$$\frac{\mu_0 g q}{\hbar} = 2\pi n \rightarrow qg = \frac{2\pi\hbar n}{\mu_0}, \qquad (1.15)$$

written in Gaussian units.

Under this new approach, one arrives naturally at the *Charge Quantization Condition*. The right-hand side (RHS) of Eq. 1.15 states that the electric charge is always a non-negative integer multiple of the magnetic charge (and vice-versa). The charge of the electron e has been observed as the smallest isolated unit of electric charge [2]. Making $n = 1$ and rewriting the RHS of Eq. 1.15 in terms of the fine structure constant, $\alpha = \frac{\mu_0 e^2}{4\pi\hbar}$, the smallest quantum of magnetic charge, g_{D}, would be

$$g = \frac{ne^2}{2\alpha q} \xrightarrow{n=1,\ q=e} g_{\mathrm{D}} = \frac{e}{2\alpha} = 68.5e \qquad (1.16)$$

in Gaussian units.

The equivalence of the Dirac magnetic charge to an electric charge of 68.5 times the electric charge, seen in Eq. 1.16, translates to an interaction with matter resulting in a large energy loss per unit

[2] Although quarks are known to have smaller charges, 2/3 or 1/3 times e, they are not observed outside the hadron.

path-length, due to ionization, which will be explained in Chapter 3. This key property is exploited by some search experiments described in Section 1.3.

Analogous to the fine structure constant, the magnetic-coupling constant for the Dirac magnetic monopole describes the strength of the interaction between the photon and the Dirac magnetic monopole, and is defined by substituting $e \to ng_{\mathrm{D}}/c$,

$$\alpha = \frac{\mu_0 e^2 c}{4\pi\hbar} \xrightarrow{e \to ng_{\mathrm{D}}/c} \alpha_m = \frac{\mu_0 n^2 g_{\mathrm{D}}^2}{4\pi\hbar c}. \tag{1.17}$$

Assuming $n = 1$, the magnetic coupling of a $1g_{\mathrm{D}}$ magnetic monopole is $\alpha_m \simeq 34.25$, four orders of magnitude larger than α.

1.2.3 Theoretical charge and mass constraints on the Dirac magnetic monopole

Dirac's proposal of the magnetic monopole is that of a fundamental point particle. His theory, however, does not impose any conditions on the spin or the mass of such particles. Many specialized theories of magnetic monopoles have been developed after Dirac formalized his theory but only those fundamental in defining charge and mass constraints on the Dirac magnetic monopole, compatible with collider energies, are mentioned in this thesis. Schwinger elaborated on Dirac's theory, proposing a new vector potential solution for a magnetic monopole field that results in the minimal magnetic charge of $2g_{\mathrm{D}}$ [7]. Building on Schwinger's work, including the new definition of the minimum value of the magnetic charge, Cho and Maison developed a theory for electroweak magnetic monopoles, i.e., monopoles in the mass range of $10^2 - 10^3$ GeV in the Standard Model [8]. Later, Cho, Kimm and Yoon proposed a model (CKY model) that constrains the electroweak monopole mass between 4 TeV and 10 TeV [9]. This model is incompatible with the LHC measurements of the $H \to \gamma\gamma$ decay, but Ellis, Mavromatos and You constructed generalizations of the CKY model compatible with the observed rate of this Higgs decay that further constrains the electroweak monopole mass to below 5.5 TeV [10].

1.2.4 Other theories of magnetic monopoles

Parallel to the definition of O(few TeV) magnetic monopoles, Grand Unified Theories (GUTs) predict the existence of magnetic monopoles. Both 't Hooft [11] and Polyakov [12] established the necessity for magnetic monopoles in GUTs.

The properties (mass, size) of GUT magnetic monopoles vary from one unified model to another and are determined by the unification scale of the theory. As Preskill indicates, the mass of GUT magnetic monopoles can easily be expected to be extremely large, O(10^{16} GeV) [13]. An additional difference from the Dirac magnetic monopole defined in Section 1.2.2 is that GUTs magnetic monopoles are not point particles.

1.3 Searches for magnetic monopoles

Searches for magnetic monopoles consider two possible sources: naturally occurring (or primordial) and collider-produced magnetic monopoles. Because this search aims to look for magnetic monopoles produced in a collider, I will briefly describe searches for cosmic/primordial magnetic monopoles and list a few, but this section will focus on collider searches.

Cosmic Searches

Cosmic searches for magnetic monopoles are based on the idea that GUTs predict that magnetic monopoles were created in an abundance similar to that of baryons in the early universe and later their concentration diluted, as explained by the cosmological inflation theory [14].

Cosmic magnetic monopoles include both very heavy GUT monopoles as well as lighter primordial monopoles which might have survived cosmic inflation [15]. One important characteristic of these monopoles is that their speed, relative to the speed of light $\beta = \frac{v}{c}$, is only about $\beta = 10^{-3}$ because they are accelerated either by gravitational attraction (in the case of GUT monopoles) or by galactic magnetic fields (in the case of lighter monopoles). Low-velocity monopoles interact too weakly for detection methods that rely on high ionization signatures. Moreover, in many cases these low-velocity monopoles can pass through the Earth without interacting.

Among the experiments searching for cosmic magnetic monopoles are: the underground general-purpose detector MACRO [16], the array of nuclear track detectors at high altitude SLIM [17] and the balloon-borne radio interferometer ANITA [18]. There is also a group of experiments designed for the detection of neutrinos that double as magnetic monopole detectors: ANTARES [19], IceCube [20], Baikal [21], Super-Kamiokande [22], NOva [23] and AMANDA [24]. No observation of cosmic magnetic monopoles has been made by any of these searches. The results from these set cosmological flux limits, for different mass and speed hypotheses. The most stringent flux upper limits, over a broad β range, are set by MACRO, while ANTARES, AMANDA and IceCube's results are better at near-light speeds.

Collider Searches

There have been multiple collider searches for magnetic monopoles. These have used different detection mechanisms, which mostly concentrate on detecting monopoles trapped in matter (induction technique) or recording the characteristic highly ionizing signature mentioned in Section 1.2.2, which is the method used in this thesis and will be explained in Chapter 3. Some searches will be briefly described in this section and a more complete review can be found in reference [25].

Collider searches for magnetic monopoles go as far back as the first hadron collider: the CERN Intersecting Storage Ring (ISR). Searches at the ISR and later the Super ProtonAntiproton Synchrotron (Sp$\bar{\text{p}}$S) employed both plastic track detectors [26, 27], as well as an extraction method, consisting of exposing a material to the magnetic field of a superconducting solenoid, to search for trapped monopoles in beam dumps exposed to 300 GeV and 400 GeV proton beams. In the 1980's experiments CLEO and TASSO analyzed events from e^+e^- collisions from CESR and PETRA respectively, exploring the detection of magnetic monopoles through their unique non-helical trajectories in uniform magnetic fields. Unlike charged particles, magnetic monopole trajectories do not bend in the plane perpendicular to the magnetic field, rather they are accelerated in the direction of the magnetic field. Later in the 90's, at LEP-1, L6-MODAL [28] used Nuclear Track Detectors (NDTs), which detect high ionization, around the interaction region to study the range of charges between 0.9 and 3.6g_{D} for monopole masses up to ~45 GeV. Deployment of NTDs around the beam interaction point was also applied at other e^+e^- colliders, such as PEP [29], PETRA [30] and TRISTAN [31].

In the early 2000's, searches at the Tevatron $\sqrt{s}$ =1.8 TeV proton-antiproton collider employed NTDs [32]. Two more recent searches at the Tevatron collider used 35.7 pb^{-1} of $\sqrt{s}$ =1.96 TeV proton-antiproton collisions: the Collider Detector at Fermilab (CDF) used a time-of-flight system; and the E882 experiment used the induction technique to look for stopped monopoles in discarded material, such as the beryllium beam pipe and other parts of the CDF and D0 detectors [33]. OPAL searched for magnetic monopoles at the $\sqrt{s}$ =206.3 GeV LEP-2 e^+e^- collider by looking for back-to-back particles with anomalously high ionization energy loss per unit distance in the tracking chambers [34]. The only lepton-hadron scattering search was performed by the H1 experiment at HERA, using the induction technique [35].

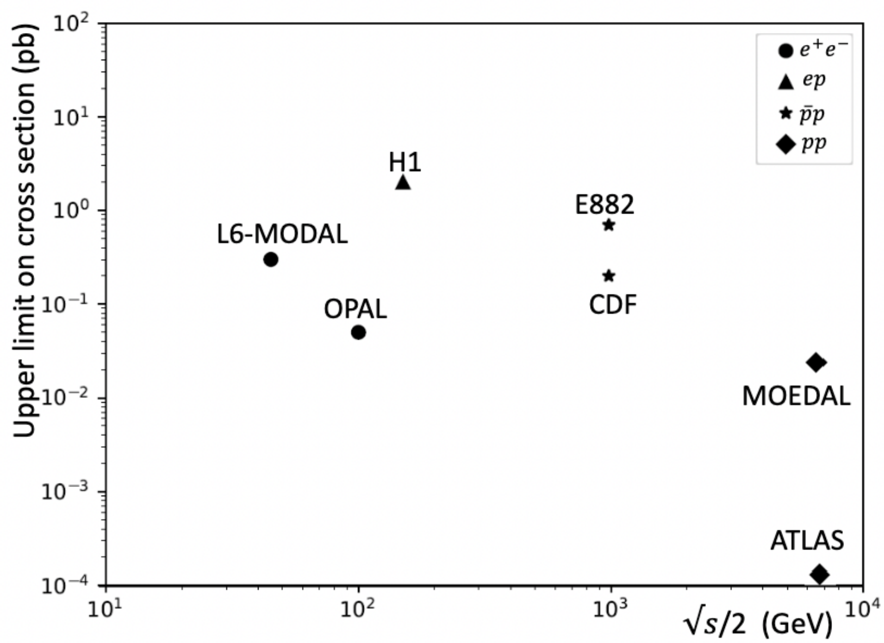

Figure 1.4: Cross section upper limits on collider-based 1g_{D} magnetic monopole searches [36].

Recent searches for magnetic monopoles in the highest centre-of-mass energies available to date have been performed at the LHC by the Monopole and Exotics Detector at the LHC (MoEDAL) [37] and ATLAS [38], studying proton-proton collisions. While MoEDAL looks for magnetic monopoles

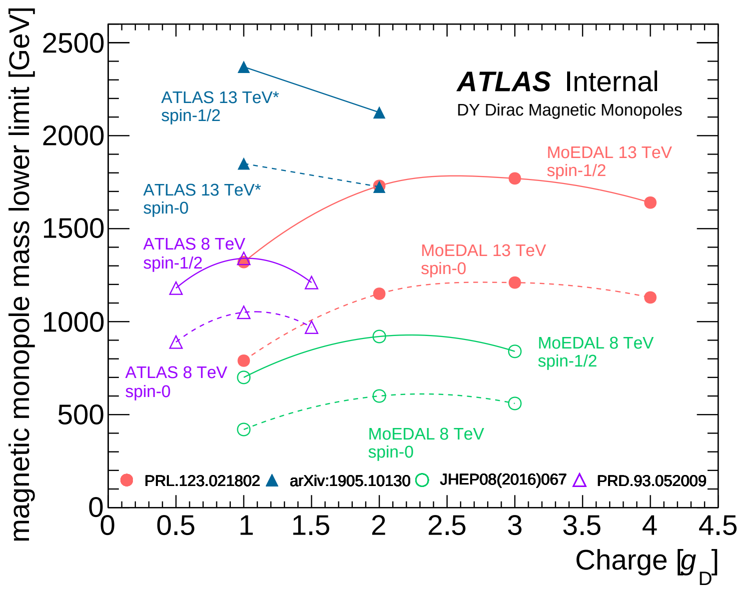

Figure 1.5: Comparison of the mass lower limits obtained by LHC searches in Run 1 and complete or partial results from Run 2 for Drell-Yan pair produced magnetic monopoles.

trapped in matter, ATLAS looks for highly ionizing particle signals. Both search for particles of mass up to 4 TeV. Two pair production modes, Drell-Yan and photon fusion which will be described in Section 3.1, have been considered by MoEDAL [37, 39–41]. In the past, ATLAS studied only Drell-Yan pair-produced monopoles in the range of 0.5 to $2g_{\mathrm{D}}$ for $\sqrt{s}$ =7 TeV [42] as well as $\sqrt{s}$ =8 TeV [43], and a search on 34.4 fb^{-1} of $\sqrt{s}$ =13 TeV proton-proton collisions [38] which considered magnetic charges of 1 and $2g_{\mathrm{D}}$. MoEDAL is sensitive up to $5g_{\mathrm{D}}$.

In the absence of an observation of magnetic monopoles, experimental cross section upper limits are computed. These values indicate the expected maximum cross section under the experimental parameters of the search, making it possible to fairly compare the results of different experimental approaches. Figure 1.4 summarizes the upper cross section limits of some of the searches discussed in this section. Additionally, lower mass limits on the magnetic monopole can also be set. Figure 1.5 compares the mass limits set by MoEDAL and ATLAS. Currently, ATLAS has the best mass limits for Drell-Yan magnetic monopoles with charge up to $2g_{\mathrm{D}}$.

1.4 High Electric Charge Objects

The search method for Dirac magnetic monopoles in this thesis relies on the highly ionizing nature of magnetic monopoles and the fact that, due to charge conservation, they do not decay into other particles making them long-lived. The selection criteria for magnetic monopoles of a few g_{D} in ATLAS is designed to detect long-lived Highly Ionizing Particles (HIPs), which also include particles with electric charges close to $|z| = 68.5$, as follows from Eq. 1.16. These are known as High Electric Charge Objects (HECOs). The electromagnetic coupling of HECOs is proportional to their charge $|z|$. Some examples of HECOs include micro-black hole remnants, up-down quark matter and strangelets, and Q-balls.

1.4.1 Micro-black hole remnants

If micro-black holes exist, they may be produced in the collisions at the LHC [44]. Remnants of these objects, such as collapsed nuclei with atomic mass A $>$ 1 and a radius smaller than ordinary nuclei, can have high electric charges and might be stable [45]. These objects are interesting to BSM searches because they are considered a dark matter candidates [46].

1.4.2 Up-down quark matter and strangelets

Ordinary nuclear matter is composed of up and down quarks confined in nucleons. Up-down quark matter (udQM) differs from ordinary matter in that the quarks are free to roam. Strange Quark Matter (SQM) is essentially udQM with equal numbers of up, down and strange quarks [47]. For low baryon number, $A \leq 10^2$, lumps of SQM are called strangelets. These have been suggested to be dark matter candidates [48]. Under certain conditions, strangelet matter is considered to be stable [49]. Studies on the stability of SQM have concluded that they can be composed of many particles, from a few to 10^{57} baryons [50], thus carrying a large electric charge. Searches for strangelets are mostly done in ultra-relativistic heavy-ion collisions.

1.4.3 Q-balls

Q-balls are localized fields that are stable. They get their name because they behave like homogeneous spheres of matter composed of many ($O(10)$) bosonic particles with electric charge [51] (where Q stands for electric charge). It is hypothesised that these particles existed as lumps of energy in the early universe. These configurations are stable because they are the lowest energy configuration of a set of particles. Since they are composed of many particles they can carry a large electric charge.

1.5 Outline of the thesis

This thesis documents the search for magnetic monopoles and other HIPs on data collected by the ATLAS detector from proton-proton collisions during Run 2 of the LHC (between 2015-2018). Chapter 1 covered the motivation behind a search for magnetic monopoles and other highly ionizing particles under the theory developed by Paul Dirac. Chapter 2 contains a brief description of the Large Hadron Collider and the ATLAS detector, outlining the experiment that allows for the collection of the studied data. The production of HIPs at the LHC, including the two pair-production mechanisms considered in this study, and the interaction of HIPs with matter are discussed in Chapter 3. This leads to a description of the simulation of such particles in the ATLAS detector in Chapter 4.

Once the conditions of the detector response to HIPs are known, Chapter 5 discusses the hardware and software triggers in place for data collection, as well as the variables used for signal selection. The studies for optimization of the selection criteria are consigned in Chapter 5. Chapter 6 addresses an attempt to improve signal discrimination with the use of machine learning which, although not applied for this particular study, is currently being considered for the next search for HIPs in ATLAS. Systematic uncertainties of the signal selection efficiencies are described in Chapter 7. The estimation on the number of background events in the signal region is found in Chapter 8 and the results of the analysis are presented in Chapter 9.

CHAPTER 2

The Large Hadron Collider and the ATLAS Experiment

The HIPs described in Chapter 1, such as Dirac magnetic monopoles, in the mass range of a few TeV might be produced by proton-proton collisions in the CERN Large Hadron Collider, and the ATLAS detector could be able to identify them. This chapter first describes the functioning of the LHC during the four-year period producing proton-proton (pp) collisions at a centre-of-mass energy of $\sqrt{s} = 13\,\text{TeV}$ known as Run 2, followed by some concepts used when discussing pp collisions. The ATLAS detector is then introduced, with special emphasis on the parts of the detector used in this work to detect HIPs.

2.1 The Large Hadron Collider

The LHC is a particle accelerator designed to produce high energy pp, lead ion-proton (Pb+p) and lead ion-lead ion collisions (Pb+Pb). This work only involves pp collisions.

Located at the CERN particle physics laboratory on the Swiss-French border near Geneva, the LHC consists of a 27 km circumference ring of superconducting electromagnets surrounding two beam pipes

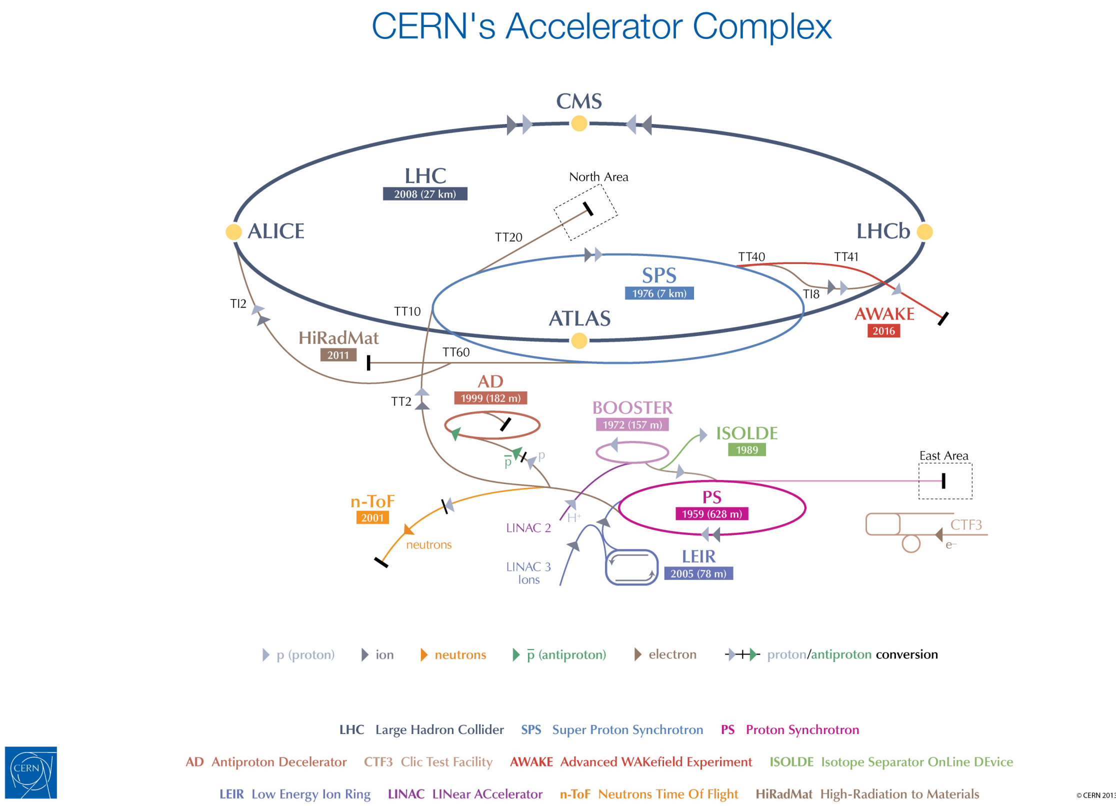

Figure 2.1: CERN's accelerator complex [52].

100 m below the surface. The magnets, which are kept at a temperature of −271.3 °C, both accelerate and guide particles inside the two ultra-vacuum beam pipes in which they travel. The LHC accelerates beams of protons up to 99.9999991% the speed of light and collides them at a centre of mass energy of $\sqrt{s} = 13\,\text{TeV}$. Protons are extracted from hydrogen gas by stripping the electrons. Prior to entering the LHC, protons are first accelerated in four stages, which take place in a chain of other linear and circular accelerators of the CERN accelerator complex shown in Figure 2.1. In the first stage, a linear accelerator (LINAC2) accelerates the protons to 50 MeV. In stage two, they reach energies of 1.4 GeV in the Proton Synchrotron Booster (PSB). The proton's energy is further increased to 25 GeV in the Proton Synchrotron (PS) and finally they are accelerated to 450 GeV in the Super Protron Synchrotron (SPS) before entering the LHC. These stages happen in a matter of seconds. When the proton beams are injected into the LHC, they are kept at an energy plateau for 20 minutes before ultimately accelerating them to 6.5 TeV, which takes 25 minutes.

Proton beams are injected into the two rings of the LHC, where they travel in opposite directions arranged in tightly packed groups of protons called **bunches**. During the final two years of Run 2, beams were made up of 2556 bunches. Each bunch contained anywhere between 1 and 1.25×10^{11} protons. A linear array of bunches (approximately 144 bunches) makes up a *train* [53].

At the four interaction points of the LHC ring, where each one of the main experiments (ATLAS, CMS, ALICE and LHCb) are located, collisions take place. Every 25 ns, bunches meet at these interaction points. In nominal conditions, interactions between bunches, or **bunch crossings**, continue taking place for approximately 10 hours until proton losses due to collisions reduce the number of protons in the beam to an amount that no longer provides sufficient collisions worthy of data collection. The data collected during the lifetime of a proton beam is called a **run** and the time intervals, of the order of 1 minute, within a run over which the luminosity and data taking conditions are considered constant are called **luminosity blocks**.

2.1.1 Luminosity

At a collider, the rate of events per second R is given by relating the probability of a collision, known as **Cross Section**[1] *(σ)*, and the **Luminosity** L of the collider:

$$R = L \times \sigma. \tag{2.1}$$

Luminosity (with units of $\mathrm{m^{-2}s^{-1}}$ or $\mathrm{b^{-1}s^{-1}}$) is the number of collisions that can be produced in a unit area each second, and depends on the design parameters of the collider. The cross section depends on the physical process taking place, in this case, a pp collision. The luminosity of the LHC at the beginning of a run is $1{\times}10^{32}\,\mathrm{cm^{-2}\,s^{-1}}$.

Integrating the luminosity over time results in the number of collisions per unit area, also known as integrated luminosity $\mathcal{L}$:

$$\mathcal{L} = \int L dt. \tag{2.2}$$

[1]The cross section is given in units of area known as *barn*: $b = 10^{-28}$ m^2.

The integrated luminosity delivered by the LHC during Run 2 was $156\,\mathrm{fb}^{-1}$ [54].

2.1.2 pp collisions

Protons are composed of three valence quarks: up, up and down. The large mass difference between the proton and the mass of the valence quarks is due to binding energy. Valence quarks exchange gluons that may decay into quark-antiquark pairs; these are known as the *sea quarks*, which can later recombine into gluons. Valence quarks, gluons and sea quarks are called *partons*. High energy beams of protons, such as the ones created at the LHC, can be thought of as beams of quasi-free partons, which share the momentum of the proton [55]. High momentum transfer interactions of two partons, one from each proton in the collision, are known as a **hard scatter**. The rest of the proton constituents may participate in lower momentum transfer interactions in what is called the **underlying event** (UE).

During the interaction between two proton bunches, multiple hard scatter events may happen. These simultaneous events are known as **pileup**. The variable that accounts for the average number of interactions per bunch crossing across a luminosity block is average μ, $\langle\mu\rangle$.

2.2 The ATLAS experiment

The A Toroidal LHC ApparatuS (ATLAS) experiment is a general-purpose detector located at one of the collision points of the LHC. During Run 2 of the LHC, ATLAS recorded a total integrated luminosity of $147\,\mathrm{fb}^{-1}$. The $\langle\mu\rangle$ range covered in these four years of data collection is summarized in Figure 2.2. The ATLAS detector is a 44 meter-long cylinder with 25 m diameter end-caps. The LHC beam-pipe runs through its centre, lengthwise, defining the z-axis, where the nominal collision point defines the origin of the coordinate system, as illustrated in Figure 2.3. The x-axis points towards the centre of the LHC ring and the y-axis upwards. The azimuthal angle ϕ is measured around the z-axis, and the polar angle θ is measured from the z-axis. These two angles are measured in radians. The

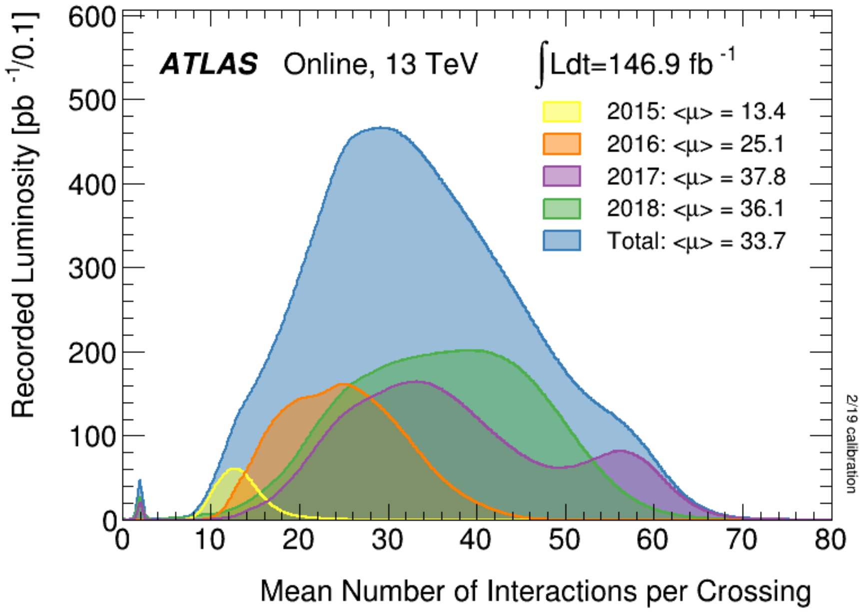

Figure 2.2: Recorded luminosity over the four years of Run 2 collected by ATLAS as a function of the number of interactions per bunch crossing [54].

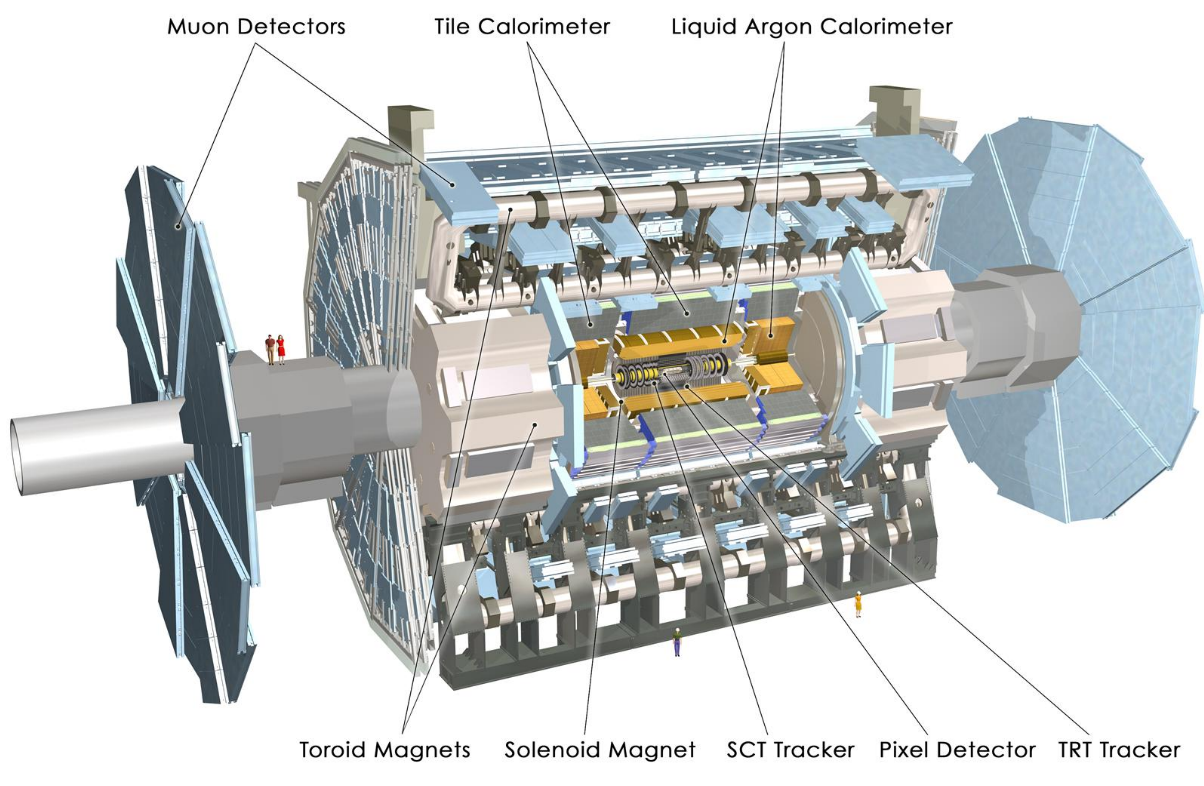

Figure 2.3: Computer generated image of the ATLAS detector [56].

pseudorapidity[2] η describes the angle with respect to a line perpendicular to the z-axis ($\eta = 0$ being completely perpendicular to the beam-pipe, and $\eta = \infty$ in the direction of the beam-pipe). The ATLAS detector is composed of the Inner Detector, which is the tracking system, the Calorimeter System, and the Muon Spectrometer. Two superconducting magnet systems, one solenoidal surrounding the ID and the other toroidal containing the Muon Spectrometer, bend the trajectory of charged particles. A trigger system is also in place to make quick decisions on which events have characteristics that are considered interesting for physics analysis and are worth recording.

For the purpose of this work, our attention will be mainly focused on the Transition Radiation Tracker (TRT), which is the outermost layer of the Inner Detector, and the calorimeters.

2.2.1 Inner Detector

The ATLAS Inner Detector (ID) provides high precision tracking of charged particles covering the pseudorapidity region $|\eta| < 2.5$. The primary role of the Inner Detector is to determine the momentum of charged particles. To achieve this, energy depositions recorded in individual detector elements, i.e., pixels, semi-conductor sensors or drift chambers, are used to reconstruct the trajectories of charged particles immersed in a 2 T magnetic field. The Inner Detector is able to reconstruct particle trajectories, known as *tracks*, with transverse momentum [3] $p_T > 0.5$ GeV.

The Inner Detector is composed of four independent subdetectors and is surrounded by a superconducting solenoid magnet. Figure 2.4 illustrates the barrel configuration of the subdetectors in the ID and the radial range they cover with respect to the LHC beam pipe. The subdetectors are the Insertable B-Layer (IBL), the Pixel detector, the Semi-Conductor Tracker (SCT) and the TRT. The IBL, Pixel and SCT detectors use semiconductor technology, while the TRT is a Xenon-based drift chamber composed of straw tubes. A layout of the different components with the $|\eta|$ ranges covered by each is found in Figure 2.5.

The IBL was introduced for Run 2 with the purpose of observing particle signals closer to the collision point [59]. Located only 3.35 cm away from the beam-pipe axis, the IBL consists of 14 staves providing

[2] Defined as $\eta = -\ln[\tan(\theta/2)]$, where θ is the angle with respect to the z-axis.
[3] The transverse momentum is the component of momentum perpendicular to the beam axis.

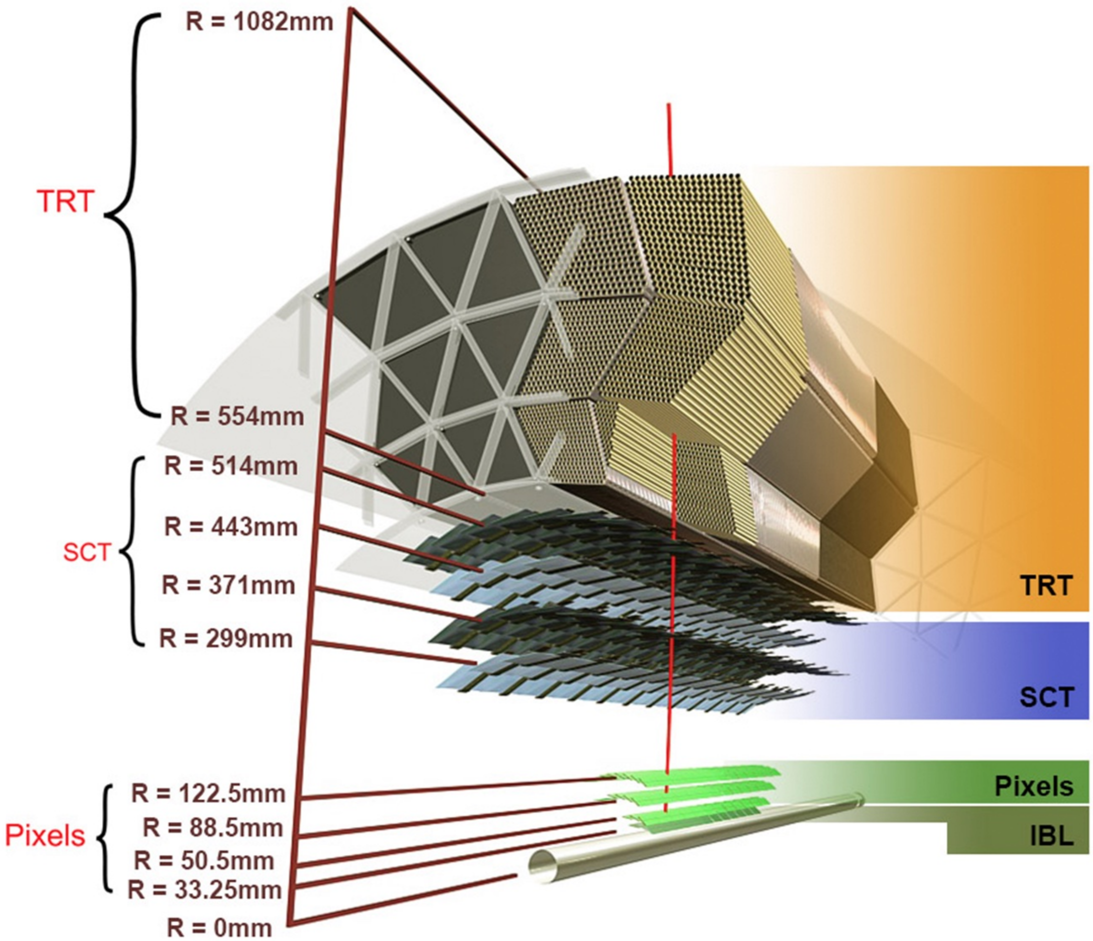

Figure 2.4: Transverse slice of the structure of the barrel portion of the ATLAS Inner Detector [57].

full azimuthal coverage. Each stave supports 20 pixel sensor modules composed of pixel cells of size $250 \times 50\,\mu\text{m}^2$, allowing for high track extrapolation capabilities. It was designed to resist the high radiation conditions near the collision point.

The pixel detector consists of three concentric barrel layers and end-caps at each end. Due to its high granularity pixel cells ($50{\times}400\,\mu\text{m}^2$), it provides three precision measurements for each track. The readout electronics of the pixel sensors measure dE/dx by integrating over the time during which the collected charge was above a threshold value, known as time-over-threshold (ToT) [60].

The SCT surrounds the pixel detector and is composed of a four-layer barrel and nine disks making up end-caps at both ends of the barrel. The SCT modules consist of two misaligned back-to-back

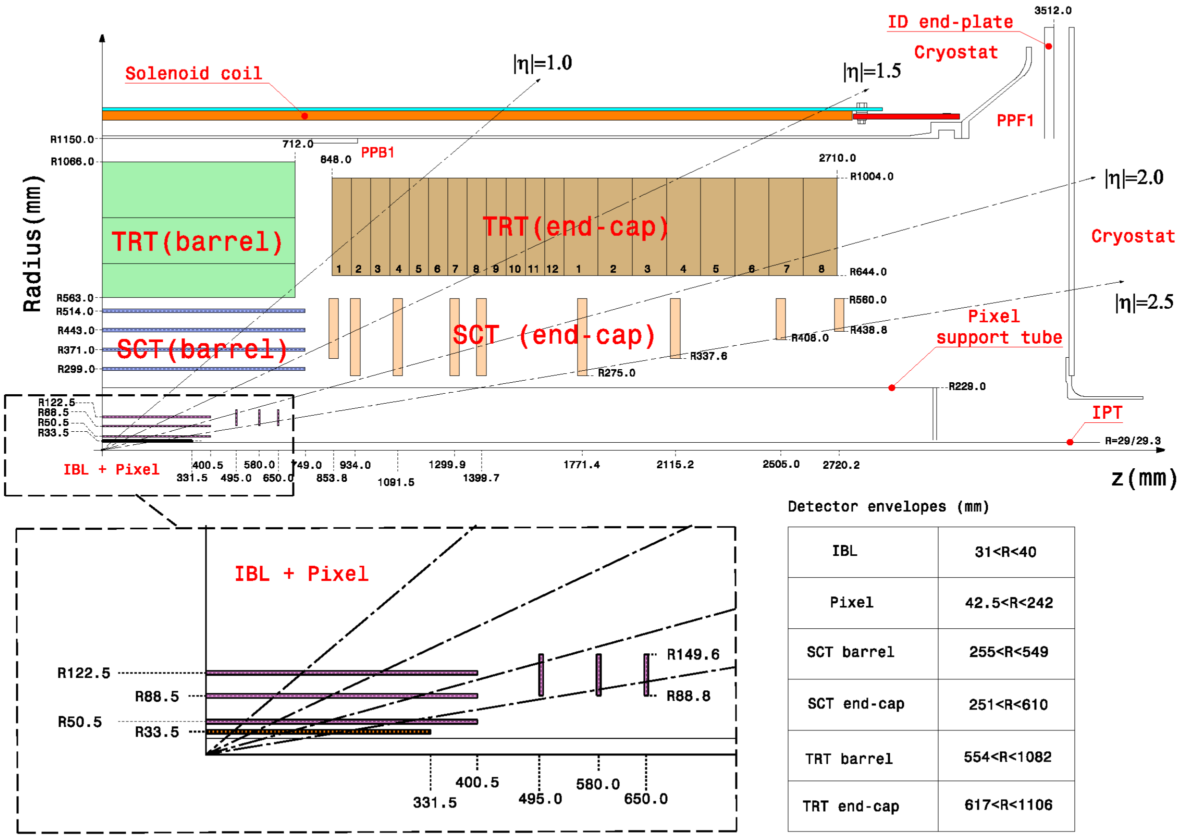

IBL	31<R<40
Pixel	42.5<R<242
SCT barrel	255<R<549
SCT end-cap	251<R<610
TRT barrel	554<R<1082
TRT end-cap	617<R<1106

Figure 2.5: Quarter portion schematic of the layout of the ATLAS Inner Detector. The Inner Detector has azimuthal as well as z symmetry. [58]

micro-strip sensors. The 40 mrad misalignment increases precision in the z-axis. The SCT provides at least eight high precision measurements per track, which contribute to the measurement of momentum, impact parameter and vertex position [61].

The outermost layer of the Inner Detector is the TRT. It is a drift tube tracking detector composed of a barrel covering the range $|\eta| < 1.07$, where 73 layers of 4 mm diameter straws run parallel to the beam-pipe, and two end-caps, covering the range $0.625 < |\eta| < 2.0$, composed of 160 layers of straws arranged radially around the beam-pipe distributed along 12 wheels at each end of the barrel. The $0.625 < |\eta| < 1.07$ region is called the *transition region*, given that a track with a pseudorapidity in this range would traverse both barrel and end-cap. The straws that make up the TRT are filled with a mixture of either 70% Xenon or Argon mixed with 27% CO_2 and 3% O_2, which is ionized when a charged particle traverses the straw. The wall of the straw, made of Kapton, is held at a potential

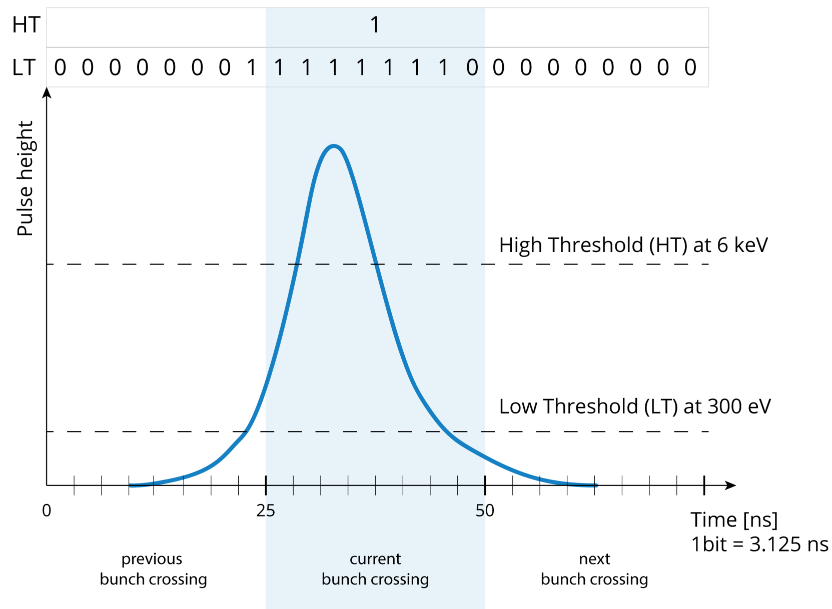

Figure 2.6: TRT readout of a signal pulse in one TRT straw. Each of the three 25 ns bunch crossings considered in the digitization of the pulse is recorded as a byte of information. The information of the low threshold is recorded for all three bunch crossings, while the digitization of the high threshold only considers the current bunch crossing. The high and low threshold values shown are for Xenon gas.

with respect to a wire in its centre, making the electrons drift in the electric field and produce a signal that is discriminated against two thresholds: a low threshold of 300 eV (100 eV) and a high threshold of 6 keV (2 keV) for Xenon (Argon), as seen in Figure 2.6. Energy deposits exceeding these thresholds are called *low-threshold* and *high-threshold* hits, respectively. Low-threshold (Low Threshold (LT)) hits are considered for track reconstruction. High-threshold (High Threshold (HT)) hits are used mostly for particle-ID purposes.

2.2.2 Calorimeter

Surrounding the solenoid magnet of the Inner Detector, the calorimeter system is responsible for measuring the energy of particles and contributing to particle identification. It is composed of a Liquid Argon calorimeter (LAr) Electromagnetic (EM) calorimeter, a Hadronic Calorimeter (HCal) and a forward calorimeter (see Figure 2.7).

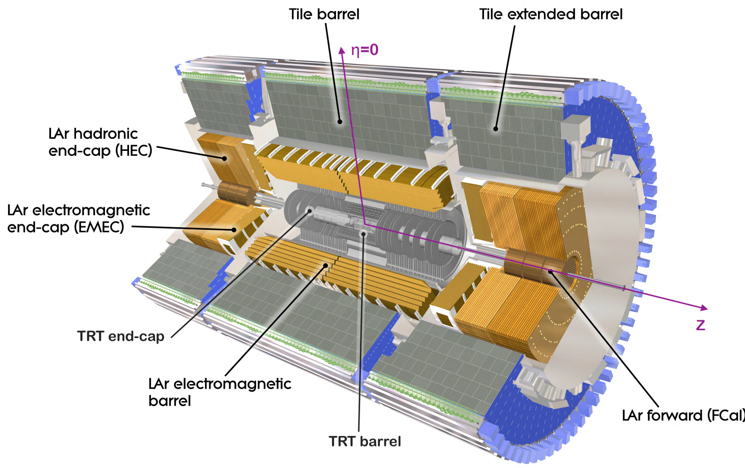

Figure 2.7: Cut away view of the Inner Detector and Calorimeters in the ATLAS Detector. The Calorimeter components are highlighted and labelled.

The LAr Electromagnetic Calorimeter consists of a barrel (in the $|\eta| < 3.2$ region) and end-caps (covering $1.375 < |\eta| < 3.2$). It is made of an accordion-shaped structure of passive lead absorbers and cells of copper electrodes, separated by active absorption layers of liquid Argon. Energy absorption happens when an incident particle interacts with the passive lead absorber, ionizing electrons that drift in the LAr gap where an electric field is applied. A signal is then induced in the readout electrodes on the copper cells. There are 2-4 layers in the whole LAr calorimeter, depending on the η region. The granularity ($\Delta\eta \times \Delta\phi$) of the copper cells varies for each layer, as seen from Figure 2.8. The hadronic calorimeter consists of steel absorbers and scintillating tiles, covering the barrel region ($|\eta| < 1.7$) and end-caps ($1.5 < |\eta| < 3.2$). A *tower* is an array of cells that are stacked up on top of each other in the radial direction for the different layers of the calorimeter.

2.2.3 Muon Spectrometer

The outermost system of the ATLAS detector is the Muon Spectrometer. Muons are the only charged particles expected to reach beyond the calorimeters. The spectrometer covers the range of $|\eta| < 1.4$ with its barrel, $1.6 < |\eta| < 2.7$ with end-caps, with a transition region between $1.4 < |\eta| < 1.6$. Immersed in a magnetic field produced by the large superconducting air-core toroid magnets for track bending purposes, it takes measurements with both separate fast trigger components and high-precision

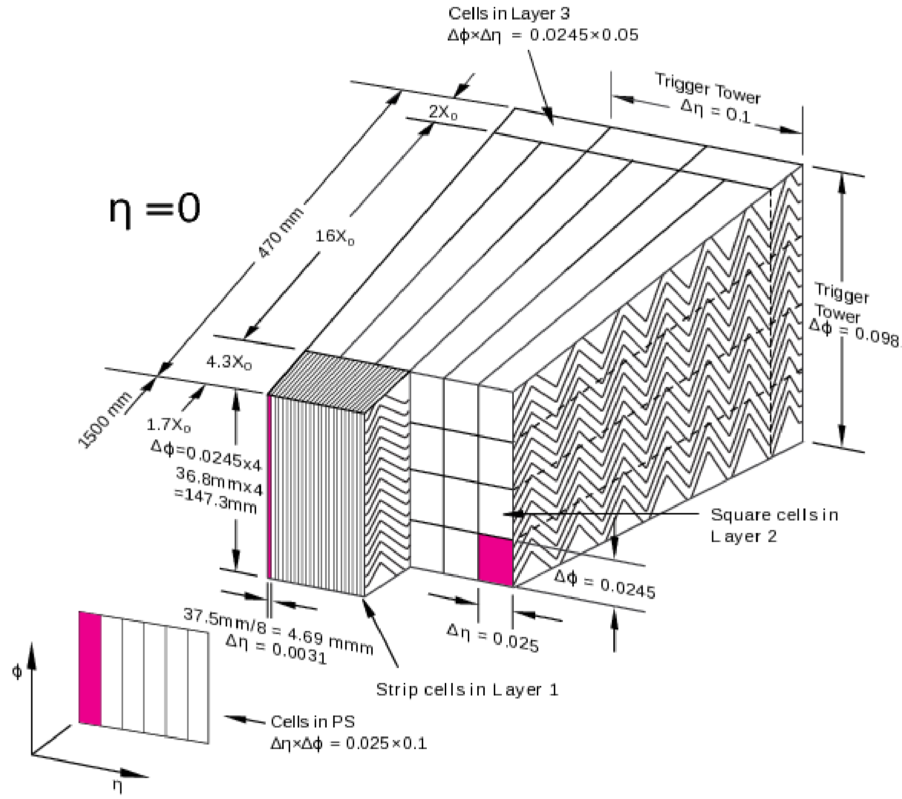

Figure 2.8: Schematic with granularity values of a section of the Liquid Argon Electromagnetic calorimeter at $\eta = 0$ [62].

tracking chambers.

2.2.4 Trigger system

Each event recorded by the ATLAS detector takes up around 1.7 MB of memory. Storing the information for every event that takes place during a second would require about $O(100)$ TB. The ATLAS trigger system reduces the recorded event rate from 40 MHz to approximately 1.2 kHz (around 1.5 GB of data per second) by making quick decisions on which events are interesting for physics analysis. The decision is made by *trigger chains*, which are combinations of a Level 1 (L1) hardware trigger and one or more software triggers known as High Level Triggers [63]. L1 triggers are hardware triggers in the calorimeters or the muon system that reduce the rate from 40 MHz to a read-out rate of 100 kHz with a 2.5 μs response latency. L1 also flags sets of information in the collected data known as detector Regions of Interest (RoIs), such as a group of calorimeter cells, which are relevant for further consideration.

The High Level Triggers (HLT) are a set of software algorithms run online that use the information either from the RoIs or the full event to make decisions about whether or not an event that passed the L1 trigger should be kept. The physics trigger menu contains all chains and prescaling values[4] for physics analyses. The data collected by the entirety of the physics menu is limited by the bandwidth of the output, which is $\sim$2.5 GB s^{-1}. Thus, each chain has a limit in the acceptance rate. Ultimately, within 0.2 s the HLT reduces the rate to $\sim$1.2 kHz.

The L1 and HLT triggers used for data collection in this thesis take advantage of the signature of the particles studied, described in Chapter 3. This trigger chain will be described in Chapter 5.

[4]For a prescale value of n, an event has a probability of 1/n to be kept e.g., a prescaling of five means that one out of every five events that passed the L1 trigger will be considered by the HLT.

CHAPTER 3

Physics of Highly Ionizing Particles

The proton-proton collisions at the LHC are compatible with two pair-production mechanisms for highly ionizing particles, i.e., Drell-Yan and photon fusion, both of which are considered for the interpretation of the results of this search. An explanation of the interactions of HIPs with matter, in the kinematic regime considered in this search, is presented.

3.1 Creation of HIPs at the LHC

Two pair-production mechanisms are considered as benchmark models to interpret and compare the results of this search. Given the strong coupling of the HIP with the photon, perturbative calculations beyond leading order of the production cross sections are precluded. The Drell-Yan (DY) pair-production mechanism consists of a quark-antiquark annihilation mediated by a virtual photon, which decays into a HIP-anti-HIP pair. The Photon Fusion (PF) mechanism is included for the first time in a HIP search at the ATLAS detector, and consists of a pair of photons radiated from the colliding

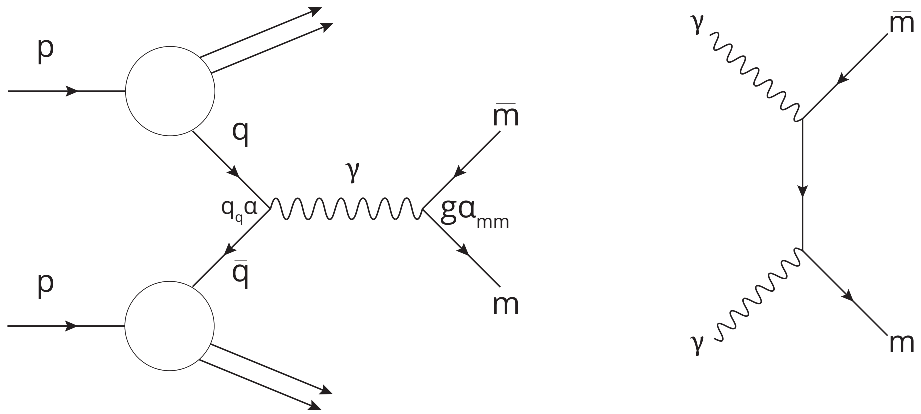

Figure 3.1: Feynman-like diagrams for the DY (left) and PF (right) production mechanisms for monopoles. The coupling strength given by the charge of the quark q_q times the electromagnetic coupling constant α and the magnetic charge g times the magnetic coupling constant α_{mm}. Analogous diagrams describe HECO production.

protons fusing and producing a HIP-anti-HIP pair. Both Drell-Yan and photon fusion production mechanisms are illustrated in Feynman-like diagrams in Figure 3.1. Through the Drell-Yan and photon fusion mechanisms, fermionic (spin-½) and bosonic (spin-0) HIPs can be produced, both of which are considered in this thesis. Two properties of these pair production mechanisms that are not illustrated in Figure 3.1 are that the production of scalar HIPs via the photon fusion pair-production mechanism also has contributions from a 4-point vertex and the HECO spin-½ Drell-Yan production can be mediated by either the photon or Z boson. Magnetic monopole production through the Drell-Yan mechanism cannot be mediated by the Z boson because they do not interact via the weak force. Additionally, spin-0 HECOs cannot be produced by Z boson exchange because, assuming SM interactions, they only couple with the Z boson through tri-linear or quadra-linear interactions. Furthermore, the 4-point vertex only produces spin-0 HIPs due to angular momentum conservation.

HIPs produced at the LHC in $\sqrt{s}$ =13 TeV proton-proton collisions through these production mechanisms can take masses up to 4 TeV [64]. Additionally, their speed is relativistic, with the bulk of them having velocities relative to the speed of light $\beta = \frac{v}{c} > 0.1$ and a Lorentz factor $\gamma < 100$.

3.2 Interaction with matter

A particle with electric and/or magnetic charge interacts electromagnetically, experiencing a force defined by the modified Lorentz force:

$$\vec{F} = q(\vec{E} + \vec{v} \times \vec{B}) + g(\vec{B} + \vec{v} \times \vec{E}). \tag{3.1}$$

From the Lorentz force in Eq. 3.1 it is seen that an magnetic monopole of magnetic charge g, with velocity relative to the speed of light β, in the presence of the electric field $\vec{E}$ of an electron, would experience a force with magnitude $gc\beta e$. The magnitude of the force of the electric field $\vec{E}$ on the magnetic monopole is almost two orders of magnitude greater than that of an electron in the same field, considering the electric charge equivalence given by Eq. 1.16, i.e., $g_{\mathrm{D}} = 68.5\ e$. This dictates the way in which magnetic monopoles interact with electrons in atoms, as will be described in the following sections.

3.2.1 Ionization

As an electrically charged particle traverses matter, it interacts with atoms through a process known as ionization, losing energy at a mean rate per unit length (also known as stopping power) given by the Bethe-Bloch formula found in Eq. 3.2 [65],

$$-\frac{dE}{dx} = \frac{4\pi e^4 z^2 N_e}{m_e c^2 \beta^2}\left[\ln\left(\frac{2m_e c^2 \beta^2 \gamma^2}{I}\right) - \beta^2 - \frac{\delta}{2}\right], \tag{3.2}$$

where z is the electric charge of the traveling particle in units of e, N_e is the electron density of the material, $m_e c^2$ is the electron rest energy, I the mean ionization energy of the material and δ is the density effect correction.

For particles with magnetic charge g, an analogous formula to describe ionization stopping power is needed. As mentioned above, the magnitude of the force between magnetic monopoles and the field of an electron is dictated by β, to first order replacing the parameter for the electric charge z with $gc\beta$ in Eq. 3.2 would give approximate values for the stopping power. Steven Ahlen developed the formula found in Eq. 3.3 to describe the stopping power of magnetic monopoles due to ionization [66]. This formula considers both the high-momentum transfer (characteristic of close interactions) by introducing the $k(g)$ term known as the KYG correction [67] written explicitly in Eq. 3.4, and the low-momentum transfer (for long distance interactions) through the Bloch correction $B(g)$ in Eq. 3.5, arising from low-energy collisions in which the monopole velocity approaches the orbital velocity of the electron. According to Ref. [66], dE/dx has an uncertainty of 3% for monopoles in the energy regime studied in this analysis.

$$-\frac{dE}{dx} = \frac{4\pi e^2 g^2 N_e}{m_e c^2}\left[\ln\left(\frac{2m_e c^2\beta^2\gamma^2}{I}\right) + \frac{k(g)}{2} - \frac{1}{2} - \frac{\delta}{2} - B(g))\right] \tag{3.3}$$

$$k(g) = \begin{cases} 0.406 & |g| \leq 1\ g_{\mathrm{D}}, \\ 0.346 & |g| \geq 1.5\ g_{\mathrm{D}}, \end{cases} \tag{3.4}$$

$$B(g) = \begin{cases} 0.248 & |g| \leq 1 g_{\mathrm{D}}, \\ 0.672 & |g| \geq 1.5 g_{\mathrm{D}}, \end{cases} \tag{3.5}$$

Both the stopping powers of electrically (Eq. 3.2) and magnetically (Eq. 3.3) charged particles are directly proportional to the square of the charge. As expected, the energy losses by ionization of a $|g| = 1g_{\mathrm{D}}$ magnetic monopole are four orders of magnitude larger than those of an electrically charged particle with charge $|z| = 1$. Thus, magnetic monopoles and HECOs are highly ionizing.

Figure 3.2 illustrates the ionizing stopping power of HECOs with charge $|z| = 68.5$ and magnetic monopoles with charge $|g| = 1g_{\mathrm{D}}$. The energy loss due to ionization of HECOs, following the Bethe-Bloch formula, decreases with increasing β. As the HECO slows down at the end of its trajectory, it loses a larger amount of energy. The opposite happens with magnetic monopoles, due to the missing $1/\beta^2$ dependence; the larger monopole energy depositions occur at higher speeds.

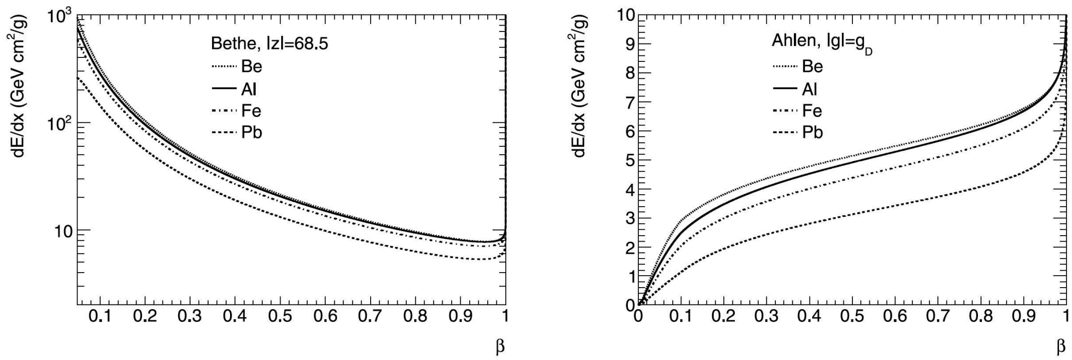

Figure 3.2: Ionization stopping power of HECOs with charge $|z| = 68.5$ (left) and magnetic monopoles of charge $|g| = 1g_{\mathrm{D}}$ (right) as a function of the speed relative to the speed of light β for non-relativistic and relativistic particles, in various materials [68].

3.2.2 Bremsstrahlung

Charged particles also lose energy through the Bremsstrahlung mechanism. This energy loss occurs through the emission of photons when the charged particle is accelerated by the field of another charged particle or a nucleus. The amount of Bremsstrahlung energy loss of a magnetic monopole is given by Eq. 3.6 (for electrically charged particles it can be found in Ref. [69],

$$-\frac{dE_{rad}}{dx} = \begin{cases} \dfrac{16NZ^2e^2g^4}{3\hbar Mc^3} & \beta \ll 1, \\ \dfrac{16NZ^2e^2g^4}{3\hbar Mc^3}\gamma \ln\left(\dfrac{233M}{Z^{1/3}m_e}\right) & \gamma \gg 1, \end{cases} \tag{3.6}$$

where M, g and γ are the mass, magnetic charge and Lorentz factor of the magnetic monopole, respectively. N and Z are the atomic density and number of the material. The mass of the HIP in the denominator becomes an important factor when comparing energy loss due to Bremsstrahlung and the stopping power through ionization.

3.2.3 Pair production

The magnetic field of fast ($\gamma \gg 1$) magnetic monopoles can induce a transverse electric field given by

$$\vec{E}_{\perp} = -\gamma\vec{\beta} \times \vec{B}. \tag{3.7}$$

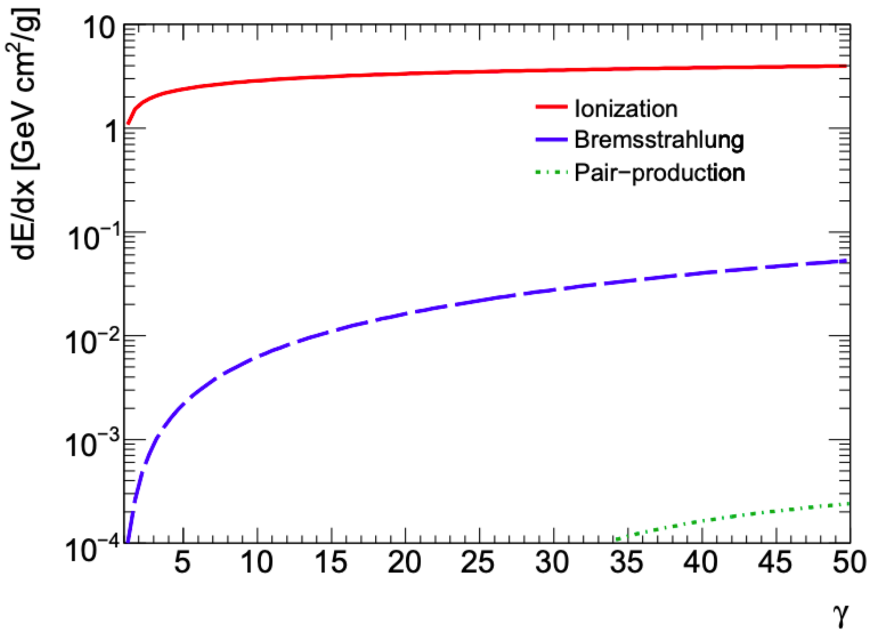

Figure 3.3: Energy loss as a function of the Lorentz factor, γ, for $1g_D$ magnetic monopoles of mass 1000 GeV, traversing Argon. Three energy loss mechanisms are considered: Ionization (solid-red), Bremsstrahlung (dashed-blue) and Pair-production (dotted-green).

The equivalent photon approximation described in Ref. [70] indicates that this field would resemble a beam of photons. Papageorgiu and Stodolsky argue that these quasi-photons can decay into electron-positron pairs when interacting with matter. Nevertheless, the energy loss due to the production of these pairs is only significant for ultra-relativistic particles with $\gamma \gg 1$, which is not the case for HIPs produced at colliders in the mass range considered here [71].

Figure 3.3 shows the three energy-loss mechanisms described in this chapter for a representative mass 1 TeV HIP, in the range of $0 < \gamma < 50$. HIPs produced at the LHC would mostly have $\gamma < 10$, making ionization the dominant mechanism of energy loss by two orders of magnitude.

CHAPTER 4

Signal Simulation and Data

The highly ionizing nature of HIPs creates a distinct signal in the ATLAS detector. In this chapter, the response of the two subdetectors that record the signal relevant for identification of a HIP is discussed. The simulation of HIP kinematic properties and detector signal response is briefly described. The types of Monte Carlo signal samples generated are listed with their intended purposes. Finally, the data sample collected is described.

4.1 Detection of HIPs in ATLAS

Figure 4.1 illustrates the acceptance of HIPs for ranges of charge and mass, allowed by Drell-Yan spin-½ pair production at $\sqrt{s}$ =14 TeV, in the ATLAS detector. The magnetic and electric charges considered in this thesis are: HECOs with charges $|z| = 20, 40, 60, 80$ and 100, and monopoles with charges $|g| = 1$ and $2g_{\mathrm{D}}$. The journey of a HIP with the mass and charge characteristics studied in this thesis, in the ATLAS detector, can be roughly described as follows: the particle is created close to the

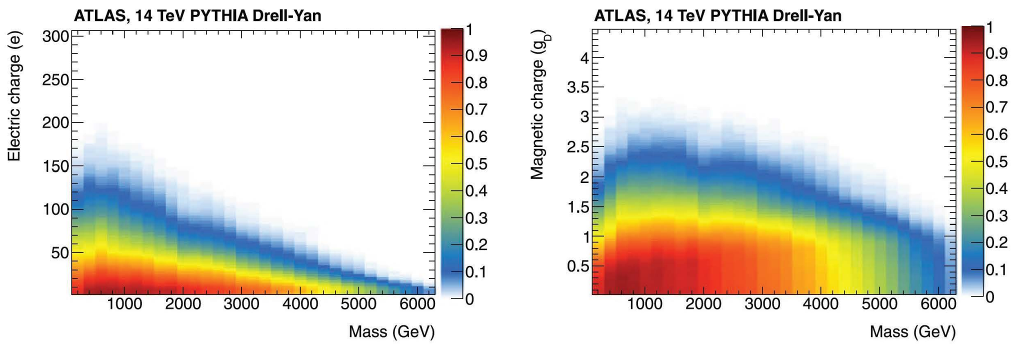

Figure 4.1: Acceptance of spin-½ HECOs (left) and spin-½ magnetic monopoles (right) as a function of electric (magnetic) charge and mass produced through the Drell-Yan mechanism with $\sqrt{s}$ =14 TeV proton-proton collisions [68].

interaction point inside the beam-pipe, those with sufficient energy to punch through the beryllium tube will travel across the inner detector, most likely reaching the second or third layer of the LAr EM Calorimeter before losing all of their kinetic energy and stopping completely. A more detailed explanation on the penetration depth of HIPs in ATLAS can be found in Ref. [68]. Figure 4.2 is an event display of the signal left by a simulated magnetic monopole with charge $1g_{\mathrm{D}}$ and mass 1000 GeV in the TRT and LAr EM calorimeter of the ATLAS detector. The information collected by these two subdetectors is used to discriminate the signal of a HIP from other particles.

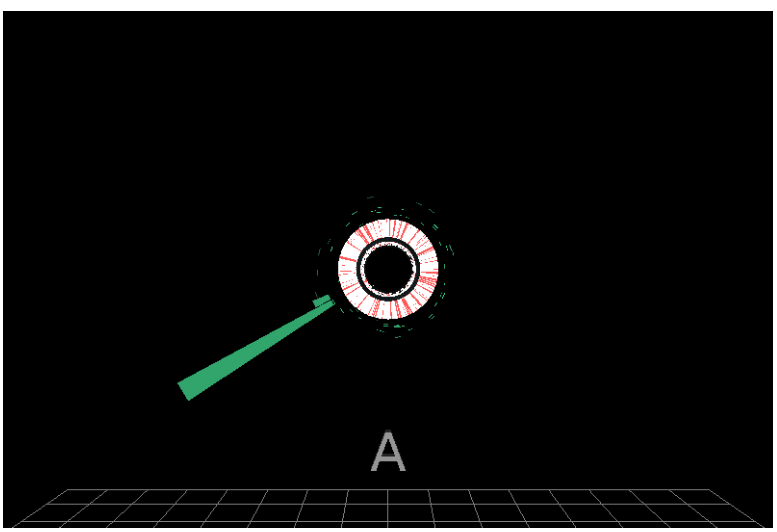

Figure 4.2: Event display of a single $1g_{\mathrm{D}}$ magnetic monopole. The ATLAS detector is seen through a transverse slice of the detector from side A. The green segments represent energy clusters in the LAr EM calorimeter and the white and red dots are LT and HT hits in the TRT detector.

4.1.1 Signal of a HIP in the TRT

Unlike some subdetectors of the Inner Detector, the TRT produces a signal for energy depositions of any magnitude. The pulse containing the energy deposition in a straw of the TRT, described in Section 2.2.1 and illustrated in Figure 2.6, is digitised for three consecutive bunch crossings each represented by nine bits. The first bit of each bunch crossing is the flag indicating whether this was a High Threshold (HT) hit. The following eight bits indicate if the Low Threshold (LT) was passed. For the 2016, 2017 and 2018 data collection years, only the middle bunch crossing HT flag was considered to identify HT hits. To make the information from the data collection uniform, this same condition was applied to the 2015 data and all the simulated samples when the analysis ntuples were made.

The energy deposition of a HIP in a straw of the TRT is three to four orders of magnitude larger than that of minimum ionizing particle. Additionally, the energy deposited is large enough to eject electrons from the inner orbitals of the atom. These electrons, known as δ-rays, have energies that can ionize the material further. The energy of the δ-rays, which account for 30% of the energy lost by HIPs [72], is given by

$$E_{\delta,max} = 2m_e \frac{E_{\text{HIP, kin}}}{m_{\text{HIP}}} \left(\frac{E_{\text{HIP, kin}}}{m_{\text{HIP}}} + 2 \right). \tag{4.1}$$

For the HIP masses considered in this search and corresponding kinetic energies, $E_{\delta,max}$ ranges from 0.1 MeV to over 100 MeV. The trajectory in the TRT is defined by the 2 T field, which in the energy ranges described, can produce a radius of curvature on the order of a few millimeters. Consequently, the δ-rays can reach an adjacent straw. Although a single δ-ray, which typically deposits 2 keV in each straw, will not produce an HT hit, a combination of several δ-rays can deposit enough energy to produce HT hits in neighbouring straws to the path of the HIP. Hence, the signature of HIPs is defined by numerous HT hits within a few millimeters of the path of the HIP. On average, 70% of the straws within an 8 mm-wide road around the HIP trajectory will have HT hits, while the probability for minimum ionizing particles to produce a HT hit in a straw is around 10% and for electrons it is between 30 to 40% [73].

4.1.2 Signal of a HIP in the LAr EM calorimeter

As HIPs traverse the electromagnetic calorimeter, they ionize the argon atoms and the liberated electrons are detected. Since HIPs produce a high ionization, there is a possibility of electron-ion recombination, reducing the observed energy deposition in the calorimeter. At low dE/dx the energy recorded considering this recombination effect is described by Birks' law [74, 75],

$$E_{\text{vis}} = E_0 \frac{1 + A' k / E_D}{1 + k/(\rho E_D) dE/dx}, \tag{4.2}$$

where E_{vis} is the detected energy, E_0 the true energy deposited, $A = 1.51$ is a renormalization parameter specific to the ATLAS detector [76], dE/dx is the energy deposited per unit length, ρ is the density of liquid argon and E_D is the voltage of the drift electric field: $10\,\mathrm{kV\,cm^{-1}}$. Birks' constant, k, is taken to be $k = 0.0486$ (kV/cm)(g/cm2)(1/MeV) [77]. For large dE/dx, as is the case with HIPs, this law requires a correction defined in Ref. [72]. This correction is included in the simulation of HIPs in the ATLAS detector.

The dominance of ionization over Bremsstrahlung and pair production results in a lack of electromagnetic cascades from the HIP in the LAr EM calorimeter. Thus, the energy deposition in the LAr EM calorimeter has a characteristic narrow lateral dispersion.

The reconstruction of information in the ATLAS calorimeters is done in different ways, most of which lead to objects known as clusters. These objects are sets of calorimeter cells that are grouped based on proximity and energy deposition. For the purpose of this study, clusters are processed through a topological cell clustering algorithm which creates calorimeter cluster objects known as topological clusters, or topo-clusters, based on cell proximity and removes cells that are deemed to have large noise-to-signal ratios or very low energy deposition [78].

4.2 Monte Carlo signal samples

In high energy physics Monte Carlo (Monte Carlo (MC)) signal samples are vital. Regardless of their limitations in this analysis due to the non-perturbative nature of the production of HIPs, they are used to compute the production cross sections of the production mechanism and to understand the signal of a HIP in the detector, ultimately leading to the computation of signal selection efficiencies.

Three types of signal samples are produced: model-independent fully simulated samples, Drell-Yan spin-½ fully simulated samples and generator-level signal samples. Additional model-independent fully simulated samples with parameter variations are generated to compute systematic uncertainties. Each of type of signal sample will be described in Section 4.2.1. The model-independent, Drell-Yan spin-½ and model-independent for systematics MC samples are fully simulated. The steps of the full simulation are described in Sections 4.2 and 4.2.4.

4.2.1 Event generation

Model-independent fully simulated samples

The detector response to a specific particle (of a given mass and charge) is only dependent on the kinematic properties of the particle, i.e., all magnetic monopoles of a given mass and charge combination with the same kinematic properties will produce the same signal in the detector, barring random fluctuations. Therefore, the signal selection efficiencies for any production mechanism can be computed from model-independent fully simulated signal samples. Model-independent MC signal samples are composed of single particle events with uniform kinematic distributions of kinetic energy E_{K} and pseudorapidity η. The η range of these samples is limited by the TRT acceptance region, $-2 < \eta < 2$, and the kinetic energy range is defined by the maximum allowed pair-production energy, $10\,\mathrm{GeV} < E_{\mathrm{kin}} < 4000\,\mathrm{GeV}$. These samples are produced in this HIP search for two reasons. First, it is possible to determine the minimum values of transverse momentum, p_{T}, at which a HIP of a given mass and charge is able to fire a trigger and consequently use computing resources more efficiently by only simulating particles with enough transverse momentum to be recorded by the detector. This is computed in Section 5.1.3. Second, signal selection efficiencies for any production mechanism can be estimated from model-independent signal selection efficiency maps. This will be further explained in Section 5.3.

The production of model-independent HIP MC samples is done through the ParticleGun generator ATLAS software (particularly, AtlasProduction 19.2.5.38, tag e7852). MC samples with 120 000 events were created for the 56 mass and charge combinations considered in the analysis. To better represent the conditions of the data collected across the different years of Run 2, three conditions profiles, known as campaigns, are used: MC16a for 2015 and 2016, MC16d for 2017 and M16e for 2018. Each sample has 30 000 events in MC16a, 40 000 events in MC16d and 50 000 events in MC16e.

The remaining three stages of MC sample production (simulation, digitization and reconstruction) will be explained in Sections 4.2 and 4.2.4.

Systematic uncertainty signal samples

MC samples with variations of the simulation parameters are necessary to assess systematic effects on signal efficiencies. These model-independent signal samples are created with 10 000 events and the extrapolation method described in Section 5.3 is used to estimate signal efficiencies in these modified conditions to ultimately assign systematic uncertainties to the signal efficiency, as will be explained in Chapter 7.

Generator-level signal samples

The MadGraph5_aMC@NLO [79] leading-order matrix element generator is used to compute production cross sections and generate particle four vectors [E, $\vec{p}$]. The A14 tune [80] is applied and two Parton Distribution Functions (PDFs) are used: NNPDF23LO [81] for the Drell-Yan pair production and LUXqed [82] for the photon fusion pair production samples. Different PDFs are used considering the Drell-Yan pair production occurs when quarks interact and the photon fusion occurs when photons interact. Transverse momentum cuts, derived as will be explained in Section 5.1.3, are applied. The four-vectors are processed by the Monte Carlo generator Pythia [83], which adds momentum smearing, parton shower and hadronization effects, and decays of the byproducts of the simulated proton-proton collisions.

Theoretical production cross sections are computed for the four production mechanisms for all 56 mass and charge combinations, as seen in Figure 4.3. Truth kinematics properties for particles of all

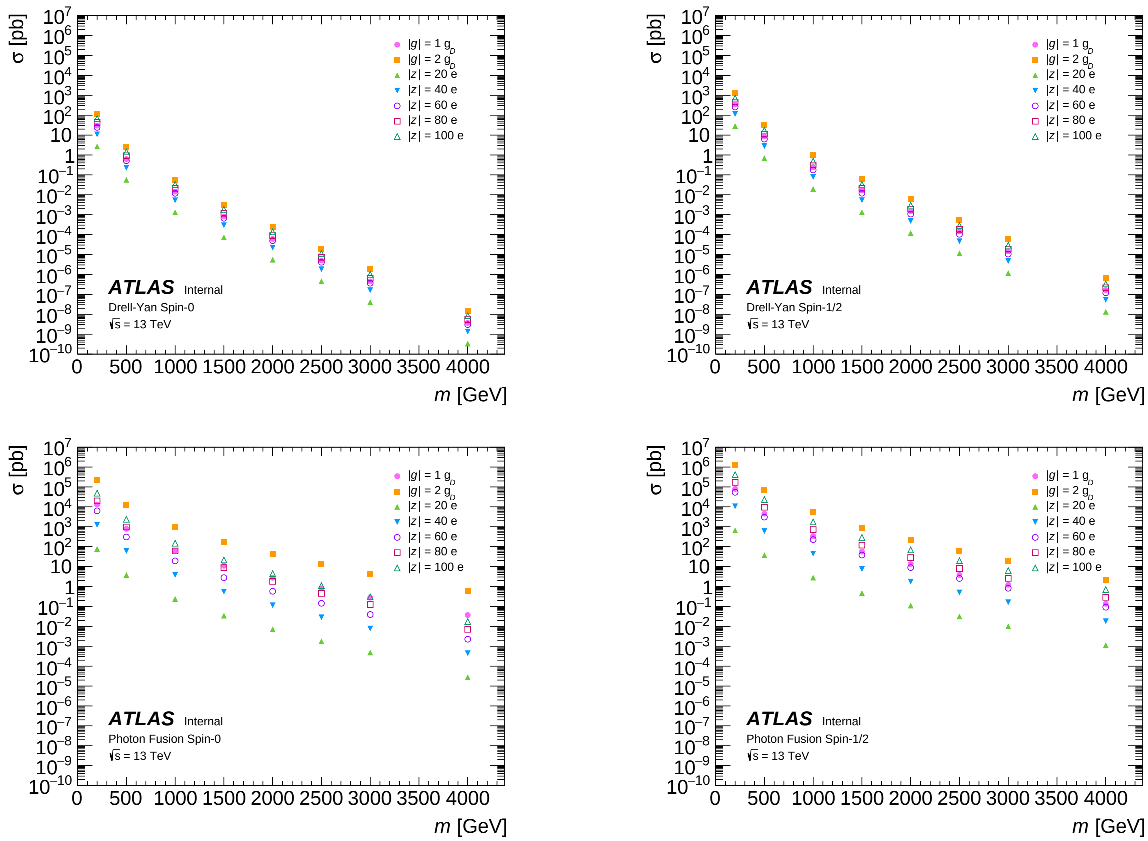

Figure 4.3: Theoretical cross-sections as a function of mass, for Drell-Yan (top) and Photon Fusion (bottom) production mechanisms for spin-0 (left) and spin-½ (right) before p_T cuts.

four production mechanisms are extracted from the output produced by MadGraph and stored in flat ntuples. These include transverse kinetic energy E_T^{kin}, pseudorapidity η, kinetic energy E_K, relativistic velocity β, transverse momentum p_T, and relativistic factor γ distributions. Plots for these kinematic distributions are found in Appendix A. The information contained in the ntuples is used to estimate signal selection efficiencies via the extrapolation method explained in Section 5.3.

Other than the model-independent samples, only the Drell-Yan spin-½ pair production mechanism is fully simulated. Samples were produced for each mass and charge combination containing 10 000 events from MC16a, 20 000 events from MC16d and 30 000 events from MC16e, for a total of 60 000 events (with the exception of HECOs charge $|z| = 100$, which contain 10 000 events per campaign for a total of 30 000 events.). Generator-level samples for alternative production mechanisms, Drell-Yan spin-0 and photon fusion spin-0 and spin-½, contain 50 000 events.

4.2.2 Simulation

The simulation of HIPs in ATLAS is done through the use of the Geant4 toolkit [84]. Geant4 contains a simulation of the material in the ATLAS detector and propagates the particle in steps to simulate the interaction with the material. Interactions between the detector and other particles in the event are also simulated. A special package for the simulation of particles with magnetic charge designed in previous iterations of this analysis [85, 86] is used (Simulation/G4Extensions/Monopole). This package includes the HIP propagation and ionization, the simulation of δ-ray production and propagation, and the effect of the magnetic field on the magnetic monopole.

4.2.3 Digitization

The simulated energy depositions are converted into simulated digital signals in the ATLAS detector, through the use of the ATLAS software. This includes the digitization of the TRT pulse, as described in Section 4.1. Additional collisions, known as pile-up, are overlaid in this step. The pile-up depends on the number of collisions per bunch crossing. A simulation of these additional collisions is designed to reflect the conditions in data as closely as possible. Since this is not possible to predict a priori, an event based pile-up reweighing step is performed on the MC samples at the analysis level to account for the discrepancies.

4.2.4 Reconstruction

The simulated digital signals are processed by the ATLAS software to reconstruct information such as particle tracks and calorimeter clusters. Ultimately, this would lead to the identification of particles, jets and missing transverse kinetic energy. There are no specific reconstruction packages for the HIP analysis, rather, it relies on low-level variables from the calorimeter cells and the TRT straws for signal identification.

In this stage, TRT hits with a pulse that begins too late ($> 60\,\mathrm{ns}$) or ends too soon ($< 11\,\mathrm{ns}$) are rejected as out-of-time pile-up. Hits which are not rejected are considered TRT LT hits. If the HT bit is flagged, then the hit is also counted as a TRT HT hit.

The calorimeter topo-clusters discussed in Section 4.1.2 are also reconstructed in this stage. The reconstruction of topological clusters consists of two general steps. In the first part, a cell with a signal-to-noise ratio above four is selected by the algorithm and neighbouring cells in all directions with a signal-to-noise ratio above two are added to the cluster. If one of these cells is a neighbour to two clusters then the clusters are merged. All cells adjacent to the ones in the cluster are added as well to include tails of electromagnetic cascades and jets. The second part consists of splitting the newly created clusters. This is done because it is common that a cluster actually contains the signal from more than one particle. To do this, the algorithm finds local maxima in the cluster locating cells with energy depositions of at least $500\,\mathrm{MeV}$ and at least four other cluster cells with energies less than that of the local maxima. The new cluster is split from the original one and a new iteration of the clustering described above is performed. Local maxima are only selected from the presampler and first layer of the LAr EM calorimeter if they do not overlap in η and ϕ with maxima found in the other two layers.

Trigger reconstruction

Hardware-trigger emulations are also done at this stage. The same trigger algorithms for software-based triggers applied online are run on the MC samples. Hence, trigger response can be validated and trigger efficiencies computed.

4.3 Run 2 data

The complete dataset collected by the ATLAS detector from $\sqrt{s}$=13 TeV proton-proton collisions [87] during Run 2 for the HIP analysis contains an integrated luminosity of 138 fb^{-1}, with an uncertainty of 0.83%. Only 1.33 fb^{-1} comes from the collisions delivered during 2015 because the algorithm for HIP data collection (which will be described in Section 5.1.2) was deployed late in the year. The dataset is filtered by using the Good Run Lists [88], which indicate the luminosity blocks satisfying quality requirements of stable beam conditions and optimal functioning of the ATLAS subsystems.

The data collected by the ATLAS detector goes through reconstruction as described in Section 4.2.4.

4.4 Analysis tuples

The reconstructed lower level variables described in Section 4.2.4 are further processed by the HIP analysis Ntuple Maker Code (Ntuple Maker Code (NMC)). The NMC uses the calorimeter topo-clusters and the TRT hit information from the reconstruction output files to create higher level variables, which will be described in Chapter 5. These are stored in flat ntuples along with the trigger flags, TRT hit and LAr EM calorimeter cluster information.

CHAPTER 5

Signal Selection

With the knowledge of the signature of HIPs in the ATLAS detector from Chapter 4, the next step is to design the selection criteria that will distinguish an event with a HIP from events with other particles. The chain of selection starts with the triggers that indicate the event should be recorded. After, a set of preselection cuts are applied to remove events that do not have good quality conditions for further consideration. Finally, a pair of signal selection variables and corresponding signal selection cuts are defined such that HIP events are discriminated from all other events. This chapter describes the triggers used as well as the preselection and selection criteria. It discusses the discriminating power of the selection variables and the optimization of the signal selection cuts. Finally, it reports the efficiency in selecting signal for all combinations of mass, charge, spin and production mechanism considered in this thesis.

5.1 Triggers

As explained in Section 2.2.4, only events that are considered interesting are saved. In order to be recorded, HIP events must fire two triggers: the L1EM22VHI hardware-based level 1 trigger and a bespoke high-level trigger developed for this analysis: HLT_g0_hiptrt_L1EM22VHI.

5.1.1 L1 trigger

The L1EM22VHI trigger is the lowest energy threshold un-prescaled hardware-based single electron/photon level 1 trigger. It was chosen for this analysis because, as explained in Section 4.1, while HIPs deposit a portion of their energy in the inner detector, there are no track-based level 1 triggers available in ATLAS. Thus, it is necessary to rely on a low-threshold hardware-based trigger from the LAr EM calorimeter. The L1EM22VHI trigger requires an energy deposition of 22 GeV in the EM calorimeter. The trigger also applies a Hadronic Veto (VH), which means that it discards events in which energy depositions greater than 1 GeV but smaller than 50 GeV are found in the Hadronic Calorimeter. This significantly affects the $|z| = 20$ HECOs, as seen in Figure 5.1 where there is an efficiency loss of the L1 trigger for transverse kinetic energies below 2 TeV.

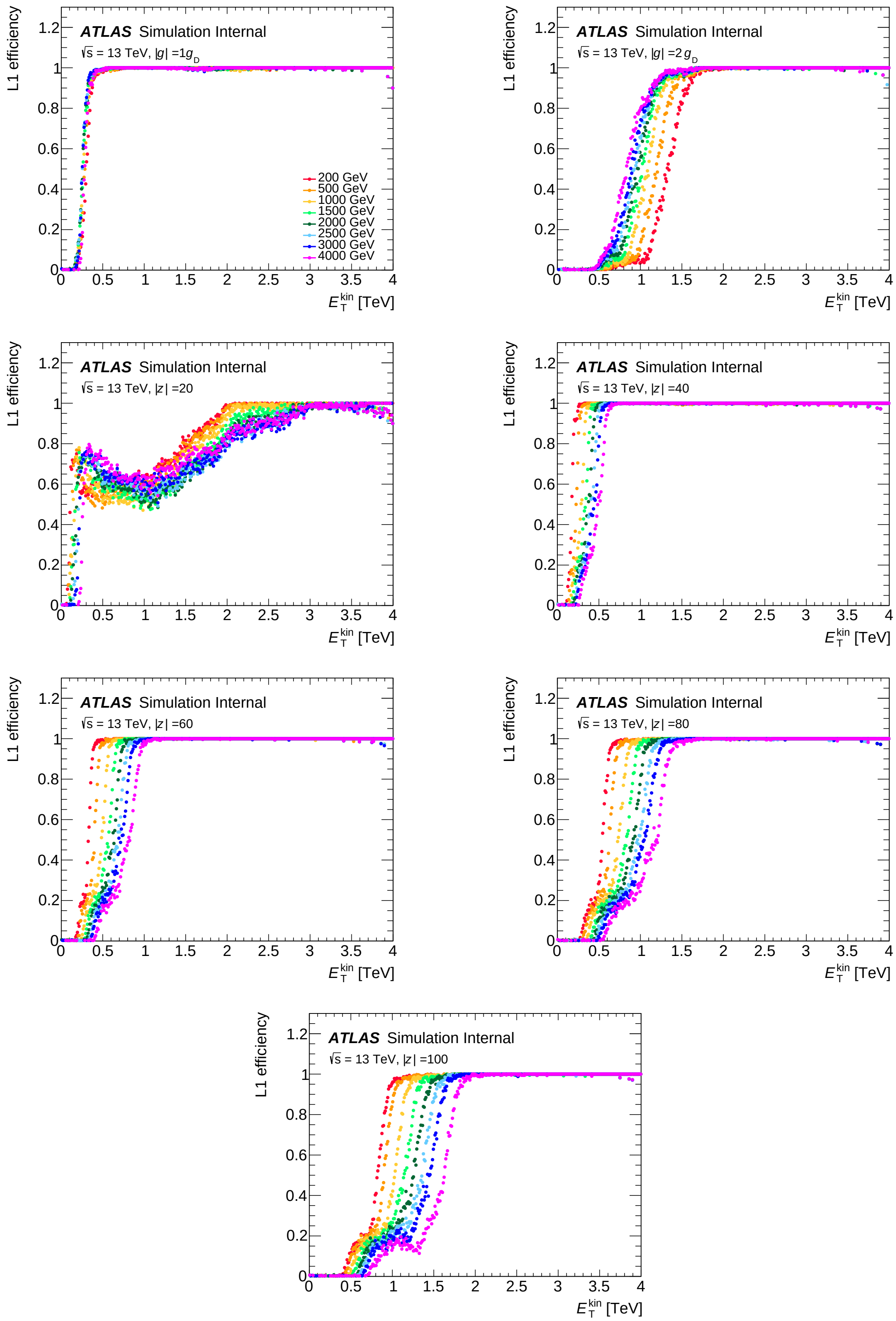

Figure 5.1: L1 trigger efficiency as a function of the transverse kinetic energy for all magnetic monopole and HECO mass and charge combinations considered. These plots are obtained from the model-independent MC samples.

5.1.2 HLT trigger

The High Level Trigger (HLT) designed for the HIP analysis, HLT_g0_hiptrt_L1EM22VHI, decides if an event may have a HIP, considering the number of low-threshold hits, $\mathrm{nLT}_{\mathrm{trig.}}$, the number of high-threshold hits, $\mathrm{nHT}_{\mathrm{trig.}}$, and the fraction of high-threshold hits $f_{\mathrm{HT,\ trig.}}$ in a wedge of the TRT based on a RoI defined by the L1 trigger.

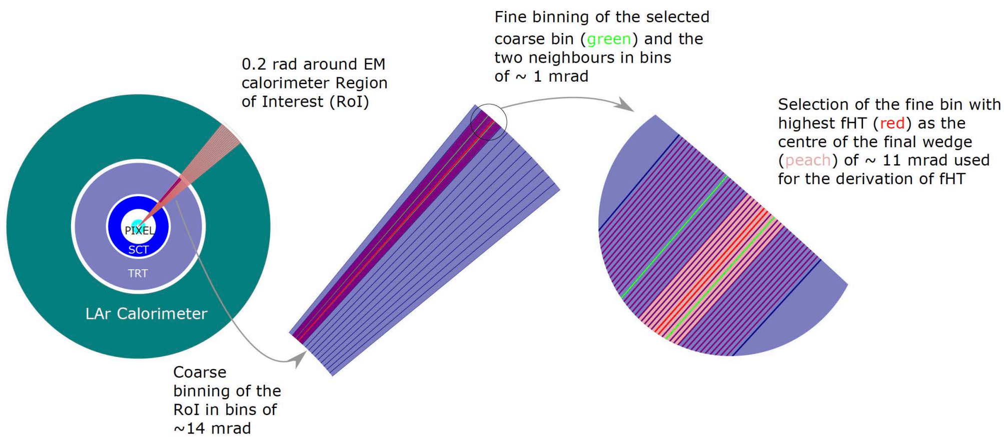

Figure 5.2: HIP High Level Trigger algorithm centering of the TRT wedge around the path of the particles [89].

The definition of this 11 mrad wedge is illustrated in Figure 5.2 and happens in two steps. In the first step, the Region of Interest (RoI) from the L1 trigger, which is a 0.2 rad wedge, is located and divided into 14 bins. The TRT hit counting algorithm is used in the second step, which consists of locating the bin with the largest $\mathrm{nHT}_{\mathrm{trig.}}$, and the two bins adjacent to it, and subdividing each into 14 bins. Each of the 42 bins is roughly 1 mrad. An 11 mrad wedge is defined by the bin with the maximum $\mathrm{nHT}_{\mathrm{trig.}}$ and ten neighbouring bins. This wedge goes from 6 mm to 12 mm in width, or in other words one and a half to three TRT straws wide with increasing radius from the beampipe. The $f_{\mathrm{HT,\ trig.}}$ is defined as

$$f_{\mathrm{HT,\ trig.}} = \frac{\mathrm{nHT}_{\mathrm{trig.}}}{\mathrm{nHT}_{\mathrm{trig.}} + \mathrm{nLT}_{\mathrm{trig.}}}, \tag{5.1}$$

where both the $\mathrm{nHT}_{\mathrm{trig.}}$ and $\mathrm{nLT}_{\mathrm{trig.}}$ are counted in the newly defined wedge. An event will fire the trigger if $\mathrm{nHT}_{\mathrm{trig.}} > 30$ and $f_{\mathrm{HT,\ trig.}} > 0.5$.

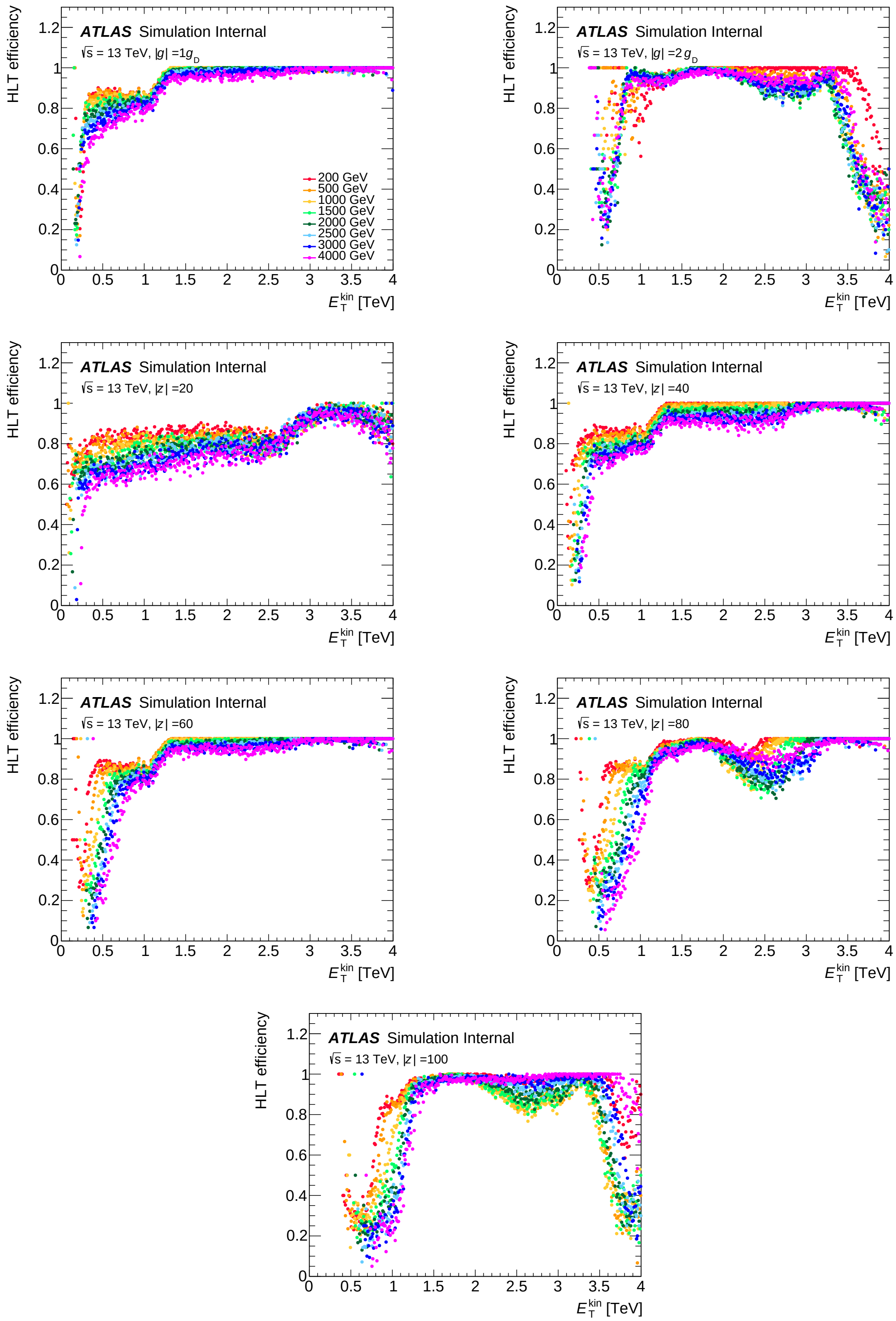

Figure 5.3: HLT efficiency as a function of the transverse kinetic energy for all magnetic monopole and HECO mass and charge combinations considered. These plots are obtained from the model-independent MC samples.

Figure 5.3 indicates the HLT efficiency with respect to the L1 trigger as a function of the transverse kinetic energy for the central region of the ATLAS detector ($|\eta| < 1.375$). The efficiencies of most HECOs with charge $|z| = 20$ plateau below 1 because many of these particles are unable to deposit sufficient energy in the TRT to pass the $f_{\text{HT, trig.}} > 0.5$ requirement.

5.1.3 Transverse momentum cuts

As mentioned in Section 4.2.1, model-independent MC signal samples are used to compute the minimum transverse momentum required to fire the L1 trigger. This is useful to save computational resources when generating MC signal samples for all pair production mechanisms. Figure 5.4 illustrates what are known as turn-on curves of the L1 trigger as a function of p_{T}, for magnetic monopoles and HECOs of all mass and charge combinations considered in this study. The HIP p_{T} cut for each mass/charge point is determined at the point when the L1 trigger efficiency is greater than 1%, with a precision of 100 GeV.

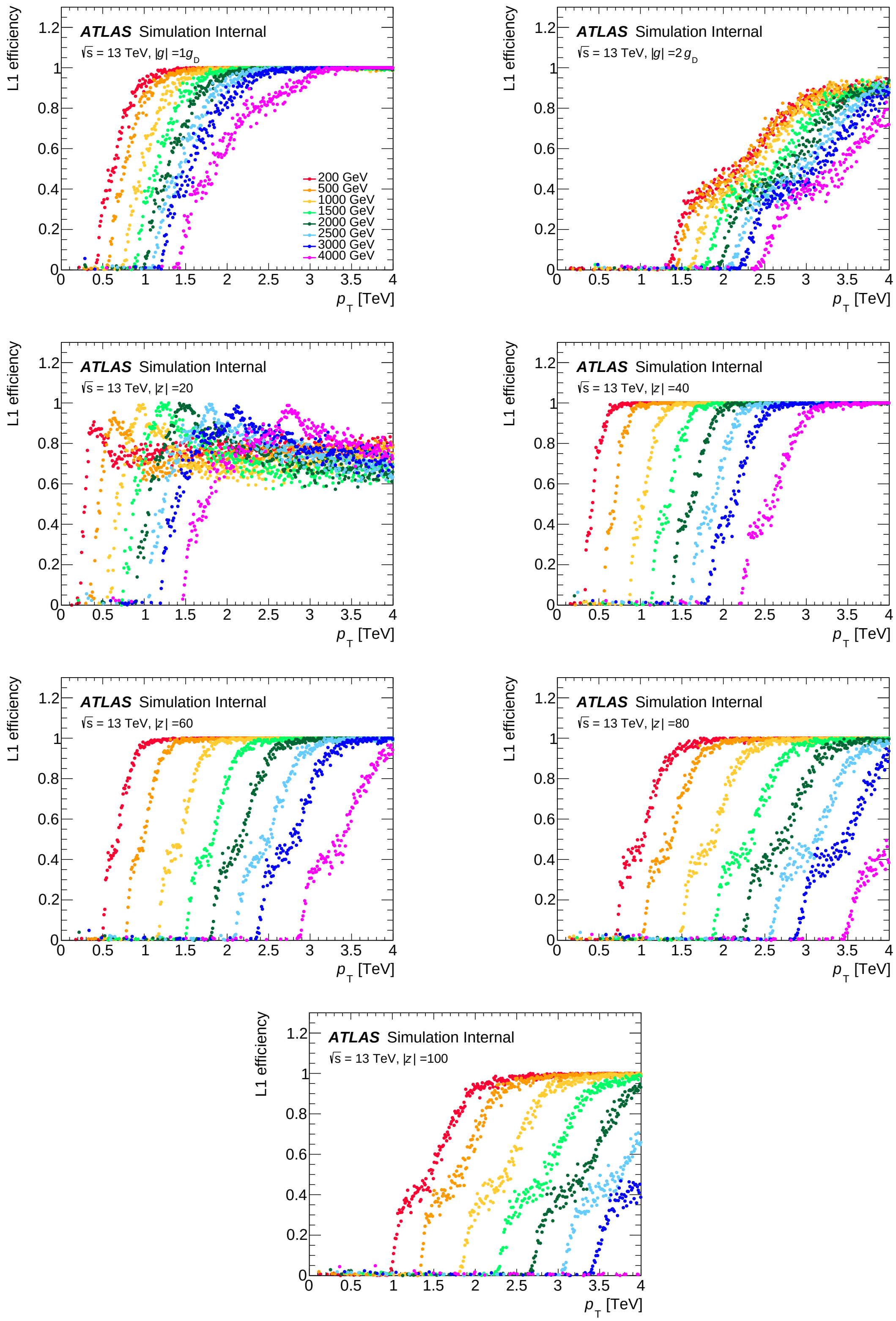

Figure 5.4: L1 trigger efficiency as a function of the transverse momentum for all magnetic monopole and HECO mass and charge combinations considered. These plots are obtained from the model-independent MC samples.

To account for the inefficiency of the L1 trigger, from events that are not simulated once the p_{T} cut is applied, the ratio between the production cross section after and before applying p_{T} cuts is computed for every mass/charge/pair production mechanism combinations considered. These values will be henceforth referred to as *p_T efficiencies* and are summarized in Table B.1, along with the p_{T} cut value applied.

5.2 Event selection

5.2.1 Signal discriminating variables

Considering the characteristic signature of HIPs in the ATLAS detector, the large number of high-threshold hits in the TRT and the large and narrow energy deposition in the LAr EM calorimeter, two variables are defined to discriminate signal from all other HIP candidates. The variables are defined from information recorded by the ATLAS detector and computed "offline", i.e., after data collection has taken place.

Energy dispersion in the LAr EM calorimeter: w

The energy depositions in the ATLAS EM calorimeter are stored in objects known as clusters, as described in Section 4.1. The lateral shape of a cluster associated with a HIP candidate is distinct given that HIPs do not induce an electromagnetic shower. Therefore, the energy deposition of HIPs will be contained in a small group of cells, making the shape of the cluster relatively narrow compared to electrons or photons. The energy dispersion, w_i, in a layer i of the LAr EM calorimeter, is defined as the fraction of cluster energy in that layer (E_0, E_1, E_2) contained in the m most energetic cells, where $m = 2$, 4, 5 for the presampler layer ($i = 0$), layer 1 ($i = 1$) and layer 2 ($i = 2$), respectively, as

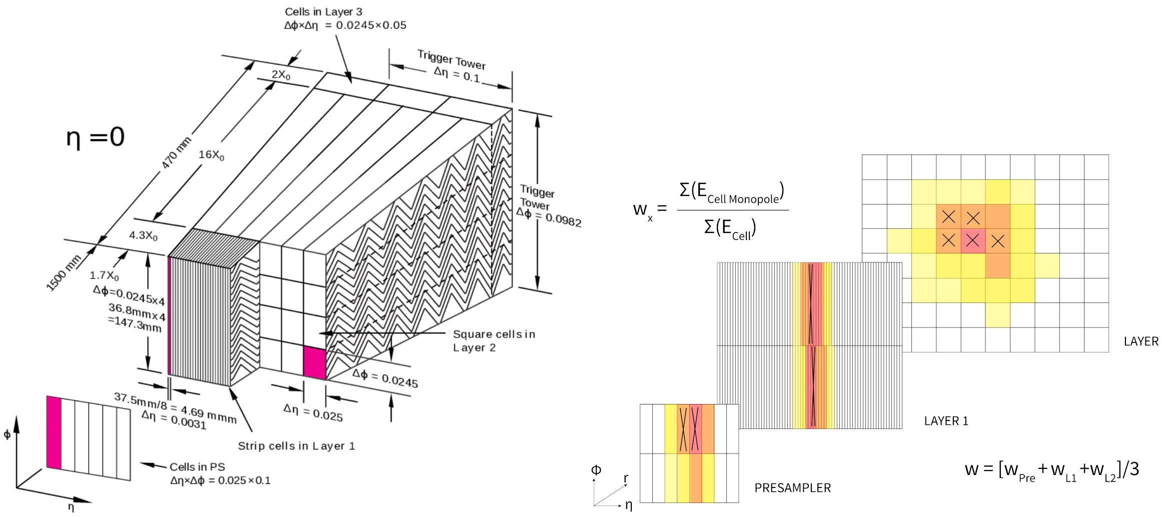

Figure 5.5: Sketch of the lateral and longitudinal segmentation of the ATLAS barrel LAr EM Calorimeter (left) [62]. Illustration of the energy depositions in each layer (right). Crosses represent the cells selected due to their high energy deposition for each layer.

illustrated in Figure 5.5. The energy dispersion variable w is defined in Eq. 5.2.

$$w = \begin{cases} w_0 & E_0 > 10\,\text{GeV}\ ,\ E_1 < 10\,\text{GeV and } E_2 < 5\,\text{GeV} \\ w_1 & E_1 > 10\,\text{GeV}\ ,\ E_0 < 10\,\text{GeV and } E_2 < 5\,\text{GeV} \\ \dfrac{w_0 + w_1}{2} & E_0, E_1 > 10\,\text{GeV and } E_2 < 5\,\text{GeV} \\ \dfrac{w_1 + w_2}{2} & E_1 > 10\,\text{GeV}\ ,\ E_2 > 5\,\text{GeV and } E_0 < 10\,\text{GeV} \\ \dfrac{w_0 + w_1 + w_2}{3} & E_0, E_1 > 10\,\text{GeV and } E_2 > 5\,\text{GeV} \end{cases} \tag{5.2}$$

w is defined requiring a minimum energy deposition in either the presampler layer or the first layer of the LAr EM calorimeter. The second layer is only considered if the cluster has a minimum energy deposition of 5 GeV. The optimization of the number of cells to compute w_i to achieve maximum discrimination through this variable has been studied extensively in previous iterations of the analysis [90].

Offline fraction of high-threshold hits: $f_{\mathbf{HT}}$

HIPs are expected to produce a large number of HT hits in the TRT. For each cluster in the LAr EM calorimeter, the density of HT hits is quantified in a corresponding region in the TRT. The region of

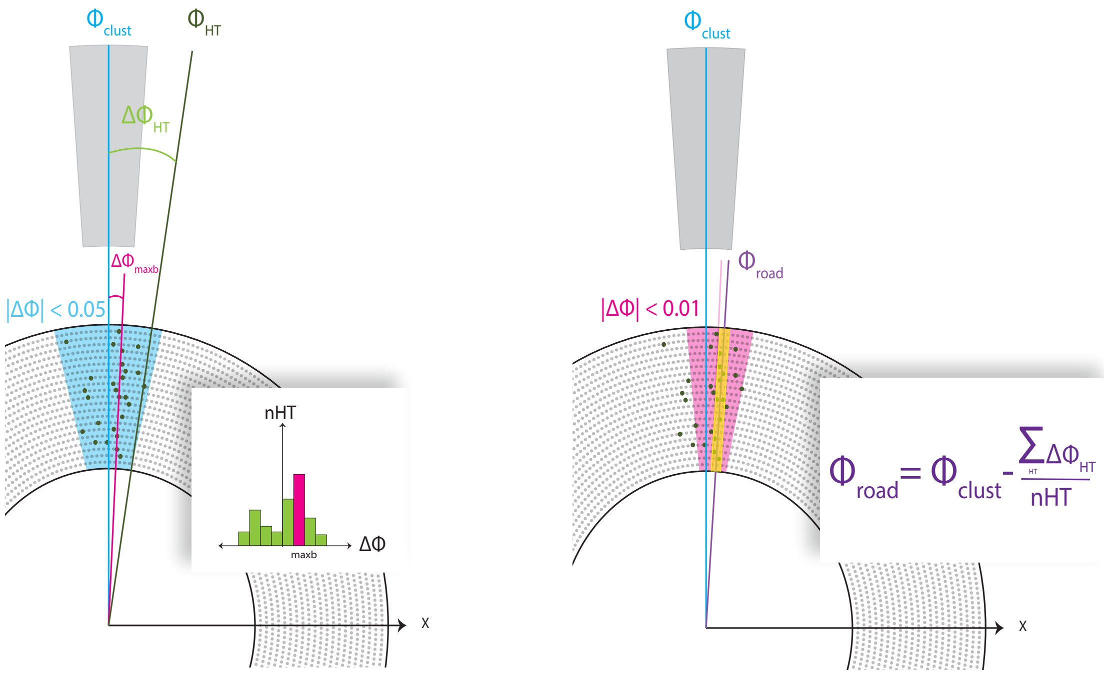

Figure 5.6: Schematic depicting the TRT road-centering and hit-counting algorithms for HIP candidates. Centering of the road happens in two stages. In the first stage (left), a ± 0.05-rad wedge (shaded blue) is defined around the azimuthal angle ϕ_{clust} of the EM cluster (blue solid line). In that wedge, the HT hit ϕ_{HT} distribution with an 0.8-mrad bin size is determined. The center of the bin containing the largest number of HT hits defines the azimuthal angle ϕ_{maxb} (pink solid line). For the second stage (right), a new ± 0.01-rad wedge (shaded pink) is centered around ϕ_{maxb}. The azimuthal angle ϕ_{road} (purple) is computed from the angular difference of each HT hit in this wedge with respect to ϕ_{clust}. The final ± 4-mm road (shaded yellow) is defined around ϕ_{road}.

the TRT from which the number of HT hits, nHT, and the number of LT hits, nLT, are counted is based on the position of the LAr EM calorimeter cluster and defined as an 8-mm-wide rectangular road for the barrel and a 12 mrad wedge for the end-caps [1]. For both barrel and end-caps, a wedge is centered at an azimuthal angle (ϕ_{road}) found in a two-step binning process that looks for the region with the largest nHT, as illustrated and described in Figure 5.6. TRT hits are not identified with exact η values, but only the side (in the z-axis) of the detector to which they belong ($\eta < 0$ or $\eta > 0$). On the other hand, the cluster information does include an η_{clust} variable. When counting LT or HT hits, they are included on the side of the detector dictated by η_{clust}, with the exception of the region $|\eta_{\text{clust}}| < 0.1$ at which there is ambiguity of the origin of the trajectory and, therefore, hits from either

[1] The width of the wedge is consistent with the 8 mm road at the innermost point (radially) of the TRT end-caps.

side of the TRT are counted. Similar to $f_{\mathrm{HT,\,trig}}$ in Eq. 5.1 for the HLT in Section 5.1.2, an offline f_{HT} variable is defined in Eq. 5.3.

$$f_{\mathrm{HT}} = \frac{\mathrm{nHT}}{\mathrm{nHT} + \mathrm{nLT}}. \tag{5.3}$$

5.2.2 Preselection

A series a preselection criteria are applied at the analysis level to discard events that should not be further considered, either because of the quality of the event or because they are outside the scope of this study. The preselection criteria are the following:

- Events must be part of an LHC run with optimal data-taking characteristics, i.e., be part of the Good Run List (GRL) [88].
- Events with noisy cells in the LAr EM calorimeter are discarded.
- Events must fire both L1EM22VHI and HLT_g0_hiptrt_L1EM22VHI triggers.
- Events should have at least one EM cluster and with an associated road/wedge with either: $w > 0.7$ or nHT > 10 or $f_{\mathrm{HT}} > 0.4$ to be recorded in the analysis ntuples.

Events can have more than one EM cluster that passes the preselection cuts. To choose a HIP candidate, EM clusters with $E_T > 22\,\mathrm{GeV}$, $|\eta| < 1.375$ and an associated TRT road (wedge) in the barrel (end caps) containing nHT > 30 are compared, and the one with the largest f_{HT} is selected.

5.2.3 Signal discrimination variable cut optimization

In order for a preselected HIP candidate to be considered a HIP signal candidate, it must simultaneously pass minimum values[2] on each of the signal discriminating variables, w and f_{HT}. Most HIP candidates in data do not have the necessary combination of narrow energy dispersion (large w) and large fraction of HT hits, i.e., HIP candidates in data are mostly background events. For this reason, the one dimensional w and f_{HT} distributions in Figures 5.7 and 5.8 for MC signal samples and 10% of the data

[2]Also known as thresholds or cuts, both of which will be used interchangeably in this thesis.

illustrate the discriminating power of each variable. One can further quantify the discrimination power

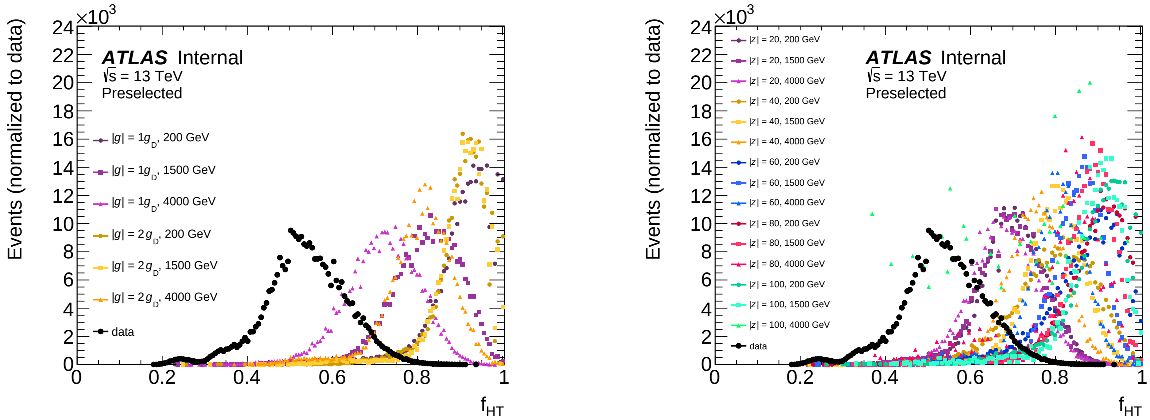

Figure 5.7: Distribution of the offline computation of the fraction of high-threshold hits, f_{HT}, for events that passed the HIPTRT trigger and candidates that passed the preselection criteria ($|\eta| < 1.375$, nHT > 30). Only the TRT road candidate with the highest f_{HT} value in each event is included in the plot. The black dots correspond to 10% of the data from Run 2 and the coloured dots correspond to a few representative masses for Drell-Yan spin-½ monopole (left) and HECO (right) signal samples.

of w and f_{HT} by looking at receiver operating characteristic (ROC) curves for each variable. These are plots of the signal efficiency as a function of the background efficiency, for the Drell-Yan spin-½ fully simulated samples, as one varies the cut along a range of the discriminating variable. The larger the area under the curve, the greater the discrimination power of the variable. Figure 5.9 illustrates a sample of ROC curves for representative masses and charges. These do not include the full ranges of the w and f_{HT} distributions but a range for each where the signal and background distributions overlap. ROC curves for all other charges are found in Appendix D. From these, it is clear that while f_{HT} has good discrimination power across most masses and charges considered, w, is a much better discriminant. To choose the pair of cuts for the w and f_{HT} variables, the F-score [91] was used to quantify the signal efficiency and background rejection simultaneously. It is important to emphasize that any cut optimization procedure will be sensitive to either the strength of the signal-to-background ratio or to the MC signal sample size. In past iterations of this search, the sensitivity variable [92] was used to optimize the cuts, because this variable is defined in such a way that it is independent of the strength of the signal-to-background ratio. Studies performed in this analysis found that the sensitivity variable was highly unstable under variations of the MC signal sample size. The F-score does not suffer from such sensitivity. Nevertheless, this is a search for new physics in which, as explained

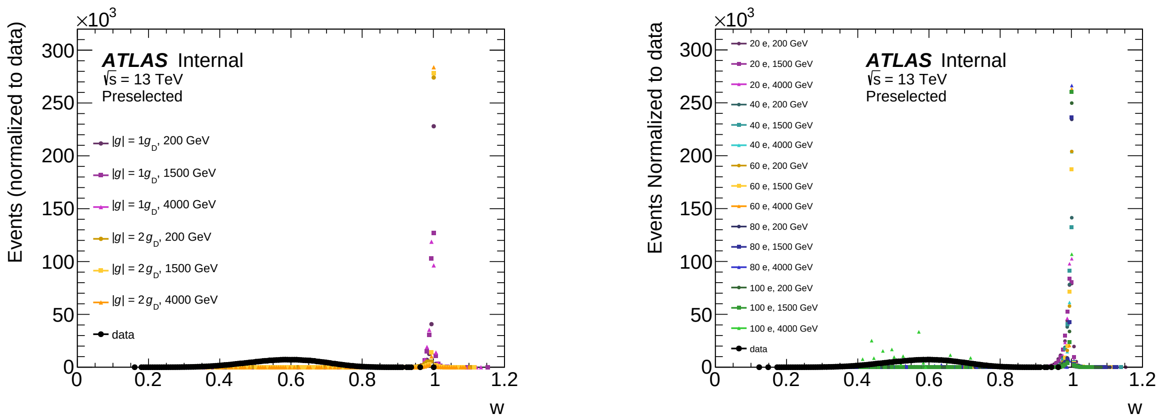

Figure 5.8: Distribution of the w variable for events that passed the HLT and candidates that passed the preselection criteria ($|\eta| < 1.375$, nHT > 30). Only the cluster corresponding to the TRT road candidate with the highest f_{HT} value in each event is included in the plot. The black dots correspond to 10% of the data from Run 2 and the coloured dots correspond to a few representative masses for Drell-Yan spin-½ monopole (left) and HECO (right) signal samples.

in Section 3.1, the coupling constant is non-perturbative and therefore theoretical production cross sections are unreliable. This makes it impossible to determine the strength of the signal-to-background ratio; thus, the F-score can only give us an approximate range in which to define the cuts.

F-score

In a labeled[3] dataset, composed of signal and background, when a cut is defined on a variable to discriminate signal from background, four quantities appear:

- True signal (TS): signal events that pass the cut and are classified as signal events.
- False signal (FS): background events that pass the cut and are classified as signal events.
- True background (TB): background events that fail to pass the cut and are classified as background events.
- False background (FB): signal events that fail to pass the cut and are classified as background events.

[3] Meaning that the true nature of each event is known, either signal or background.

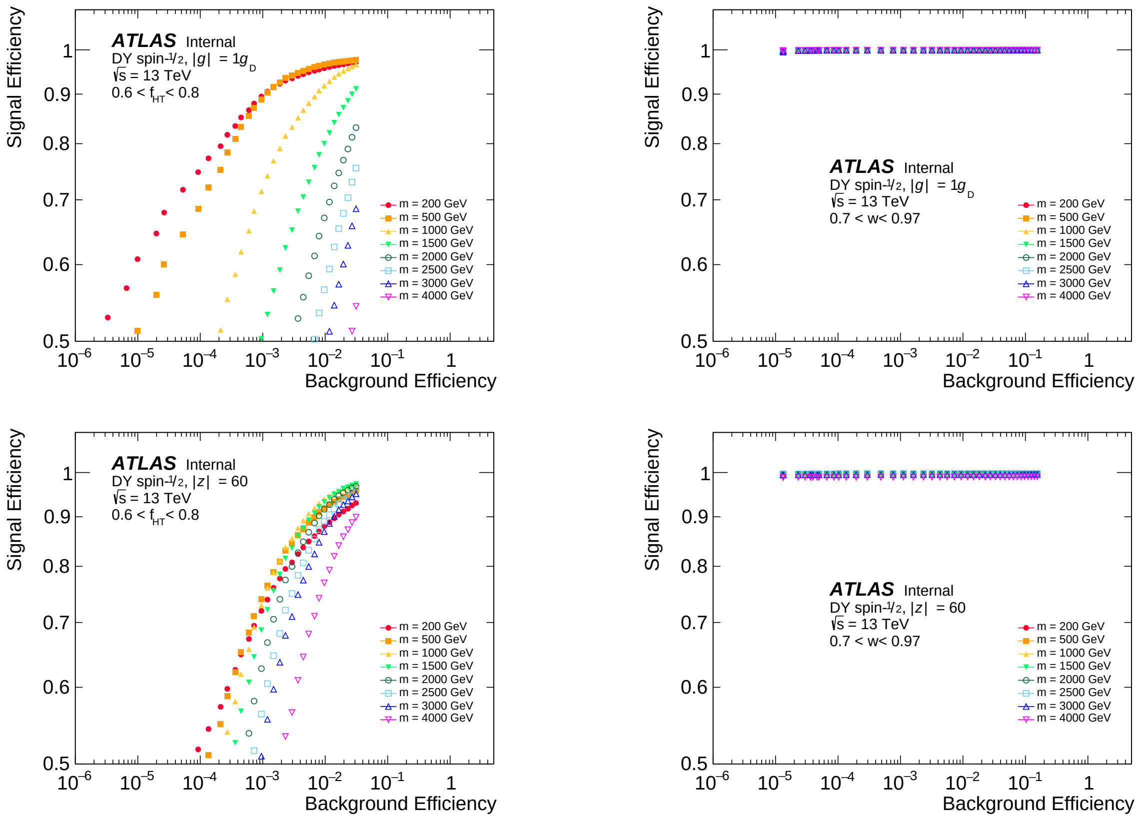

Figure 5.9: ROC curves of f_{HT} (left) and w (right) for Drell Yan spin-½ $1g_{\mathrm{D}}$ magnetic monopoles (top) and $|z| = 60$ HECOs (bottom) for all masses.

These are illustrated in Figure 5.10. Signal efficiency, defined in Eq. 5.4, is the ratio of true signal over all the signal events in the sample:

$$\text{efficiency} = \frac{TS}{TS + FB}. \tag{5.4}$$

Precision, defined by Eq. 5.5, is the ratio of the true signal over all predicted signal events:

$$\text{precision} = \frac{TS}{TS + FS}. \tag{5.5}$$

The F-score, defined by Eq. 5.6, is the harmonic mean of efficiency and precision,

$$F_\beta = (1 + \beta^2)\frac{\text{precision} \times \text{efficiency}}{\beta^2 \times (\text{precision+efficiency})}, \tag{5.6}$$

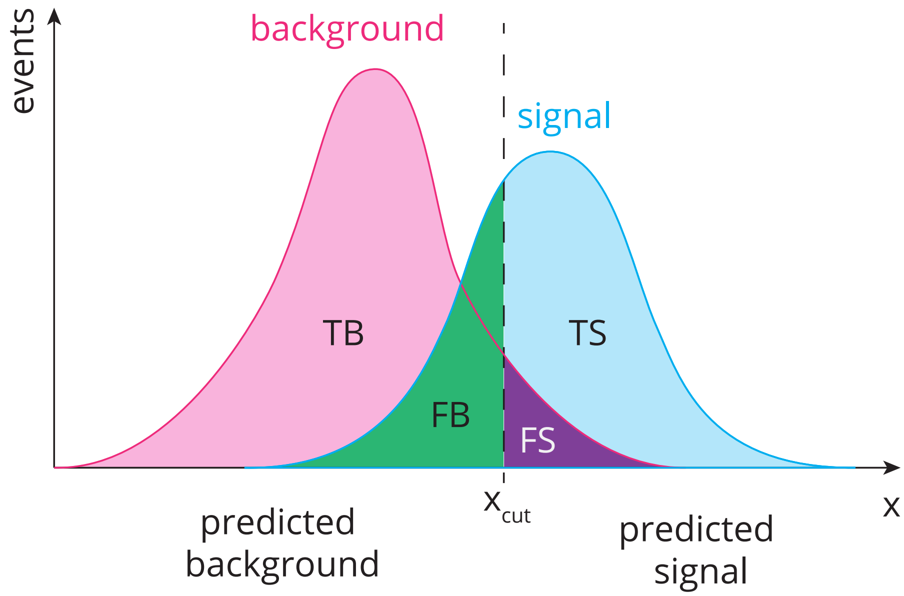

Figure 5.10: A 1D distribution in x of the dataset composed of signal (solid blue line) and background (solid pink line). Any events to the right of the discriminating cut "x_{cut}" (dotted line) are predicted signal, while those to the left are predicted background. Four populations appear: True Signal - TS (shaded blue), True Background - TB (shaded pink), False Signal - FS (shaded purple) and False Background - FB (shaded green).

where the parameter β is a positive number that assigns a higher weight ($\beta < 1$) on precision or ($\beta > 1$) efficiency.

Cut range optimization

Cut ranges for w and f_{HT} that showed high F-score on average[4] across the masses and charges considered in the analysis were found. No preference on the precision or efficiency was given and β was set to one.

The signal distribution was obtained from the model-independent MC samples. In order to produce a background sample with truth information, a pseudo-data sample is made by randomly re-pairing f_{HT} and w values from HIP candidates in the data collected. Because the pseudo-data are used to represent a background-only distribution, pairs with both large f_{HT} and large w are prohibited.

The F-score was calculated, for w and f_{HT} separately, in samples of various sizes. This is to account

[4]This average was computed by weighting the F-score of each signal sample according to its preselection efficiency.

for the sensitivity to the sample size. For the same reason, different signal-to-background sample size ratios were considered. The F-score was not significantly sensitive to sample size, but as expected, was biased by the signal-to-background ratio. Maximum values of F-score were obtained for a w cut in the range between [0.89,0.98] and an f_{HT} cut in the range of [0.66, 0.87]. Within these ranges, the middle region was preferred, being conservative with both the possibility of background contamination as well as the statistical power of the background estimation method. The signal selection cuts are defined as $w \geq 0.93$ and $f_{\mathrm{HT}} \geq 0.77$.

The application of all the preselection criteria described in Section 5.2.2 and the signal selection cuts on events is called the *cut-and-count* method. This is only possible when the events are data or fully simulated MC.

5.3 Extrapolation method

As mentioned in Section 4.2.1 the interaction of a HIP, of a given mass and charge, with the detector only depends on the kinematics of the particle. This study takes advantage of that fact and uses an extrapolation technique to estimate signal selection efficiencies of particles with a given set of kinematic properties from model-independent fully simulated signal samples. The technique was developed and validated in previous iterations of the analysis [93].

First, two-dimensional efficiency maps, such as the one seen in Figure 5.11, of the signal selection efficiency as a function of transverse kinetic energy (E_T^{kin}) and the pseudorapidity ($|\eta|$) are constructed from the model-independent simulated signal sample for each mass and charge combination.

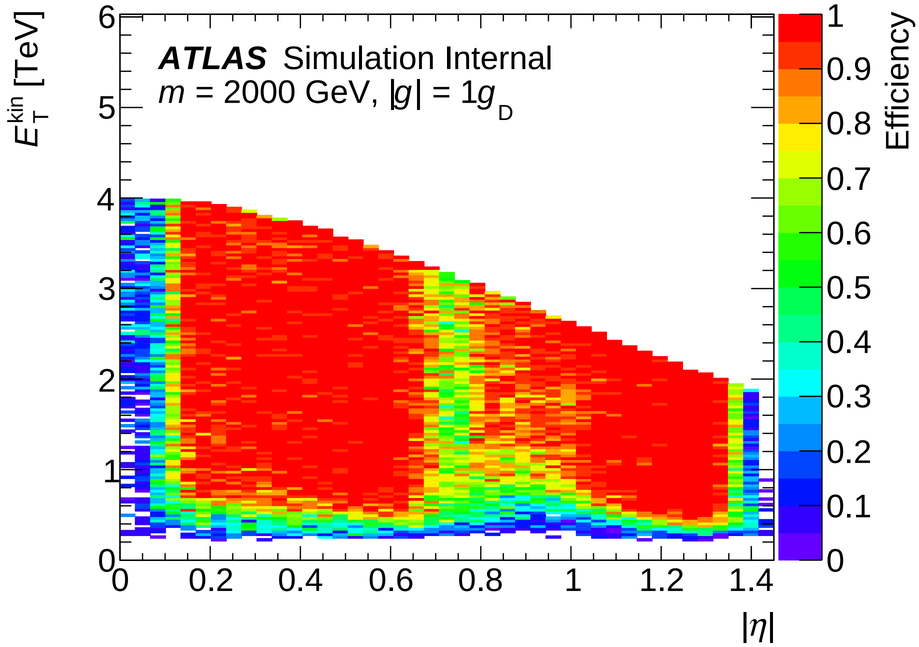

Figure 5.11: Two dimensional histogram, or map, of the signal selection efficiency as a function of the transverse kinetic energy E_T^{kin} and the pseudorapidity $|\eta|$.

The signal selection efficiency in each bin of the map comes from applying the selection criteria described in Section 5.2. Once the two-dimensional histogram has been constructed, it is a matter of testing the probability of whether or not a particle with a pair of kinematic properties (E_T^{kin}, $|\eta|$) would be selected. This is done using the generator-level samples mentioned in Section 4.2.1. Given the kinematic properties pair, (E_T^{kin}, $|\eta|$), the corresponding bin in the appropriate map is identified and the probability of selection is known. A random number r between 0 and 1 is generated and compared against this probability: if $r \leq$ efficiency, then the particle is considered to have passed the selection criteria. Because the analysis considers pair-production mechanisms, the event is counted as selected when either one of the HIPs in the pair is selected. This is done for all particles in the generator-level sample and a signal selection efficiency is computed as the number of events selected over the total number of events in the sample. A statistical uncertainty to the signal selection efficiency is assigned by propagating the uncertainty of the efficiency from the sampled bin. To account for possible fluctuations of using a random number, the signal selection efficiency is defined as the mean from the Gaussian distribution that results from repeating the extrapolation 50 times. The statistical uncertainty to the mean signal selection efficiency is the binomial error of the efficiency.

The performance of the extrapolation method is evaluated by comparing the signal selection efficiencies computed through the cut-and-count method and those obtained through extrapolation for the Drell-Yan spin-½ samples. This will be discussed in Section 7.4.

5.4 Signal efficiencies

Signal selection efficiencies for all production mechanisms are found in Figures 5.12–5.15. A selection cut flow table for some representative masses and charges of the Drell-Yan spin-½ mode compared to data is shown in Table 5.1. A cut flow of the signal selection efficiency for the Drell Yan spin- ½ mode is found in Appendix F.

		Total	**p_T cut eff.**	**L1**	**HLT**	**Pres.**	w	f_{HT}
data	counts	11088272	-	10966159	10961601	1509234	15	0
	rel. eff.	1		0.99	1.00	0.14	1×10^{-5}	0
$1g_D$	eff [%]	100	63.9	47.9	40.7	35.9	35.8	22.1
	rel. eff.	1	0.64	0.75	0.85	0.88	1.00	0.62
$2g_D$	eff [%]	100	8.2	3.4	2.64	2.58	2.57	2.49
	rel. eff.	1	0.08	0.41	0.78	0.98	1.00	0.97
$\|z\| = 20$	eff [%]	100	73.11	57.67	44.61	40.08	39.93	5.46
	rel. eff.	1	0.73	0.79	0.77	0.90	1.00	0.14
$\|z\| = 60$	eff [%]	100	23.99	10.98	8.25	7.33	7.31	6.51
	rel. eff.	1	0.24	0.46	0.75	0.89	1.00	0.89
$\|z\| = 100$	eff [%]	100	3.23	0.82	0.39	0.37	0.37	0.35
	rel. eff.	1	0.03	0.25	0.48	0.95	1.00	0.95

Table 5.1: Horizontal selection cut flow for data and a few typical Drell-Yan spin-½ signal MC samples for HIPs with a mass of 2000 GeV. The “rel. eff.” row gives the efficiency relative to the selection criterion in the column to the left.

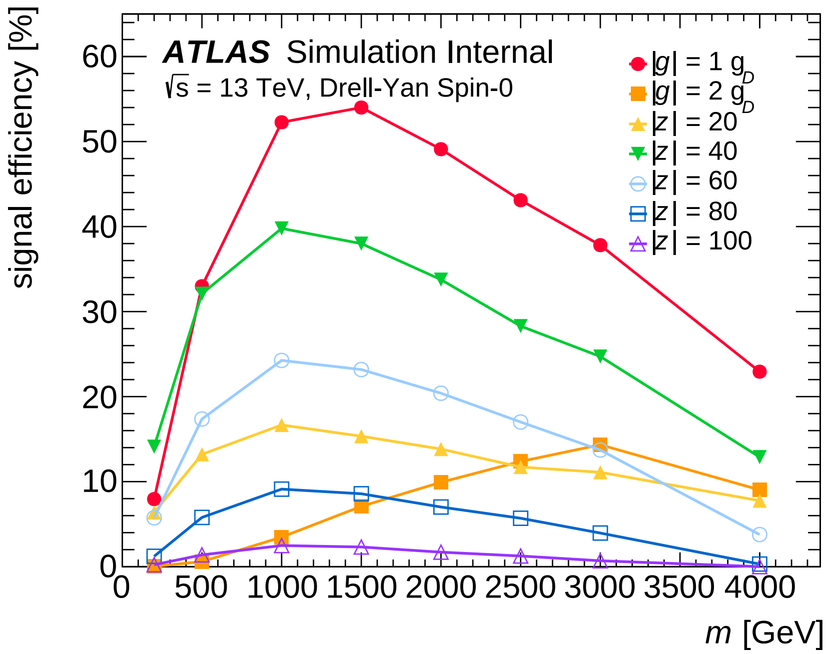

Figure 5.12: Selection efficiencies for Drell-Yan spin-0 pair-produced monopoles and HECOs, extrapolated from efficiency maps.

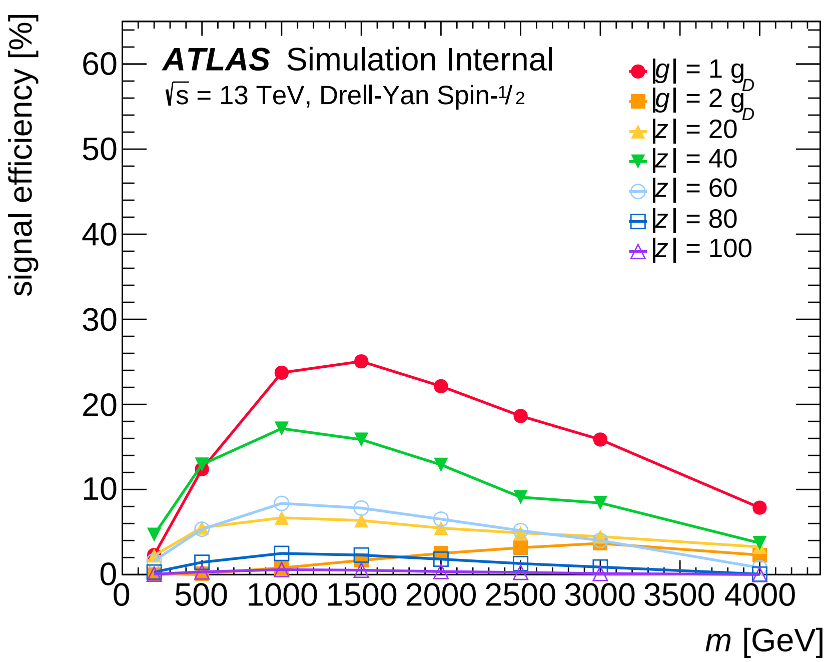

Figure 5.13: Selection efficiencies for Drell-Yan spin-½ pair-produced monopoles and HECOs, computed through the cut-and-count method.

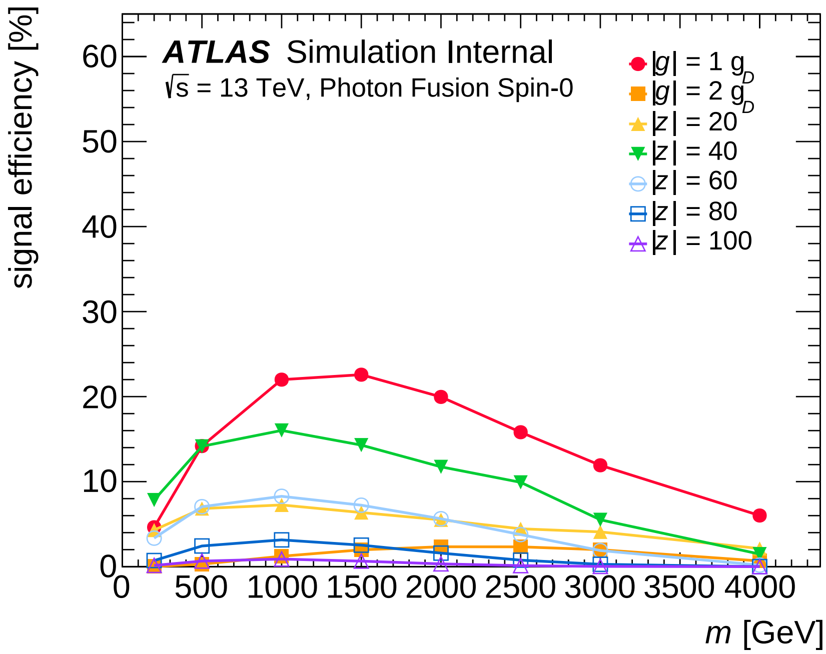

Figure 5.14: Selection efficiencies for photon fusion spin-0 pair-produced monopoles and HECOs, extrapolated from efficiency maps.

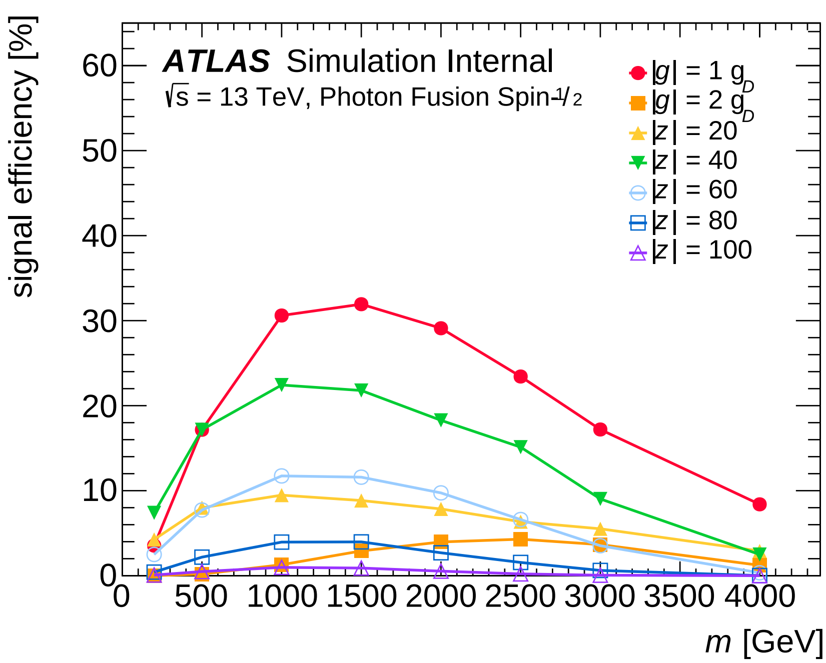

Figure 5.15: Selection efficiencies for photon fusion spin-½ pair-produced monopoles and HECOs, extrapolated from efficiency maps.

CHAPTER 6

Random Forest Classifier

The higher pile-up conditions in Run 2 dilute the f_{HT} variable. This chapter discusses an attempt to address the resulting signal selection efficiency loss, using a Machine Learning (ML) classifier built to discriminate signal TRT wedges from background TRT wedges. Some signal selection efficiency is recovered in high mass HIPs by the use of this method. This chapter discusses its potential in future iterations of the search for HIPs.

6.1 Dilution of the f_{HT} variable

The Run 2 data set spans the largest-ever range of average number of interactions per bunch crossing seen at the LHC until 2018, from 10 up to 70 on average, as seen in Figure 2.2. Figure 6.1 illustrates the behaviour of the mean number of LT and HT hits in the TRT HIP road, defined in Section 5.2.1, as a function of the average number of interactions per bunch crossing, $\langle\mu\rangle$.

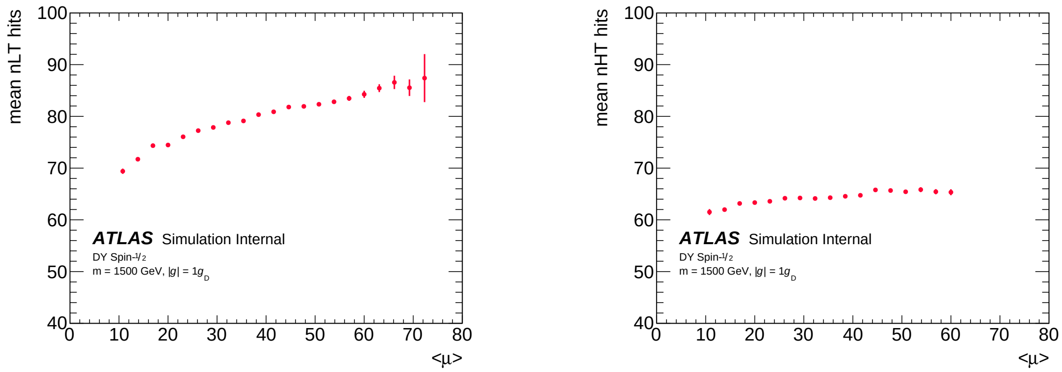

Figure 6.1: Mean number of LT hits (left) and HT hits (right) on the TRT HIP road as a function of the average number of interactions per bunch crossing $\langle \mu \rangle$ on preselected events, for an MC signal sample of DY spin-½ magnetic monopoles of charge $1g_{\mathrm{D}}$, mass 1500 GeV. The mean number of LT or HT hits was not computed for the full range of $\langle \mu \rangle$, due to statistical limitations.

Since the number of LT hits increases at a much faster rate than the number of HT hits, as a function of $\langle \mu \rangle$, the f_{HT} variable becomes diluted or reduced, as seen in Figure 6.2.

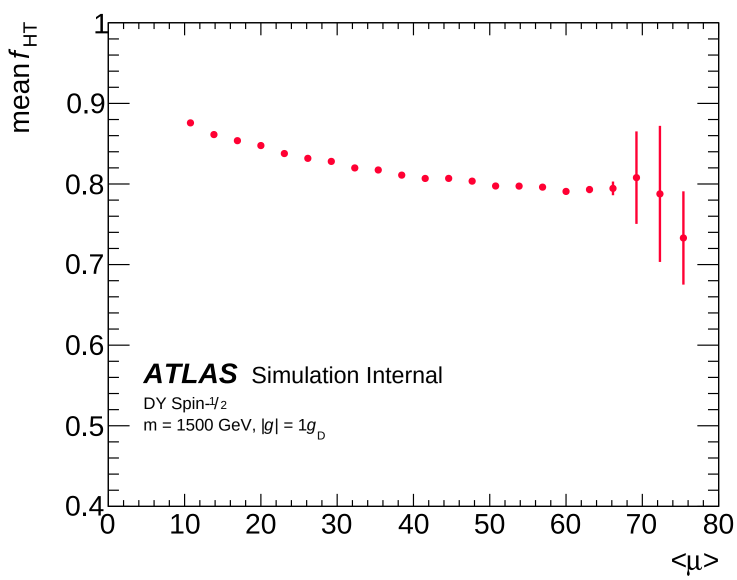

Figure 6.2: Mean f_{HT} as a function of the average number of collisions per bunch crossing $\langle \mu \rangle$ on preselected events, for an MC signal sample of DY spin-½ magnetic monopoles of charge $1g_{\mathrm{D}}$, mass 1500 GeV. The mean f_{HT} was not computed for the full range of $\langle \mu \rangle$, due to statistical limitations.

A loss of signal selection efficiency can be expected from the lower mean f_{HT}. For this reason, a new variable was designed to replace the f_{HT} variable. This new variable would not be solely defined by the number of HT or LT hits in the TRT HIP road, but rather exploit other information, such as the distribution of the hits in a wedge of the TRT.

6.2 Machine learning application

Machine learning is the development of computer algorithms that, by using statistical models, draw inferences from data without the need of a specific set of instructions. Machine learning tools were considered to overcome the f_{HT} dilution problem.

6.2.1 Definition of the input data

The idea is to train a model that will be able to discriminate a wedge on a transverse slice of the TRT that contains the signal of a HIP candidate from a TRT wedge without one. By including more information from the TRT beyond the hit counts, such as the position of the hits, an artificial intelligence algorithm could on its own find patterns to discriminate between the two types of wedges. Both wedges, which will be called the signal wedge and background wedge, respectively, are illustrated in Figure 6.3. The signal wedge is centered where the HIP TRT road is defined (see the definition of ϕ_{road} in Section 5.2.1). The transverse slice of the TRT barrel[1] is divided into 12 equal 0.52 rad-wide wedges, starting from the signal wedge. A random wedge from the remaining 11 is selected as the background wedge. Under high pileup conditions, both wedges would contain a large amount of LT hits, therefore, this feature would be overlooked by the algorithm when discriminating.

For the purposes of training the machine learning algorithm (or model), a single event of an MC signal sample yields two wedges, one signal and one background. Each wedge is treated as an image, which is translated into an image feature vector. An image feature vector is an ordered list of numbers that represent an image. The position of each element in the vector has a one-to-one correspondence to the

[1] These studies were only done on the barrel section of the TRT.

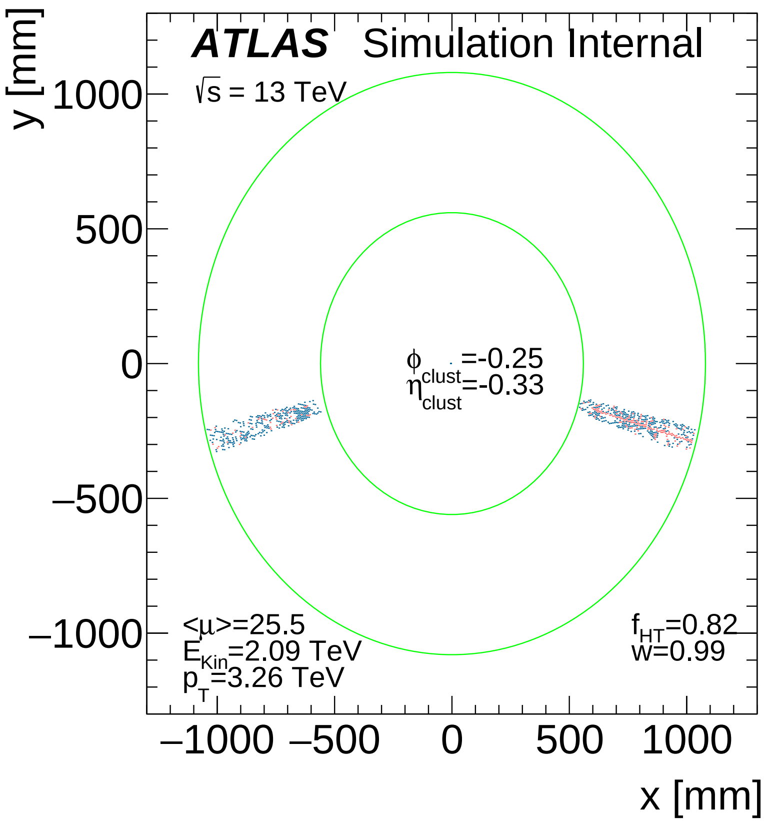

Figure 6.3: Transverse slice of the TRT barrel containing a signal and a background wedge of a simulated $2g_{\mathrm{D}}$, mass 1500 GeV magnetic monopole event. Additional information such as position, some kinematic properties of the monopole, and $\langle\mu\rangle$ of the event are included.

position of a straw in the wedge. Each element in the vector can be one of three numbers, representing the information recorded by the straw: no hit, HT hit or LT hit.

The datasets used for training and testing the model contain vectors for 20,000 signal wedges and 20,000 background wedges and label each vector as signal or background.

6.2.2 Random forest classifier

A Random Forest Classifier (RFC) [94] is a machine learning algorithm that belongs to the ensemble learning family. It is designed to solve classification problems, where the task is to predict which class a data point belongs to.

The RFC uses multiple decision trees to make such predictions. By using multiple decision trees, an RFC can make more accurate predictions and handle complex patterns in the data. The "random" aspect of random forest comes from two sources: random feature selection and creation of random data subsets. The random feature selection reduces the correlation between trees and introduces diversity, leading to better generalization and robustness. On the other hand, randomness in training data subsets creates random subsets of the original data, ensuring that each decision tree is trained on a slightly different set of examples. The following are some advantages of using a random forest classifier:

- Robustness to over-fitting. An over-fitted model performs exceptionally well on the training data but fails to generalize accurately to new, unseen data. The combination of multiple decision trees helps prevent over-fitting, as individual trees may have different biases and errors, but the "forest" tends to have better generalization performance.
- Feature importance. RFCs can provide insights into the importance of features in the classification task. By measuring how much each feature contributes to the accuracy of the model, feature importance rankings can be derived.

6.3 Discussion and outlook

Three datasets of MC Drell-Yan pair produced $2g_{\mathrm{D}}$ magnetic monopoles of masses 200, 1500 and 4000 GeV were prepared for training and testing a total of three RFC models. The datasets were split, such that the testing dataset would not be used during the training of the machine learning model. The prediction accuracy for the training stage and testing stage was computed and no over- or under-fitting[2] of the model was observed, given that the training and testing accuracy differed only by 6%, on average. Figure 6.4 illustrates the signal selection efficiency of each of the three RFCs, RFC 200 GeV, RFC 1500 GeV, RFC 4000 GeV, applied to Drell-Yan pair produced $1g_{\mathrm{D}}$ magnetic monopoles of masses 200, 1500 and 4000 GeV, compared with the signal selection efficiency of the f_{HT} variable.

[2]Under-fitting is when a model cannot make accurate predictions of the training dataset, nor generalize to new data.

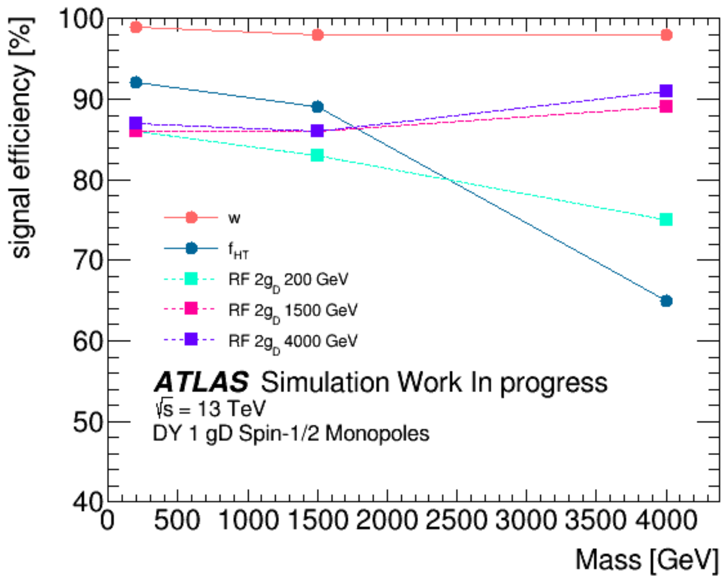

Figure 6.4: Comparison between the signal selection efficiency when using the f_{HT} variable and three RFC models, on preselected Drell-Yan pair-produced magnetic monopoles for spin-½ of masses 200, 1500 and 4000 GeV.

This classifier improved the selection efficiency of preselected Drell-Yan spin-½, $1g_{\mathrm{D}}$ monopoles of mass 4000 GeV between 10 and 26%.

These preliminary results showed that there was room for improvement of the signal selection efficiency by a redefinition of the TRT signal discrimination variable through a machine learning approach. Although the results obtained through these studies include very limited tuning of the RFC hyper-parameters (i.e., the number of trees or estimators, the depth of the trees, the criteria used to measure the quality of the split, etc), they are still considered reliable based on the consistency of the scores obtained when modifications when made. Furthermore, even though the RFC allows to obtain insight on feature importance, this was not attempted considering the input consists on hit information which is assumed uniform in the TRT barrel. Currently, there are more studies ongoing to improve this rudimentary first approach with the goal of implementing it on the data collected during Run 3.

CHAPTER 7

Systematic Uncertainties

Any simulation is an approximation of the reality of the physical process it represents. Both the lack of knowledge of the exact parameters and the inability to accurately reproduce them introduce biases in variables that are used to compute the signal selection efficiency. Systematic uncertainties of the signal efficiency account for the discrepancy between the estimated and true signal selection efficiency of the experiment.

This chapter describes the sources of systematic uncertainty considered in the analysis and explains how they were estimated. Systematic uncertainties on signal efficiencies are computed by finding the discrepancy between the signal selection efficiency under nominal conditions used in the MC signal samples of the analysis and comparing it to the signal selection efficiency of alternative conditions. To estimate the systematic uncertainty due to the effects described in Sections 7.1–7.3, production of model-independent signal MC samples with alternative simulation parameters or detector conditions are required. In these cases, the alternative signal efficiencies are computed via the extrapolation method. In all other cases, systematic uncertainties are estimated through modifications of variables at the analysis level. The values for all systematic uncertainties are found in Appendix G and summarized as averages across all model/mass/charge combinations in Section 7.10.

7.1 Detector material modelling

The ATLAS detector simulation is configured with a detector material profile that tries to reflect the actual composition of the detector as closely as possible. Nevertheless, there is uncertainty in the true detector material distribution. Due to the highly ionizing nature of HIPs, the signal efficiency is sensitive to the material up to the electromagnetic calorimeter. Thus, by increasing the detector material in all elements of the ATLAS detector up until the LAr EM calorimeter, a more conservative value of the signal selection efficiency is found. A suitable alternative profile that modifies the material of the Inner Detector is used. This profile increases the Pixel and SCT material by 10%, adds 7.5% X0 in the SCT and TRT endcaps, as well as the ID endplate, and it also adds 5% X0 radial barrel cryo, radial PS-Layer1 barrel and presampler-Layer1 endcap. The model-independent fully simulated alternative samples were only made for mass 1500 GeV, for all charges considered. The systematic uncertainty is assigned to all other masses of the same charge and is taken as symmetric.

7.2 HIP correction to Birks' Law

The correction described in Section 4.1.2 has an uncertainty that is proportional to dE/dX. Alternative model-independent MC samples were simulated for the high and low Birks' Law parameters that come from the uncertainty of the correction. The systematic uncertainty is one-sided, taking the maximum between the absolute values of the high and low variations. If no variation on the signal selection efficiency is observed, a conservative uncertainty of 5% is assigned.

7.3 δ-ray production modelling

The ionization energy loss of HIPs, dE/dx, has a theoretical uncertainty of $\pm$ 3%, as described in Refs. [66, 95]. The HLT trigger and the two discriminating variables are sensitive to the amount of energy deposited in the TRT and the LAr electromagnetic calorimeter. This uncertainty is propagated into the analysis by simulating alternative model-independent magnetic monopole samples, with a reduction of 3% in the production of δ-rays. For technical reasons, it was impossible to simulate the same alternative samples for HECOs; therefore, the systematic uncertainty of the $1g_{\mathbf{D}}$ magnetic monopole is assigned to the $|z| = 20$, 40 and 60 HECOs and that of the $2g_{\mathbf{D}}$ magnetic monopole is assigned to the $|z| = 80$ and 100 HECOs. The relative uncertainty is considered symmetric.

7.4 Extrapolation method for efficiency estimation

The extrapolation method described in Section 5.3 computes an estimate of the signal selection efficiency of HIPs pair produced through production mechanisms for which fully simulated signal samples are not available, i.e., Drell-Yan spin-0, Photon Fusion spin-0 and Photon Fusion spin-½. Since the nominal selection efficiency for the Drell Yan spin-½ production mode comes from a fully simulated signal and computed through the cut-and-count analysis, a comparison with the efficiency obtained when using the extrapolation method quantifies the uncertainty of applying the latter.

7.5 TRT gas distribution

The gas contained in the straws of the TRT has been known to leak. Due to the high cost of replacing Xenon gas, less expensive alternatives such as Argon and Krypton have been considered. During the data collection years, the baseline gas content of the TRT was as illustrated in Figure 7.1. The definition of the high and low thresholds in the TRT hit readout, explained in Section 4.1, are different for Xenon and Argon gas; thus, the numbers of low and high threshold hits are sensitive to changes in the gas configuration. All three MC campaigns reflect the detector's 2016 gas distribution. Mismodelling of the gas conditions introduce a bias in the trigger and the f_{HT} values. The effect is considered negligible in this analysis since the only difference between the 2016 and 2017/2018 gas distribution was a change of the gas in a wheel on side C, which has insignificant consequences to the analysis. Furthermore, although the difference with the 2015 gas distribution is more significant, 2015 data only accounts for 2.6% of the total data.

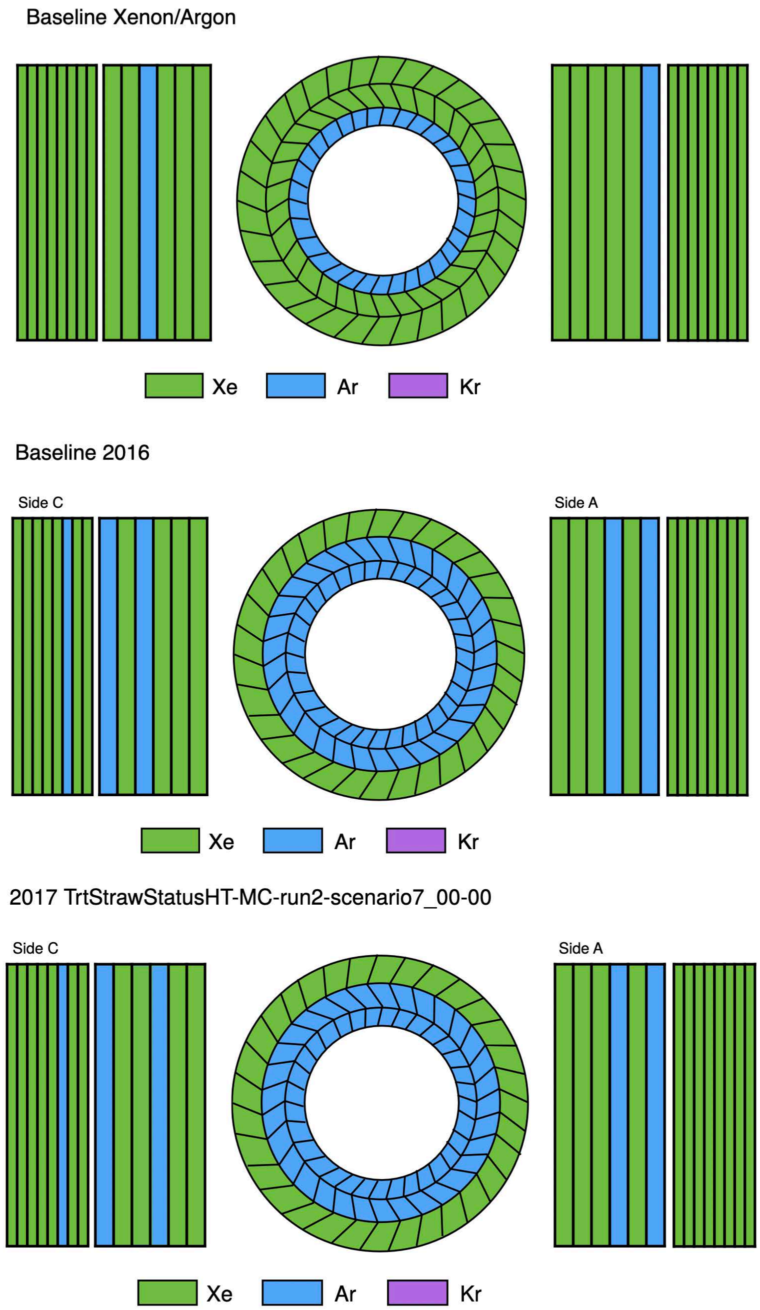

Figure 7.1: The TRT baseline gas distributions in 2015 (top), 2016 (middle), and 2017-2018 (bottom). The doughnut shape represents the TRT barrel and the rectangular sections on each side are wheels of the end-caps [96].

7.6 TRT occupancy

The increase in the average number of proton-proton collisions per bunch crossing, illustrated in Figure 2.2, results in a higher particle multiplicity. In the TRT, this is seen as an increase in the number of low- or high-threshold hits. The TRT global occupancy is the probability of a low-threshold hit being recorded during the 75 ns readout window, in the whole TRT sub-detector. The $\langle\mu\rangle$ variable is directly correlated with TRT global occupancy, due to an increase mostly in the number of low threshold hits. Since this dilutes the f_{HT} variable, a systematic uncertainty to account for this loss in efficiency needs to be included if the MC does not reflect the true conditions in the detector. The TRT global occupancy as a function of $\langle\mu\rangle$ for MC and data are compared. An MC signal sample of electrons from Z decays is chosen, since electrons have a similar TRT response as HIPs, which allows a comparison to data. The ratio of the discrepancy as a function of $\langle\mu\rangle$ in Figure 7.2 is used as a correction factor to the number of low-threshold hits. This correction changes the f_{HT} value and an alternative signal selection efficiency is produced. The relative discrepancy with the nominal selection efficiency results in a one-sided systematic uncertainty.

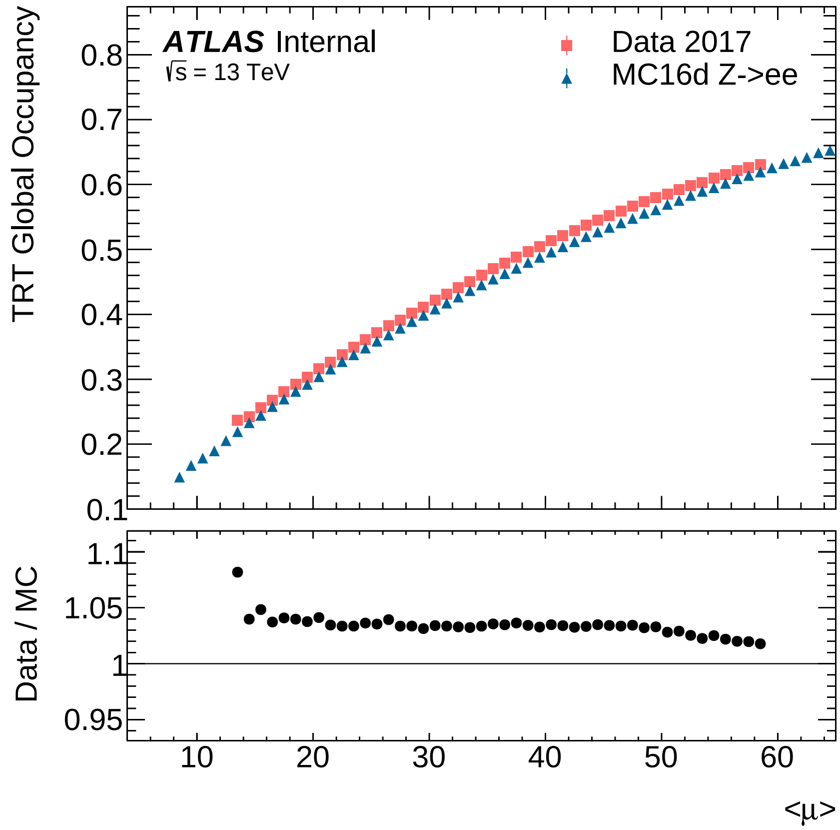

Figure 7.2: Comparison of the global TRT occupancy as a function of the average number of collisions per bunch crossing, $\langle\mu\rangle$, for data and an MC $Z^0 \rightarrow e^+e^-$ signal sample [97].

7.7 Pile-up re-weighting

The true hadronic activity in the detector cannot be perfectly simulated for various reasons, including inaccuracy of the MC particle spectra and detector conditions, and limitations in the computing resources [98, 99]. The pile-up, which accounts for additional proton-proton interactions in the event, is simulated before the data collection is finalized and for this reason MC pile-up distributions differ from those of data [100]. A procedure to implement scale factors, i.e., pile-up re-weighting, is prepared by simulation experts to adjust the MC distributions to data, once data collection is done. Any remaining discrepancies could introduce a bias in the signal selection efficiency. This procedure includes scale-up and scale-down systematic uncertainties of the pile-up re-weighing scale factors, as illustrated in Figure 7.3.

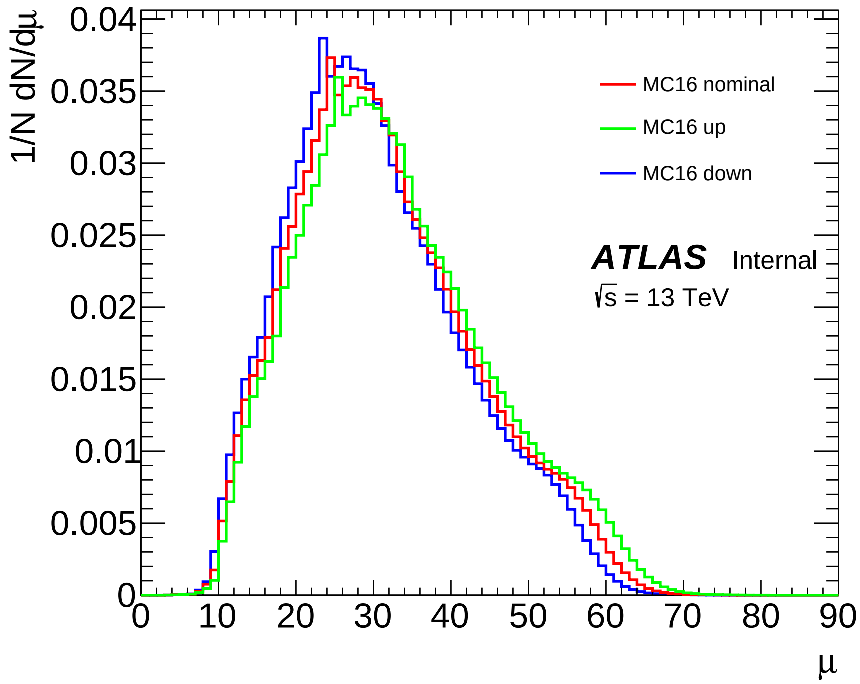

Figure 7.3: Pile-up weights and their up or down variations as a function of the number of collisions per bunch crossing μ [97].

7.8 Calorimeter cross-talk

Cross-talk refers to the induction of a noise signal between the electrons of neighboring calorimeter cells. This effect is accounted for in the simulation from all sources, except inductive cross-talk in ϕ, which may produce an increase of 1.8% of the next-in-ϕ neighboring cells' energy [101]. The w variable is affected by this energy increase when it changes the cluster's width. To compute this source of uncertainty, using the cluster information stored in the analysis ntuples, the energy of all the next-in-ϕ neighbours of each cell in a cluster is increased by 1.8% and a new w value is computed. The effect on the signal selection efficiency is found to be negligible.

7.9 Calorimeter arrival time

For a HIP signal to be recorded, it needs to interact with the electromagnetic calorimeter within the time window of triggering. Energy depositions in the LAr EM calorimeter after 10 ns of the collision are less likely to be triggered in the correct bunch crossing. The speed of the particle and the distance travelled determine the time delay, i.e., particles travelling perpendicular to the beam pipe with $\beta < 0.37$ will arrive after 10 ns to the LAr calorimeter. Since HIPs are heavy particles, a fraction of them may arrive too late to trigger the event. To account for a possible mismodelling of the arrival time, the signal selection efficiency loss in MC samples is computed when a cut $\beta \sin\theta > 0.37$ on the particle's velocity is implemented. This systematic uncertainty is one-sided.

Additionally, late arrival times can also affect cluster reconstruction. Calorimeter experts report losses of up to 2% in the energy deposited in the electromagnetic calorimeter cluster due to late arrival times. The effect of these cluster energy losses is simulated by reducing the transverse kinetic energy of each MC event by this amount and recomputing the signal selection efficiency. Considering the 20 GeV preselection cut, the effect of the late arrival time energy deposit on the signal selection efficiency is negligible.

7.10 Summary

Table 7.1 summarizes the systematic uncertainties as an average over all combinations of pair production models, masses and charges. A statistical uncertainty is computed for each value considering the statistics of the MC samples used to evaluate the systematic uncertainty. These statistical uncertainties are reported only to account for possible statistical fluctuations in the determination of the systematic uncertainties.

Systematic Uncertainty	Value in %
Detector material modelling	$\pm(8 \pm 4)$
HIP correction to Birks' Law	8 ± 0
δ-ray production modelling	$\pm(2 \pm 0)$
Extrapolation	1 ± 0
TRT occupancy	2 ± 0
Calorimeter arrival time	-2 ± 0
Pile-up re-weighting: up and down	-2 ± 0 and 2 ± 0

Table 7.1: Summary of the systematic uncertainties with associated statistical uncertainties, i.e., syst $\pm$ stat, averaged over all models, charges and masses.

CHAPTER 8

Background Estimation

The signal selection criteria described in the previous chapter are imperfect at discriminating non-HIP events from HIP events. Jets or high-energy electrons, that produce a large number of HT hits in conjunction with an energy cluster in the LAr EM calorimeter, could contaminate the signal. These are the known sources of background in our search.

In order to estimate the number of background events we expect from our data sample, the most common approach is to simulate a MC sample of these objects, measure the selection efficiency, and compute the magnitude of the contamination of the signal based on the production cross-section of these events. Unfortunately, because these events very rarely have the large and narrow energy deposition in the LAr EM calorimeter to produce high values of w, a statistically significant Monte Carlo sample is computationally prohibitive. Thus, background estimates in this analysis are not computed from Monte Carlo background samples; instead, a method relying only on the collision data set is used.

8.1 The ABCD method

The ABCD method [102] estimates the number of background events in the signal region from a 2D distribution of the preselected data as a function of both signal selection variables, f_{HT} and w. The plane is divided into four regions, as seen in Figure 8.1, one signal region (SR) and three control regions (CR):

- Region A (SR): $w \geq 0.93$ and $f_{HT} \geq 0.77$
- Region B (CR): $0.4 \leq w < 0.93$ and $f_{HT} \geq 0.77$
- Region C (CR): $w \geq 0.93$ and $0.5 \leq f_{HT} < 0.77$
- Region D (CR): $0.4 \leq w < 0.93$ and $0.5 \leq f_{HT} < 0.77$.

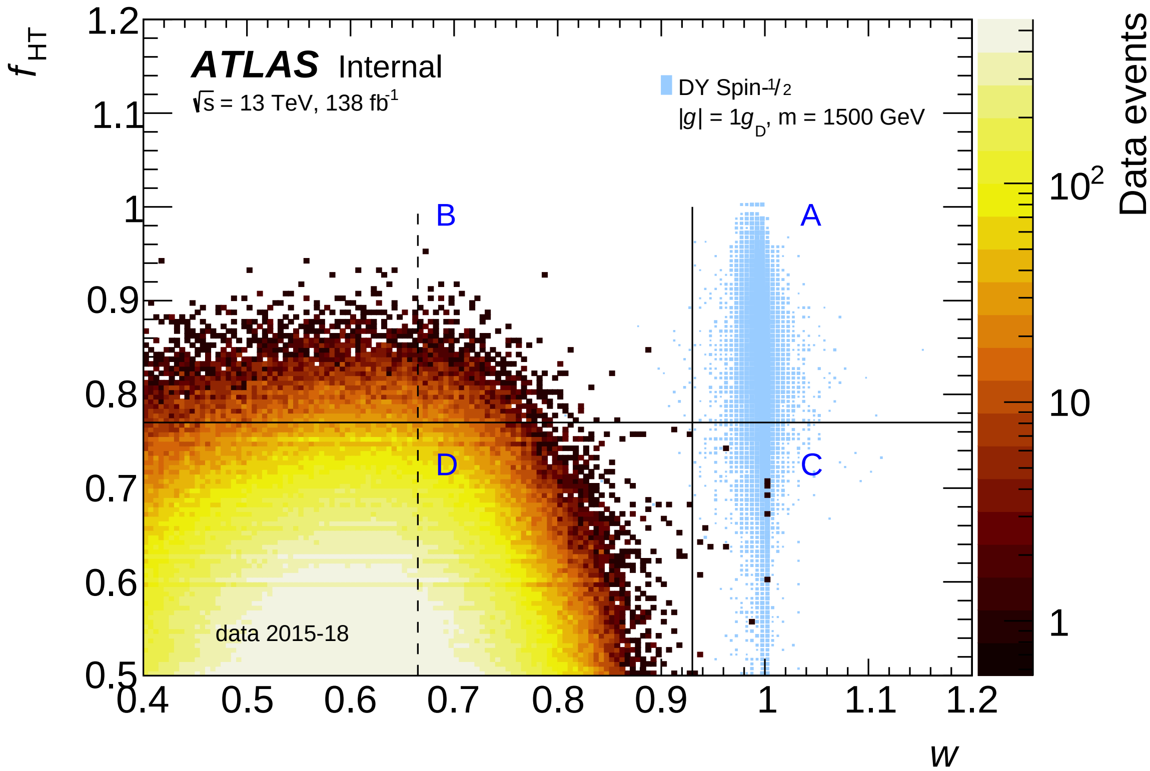

Figure 8.1: f_{HT} versus w distribution of the Run 2 data after preselection, also known as the ABCD plot. The signal region is A, and the control regions are B, C and D. The dotted line creates sub-regions B', B", D' and D" used for validation. A representative MC signal sample is shown in blue.

If the signal selection variables, w and f_{HT}, are largely uncorrelated, then there is a proportion between the ratios of the data yields of two adjacent regions of the ABCD plane,

$$\frac{N_A^{est}}{N_C} = \frac{N_B}{N_D}, \tag{8.1}$$

where N_A^{est}, N_B, N_C and N_D are the number of events in each of the regions, found in Table 8.1.

Region	N_B	N_C	N_D
Events	9847	15	986500

Table 8.1: Number of preselected Run 2 data events in each of the control regions.

If the signal events are fully confined to the signal region A, then the distribution in the control regions consists solely of background events. With enough events in each control region, one can solve Equation 8.1 for N_A^{est} to get the background estimate in the signal region.

The ratio $\frac{N_B}{N_D}$ is known as the *transfer factor* (TF). If the signal selection variables, w and f_{HT}, are uncorrelated, the TF is expected to be uniform across slices of the w axis. The Pearson Correlation Coefficient[1] between w and f_{HT} for the preselected data in the ABCD plane is -0.015, which indicates the correlation between the two variables is low. From the numbers in Table 8.1, the number of background events in the signal region is estimated to be

$$N_A^{bkg} = N_C \frac{N_B}{N_D} \tag{8.2}$$

$$= 0.15 \pm 0.04, \tag{8.3}$$

where the uncertainty in Eq. 8.3 is the statistical uncertainty from the event count.

8.2 Validation of the ABCD method

To check if a background estimate from using the ABCD method can be reliable, a validation test is performed by applying the ABCD method in subregions of regions B and D, called validation regions

[1] Defined as $r = \frac{\Sigma(x_i-\bar{x})(y_i-\bar{y})}{\sqrt{\Sigma(x_i-\bar{x})^2\Sigma(y_i-\bar{y})^2}}$, where x and y are the two variables that define the plane of the distribution.

(VR), defined as:

- Region $B^{'}$: $0.4 \leq w < 0.665$ and $0.77 \leq f_{HT} < 1.0$
- Region $B^{''}$: $0.665 \leq w < 0.93$ and $0.77 \leq f_{HT} < 1.0$
- Region $D^{'}$: $0.4 \leq w < 0.665$ and $0.5 \leq f_{HT} < 0.77$
- Region $D^{''}$: $0.665 \leq w < 0.93$ and $0.5 \leq f_{HT} < 0.77$.

Eq. 8.4 contains the number of events observed in region $B^{''}$ and Eq. 8.5 gives the background estimate in region $B^{''}$ using the ABCD method defined in Eq. 8.2.

$$B''_{yield} = 2163 \pm 47 \tag{8.4}$$

$$\begin{aligned} N''_B &= N''_D \frac{N'_B}{N'_D} \\ &= 2368 \pm 28. \end{aligned} \tag{8.5}$$

The validation test shows that there is a discrepancy between the data yields and the estimation made by the ABCD method, i.e., they do not agree within uncertainties. This indicates that the small correlation between the discriminating variables, f_{HT} and w, is resulting in a TF that is not uniform across the range of w.

8.2.1 Transfer Factor (B/D) non-uniformity

Figure 8.2 illustrates the non-uniformity of the TF as a function of w: the ratio of B over D decreases close to the signal region. The source of this non-uniformity was studied in Refs. [90],[38], and can be explained by the effect of the detector's geometry on w and f_{HT}, which leads to a correlation of each of the discriminating variables, independently, with $|\eta|$. Figure 8.3 illustrates how there are three easily distinguishable regions in the f_{HT} and w distributions when plotted against $|\eta|$. The three regions can be defined in the following ranges:

- η_1: $0 \leq |\eta| < 0.32$

- η_2: $0.32 \leq |\eta| < 0.82$

- η_3: $0.82 \leq |\eta| < 1.375$.

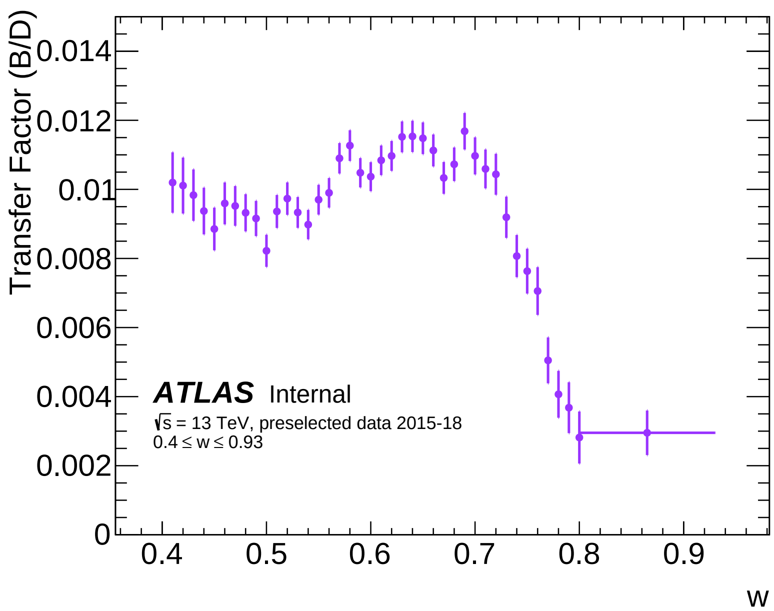

Figure 8.2: Transfer factor (B/D) as a function of w. To compute the transfer factor the w range was binned. The TF for each bin is computed based on the B and D yields for each w bin.

8.3 η-sliced ABCD method

To address the yield discrepancy observed in Section 8.2, we control the cause of the correlation by slicing the ABCD plane into the three ranges of $|\eta|$ listed in the previous section.

In Figure 8.4, the three TF vs w distributions resulting from slicing the ABCD plane in $|\eta|$ are seen. It can be observed that the difference between the TF of the η_2 region and the other two regions is one order of magnitude, which is why an average of these numbers would not return a correct background estimate. By computing the background estimate as the sum of the background estimated for each of the individual η slices, a more precise value is obtained. The background estimate for each slice is the constant fit (TF_i) of the TF as a function of w times the number of events in region C for that slice

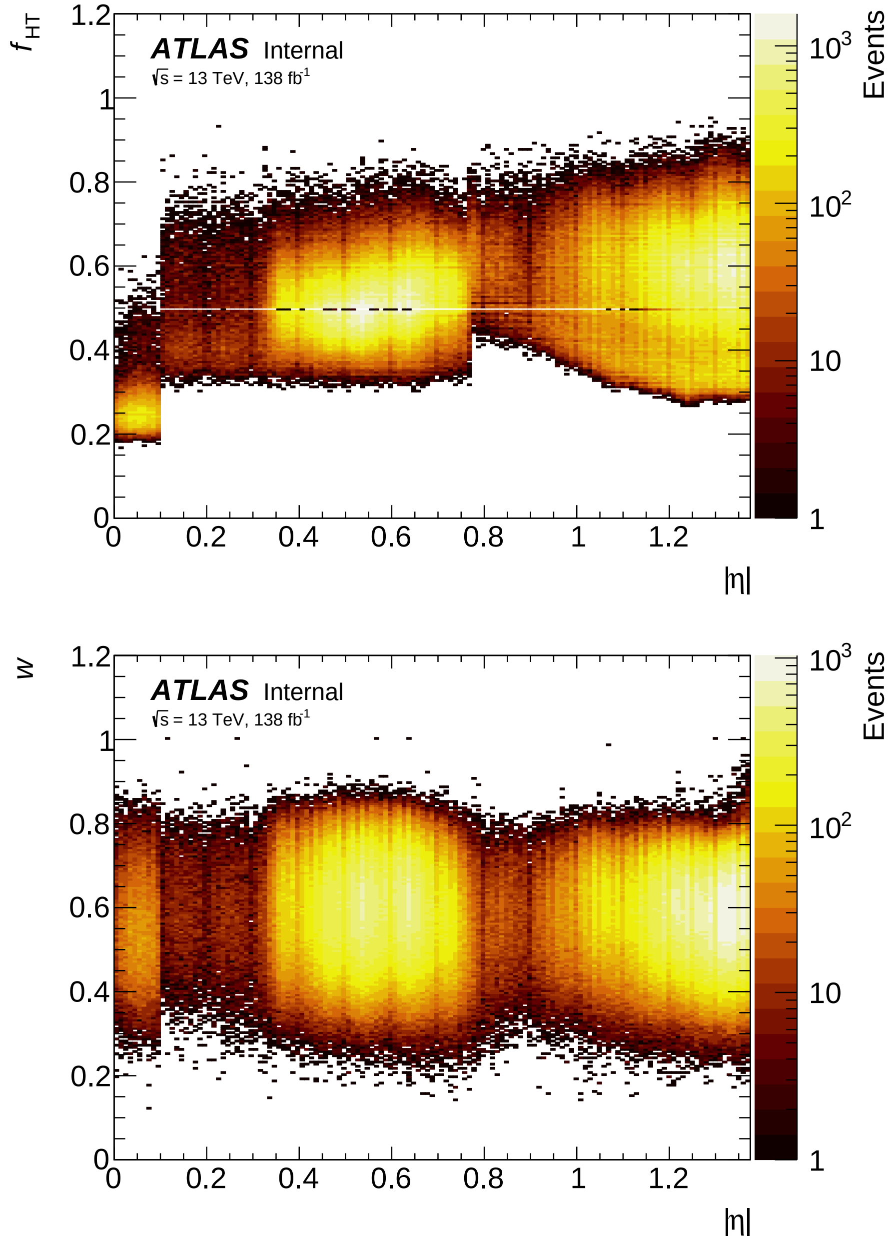

Figure 8.3: f_{HT} versus $|\eta|$ (top) and w versus $|\eta|$ (bottom) distributions of the Run 2 data after preselection.

(i), $N_{C,i}$:

$$N_{A,i}^{bkg} = \mathrm{TF}_i N_{C,i}. \tag{8.6}$$

The root-mean-square (RMS) uncertainty of the constant fit is assigned as a systematic uncertainty of TF_i, and is propagated into the background estimate for each η slice. Table 8.2 contains the computation of the background estimate via the η-sliced ABCD method. A relative systematic uncertainty of 32%, resulting from the RMS uncertainty of the constant fit, accounts for the TF non-uniformity.

η_{range}	$N_C \pm$ (stat.)	TF $\pm$ (stat.) $\pm$ (syst.)	$N_A^{est.} \pm$ (stat.) $\pm$ (syst.)
η_1	2.0 ± 1.4	$0.0087 \pm 0.0014 \pm 0.0066$	$0.0174 \pm 0.0126 \pm 0.0180$
η_2	2.0 ± 1.4	$0.0013 \pm 0.0001 \pm 0.0002$	$0.0026 \pm 0.0018 \pm 0.0018$
η_3	11.0 ± 3.3	$0.0158 \pm 0.0001 \pm 0.0027$	$0.1738 \pm 0.0524 \pm 0.0602$
Total	15		$0.19 \pm 0.05 \pm 0.06$

Table 8.2: Mean transfer factor (B/D) and resulting background estimate (the product of the mean transfer factor and the number of events in region C) in signal region A for different $|\eta|$ regions. The first uncertainty is statistical and the second is the systematic uncertainty due to the transfer factor non-uniformity. The relative uncertainties in each $|\eta|$ range are added in quadrature for the total background estimate.

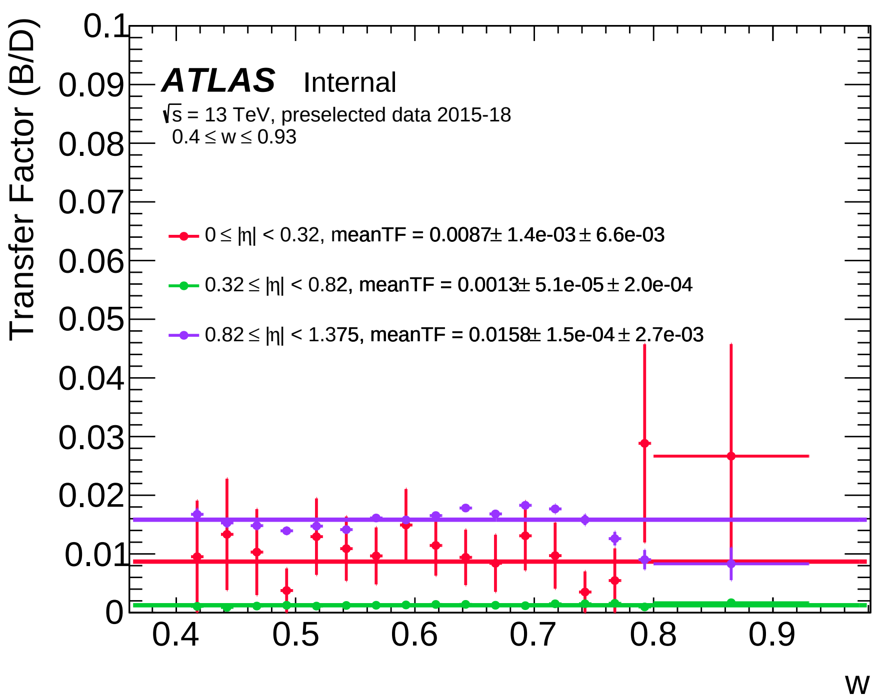

Figure 8.4: Transfer factor (B/D) as a function of w, for $w < 0.93$ for three different $|\eta|$ regions. The solid lines are the constant fits.

8.3.1 Validation of the η-sliced ABCD method

Table 8.3 contains the result of applying the method described above in the validation region. This method yields a background estimate that is in agreement with the counts in region B$''$ (Eq. 8.4).

η_{range}	**TF $\pm$ (stat.) $\pm$ (syst.)**	$N_A^{est.}$ **$\pm$ (stat.) $\pm$ (syst.)**
η_1	$0.0094 \pm 0.0017 \pm 0.0028$	$12 \pm 2 \pm 4$
η_2	$0.0012 \pm 0.0001 \pm 0.0001$	$133 \pm 6 \pm 11$
η_3	$0.0157 \pm 0.0002 \pm 0.0012$	$1885 \pm 21 \pm 144$
Total		$2030 \pm 22 \pm 145$

Table 8.3: Mean transfer factor (B/D) and resulting background estimate for the validation region B$''$, for different $|\eta|$ ranges. The first uncertainty is statistical and the second is the systematic uncertainty due to the transfer factor non-uniformity, obtained by adding the relative uncertainties in each $|\eta|$ range in quadrature.

8.4 Signal leakage

The definition of one general signal region for all masses and charges considered does not come without its challenges. Leakage of the signal distribution into the CRs is observed, to a certain degree, for all mass-charge combinations. These values are summarized in Table H.1, for the Drell-Yan spin-½ signal samples, where the last column indicates what fraction of events in the ABCD plane are contained by the signal region. The values of this column are illustrated in Figure 8.5. Significant leakage of the signal into the CRs is seen in the $|z| = 20$ HECOs. Some HIPs with smaller charges appear in region C due to the smaller ionizing power, which makes it harder to achieve large enough f_{HT} values.

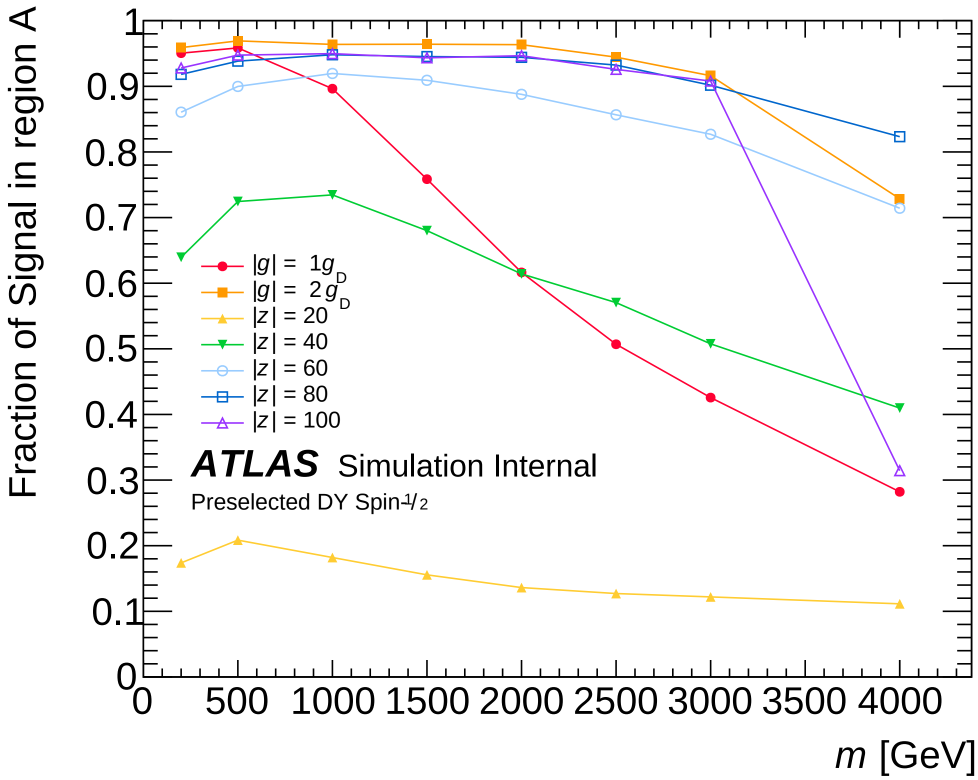

Figure 8.5: Fraction of signal events in region A for each of the Drell-Yan spin-½ MC samples.

By computing the background estimate including the signal sample fractions in the signal and control regions, we can more precisely see the effect of the signal leakage on the background estimation. This is done through a maximum likelihood fit.

8.4.1 Maximum-likelihood fit background estimate

The expected number of events M_i in each of the regions i = A, B, C and D is the sum of the number of simulated signal events (N_i^s) times the signal strength (μ), plus the background estimate (N_i^{bkg}), as follows:

$$M_A = \mu\sigma_{\text{eff}} N_A^s + N_A^{\text{bkg}} \tag{8.7}$$

$$M_B = \mu\sigma_{\text{eff}} N_B^s + N_B^{\text{bkg}} \tag{8.8}$$

$$M_C = \mu\sigma_{\text{eff}} N_C^s + N_C^{\text{bkg}} \tag{8.9}$$

$$M_D = \mu\sigma_{\text{eff}} N_D^s + N_D^{\text{bkg}}, \tag{8.10}$$

where σ_{eff} is the nuisance parameter that accounts for the total systematic uncertainty of the signal selection efficiency. Since the background estimate is constrained via the ABCD method, summarized in Eq. 8.1, parameters e_B and e_C are defined as

$$e_B = \frac{N_B^{\text{bkg}}}{N_A^{\text{bkg}}}$$

$$e_C = \frac{N_C^{\text{bkg}}}{N_A^{\text{bkg}}},$$

and Eqs. 8.7–8.10 can be rewritten as

$$M_A = \mu\sigma_{\text{eff}} N_A^s + N_A^{\text{bkg}} \tag{8.11}$$

$$M_B = \mu\sigma_{\text{eff}} N_B^s + e_B N_A^{\text{bkg}} \tag{8.12}$$

$$M_C = \mu\sigma_{\text{eff}} N_C^s + e_C N_A^{\text{bkg}} \tag{8.13}$$

$$M_D = \mu\sigma_{\text{eff}} N_D^s + e_B e_C N_A^{\text{bkg}}. \tag{8.14}$$

The probability of obtaining the observed number of events N_i in region i of a cut and count experiment is given by the Poisson distribution,

$$L(N_i|\mu, N_i^{\text{bkg}}, \sigma_{\text{eff}}) = \frac{e^{-M_i} M_i^{N_i}}{N_i!}, \tag{8.15}$$

where the signal strength μ and N_i^{bkg} are the free parameters that define M_i, as stated in Eqs. 8.7–8.10. Considering a background estimate that takes into account all four regions of the ABCD plane, the probability or *likelihood* of the result of the experiment to yield N_A, N_B, N_C and N_D is the product of the likelihoods in Eq. 8.15 for the signal and control regions of the plane:

$$L(N_A, N_B, N_C, N_D|\mu, N_A^{\text{bkg}}, e_B, e_C) = \prod_{i=A,B,C,D} \frac{e^{-M_i} M_i^{N_i}}{N_i!}, \tag{8.16}$$

The free parameters μ and N_i^{bkg} are obtained by maximizing the likelihood function, Eq. 8.16, for each mass and charge. These parameters are computed as part of the limit setting procedure using a statistical software tool called HistFitter [103].

In the case of the η-sliced approach, Equations 8.7-8.10 and Equation 8.16 are modified to reflect the three η ranges of the ABCD plane. Equation 8.17 considers the product of the likelihood of the three sub-ranges. Parameters for the maximum likelihood are obtained by fitting all three η ranges simultaneously.

$$L(N_A, N_B, N_C, N_D|\mu, N_A^{\text{bkg}}, e_B, e_C) = \prod_{k=\eta_1,\eta_2,\eta_3} \prod_{i=A,B,C,D} \frac{e^{-M_{i,k}} M_{i,k}^{N_{i,k}}}{N_{i,k}!}. \tag{8.17}$$

Post-fit background estimate values can be seen for the fully simulated Drell-Yan spin-½ signal samples in Table 8.4 for different hypotheses of the event yield in the SR, N_A.

Background estimate in A					
$\|g\|$, $\|z\|$ [g_{D}, e]	**Mass [GeV]**	$N_A = 0$	$N_A = 1$	$N_A = 2$	$N_A = 3$
1	200	0.15 ± 0.02	0.15 ± 0.02	0.15 ± 0.02	0.15 ± 0.02
1	500	0.15 ± 0.02	0.15 ± 0.02	0.15 ± 0.02	0.15 ± 0.02
1	1000	0.15 ± 0.02	0.15 ± 0.02	0.15 ± 0.02	0.15 ± 0.02
1	1500	0.15 ± 0.02	0.15 ± 0.02	0.14 ± 0.02	0.14 ± 0.02
1	2000	0.15 ± 0.02	0.14 ± 0.02	0.14 ± 0.01	0.13 ± 0.01
1	2500	0.15 ± 0.02	0.14 ± 0.02	0.13 ± 0.01	0.12 ± 0.01
1	3000	0.15 ± 0.02	0.14 ± 0.01	0.12 ± 0.01	0.11 ± 0.01
1	4000	0.15 ± 0.02	0.13 ± 0.01	0.1 ± 0.01	0.09 ± 0.01

Continued on next page

Table 8.4: Background estimate after the simultaneous signal and background fit in the full ABCD plane for $|\eta| \leq 1.375$ for all Drell-Yan spin-½ signal samples, with different signal region data hypotheses.

$\lvert g\rvert$, $\lvert z\rvert$ [g_{D}, e]	**Mass [GeV]**	$N_A = 0$	$N_A = 1$	$N_A = 2$	$N_A = 3$
2	200	0.15 ± 0.02	0.15 ± 0.02	0.15 ± 0.02	0.15 ± 0.02
2	500	0.15 ± 0.02	0.15 ± 0.02	0.15 ± 0.02	0.15 ± 0.02
2	1000	0.15 ± 0.02	0.15 ± 0.02	0.15 ± 0.02	0.15 ± 0.02
2	1500	0.15 ± 0.02	0.15 ± 0.02	0.15 ± 0.02	0.15 ± 0.02
2	2000	0.15 ± 0.02	0.15 ± 0.02	0.15 ± 0.02	0.15 ± 0.02
2	2500	0.15 ± 0.02	0.15 ± 0.02	0.15 ± 0.02	0.15 ± 0.02
2	3000	0.15 ± 0.02	0.15 ± 0.02	0.15 ± 0.02	0.15 ± 0.02
20	200	0.09 ± 0.01	0.1 ± 0.01	0.1 ± 0.01	0.09 ± 0.01
20	500	0.15 ± 0.02	0.12 ± 0.01	0.09 ± 0.01	0.09 ± 0.01
20	1000	0.15 ± 0.02	0.11 ± 0.01	0.1 ± 0.01	0.1 ± 0.01
20	1500	0.15 ± 0.02	0.1 ± 0.01	0.1 ± 0.01	0.1 ± 0.01
20	2000	0.15 ± 0.02	0.1 ± 0.01	0.1 ± 0.01	0.1 ± 0.01
20	2500	0.15 ± 0.02	0.1 ± 0.01	0.1 ± 0.01	0.1 ± 0.01
20	3000	0.15 ± 0.02	0.1 ± 0.01	0.1 ± 0.01	0.1 ± 0.01
20	4000	0.15 ± 0.02	0.1 ± 0.01	0.1 ± 0.01	0.1 ± 0.01
40	200	0.15 ± 0.02	0.14 ± 0.02	0.14 ± 0.01	0.13 ± 0.01
40	500	0.15 ± 0.02	0.15 ± 0.02	0.14 ± 0.02	0.14 ± 0.01
40	1000	0.15 ± 0.02	0.15 ± 0.02	0.14 ± 0.02	0.14 ± 0.02
40	1500	0.15 ± 0.02	0.15 ± 0.02	0.14 ± 0.02	0.14 ± 0.01
40	2000	0.15 ± 0.02	0.14 ± 0.02	0.14 ± 0.01	0.13 ± 0.01
40	2500	0.15 ± 0.02	0.14 ± 0.02	0.14 ± 0.01	0.13 ± 0.01
40	3000	0.15 ± 0.02	0.14 ± 0.02	0.13 ± 0.01	0.12 ± 0.01
40	4000	0.15 ± 0.02	0.14 ± 0.01	0.12 ± 0.01	0.11 ± 0.01
60	200	0.15 ± 0.02	0.15 ± 0.02	0.15 ± 0.02	0.15 ± 0.02
60	500	0.15 ± 0.02	0.15 ± 0.02	0.15 ± 0.02	0.15 ± 0.02

Continued on next page

Table 8.4: Background estimate after the simultaneous signal and background fit in the full ABCD plane for $|\eta| \leq 1.375$ for all Drell-Yan spin-½ signal samples, with different signal region data hypotheses.

$\lvert g \rvert$, $\lvert z \rvert$ [g_{D}, e]	**Mass [GeV]**	$N_A = 0$	$N_A = 1$	$N_A = 2$	$N_A = 3$
60	1000	0.15 ± 0.02	0.15 ± 0.02	0.15 ± 0.02	0.15 ± 0.02
60	1500	0.15 ± 0.02	0.15 ± 0.02	0.15 ± 0.02	0.15 ± 0.02
60	2000	0.15 ± 0.02	0.15 ± 0.02	0.15 ± 0.02	0.15 ± 0.02
60	2500	0.15 ± 0.02	0.15 ± 0.02	0.15 ± 0.02	0.14 ± 0.02
60	3000	0.15 ± 0.02	0.15 ± 0.02	0.15 ± 0.02	0.14 ± 0.02
60	4000	0.15 ± 0.02	0.15 ± 0.02	0.14 ± 0.02	0.13 ± 0.01
80	200	0.15 ± 0.02	0.15 ± 0.02	0.15 ± 0.02	0.15 ± 0.02
80	500	0.15 ± 0.02	0.15 ± 0.02	0.15 ± 0.02	0.15 ± 0.02
80	1000	0.15 ± 0.02	0.15 ± 0.02	0.15 ± 0.02	0.15 ± 0.02
80	1500	0.15 ± 0.02	0.15 ± 0.02	0.15 ± 0.02	0.15 ± 0.02
80	2000	0.15 ± 0.02	0.15 ± 0.02	0.15 ± 0.02	0.15 ± 0.02
80	2500	0.09 ± 0.01	0.15 ± 0.02	0.15 ± 0.02	0.15 ± 0.02
80	3000	0.15 ± 0.02	0.15 ± 0.02	0.15 ± 0.02	0.1 ± 0.01
80	4000	0.15 ± 0.02	0.15 ± 0.02	0.15 ± 0.02	0.15 ± 0.02
100	200	0.15 ± 0.02	0.15 ± 0.02	0.15 ± 0.02	0.15 ± 0.02
100	500	0.15 ± 0.02	0.15 ± 0.02	0.15 ± 0.02	0.15 ± 0.02
100	1000	0.15 ± 0.02	0.15 ± 0.02	0.15 ± 0.02	0.15 ± 0.02
100	1500	0.15 ± 0.02	0.11 ± 0.01	0.15 ± 0.02	0.15 ± 0.02
100	2000	0.1 ± 0.01	0.15 ± 0.02	0.15 ± 0.02	0.15 ± 0.02
100	2500	0.15 ± 0.02	0.15 ± 0.02	0.15 ± 0.02	0.15 ± 0.02
100	3000	0.15 ± 0.02	0.15 ± 0.02	0.15 ± 0.02	0.15 ± 0.02

Table 8.4: Background estimate after the simultaneous signal and background fit in the full ABCD plane for $|\eta| \leq 1.375$ for all Drell-Yan spin-½ signal samples, with different signal region data hypotheses.

It is important to note that the results contained in Table 8.4 do not follow the η-sliced approach and thus resemble the default ABCD method result. Signal samples of specific mass/charge combinations with high leakage in region C result in smaller post-fit background estimates when the hypothesis N_A is larger. The reason for this is that the signal strength μ increases, resulting in an increase of the signal in all regions. In region C, where N_C^s is large, the background estimate has to compensate. As a result of the constraint given by Eq. 8.1, N_A^{bkg} becomes smaller.

8.5 Background estimate

The background estimated through the η-sliced method is not quoted as the background estimate of the analysis for two reasons related to the cross section limit setting procedure explained in Chapter 9. First, the η-sliced background estimate would only be compatible in the limit setting procedure with the fully simulated Drell-Yan spin-½ production mode. Second, the analysis team ran into technical problems when running the cross section limit setting procedure for the η-sliced likelihood function, Eq. 8.17. The limit setting algorithm did not yield cross section limits for a non-negligible number of HIP mass/charge combinations. Both of these situations will be explained in Section 9.3. Ultimately, the background estimate in the signal region A is stated by Eq. 8.18,

$$N_A^{bkg} = 0.15 \pm 0.04(stat.) \pm 0.05(syst.), \tag{8.18}$$

where the first uncertainty is statistical reported in Eq. 8.3, and the second is the systematic uncertainty of the TF non-uniformity.

CHAPTER 9

Results and Interpretation

After unblinding the signal region of the ABCD plane, no event was observed. The next step is to interpret this result by setting upper limits on the production cross sections of each of the signal samples considered, for the data collected. The CLs technique is used to set cross section upper limits that can be fairly compared to other experiments.

9.1 CLs technique

The CLs technique [104] was designed for the purpose of presenting search results that could be compared with other results under different experimental conditions. The technique is used to determine exclusion intervals. Using a frequentist approach, these intervals present a statement about the compatibility of the data with the theory.

In searches for new physics, like the one presented in this thesis, both confirming and falsifying a hypothesis are equally important. If the data collected can be explained without new physics theories, i.e., only background is observed, then it is said that the null hypothesis (H_0) is true. The alternative hypothesis (H_1), the signal + background hypothesis, is favoured when the null hypothesis has been rejected to a certain degree. The CLs technique is defined as

$$CLs = \frac{p(s+b)}{1-p(b)} < \alpha, \tag{9.1}$$

where the numerator of Eq. 9.2, $p(s+b)$, is the probability of the experiment to result in the observation of a parameter $q \geq q_{\text{obs}}$ compatible with the signal+background hypothesis. This is defined in Eq. 9.2. The probability of an observation of $q \leq q_{\text{obs}}$, under the assumption of a background only hypothesis, is $p(b)$, defined by Eq. 9.3.

$$p_{s+b} = P(q \geq q_{obs}|s+b) = \int_{q_{obs}}^{\infty} f(q|s+b)dq \tag{9.2}$$

$$p_b = P(q \leq q_{obs}|b) = \int_{-\infty}^{q_{obs}} f(q|b)dq. \tag{9.3}$$

In Eq. 9.1 $1-\alpha$ is the confidence level of excluding the $s+b$ hypothesis, normalized to the complement of the background-only probability. In High Energy Physics (HEP), the standard of the confidence level is 95%, and thus $\alpha = 0.05$. Functions $f(q|b)$ and $f(q|s+b)$ are the probability density functions (PDF) of the test-statistic q. These definitions are illustrated in Figure 9.1.

The CLs technique protects against excluding models to which there is little or no sensitivity. Experiments with low sensitivity like the one observed in Figure 9.2 tend to have large $p(b)$. As seen in Eq. 9.1, this will penalize the value of $p(s+b)$ by making it larger i.e., less likely to meet the criteria set by α.

The test statistic used is the logarithmic likelihood ratio [105]:

$$-2\ln\lambda(\mu) = -2\ln\frac{L(s+b)}{L(b)} \tag{9.4}$$

where $L(s+b)$ and $L(b)$ are defined in Eq. 8.16. Since the value μ cannot be negative, there are three

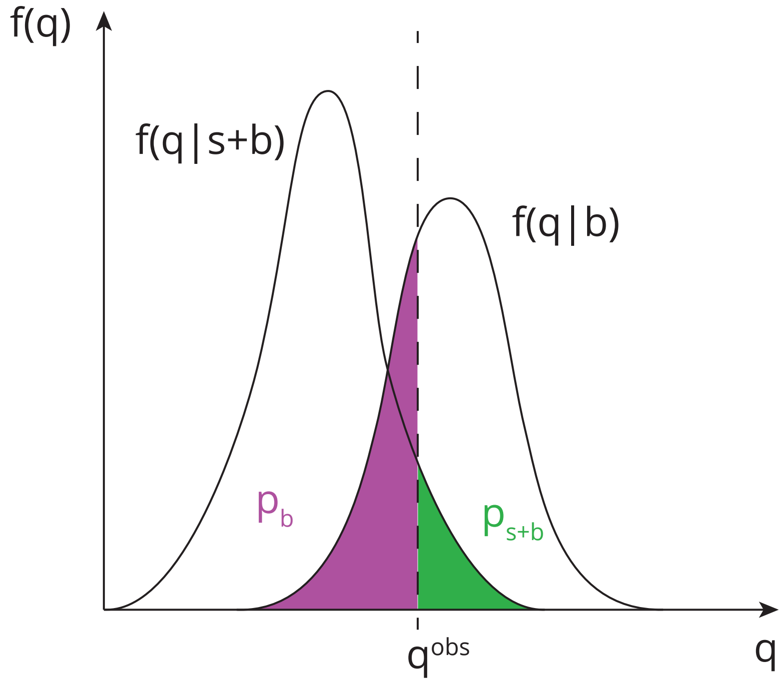

Figure 9.1: Probability density functions of the signal+background and background-only hypotheses as a function of the free parameter q. The dotted line represents the observed parameter q_{obs}. The green shaded area is the probability, assuming the s+b hypothesis, of finding a value $q \geq q_{\text{obs}}$ that is compatible with the s+b hypothesis. The purple shaded area is the probability, under the background only hypothesis, of finding a $q \leq q_{\text{obs}}$ compatible with the background only hypothesis.

cases:

$$-2\ln\lambda(\mu) = \begin{cases} -2\ln\frac{L(\mu,\hat{\hat{\theta}}(\mu))}{L(0,\hat{\hat{\theta}}(0))} & \text{if } \hat{\mu} \leq 0 \\ -2\ln\frac{L(\mu,\hat{\hat{\theta}}(\mu))}{L(\hat{\mu},\hat{\theta})} & \text{if } 0 \leq \hat{\mu} \leq \mu \\ 0 & \text{if } \mu < \hat{\mu} \end{cases} \tag{9.5}$$

where $\hat{\mu}$ and $\hat{\theta}$ are the maximum likelihood estimators. The nuisance parameters, i.e., the total systematic uncertainty of the signal selection, are represented by θ, and $\hat{\hat{\theta}}$ is the value of θ that maximizes the likelihood for a given μ.

The asymptotic formulae defined by Eq. 9.5 are not applicable to the low statistics expected in these types of searches, thus, the test-statistics distributions are computed through multiple pseudo-experiments, also known as "toys".

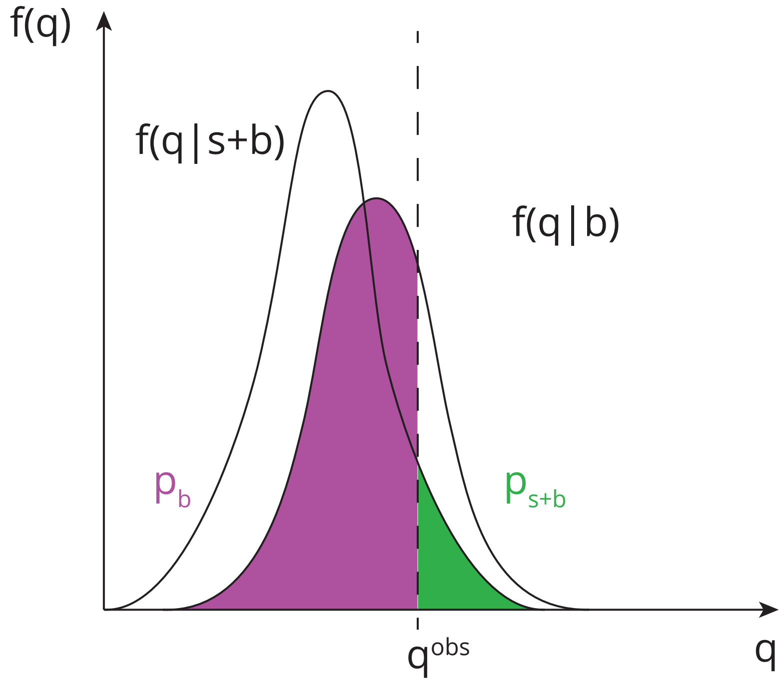

Figure 9.2: Probability density functions of the signal+background and background only hypothesis as a function of the free parameter q for a low sensitivity model.

9.2 HistFitter

HistFitter [103] is a software framework for statistical data analysis. It has been used in this analysis to build the PDFs defined in Eqs. 8.16 and 8.17 from the MC signal sample yields and the data observed. The framework provides three fit strategies based on the regions of the ABCD plane considered, the simulated MC signal samples used and the purpose of the fit. These strategies are: background-only fit, model-dependent signal fit and model-independent signal fit. In this particular analysis, a model-dependent signal fit was used with the purpose of computing exclusion limits for each one of the MC signal samples.

HistFitter is used to compute limits in the number of produced HIP events for each mass/charge/spin point for each production model. The calculation is performed in the frequentist profile likelihood test statistic with 95% confidence level, using 5000 toys. HistFitter produces the signal strength value, μ_{sig}.

Experimental cross-section upper limits, σ, are computed as

$$\sigma = \frac{\mu_{\mathrm{sig}}}{\epsilon \mathcal{L}}, \tag{9.6}$$

using the signal selection efficiency ϵ and the ATLAS integrated luminosity $\mathcal{L}$ collected during the period that the HIP trigger was in operation.

9.3 Cross-section upper limits

Since no event was observed in the signal region A, production cross-section upper limits with a 95% confidence level are computed. These limits state that the signal hypotheses considered have production cross-sections smaller than those in Figures 9.3–9.8 and corresponding Tables 9.1 and 9.4. Larger cross sections have been excluded.

The fit for the fully simulated Drell-Yan spin-½ production mechanism contained both signal and control region information. For all other production mechanisms, a signal region only fit was performed considering that it was statistically prohibitive to compute extrapolated efficiencies in the control regions, as described in Section 5.3.

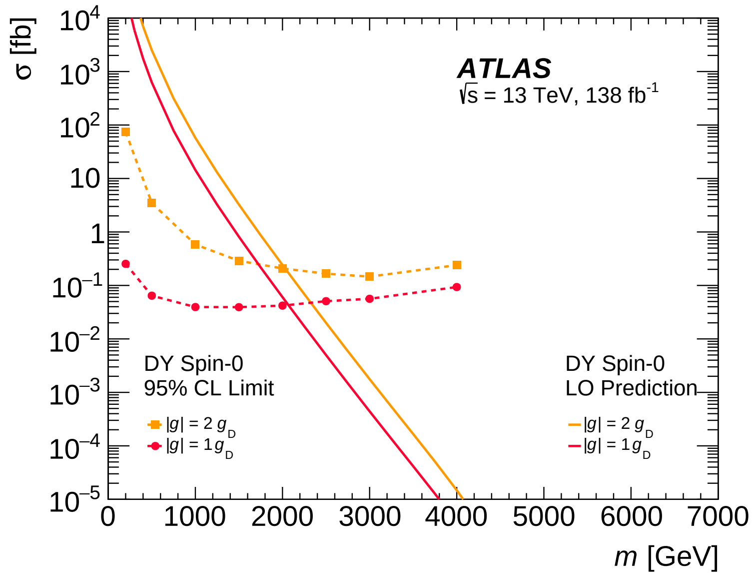

Figure 9.3: Production cross-section upper limits for masses and charges of Drell-Yan pair-produced spin-0 monopoles. Cross section upper limits for charge/mass combinations for which the selection efficiency is below 0.1% are not computed. The solid lines are the theoretical cross-sections as a function of mass.

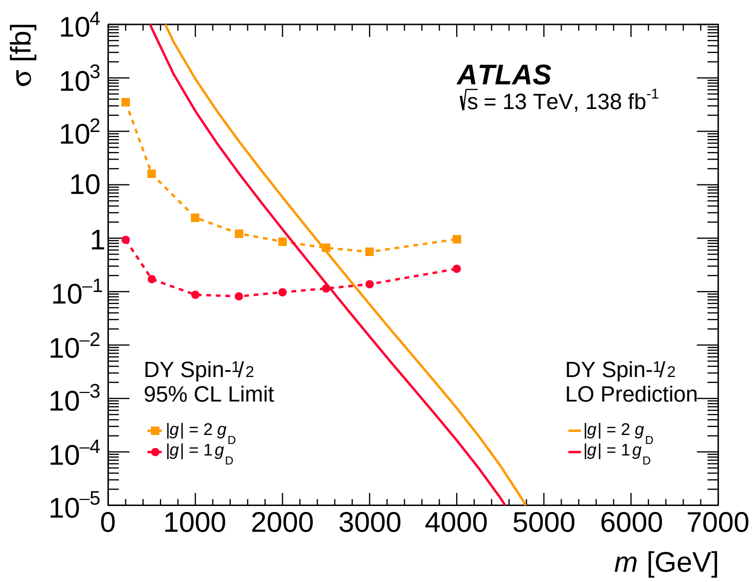

Figure 9.4: Production cross-section upper limits for masses and charges of Drell-Yan pair-produced spin-½ monopoles. Cross section upper limits for charge/mass combinations for which the selection efficiency is below 0.1% are not computed. The solid lines are the theoretical cross-sections as a function of mass.

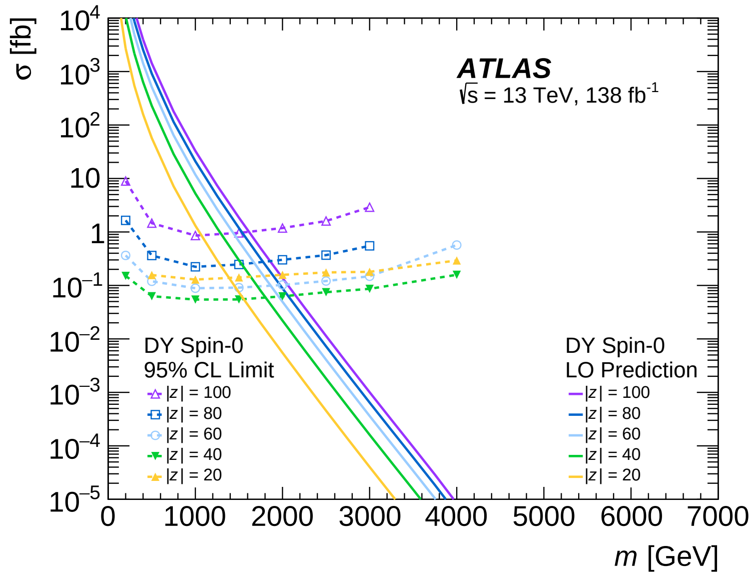

Figure 9.5: Production cross-section upper limits for masses and charges of Drell-Yan pair-produced spin-0 HECOs. Cross section upper limits for charge/mass combinations for which the selection efficiency is below 0.1% are not computed. The solid lines are the theoretical cross-sections as a function of mass.

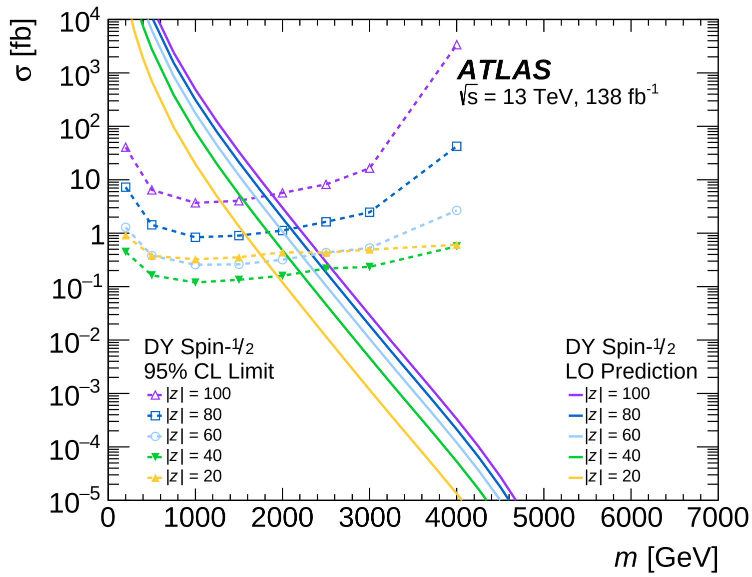

Figure 9.6: Production cross-section upper limits for masses and charges of Drell-Yan pair-produced spin-½ HECOs. Cross section upper limits for charge/mass combinations for which the selection efficiency is below 0.1% are not computed. The solid lines are the theoretical cross-sections as a function of mass.

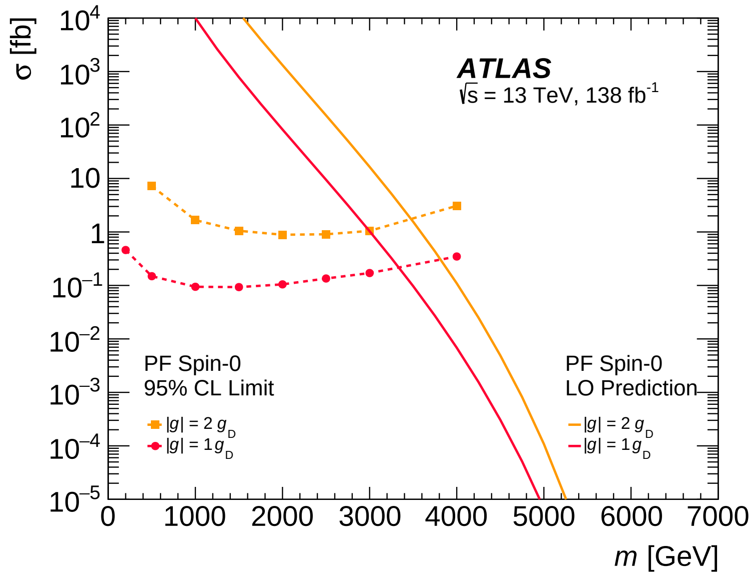

Figure 9.7: Production cross-section upper limits for masses and charges of Photon Fusion pair-produced spin-0 monopoles. Cross section upper limits for charge/mass combinations for which the selection efficiency is below 0.1% are not computed. The solid lines are the theoretical cross-sections as a function of mass.

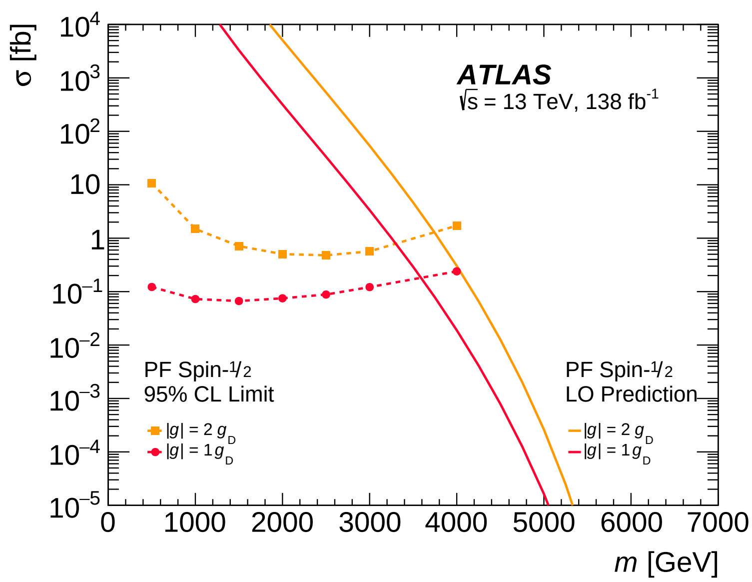

Figure 9.8: Production cross-section upper limits for masses and charges of Photon Fusion pair-produced spin-½ monopoles. Cross section upper limits for charge/mass combinations for which the selection efficiency is below 0.1% are not computed. The solid lines are the theoretical cross-sections as a function of mass.

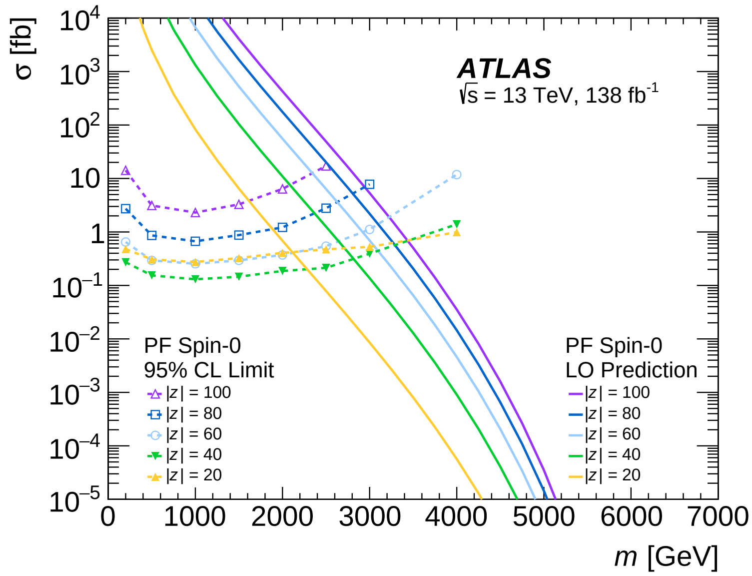

Figure 9.9: Production cross-section upper limits for masses and charges of Photon Fusion pair-produced spin-0 HECOs. Cross section upper limits for charge/mass combinations for which the selection efficiency is below 0.1% are not computed. The solid lines are the theoretical cross-sections as a function of mass.

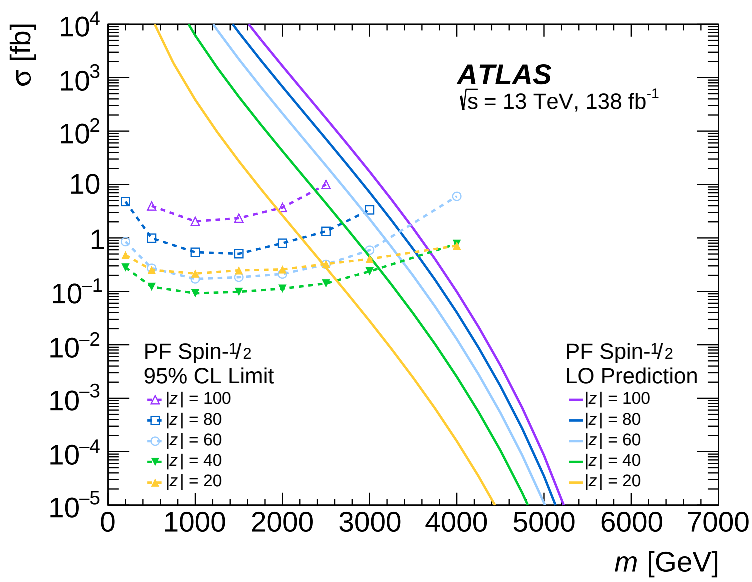

Figure 9.10: Production cross-section upper limits for masses and charges of Photon Fusion pair-produced spin-½ HECOs. Cross section upper limits for charge/mass combinations for which the selection efficiency is below 0.1% are not computed. The solid lines are the theoretical cross-sections as a function of mass.

	Drell-Yan spin-0 Cross Section Upper Limits [fb]						
Mass [GeV]	$\lvert g\rvert = 1g_{\mathrm{D}}$	$\lvert g\rvert = 2g_{\mathrm{D}}$	$\lvert z\rvert = 20$	$\lvert z\rvert = 40$	$\lvert z\rvert = 60$	$\lvert z\rvert = 80$	$\lvert z\rvert = 100$
200	0.253	74.2	0.319	0.151	0.364	1.65	8.95
500	0.0643	3.47	0.157	0.0628	0.119	0.363	1.46
1000	0.0394	0.582	0.129	0.0544	0.0887	0.223	0.857
1500	0.0392	0.289	0.141	0.0547	0.0910	0.247	0.960
2000	0.0419	0.208	0.158	0.0625	0.102	0.302	1.18
2500	0.0508	0.166	0.175	0.0747	0.121	0.369	1.60
3000	0.0562	0.146	0.180	0.0864	0.148	0.550	2.90
4000	0.0933	0.240	0.293	0.158	0.579	-	-

Table 9.1: Cross section upper limits for all masses and charges of Drell-Yan spin-0 HIPs computed with a signal-only fit. Cross section upper limits for charge/mass combinations for which the selection efficiency is below 0.1% are not computed.

	Drell-Yan spin-½ Cross Section Upper Limits [fb]						
Mass [GeV]	$\lvert g\rvert = 1g_{\mathrm{D}}$	$\lvert g\rvert = 2g_{\mathrm{D}}$	$\lvert z\rvert = 20$	$\lvert z\rvert = 40$	$\lvert z\rvert = 60$	$\lvert z\rvert = 80$	$\lvert z\rvert = 100$
200	0.868	341	0.819	0.448	1.28	7.15	-
500	0.163	17.3	0.418	0.171	0.393	1.40	6.67
1000	0.0863	2.73	0.321	0.121	0.259	0.844	3.53
1500	0.0842	1.18	0.295	0.135	0.269	0.916	4.23
2000	0.100	0.847	0.363	0.164	0.319	1.21	5.66
2500	0.118	0.650	0.329	0.229	0.413	1.60	8.36
3000	0.147	0.562	0.330	0.258	0.524	2.42	16.7
4000	0.329	0.801	0.404	0.363	2.53	-	-

Table 9.2: Cross section upper limits for all masses and charges of Drell-Yan spin-½ HIPs computed with a signal-only fit. Cross section upper limits for charge/mass combinations for which the selection efficiency is below 0.1% are not computed.

	Photon Fusion spin-0 Cross Section Upper Limits [fb]						
Mass [GeV]	$\lvert g\rvert = 1g_{\mathrm{D}}$	$\lvert g\rvert = 2g_{\mathrm{D}}$	$\lvert z\rvert = 20$	$\lvert z\rvert = 40$	$\lvert z\rvert = 60$	$\lvert z\rvert = 80$	$\lvert z\rvert = 100$
200	0.459	-	0.480	0.272	0.649	2.73	14.2
500	0.149	7.23	0.307	0.154	0.294	0.862	3.16
1000	0.094	1.67	0.275	0.130	0.254	0.670	2.31
1500	0.0931	1.05	0.325	0.146	0.294	0.874	3.28
2000	0.107	0.887	0.406	0.187	0.371	1.22	6.38
2500	0.135	0.905	0.473	0.213	0.544	2.78	17.2
3000	0.170	1.07	0.527	0.393	1.11	7.79	-
4000	0.347	3.08	0.989	1.39	11.8	-	-

Table 9.3: Cross section upper limits for all masses and charges of Photon Fusion spin-0 HIPs computed with a signal-only fit. Cross section upper limits for charge/mass combinations for which the selection efficiency is below 0.1% are not computed.

	Photon Fusion spin-½ Cross Section Upper Limits [fb]						
Mass [GeV]	$\lvert g\rvert = 1g_{\mathrm{D}}$	$\lvert g\rvert = 2g_{\mathrm{D}}$	$\lvert z\rvert = 20$	$\lvert z\rvert = 40$	$\lvert z\rvert = 60$	$\lvert z\rvert = 80$	$\lvert z\rvert = 100$
200	0.571	-	0.478	0.280	0.852	4.79	-
500	0.122	10.8	0.252	0.122	0.271	0.991	3.97
1000	0.0726	1.49	0.216	0.0920	0.171	0.540	2.05
1500	0.0666	0.711	0.247	0.0981	0.184	0.506	2.35
2000	0.0750	0.504	0.258	0.113	0.211	0.797	3.70
2500	0.0882	0.478	0.326	0.141	0.320	1.33	10.0
3000	0.121	0.566	0.404	0.237	0.591	3.35	-
4000	0.240	1.71	0.716	0.778	6.02	-	-

Table 9.4: Cross section upper limits for all masses and charges of Photon Fusion spin-½ HIPs computed with a signal-only fit. Cross section upper limits for charge/mass combinations for which the selection efficiency is below 0.1% are not computed.

Attempts were made to compute the cross section upper limits under the η-sliced likelihood function defined in Eq. 8.17, which would have allowed the use of the background estimated in Table 8.2 consistently for the Drell-Yan spin-½ signal hypothesis. Unfortunately, for some mass and charges considered, HistFitter did not converge when finding the signal strength, μ_{sig}. Figures 9.11–9.12 contain the cross section limits that were found. On average, a discrepancy of 5.5% is found between the η-sliced and the full η-range approach.

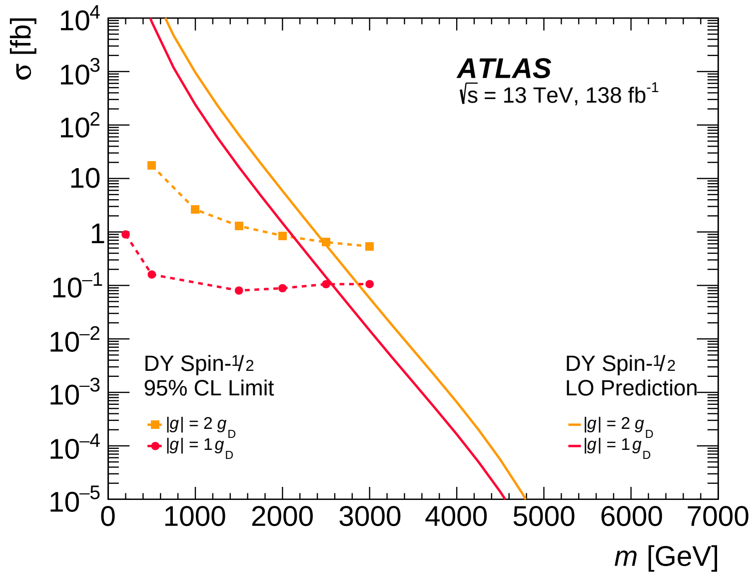

Figure 9.11: Production cross-section upper limits for masses and charges of Drell-Yan pair-produced monopoles for spin-½ considering an η-sliced ABCD plane. Cross section upper limits for charge/mass combinations for which the selection efficiency is below 0.1% are not computed. The solid lines are the theoretical cross-sections as a function of mass.

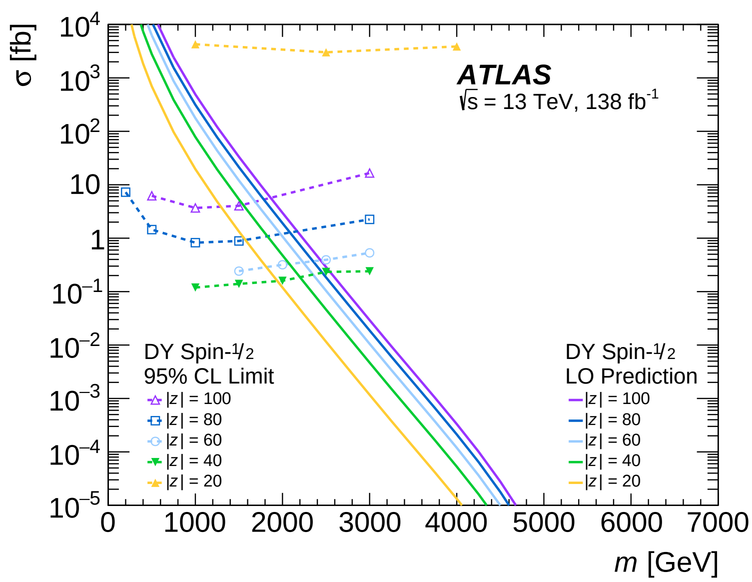

Figure 9.12: Production cross-section upper limits for masses and charges of Drell-Yan pair-produced HECOs for spin-½ considering an η-sliced ABCD plane. Cross section upper limits for charge/mass combinations for which the selection efficiency is below 0.1% are not computed. The solid lines are the theoretical cross-sections as a function of mass.

9.4 Mass lower limits

Comparing the theoretical and experimental production cross-section upper limits, one can make a statement on the lowest possible values for the mass of a HIP for each combination of production mechanism, spin and charge considered with a confidence level of 95%. Masses below that limit are excluded. These limits are found at the mass value where the experimental and theoretical cross-section lines intersect and are summarized in Table 9.5. For those mass limits in which the experimental cross-section limit line does not intersect the theoretical, the highest mass for which a cross section upper limit was determined is set as the mass limit.

	$\lvert g\rvert = 1g_{\mathrm{D}}$	$\lvert g\rvert = 2g_{\mathrm{D}}$	$\lvert z\rvert = 20$	$\lvert z\rvert = 40$	$\lvert z\rvert = 60$	$\lvert z\rvert = 80$	$\lvert z\rvert = 100$
DY spin-0	2097	2055	1425	1833	1901	1791	1651
DY spin-½	2569	2479	1797	2212	2240	2121	1910
PF spin-0	3350	3469	2143	2828	2939	2801	4000
PF spin-½	3613	3737	2480	3117	3142	4000	4000

Table 9.5: Lower mass limits, in GeV, at 95% confidence level.

9.5 Results compared to other LHC searches

This search for HIP in the ATLAS detector extends the current knowledge of experimental cross-section upper limits and mass lower limits for magnetic monopoles and HECOs produced in colliders. The study improves on the results obtained by the MoEDAL collaboration [37] and complements the range studied by the Multi Charged Particle (MCP) analysis at ATLAS [106].

Figure 9.13 illustrates how much more stringent the cross-section upper limits for magnetic monopoles with charges 1 and 2 g_{D} obtained by this ATLAS HIP search are with respect to those obtained by MoEDAL. However, it is important to note that the ATLAS search for HIPs did not combine results from the Drell-Yan and photon fusion production mechanisms. On average, the cross-section upper limits of the ATLAS HIP search is two orders of magnitude lower than those of MoEDAL.

Additionally, the lower mass limits for the magnetic monopole from ATLAS and MoEDAL searches are found in Figure 9.14. This ATLAS search sets the tightest lower mass limits for the Dirac magnetic

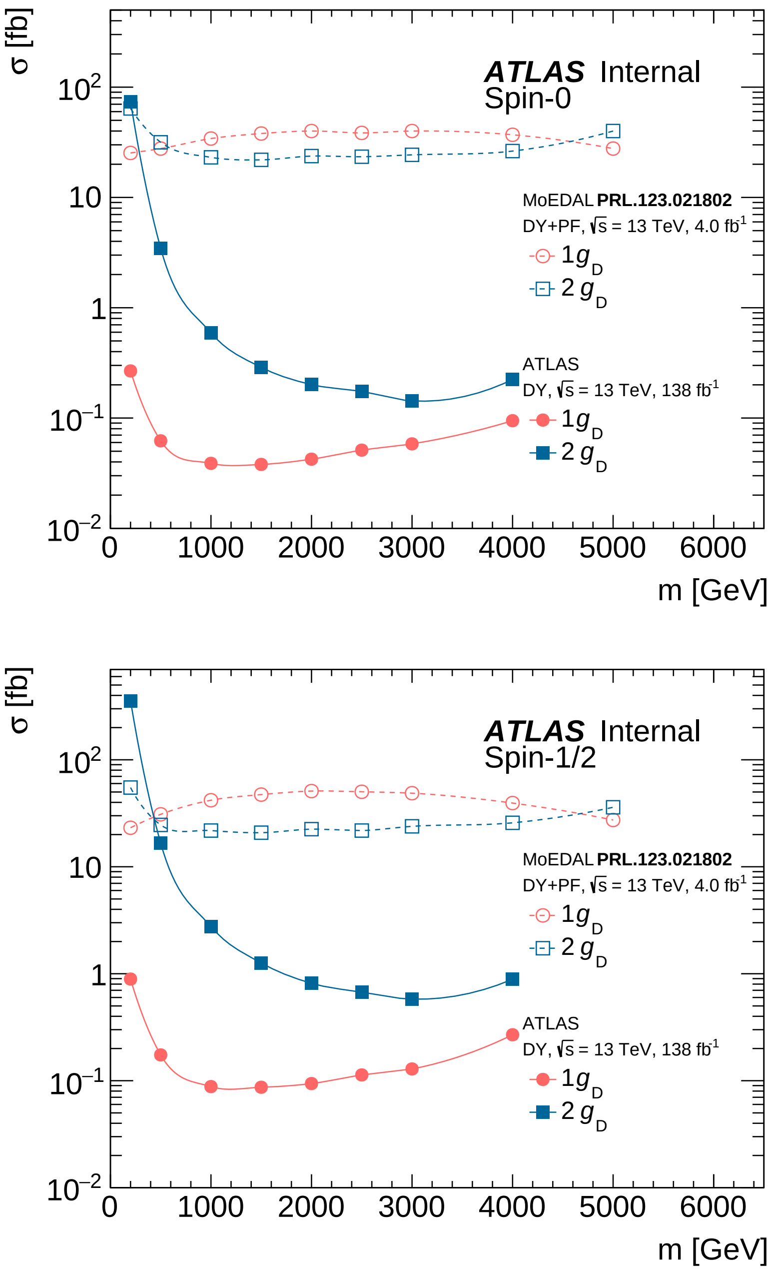

Figure 9.13: Observed 95% confidence level upper cross-section limits for spin-0 (top) and spin-½ (bottom) monopole production as a function of mass for charges $1g_{\mathrm{D}}$ and $2g_{\mathrm{D}}$. The dashed lines indicate the limits from the MoEDAL experiment, which combines the Drell-Yan and photon-fusion production modes. The corresponding Drell-Yan limits from the present search are shown with the same colour and marker, but with solid lines.

monopole of charges 1 and 2 g_{D} to date.

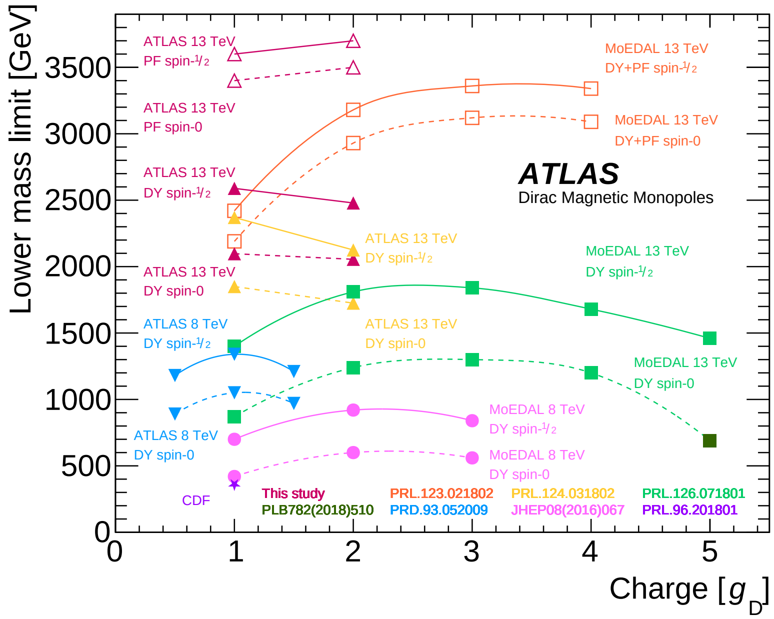

Figure 9.14: Comparison of the mass lower limits obtained by LHC searches in Run 1 and Run 2 for Drell-Yan and Photon Fusion pair produced magnetic monopoles.

Figure 9.15 combines the resulting cross-section upper limits from the MCP analysis, which searches for particles with electric charges between $2 \leq |z| \leq 7$, and those found by this search in ATLAS for HECOs. Although the experimental methods for signal discrimination of these two searches are different, the results from these two studies complement each other for both the Drell-Yan and photon fusion production mechanisms.

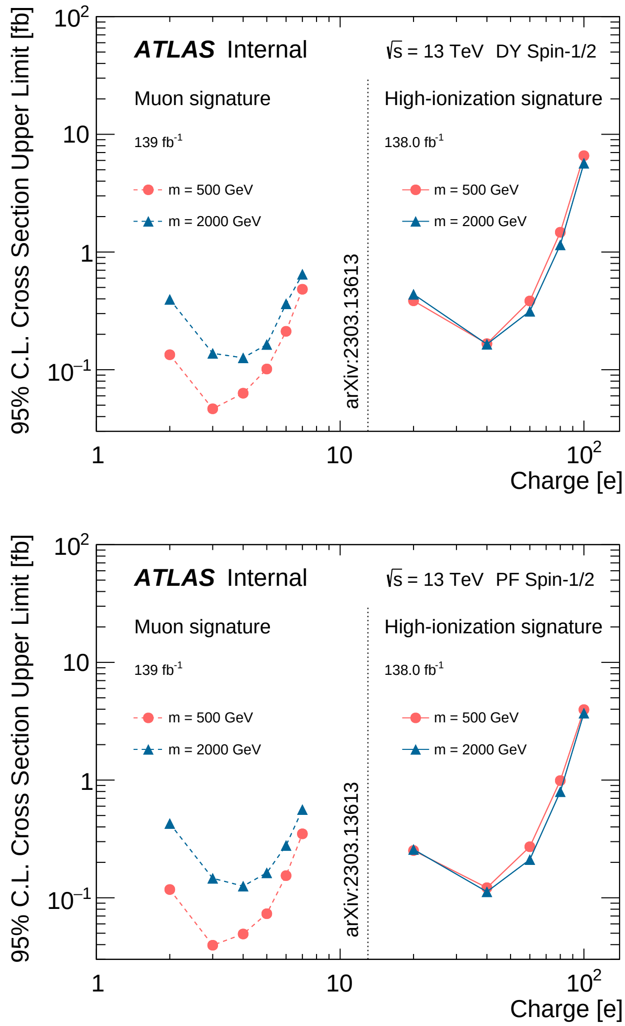

Figure 9.15: Observed 95% confidence level upper cross-section limits for spin-0 (top) and spin-½ (bottom) Drell-Yan HECO production as a function of charge. The limits for charges $2 \leq |z| \leq 7$ are obtained using a signature of highly ionizing particles reaching the muon spectrometer [106].

CHAPTER 10

Conclusion

The successful collection by the ATLAS detector of an integrated luminosity of 138 fb^{-1} from the LHC Run 2 proton-proton collisions at $\sqrt{s}$ =13 TeV permitted the search for magnetic monopoles and other long-lived HIPs. Two pair-production modes are considered as the signal hypotheses for the search: Drell-Yan pair production, which included a Z^0 boson mediator for HECO production, and for the first time in ATLAS, the photon fusion mechanism. For each mode, spin-0 and spin-½ HIP production is studied, for HECOs with charges $|z| = 20, 40, 60, 80$ and 100, and monopoles with charges $|g| = 1$ and $2g_{\text{D}}$ and masses of 200, 500, 1000, 1500, 2000, 3000 and 4000 GeV. A bespoke trigger for the search of HIPs was deployed in the first year of the data collection period and was used to identify interesting events. HIP candidates were preselected based on the quality of their recorded signal and discriminating variables f_{HT} and w, using the information from the TRT and EM LAr calorimeter subdetectors, respectively, were used to exploit HIPs' characteristic signature in the detector.

A background of $N_A^{bkg} = 0.15 \pm 0.04(stat.) \pm 0.05(syst.)$ in the signal region was estimated through the ABCD method. No evidence of HIPs was observed in the data collected by the ATLAS detector during Run 2 of the LHC. The most stringent upper cross section limits to date for the production mechanisms studied are computed with a 95% confidence level for all masses and charges considered. Lower mass limits are also reported.

Bibliography

[1] P. Curie, *On the possible existence of magnetic conductivity and free magnetism*, Seances Sic. Phys. (Paris) (1894) 76 (cit. on p. 1).

[2] S. L. Glashow, *Partial-symmetries of weak interactions*, Nuclear Physics **22** (1961) 579 (cit. on p. 2).

[3] S. Weinberg, *A Model of Leptons*, Phys. Rev. Lett. **19** (21 1967) 1264 (cit. on p. 2).

[4] A. Salam and J. Ward, *Electromagnetic and weak interactions*, Physics Letters **13** (1964) 168 (cit. on p. 2).

[5] P. Dirac, *Quantised Singularities in the Electromagnetic Field*, Proc. Roy. Soc. **A 133** (1931) 60 (cit. on p. 3).

[6] P. A. M. Dirac, *The Theory of Magnetic Poles*, Phys. Rev. **74** (7 1948) 817 (cit. on p. 4).

[7] J. Schwinger, *Magnetic Charge and Quantum Field Theory*, Phys. Rev. **144** (4 1966) 1087 (cit. on p. 8).

[8] Y. Cho and D. Maison, *Monopole configuration in Weinberg-Salam model*, Physics Letters B **391** (1997) 360 (cit. on p. 8).

[9] Y. M. Cho, K. Kimm, and J. H. Yoon, *Finite energy electroweak dyon*, Eur. Phys. J. C **75** (2 2015) (cit. on p. 8).

[10] J. Ellis, N. E. Mavromatos, and T. You, *The price of an electroweak monopole*, Physics Letters B **756** (2016) 29 (cit. on p. 8).

[11] G. 't Hooft, *Magnetic Monopoles in Unified Gauge Theories*, Nucl. Phys. B **79** (1974) 276 (cit. on p. 9).

[12] A. M. Polyakov, *Particle Spectrum in Quantum Field Theory*, JETP Lett. **20** (1974) 194 (cit. on p. 9).

[13] J. Preskill, *Magnetic monopoles*, Annual Review of Nuclear and Particle Science **34** (1984) 461 (cit. on p. 9).

[14] S. Burdin *et al.*, *Non-collider searches for stable massive particles*, Phys. Rept. **582** (2015) 1, arXiv: `1410.1374 [hep-ph]` (cit. on p. 9).

[15] T. W. Kephart, G. K. Leontaris, and Q. Shafi, *Magnetic monopoles and free fractionally charged states at accelerators and in cosmic rays*, Journal of High Energy Physics **2017** (2017) (cit. on p. 9).

[16] MACRO Collaboration, *Final results of magnetic monopole searches with the MACRO experiment*, Eur. Phys. J. C **25** (2002) 511, arXiv: `hep-ex/0207020` (cit. on p. 10).

[17] SLIM Collaboration, *Magnetic monopole search at high altitude with the SLIM experiment*, Radiat. Meas. **44** (2009) 889 (cit. on p. 10).

[18] ANITA-II Collaboration, *Ultra-Relativistic Magnetic Monopole Search with the ANITA-II Balloon-borne Radio Interferometer*, Phys. Rev. D **83** (2011) 023513, arXiv: `1008.1282 [astro-ph.HE]` (cit. on p. 10).

[19] ANTARES Collaboration, *Search for magnetic monopoles with ten years of the ANTARES neutrino telescope*, JHEAp **34** (2022) 1, arXiv: `2202.13786 [astro-ph.HE]` (cit. on p. 10).

[20] F. H. Lauber, *Search for Low Relativistic Magnetic Monopoles at the IceCube Neutrino Observatory*, (2021) (cit. on p. 10).

[21] BAIKAL Collaboration, *Search for relativistic magnetic monopoles with the Baikal Neutrino Telescope*, Astropart. Phys. **29** (2008) 366 (cit. on p. 10).

[22] Super-Kamiokande Collaboration, *Search for GUT monopoles at SuperKamiokande*, Astropart. Phys. **36** (2012) 131, arXiv: `1203.0940 [hep-ex]` (cit. on p. 10).

[23] NOvA Collaboration, *Search for slow magnetic monopoles with the NOvA detector on the surface*, Phys. Rev. D **103** (2021) 012007, arXiv: `2009.04867 [hep-ex]` (cit. on p. 10).

[24] R. Abbasi *et al.*, *Search for relativistic magnetic monopoles with the AMANDA-II neutrino telescope*, Eur. Phys. J. C **69** (2010) 361 (cit. on p. 10).

[25] N. E. Mavromatos and V. A. Mitsou, *Magnetic monopoles revisited: Models and searches at colliders and in the Cosmos*, International Journal of Modern Physics A **35** (2020) 2030012 (cit. on p. 10).

[26] H. Hoffmann *et al.*, *A New Search for Magnetic Monopoles at the CERN ISR with Plastic Detectors*, Lett. Nuovo Cim. **23** (1978) 357 (cit. on p. 10).

[27] B. Aubert, P. Musset, M. Price, and J. P. Vialle, *Search for Magnetic Monopoles in Proton - Anti-proton Interactions at 540-GeV Center-of-mass Energy*, Phys. Lett. B **120** (1983) 465 (cit. on p. 10).

[28] J. L. Pinfold *et al.*, *A Search for highly ionizing particles produced at the OPAL intersection point at LEP*, Phys. Lett. B **316** (1993) 407 (cit. on p. 10).

[29] D. Fryberger, T. E. Coan, K. Kinoshita, and P. B. Price, *Search for Highly Ionizing Particles in e^+e^- Collisions at $\sqrt{s} = 29$-GeV*, Phys. Rev. D **29** (1984) 1524 (cit. on p. 11).

[30] P. Musset, M. Price, and E. Lohrmann, *Search for Magnetic Monopoles in Electron - Positron Collisions at 34-GeV Center-of-mass Energy*, Phys. Lett. B **128** (1983) 333 (cit. on p. 11).

[31] K. Kinoshita, M. Fujii, K. Nakajima, P. B. Price, and S. Tasaka, *Search for Highly Ionizing Particles in e^+e^- Annihilations at $\sqrt{s} = 50$-GeV - 52-GeV*, Phys. Rev. Lett. **60** (1988) 1610 (cit. on p. 11).

[32] P. B. Price, G.-X. Ren, and K. Kinoshita, *Search for Highly Ionizing Particles at the Fermilab Proton Anti-proton Collider*, Phys. Rev. Lett. **59** (1987) 2523 (cit. on p. 11).

[33] M. Bertani *et al.*, *Search for Magnetic Monopoles at the Tevatron Collider*, EPL **12** (1990) 613 (cit. on p. 11).

[34] OPAL Collaboration, *Search for Dirac magnetic monopoles in e+e- collisions with the OPAL detector at LEP2*, Phys. Lett. B **663** (2008) 37, arXiv: 0707.0404 [hep-ex] (cit. on p. 11).

[35] H1 Collaboration, *A Direct search for stable magnetic monopoles produced in positron-proton collisions at HERA*, Eur. Phys. J. C **41** (2005) 133, arXiv: hep-ex/0501039 (cit. on p. 11).

[36] Particle Data Group, *Review of Particle Physics*, PTEP **2020** (2020) 083C01 (cit. on p. 11).

[37] MoEDAL Collaboration, *Magnetic Monopole Search with the Full MoEDAL Trapping Detector in 13 TeV pp Collisions Interpreted in Photon-Fusion and Drell-Yan Production*, Phys. Rev. Lett. **123** (2019) 021802, arXiv: 1903.08491 [hep-ex] (cit. on pp. 11, 12, 105).

[38] ATLAS Collaboration, *Search for Magnetic Monopoles and Stable High-Electric-Charge Objects in 13 TeV Proton-Proton Collisions with the ATLAS Detector*, Phys. Rev. Lett. **124** (2020) 031802, arXiv: 1905.10130 [hep-ex] (cit. on pp. 11, 12, 82).

[39] MoEDAL Collaboration, *Search for magnetic monopoles with the MoEDAL prototype trapping detector in 8 TeV proton-proton collisions at the LHC*, JHEP **08** (2016) 067, arXiv: 1604.06645 [hep-ex] (cit. on p. 12).

[40] MoEDAL Collaboration, *Search for Magnetic Monopoles with the MoEDAL Forward Trapping Detector in 13 TeV Proton-Proton Collisions at the LHC*, Phys. Rev. Lett. **118** (2017) 061801, arXiv: 1611.06817 [hep-ex] (cit. on p. 12).

[41] MoEDAL Collaboration, *Search for magnetic monopoles with the MoEDAL forward trapping detector in 2.11 fb^{-1} of 13 TeV proton-proton collisions at the LHC*, Phys. Lett. B **782** (2018) 510, arXiv: 1712.09849 [hep-ex] (cit. on p. 12).

[42] ATLAS Collaboration, *Search for magnetic monopoles in $\sqrt{s} = 7$ TeV pp collisions with the ATLAS detector*, Phys. Rev. Lett. **109** (2012) 261803, arXiv: 1207.6411 [hep-ex] (cit. on p. 12).

[43] ATLAS Collaboration, *Search for magnetic monopoles and stable particles with high electric charges in 8 TeV pp collisions with the ATLAS detector*, Phys. Rev. D **93** (2016) 052009, arXiv: `1509.08059 [hep-ex]` (cit. on p. 12).

[44] S. Dimopoulos and G. Landsberg, *Black Holes at the Large Hadron Collider*, Phys. Rev. Lett. **87** (16 2001) 161602 (cit. on p. 13).

[45] A. R. Bodmer, *Collapsed Nuclei*, Phys. Rev. D **4** (6 1971) 1601 (cit. on p. 13).

[46] G. Domènech and M. Sasaki, *Gravitational wave hints black hole remnants as dark matter*, Classical and Quantum Gravity **40** (2023) 177001 (cit. on p. 13).

[47] D. M. Jensen, *Strangelets – Effects of Finite Size and Exact Color Singletness*, 2019, arXiv: `1904.04534 [hep-ph]` (cit. on p. 13).

[48] E. Witten, *Cosmic separation of phases*, Phys. Rev. D **30** (2 1984) 272 (cit. on p. 13).

[49] E. Farhi and R. L. Jaffe, *Strange matter*, Phys. Rev. D **30** (11 1984) 2379 (cit. on p. 13).

[50] A. De Rujula and S. L. Glashow, *Nuclearites: A Novel Form of Cosmic Radiation*, Nature **312** (1984) 734 (cit. on p. 13).

[51] S. Coleman, *Q-balls*, Nuclear Physics B **262** (1985) 263 (cit. on p. 14).

[52] F. Marcastel, *CERN's Accelerator Complex. La chaîne des accélérateurs du CERN*, OPEN-PHO-CHART-2013-001, General Photo, 2013 (cit. on p. 16).

[53] J. Wenninger, *Operation and Configuration of the LHC in Run 2*, CERN-ACC-NOTE-2019-0007, 2019 (cit. on p. 17).

[54] ATLAS Collaboration, *Luminosity determination in pp collisions at $\sqrt{s} = 13$ TeV using the ATLAS detector at the LHC*, tech. rep., CERN, 2022, arXiv: `2212.09379 [hep-ex]` (cit. on pp. 18, 19).

[55] E. Eichten, I. Hinchliffe, K. Lane, and C. Quigg, *Supercollider physics*, Rev. Mod. Phys. **56** (4 1984) 579 (cit. on p. 18).

[56] J. Pequenao, *Computer generated image of the whole ATLAS detector*, CERN-GE-0803012, 2008 (cit. on p. 19).

[57] ATLAS Collaboration, *Experiment Briefing: Keeping the ATLAS Inner Detector in perfect alignment*, ATLAS-PHOTO-2020-018, General Photo, 2020 (cit. on p. 21).

[58] B. A. et al, *Production and integration of the ATLAS Insertable B-Layer*, Journal of Instrumentation **13** (2018) T05008 (cit. on p. 22).

[59] ATLAS Collaboration, *Production and integration of the ATLAS Insertable B-Layer*, Journal of Instrumentation **13** (2018) T05008 (cit. on p. 20).

[60] ATLAS Collaboration, *ATLAS pixel detector electronics and sensors*, Journal of Instrumentation **3** (2008) P07007 (cit. on p. 21).

[61] ATLAS Collaboration, *The barrel modules of the ATLAS semiconductor tracker*, Nuclear Instruments and Methods in Physics Research Section A: Accelerators, Spectrometers, Detectors and Associated Equipment **568** (2006) 642 (cit. on p. 22).

[62] ATLAS Collaboration, *Performance of the ATLAS Liquid Argon Calorimeter after three years of LHC operation and plans for a future upgrade*, (2013), arXiv: `1306.6756` (cit. on pp. 25, 51).

[63] G. Aad, *Operation of the ATLAS trigger system in Run 2*, Journal of Instrumentation **15** (2020) (cit. on p. 25).

[64] C. Quigg, *LHC Physics Potential vs. Energy: Considerations for the 2011 Run*, 2011, arXiv: `1101.3201 [hep-ph]` (cit. on p. 28).

[65] H. Bethe, *Zur Theorie des Durchgangs schneller Korpuskularstrahlen durch Materie*, Annalen der Physik **397** (1930) 325 (cit. on p. 29).

[66] S. Ahlen, *Stopping Power Formula for Magnetic Monopoles*, Phys. Rev. D **17** (1978) 229 (cit. on pp. 30, 71).

[67] Y. Kazama, C. N. Yang, and A. S. Goldhaber, *Scattering of a Dirac particle with charge Ze by a fixed magnetic monopole*, Phys. Rev. D **15** (8 1977) 2287 (cit. on p. 30).

[68] A. De Roeck, A. Katre, P. Mermod, D. Milstead, and T. Sloan, *Sensitivity of LHC experiments to exotic highly ionising particles*, The European Physical Journal C **72** (2012) 1985 (cit. on pp. 31, 34).

[69] J. D. Jackson, “Classical electrodynamics”, 3rd ed., New York, NY: Wiley, 1999 278, ISBN: 9780471309321 (cit. on p. 31).

[70] E. Papageorgiu and L. Stodolsky, *Identification of magnetic monopoles via electron-positron pair production*, Physics Letters B **197** (1987) 277 (cit. on p. 32).

[71] S. D. Wick, T. W. Kephart, T. J. Weiler, and P. L. Biermann, *Signatures for a cosmic flux of magnetic monopoles*, Astroparticle Physics **18** (2003) 663 (cit. on p. 32).

[72] S. Burdin, M. Horbatsch, and W. Taylor, *A correction to Birks' Law in liquid argon ionization chamber simulations for highly ionizing particles*, Nuclear Inst. and Methods in Physics Research, A **664** (2011) 111 (cit. on pp. 35, 36).

[73] ATLAS Collaboration, *Basic ATLAS TRT performance studies of Run 1*, ATL-INDET-PUB-2014-001, 2014 (cit. on p. 35).

[74] J. B. Birks, *Scintillations from Organic Crystals: Specific Fluorescence and Relative Response to Different Radiations*, Proceedings of the Physical Society. Section A **64** (1951) 874 (cit. on p. 36).

[75] J. B. Birks, *Theory of the Response of Organic Scintillation Crystals to Short-Range Particles*, Phys. Rev. **86** (4 1952) 569 (cit. on p. 36).

[76] M. Aharrouche *et al.*, *Measurement of the response of the ATLAS liquid argon barrel calorimeter to electrons at the 2004 combined test-beam*, Nuclear Instruments and Methods in Physics Research Section A: Accelerators, Spectrometers, Detectors and Associated Equipment **614** (2010) 400 (cit. on p. 36).

[77] ICARUS Collaboration, *Study of electron recombination in liquid argon with the ICARUS TPC*, Nuclear Instruments and Methods in Physics Research Section A: Accelerators, Spectrometers, Detectors and Associated Equipment **523** (2004) 275 (cit. on p. 36).

[78] ATLAS Collaboration, *Topological cell clustering in the ATLAS calorimeters and its performance in LHC Run 1*, The European Physical Journal C **77** (2017) 490 (cit. on p. 36).

[79] J. Alwall *et al.*, *The automated computation of tree-level and next-to-leading order differential cross sections, and their matching to parton shower simulations*, Journal of High Energy Physics **2014** (2014) (cit. on p. 38).

[80] ATLAS Collaboration, *ATLAS Pythia 8 tunes to* 7 *TeV data*, ATL-PHYS-PUB-2014-021, 2014 (cit. on p. 38).

[81] NNPDF Collaboration, *Parton distributions with LHC data*, Nucl. Phys. B **867** (2013) 244, arXiv: `1207.1303 [hep-ph]` (cit. on p. 38).

[82] V. Bertone, S. Carrazza, N. Hartland, and J. Rojo, *Illuminating the photon content of the proton within a global PDF analysis*, SciPost Phys. **5** (2018) 8, arXiv: `1712.07053 [hep-ph]` (cit. on p. 38).

[83] T. Sjostrand, S. Mrenna, and P. Z. Skands, *A Brief Introduction to PYTHIA 8.1*, Comput. Phys. Commun. **178** (2008) 852, arXiv: `0710.3820 [hep-ph]` (cit. on p. 39).

[84] Geant4 Collaboration, *Geant4 developments and applications*, IEEE Trans. Nucl. Sci. **53** (2006) 270 (cit. on p. 40).

[85] S. Burdin, A. Firan, and W. Taylor, *A Search for Magnetic Monopoles at ATLAS*, ATL-COM-PHYS-2012-367, 2012 (cit. on p. 40).

[86] K. Bendtz *et al.*, *Search in 8 TeV proton-proton collisions with the MoEDAL monopole-trapping test array*, Proceedings of the 14th ICATPP Conference (2014), arXiv: `1311.6940 [physics.ins-det]` (cit. on p. 40).

[87] ATLAS Collaboration, *Luminosity determination in pp collisions at* $\sqrt{s} = 13$ *TeV using the ATLAS detector at the LHC*, tech. rep., CERN, 2022, arXiv: `2212.09379 [hep-ex]` (cit. on p. 42).

[88] P. Laycock *et al.*, *ATLAS data preparation in run 2*, Journal of Physics: Conference Series **898** (2017) 042050 (cit. on pp. 42, 53).

[89] A. E. Lionti, *Search for Magnetic Monopoles and Stable High-Electric-Charge Objects in 13 TeV Proton-Proton Collisions with the ATLAS and MoEDAL Detectors*, unige (2020) (cit. on p. 46).

[90] K. Bendtz *et al.*, *Search for magnetic monopoles and new stable particles with high electric charges in 8 TeV pp collisions with the ATLAS detector*, ATL-COM-PHYS-2015-311, 2015 (cit. on pp. 51, 82).

[91] N. Chinchor, *MUC-4 Evaluation Metrics*, Proceedings of the 4th Conference on Message Understanding – MUC4 '92 (1992) 22 (cit. on p. 54).

[92] G. Punzi, *Sensitivity of searches for new signals and its optimization*, eConf **C030908** (2003) MODT002, arXiv: physics/0308063 (cit. on p. 54).

[93] R. Koniuk, E. Noordeh, and W. Taylor, *Extension of the Magnetic Monopole Search to Include Scalar Monopoles*, ATL-COM-PHYS-2014-1417, 2014 (cit. on p. 58).

[94] L. Breiman, *Random Forests*, Machine Learning **45** (2001) 5 (cit. on p. 66).

[95] S. P. Ahlen, *Theoretical and experimental aspects of the energy loss of relativistic heavily ionizing particles*, Rev. Mod. Phys. **52** (1 1980) 121 (cit. on p. 71).

[96] ATLAS Collaboration, *TRT available gas scenarios*, ATLAS twiki, 2023 (cit. on p. 73).

[97] W. Y. Song, A. M. Rodriguez Vera, W. Taylor, and M. Levchenko, *Search for magnetic monopoles and stable high-electric-charge objects in 13 TeV proton-proton collisions with the ATLAS detector*, ATL-COM-PHYS-2020-187, 2020 (cit. on pp. 75, 76).

[98] Z. Marshall and the ATLAS Collaboration, *Simulation of Pile-up in the ATLAS Experiment*, Journal of Physics: Conference Series **513** (2014) 022024 (cit. on p. 75).

[99] ATLAS Collaboration, *Measurement of the inelastic proton–proton cross-section at $\sqrt{s} = 7$ TeV with the ATLAS detector*, Nature Communications **2** (2011) 463 (cit. on p. 75).

[100] ATLAS Collaboration, *Emulating the impact of additional protonproton interactions in the ATLAS simulation by presampling sets of inelastic Monte Carlo events*, Computing and Software for Big Science **6** (2022) 3 (cit. on p. 75).

[101] J. Labbe and R. Ishmukhametov, *Crosstalk Measurements in the Electromagnetic Calorimeter during ATLAS Final Installation*, ATL-LARG-INT-2009-004, ATL-COM-LARG-2008-012, 2008 (cit. on p. 76).

[102] W. Buttinger, *Background Estimation with the ABCD Method*, ATLAS twiki, 2018 (cit. on p. 80).

[103] G. J. Besjes *et al.*, *HistFitter: a flexible framework for statistical data analysis*, Journal of Physics: Conference Series **664** (2015) 072004 (cit. on pp. 89, 96).

[104] A. L. Read, *Presentation of search results: the CLs technique*, Journal of Physics G: Nuclear and Particle Physics **28** (2002) 2693 (cit. on p. 93).

[105] G. Cowan, K. Cranmer, E. Gross, and O. Vitells, *Asymptotic formulae for likelihood-based tests of new physics*, The European Physical Journal C **71** (2011) (cit. on p. 94).

[106] ATLAS Collaboration, *Search for heavy long-lived multi-charged particles in the full LHC Run 2 pp collision data at* $\sqrt{s} = 13$ *TeV using the ATLAS detector*, (2023), arXiv: `2303.13613 [hep-ex]` (cit. on pp. 105, 108).

[107] ATLAS Collaboration, *ATLAS Fact Sheets*, ATLAS website (cit. on p. 228).

Appendices

APPENDIX A

Kinematic distributions

Generator-level kinematic distributions for Drell-Yan and Photon Fusion pair-produced events are shown in Figs. A.1–A.14 and Figs. A.15-A.21, respectively, considering all spins, masses and charges in this study for both HECOs and monopoles.

A.1 DY spin-0

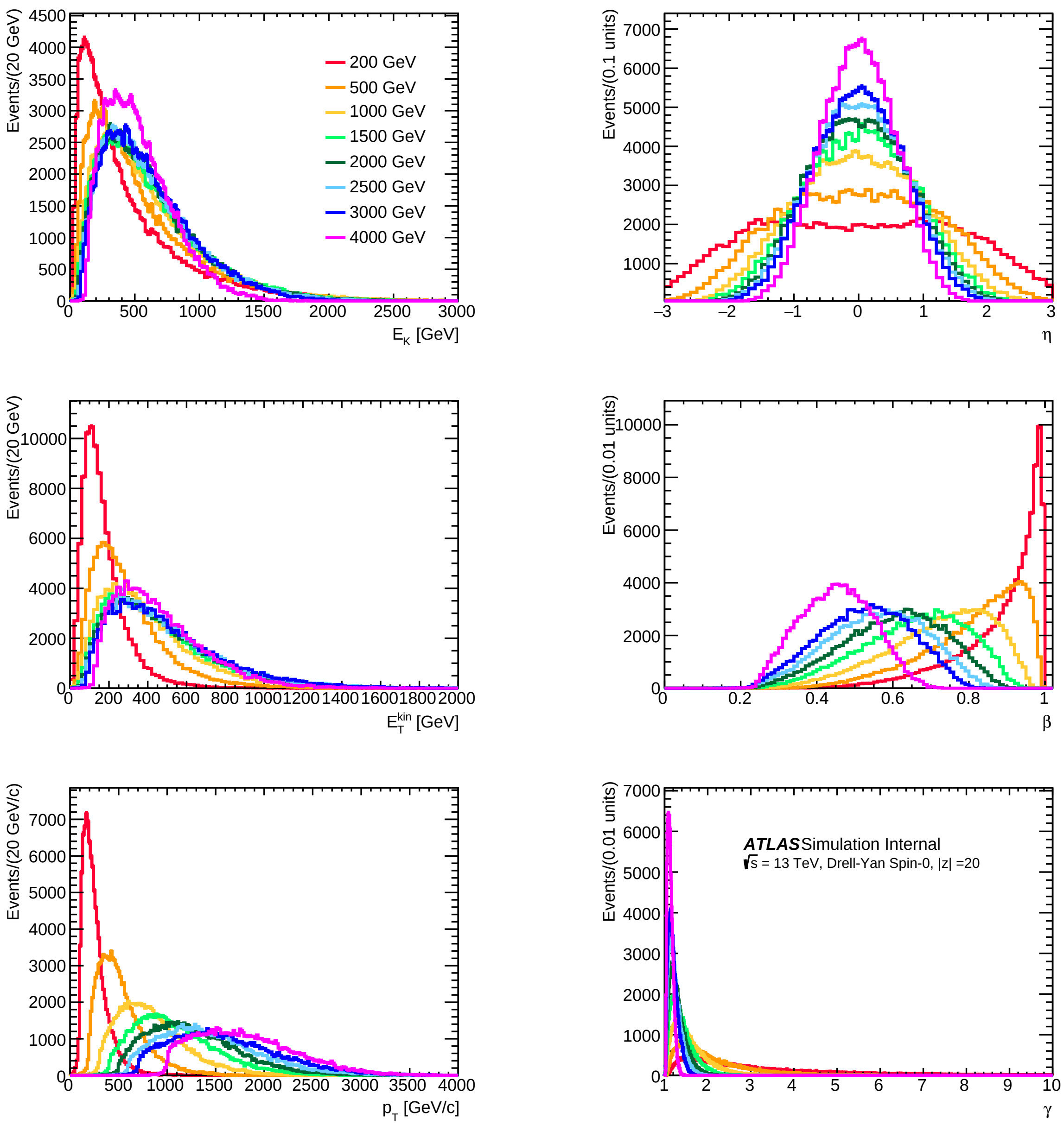

Figure A.1: Generator-level transverse kinetic energy $E_{\mathrm{T}}^{\mathrm{kin}}$, pseudorapidity η, kinetic energy E_{K}, relativistic velocity β, transverse momentum p_{T}, and relativistic γ factor, distributions for Drell-Yan pair-produced charge $|z| = 20$ spin-0 HECOs with various masses (after a minimum p_{T} cut is applied).

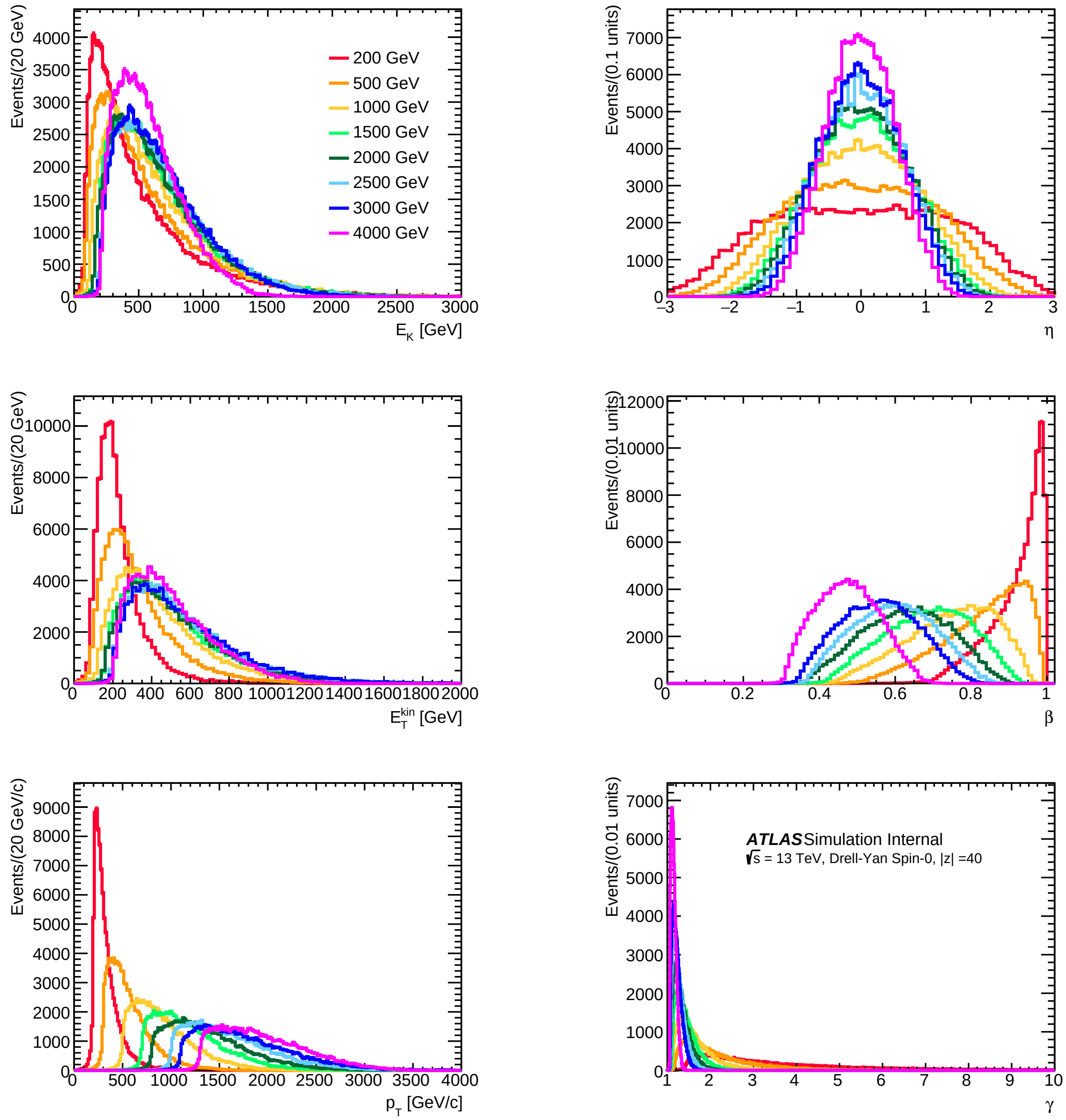

Figure A.2: Generator-level transverse kinetic energy $E_{\mathrm{T}}^{\mathrm{kin}}$, pseudorapidity η, kinetic energy E_{K}, relativistic velocity β, transverse momentum p_{T}, and relativistic γ factor, distributions for Drell-Yan pair-produced charge $|z| = 40$ spin-0 HECOs with various masses (after a minimum p_{T} cut is applied).

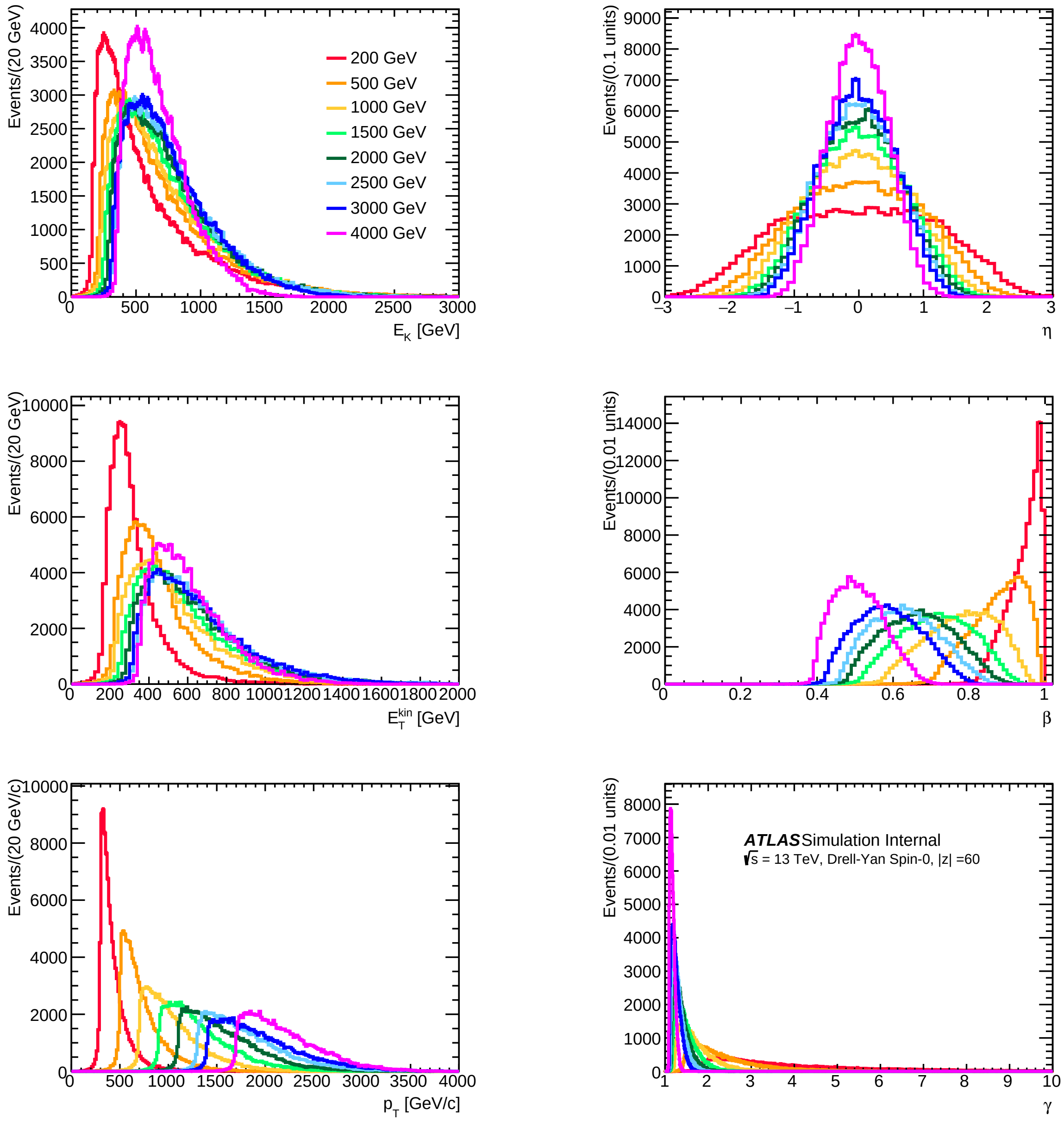

Figure A.3: Generator-level transverse kinetic energy $E_{\mathrm{T}}^{\mathrm{kin}}$, pseudorapidity η, kinetic energy E_{K}, relativistic velocity β, transverse momentum p_{T}, and relativistic γ factor, distributions for Drell-Yan pair-produced charge $|z| = 60$ spin-0 HECOs with various masses (after a minimum p_{T} cut is applied).

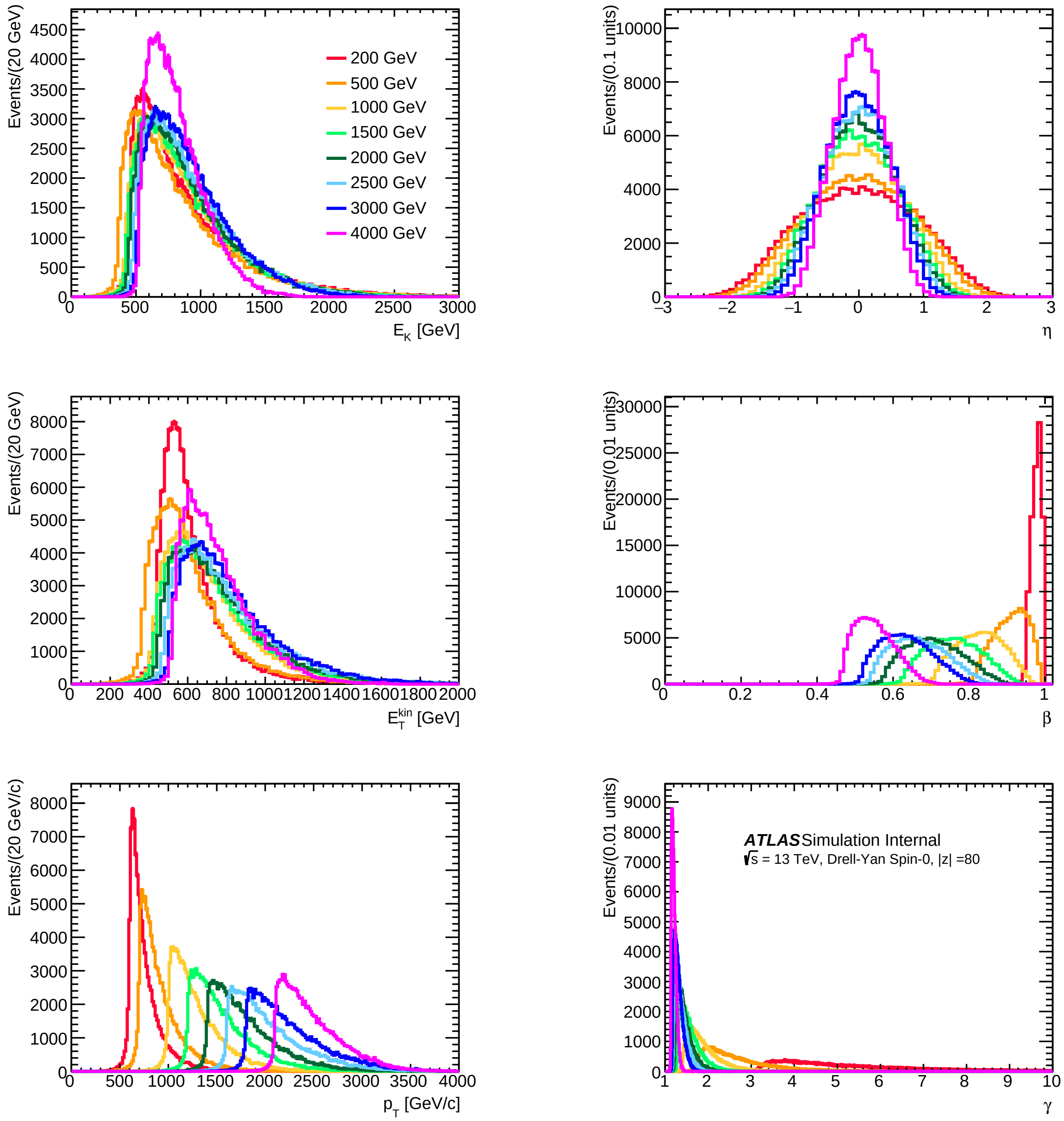

Figure A.4: Generator-level transverse kinetic energy $E_{\mathrm{T}}^{\mathrm{kin}}$, pseudorapidity η, kinetic energy E_{K}, relativistic velocity β, transverse momentum p_{T}, and relativistic γ factor, distributions for Drell-Yan pair-produced charge $|z| = 80$ spin-0 HECOs with various masses (after a minimum p_{T} cut is applied).

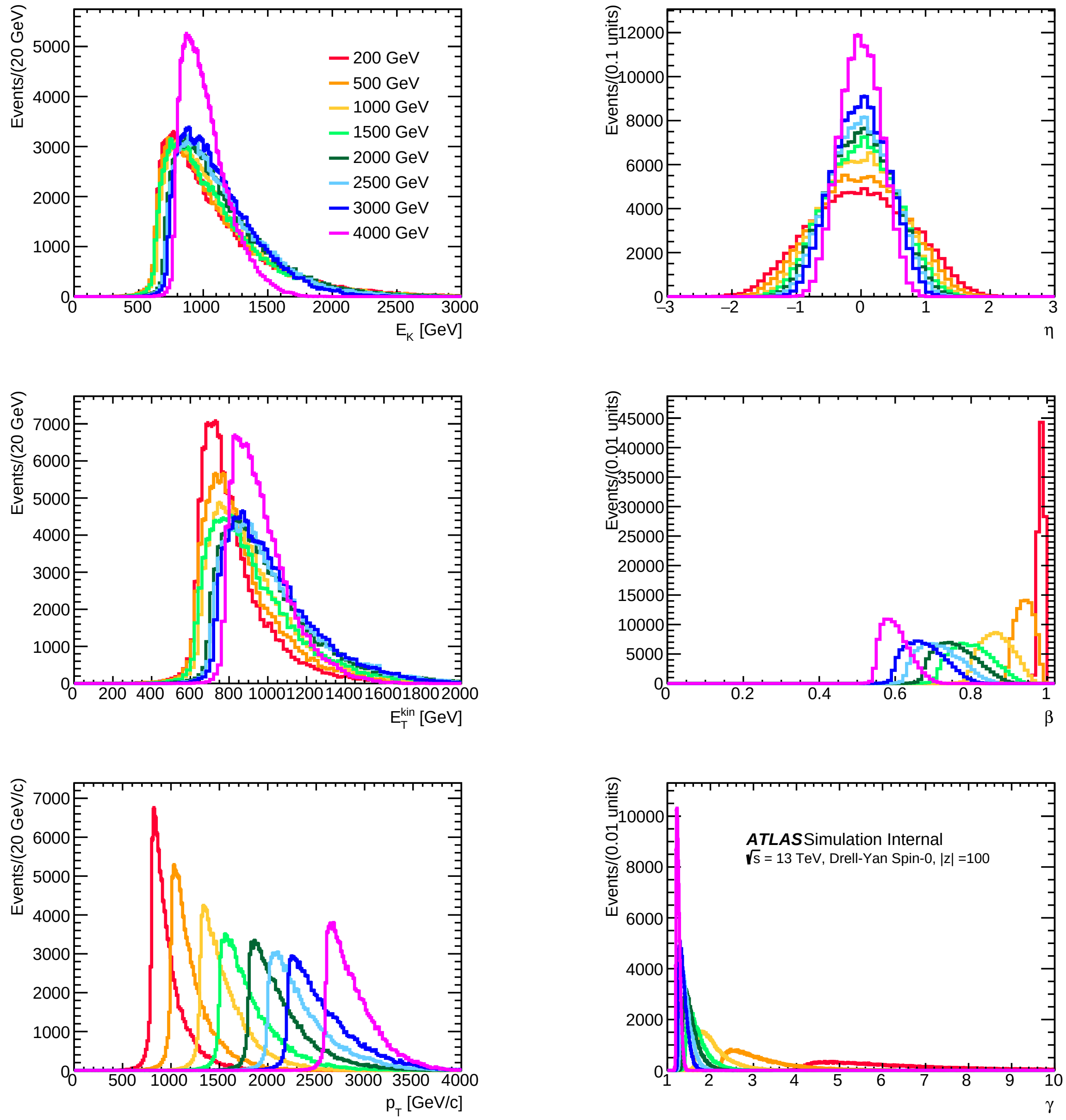

Figure A.5: Generator-level transverse kinetic energy $E_{\mathrm{T}}^{\mathrm{kin}}$, pseudorapidity η, kinetic energy E_{K}, relativistic velocity β, transverse momentum p_{T}, and relativistic γ factor, distributions for Drell-Yan pair-produced charge $|z| = 100$ spin-0 HECOs with various masses (after a minimum p_{T} cut is applied).

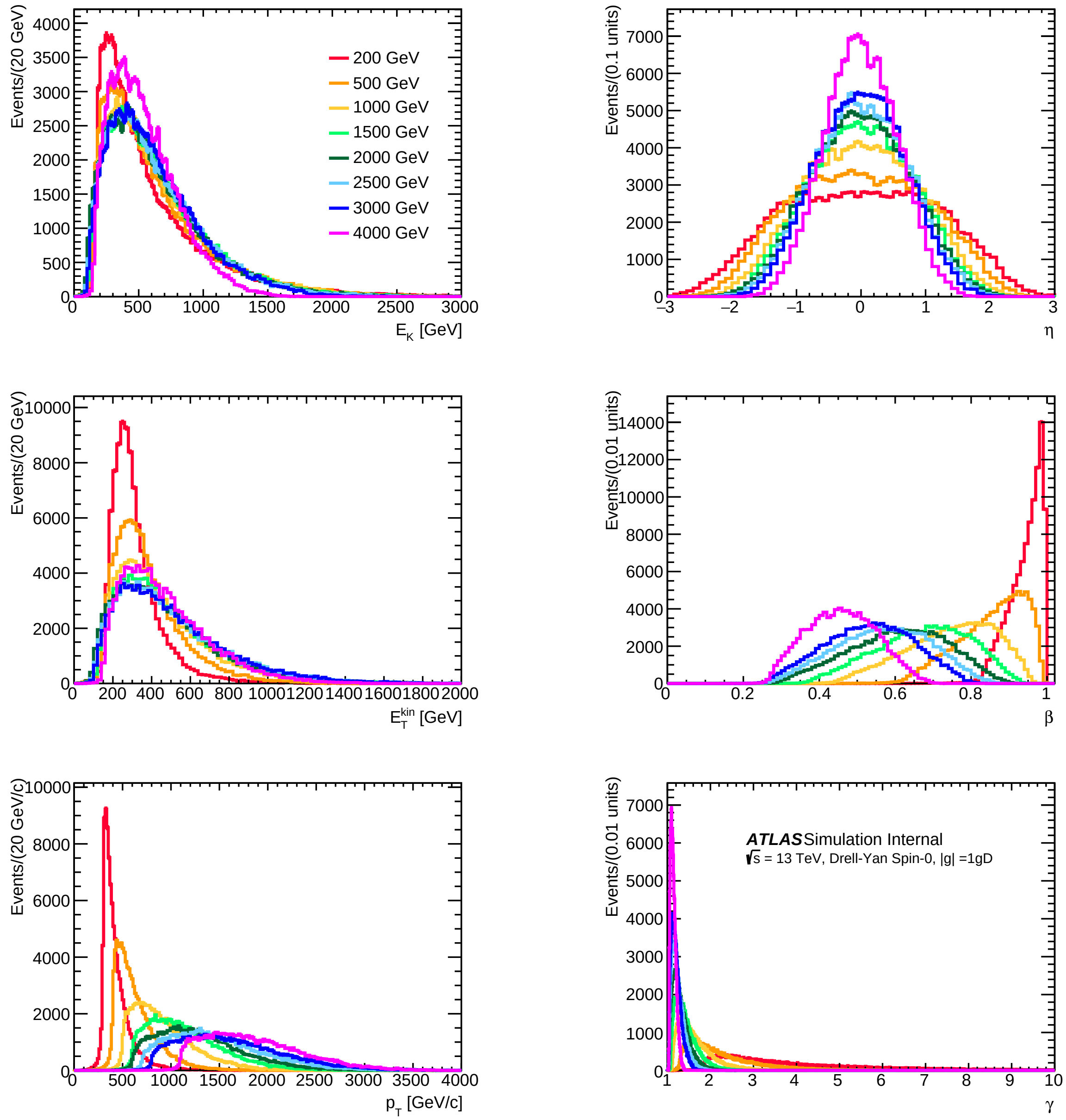

Figure A.6: Generator-level transverse kinetic energy $E_{\mathrm{T}}^{\mathrm{kin}}$, pseudorapidity η, kinetic energy E_{K}, relativistic velocity β, transverse momentum p_{T}, and relativistic γ factor, distributions for Drell-Yan pair-produced charge $1g_{\mathrm{D}}$ spin-0 monopoles with various masses (after a minimum p_{T} cut is applied).

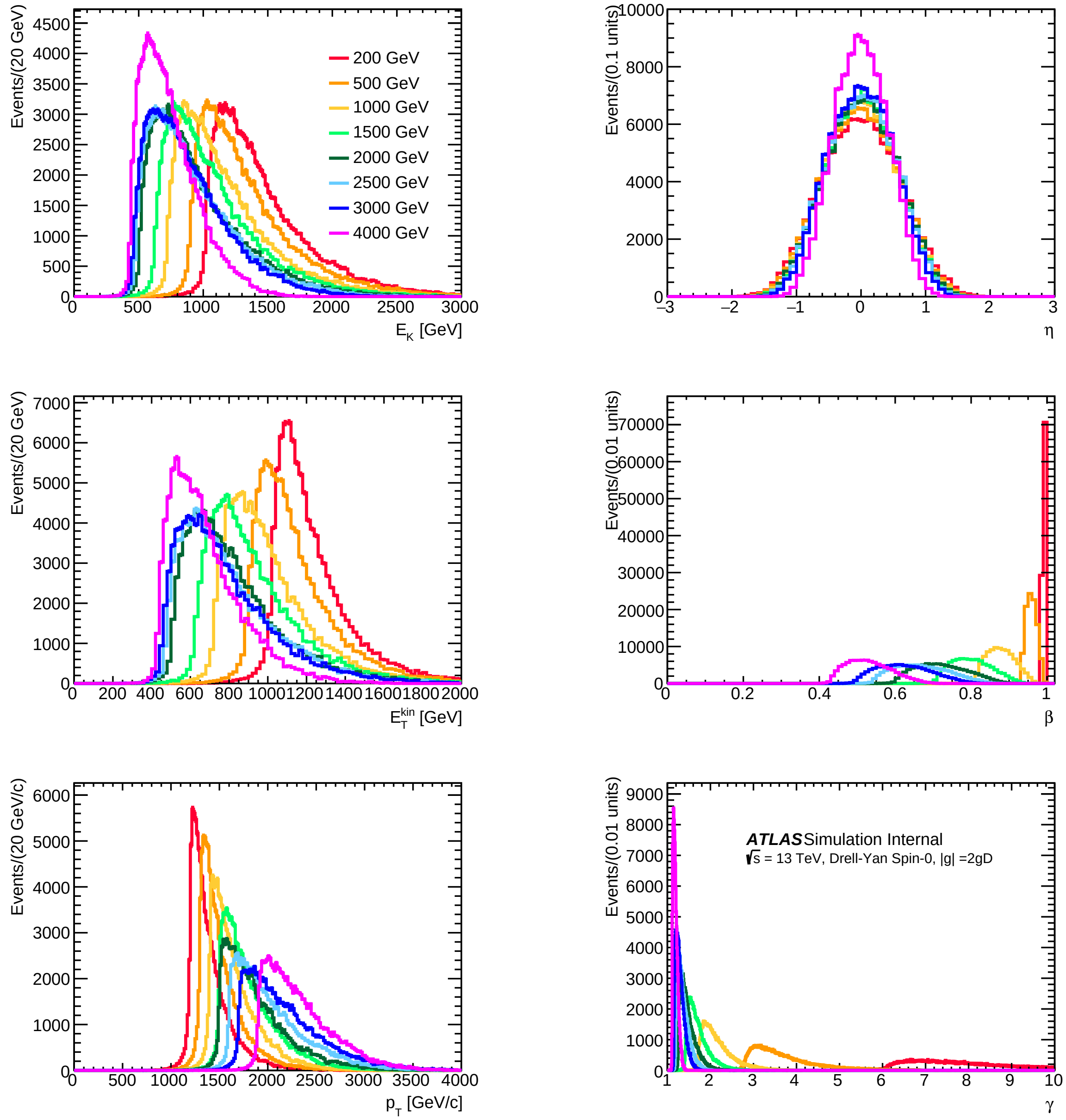

Figure A.7: Generator-level transverse kinetic energy $E_{\mathrm{T}}^{\mathrm{kin}}$, pseudorapidity η, kinetic energy E_{K}, relativistic velocity β, transverse momentum p_{T}, and relativistic γ factor, distributions for Drell-Yan pair-produced charge $2g_{\mathrm{D}}$ spin-0 monopoles with various masses (after a minimum p_{T} cut is applied).

A.2 DY spin-½

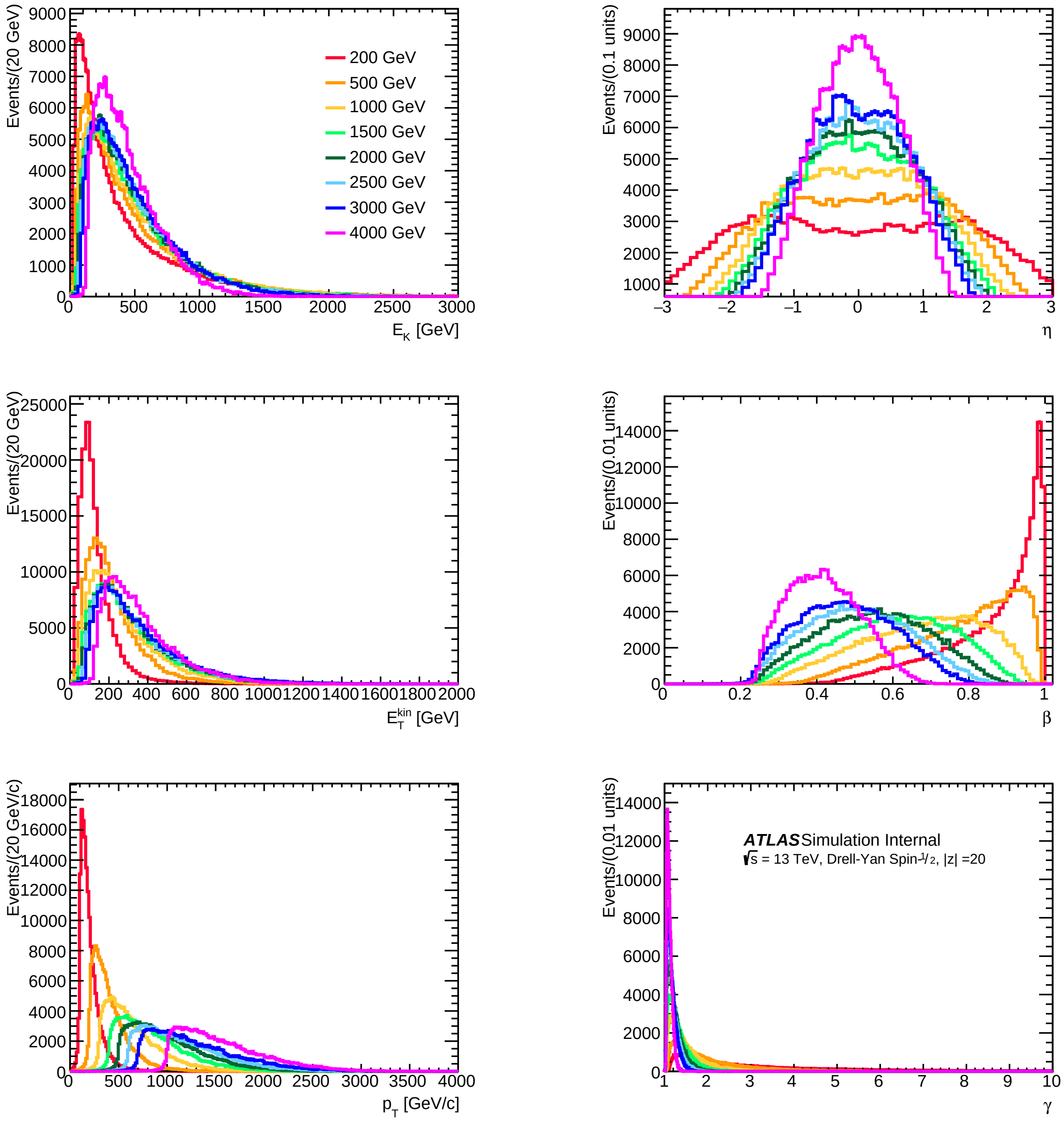

Figure A.8: Generator-level transverse kinetic energy $E_{\mathrm{T}}^{\mathrm{kin}}$, pseudorapidity η, kinetic energy E_{K}, relativistic velocity β, transverse momentum p_{T}, and relativistic γ factor, distributions for Drell-Yan pair-produced charge $|z| = 20$ spin-½ HECOs with various masses (after a minimum p_{T} cut is applied).

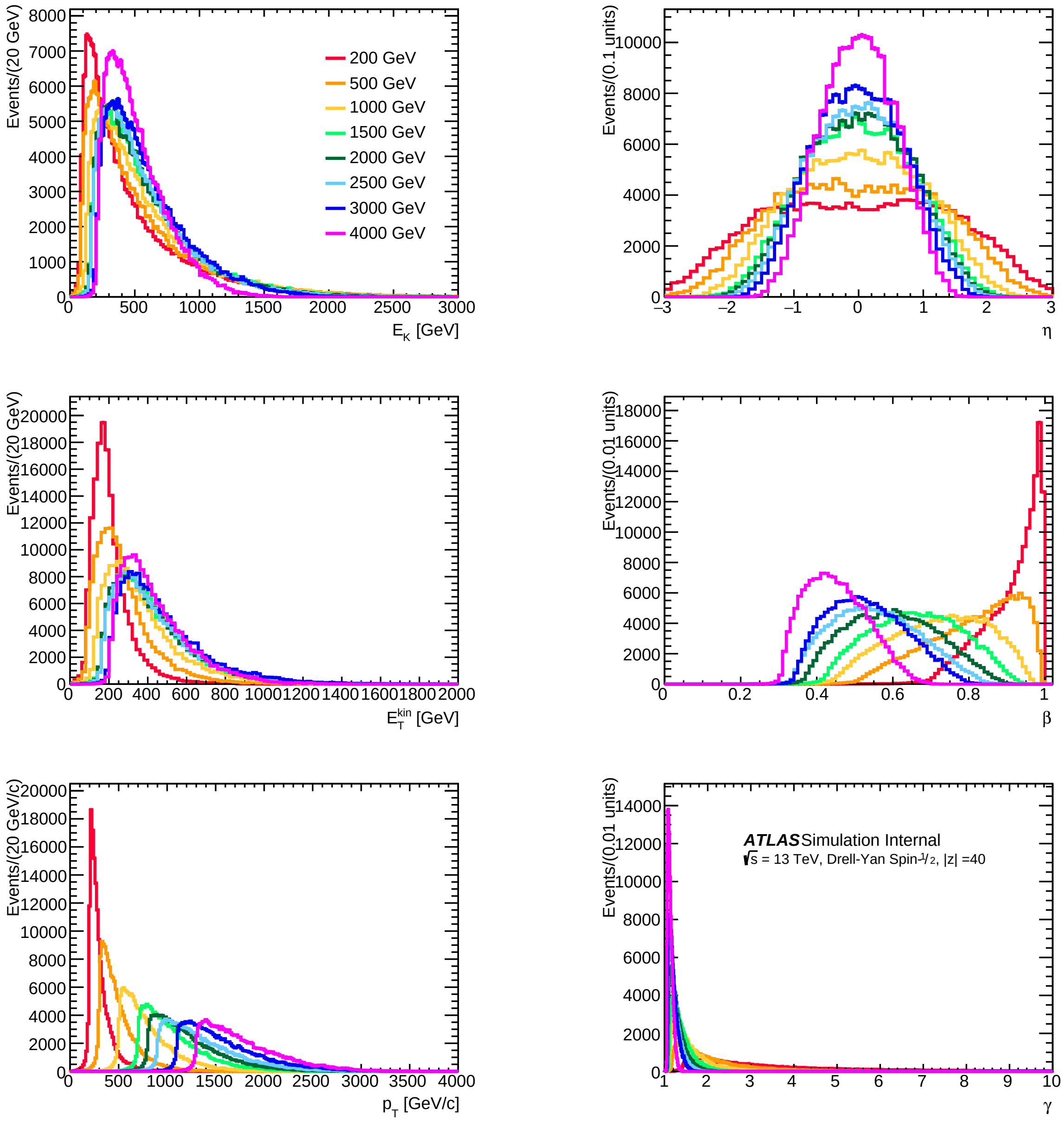

Figure A.9: Generator-level transverse kinetic energy $E_{\mathrm{T}}^{\mathrm{kin}}$, pseudorapidity η, kinetic energy E_{K}, relativistic velocity β, transverse momentum p_{T}, and relativistic γ factor, distributions for Drell-Yan pair-produced charge $|z| = 40$ spin-½ HECOs with various masses (after a minimum p_{T} cut is applied).

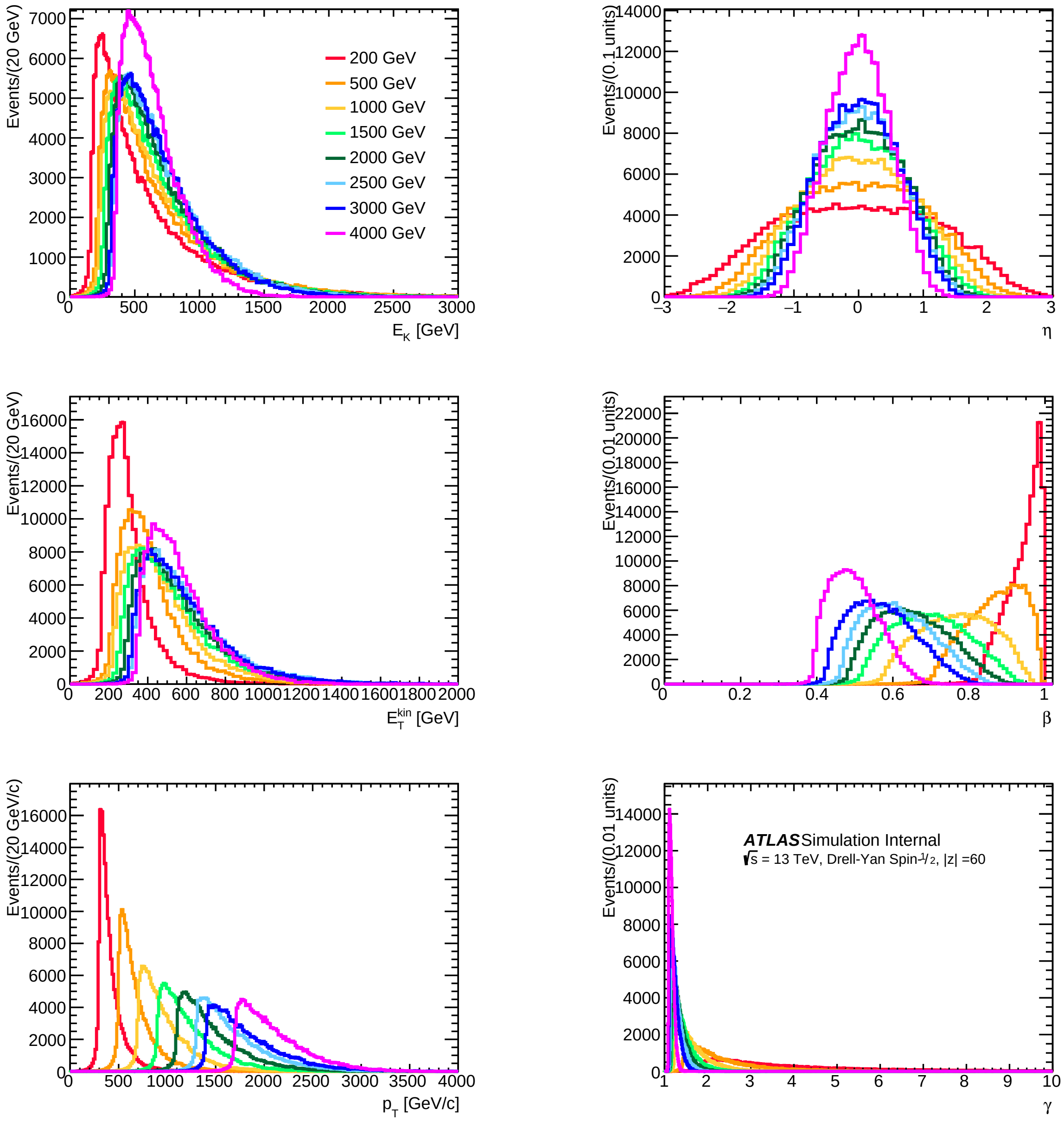

Figure A.10: Generator-level transverse kinetic energy $E_{\mathrm{T}}^{\mathrm{kin}}$, pseudorapidity η, kinetic energy E_{K}, relativistic velocity β, transverse momentum p_{T}, and relativistic γ factor, distributions for Drell-Yan pair-produced charge $|z| = 60$ spin-½ HECOs with various masses (after a minimum p_{T} cut is applied).

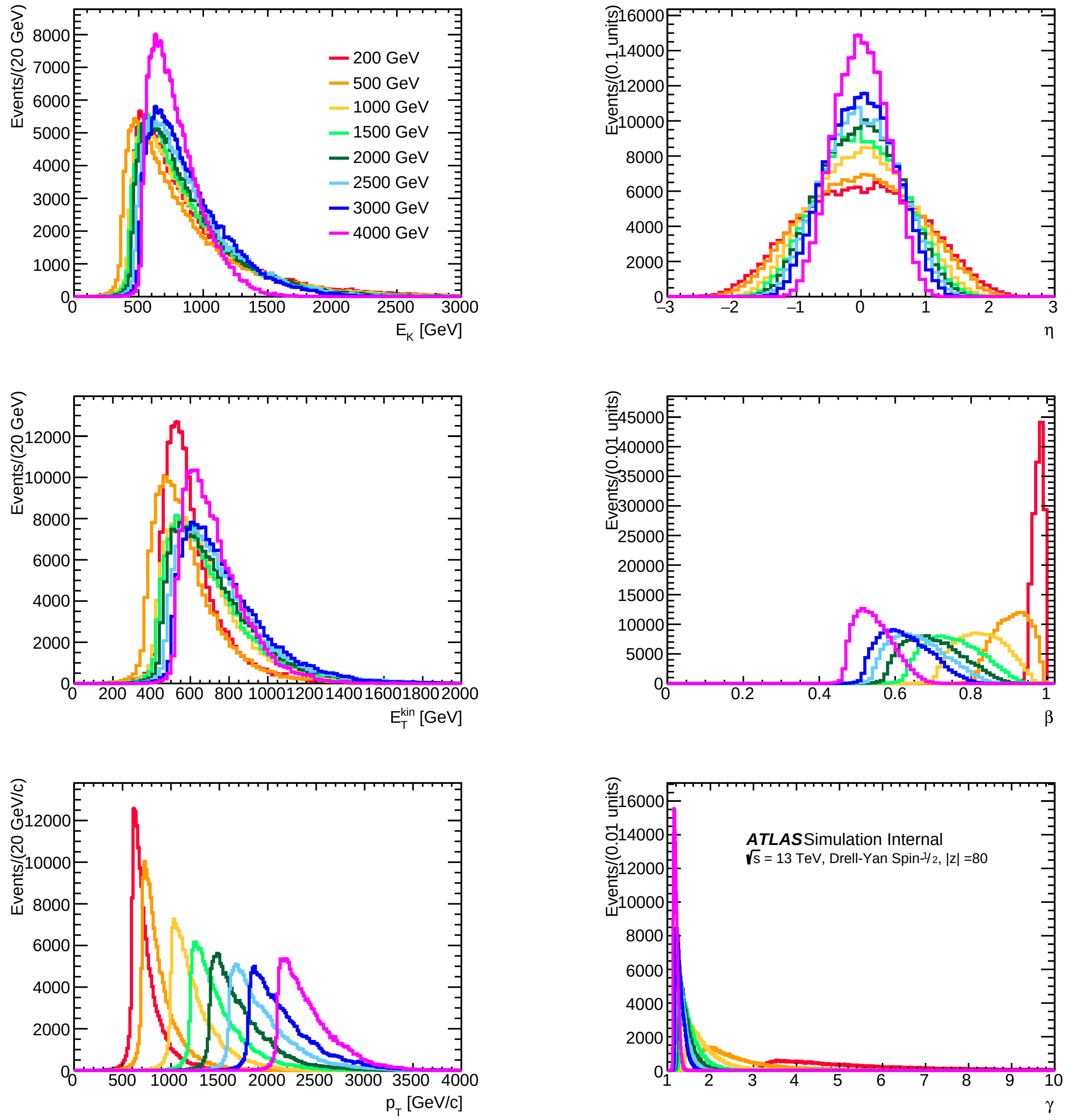

Figure A.11: Generator-level transverse kinetic energy $E_{\mathrm{T}}^{\mathrm{kin}}$, pseudorapidity η, kinetic energy E_{K}, relativistic velocity β, transverse momentum p_{T}, and relativistic γ factor, distributions for Drell-Yan pair-produced charge $|z| = 80$ spin-½ HECOs with various masses (after a minimum p_{T} cut is applied).

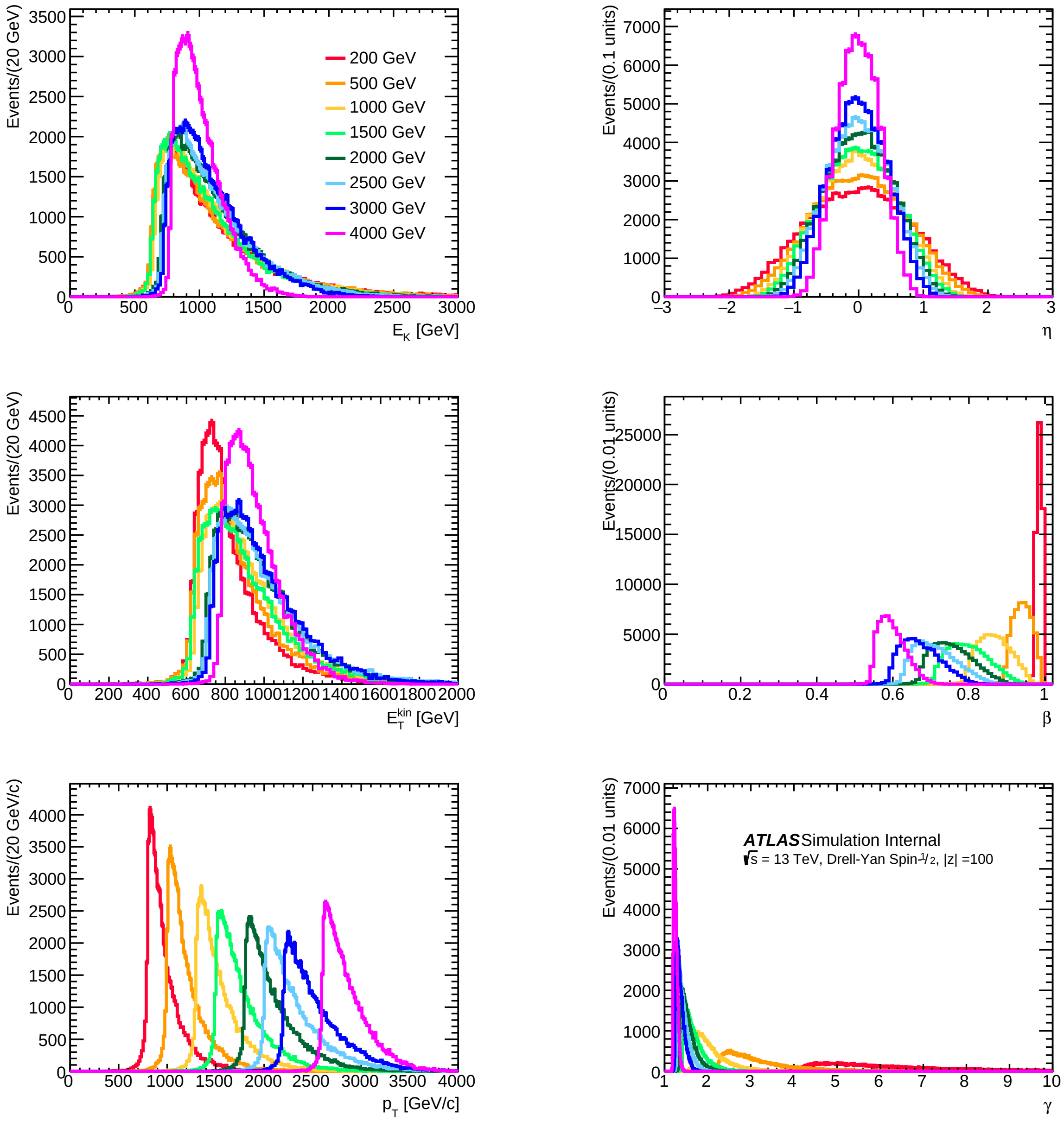

Figure A.12: Generator-level transverse kinetic energy $E_{\mathrm{T}}^{\mathrm{kin}}$, pseudorapidity η, kinetic energy E_{K}, relativistic velocity β, transverse momentum p_{T}, and relativistic γ factor, distributions for Drell-Yan pair-produced charge $|z| = 100$ spin-½ HECOs with various masses (after a minimum p_{T} cut is applied).

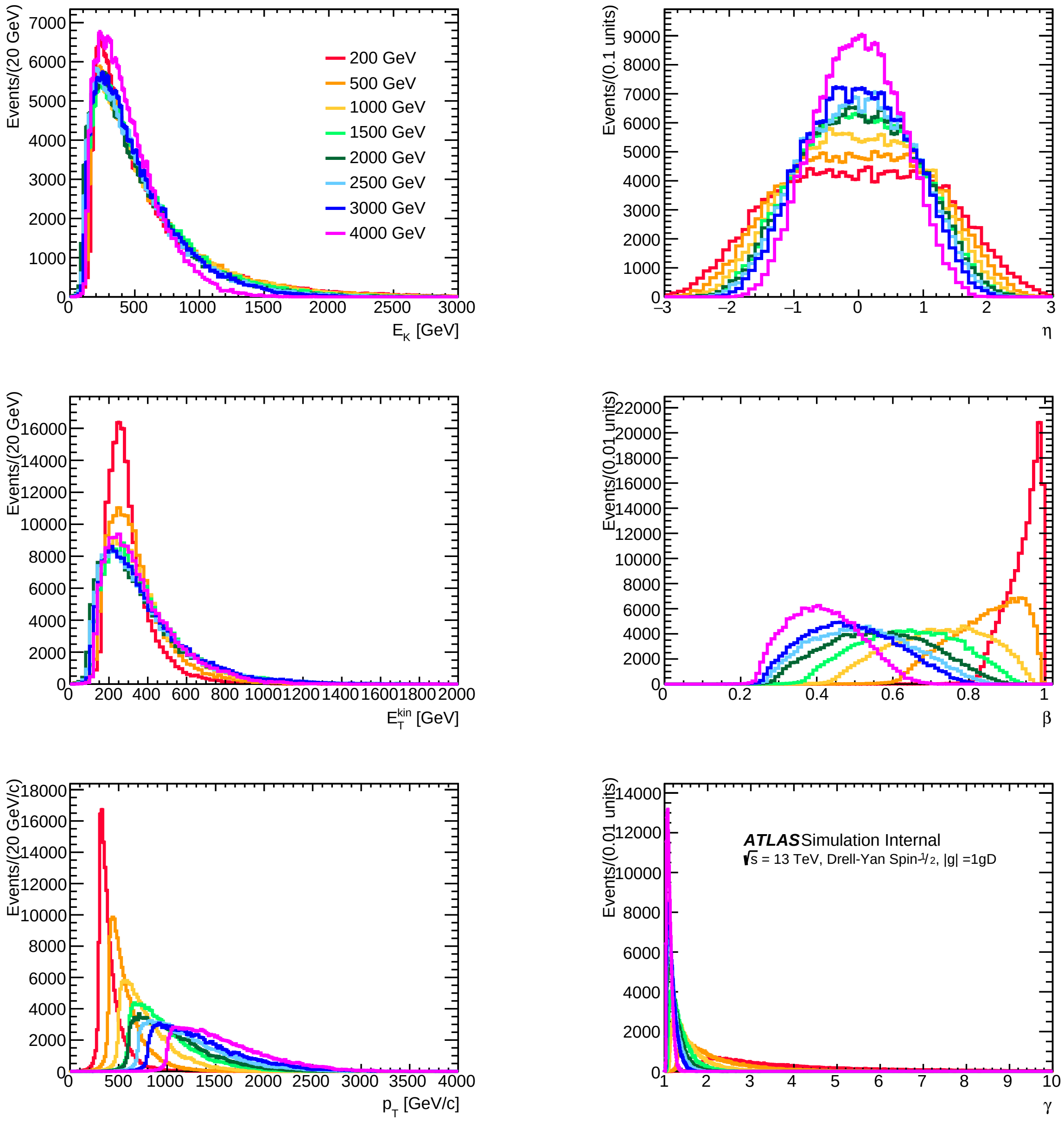

Figure A.13: Generator-level transverse kinetic energy $E_{\mathrm{T}}^{\mathrm{kin}}$, pseudorapidity η, kinetic energy E_{K}, relativistic velocity β, transverse momentum p_{T}, and relativistic γ factor, distributions for Drell-Yan pair-produced charge $1g_{\mathrm{D}}$ spin-½ monopoles with various masses (after a minimum p_{T} cut is applied).

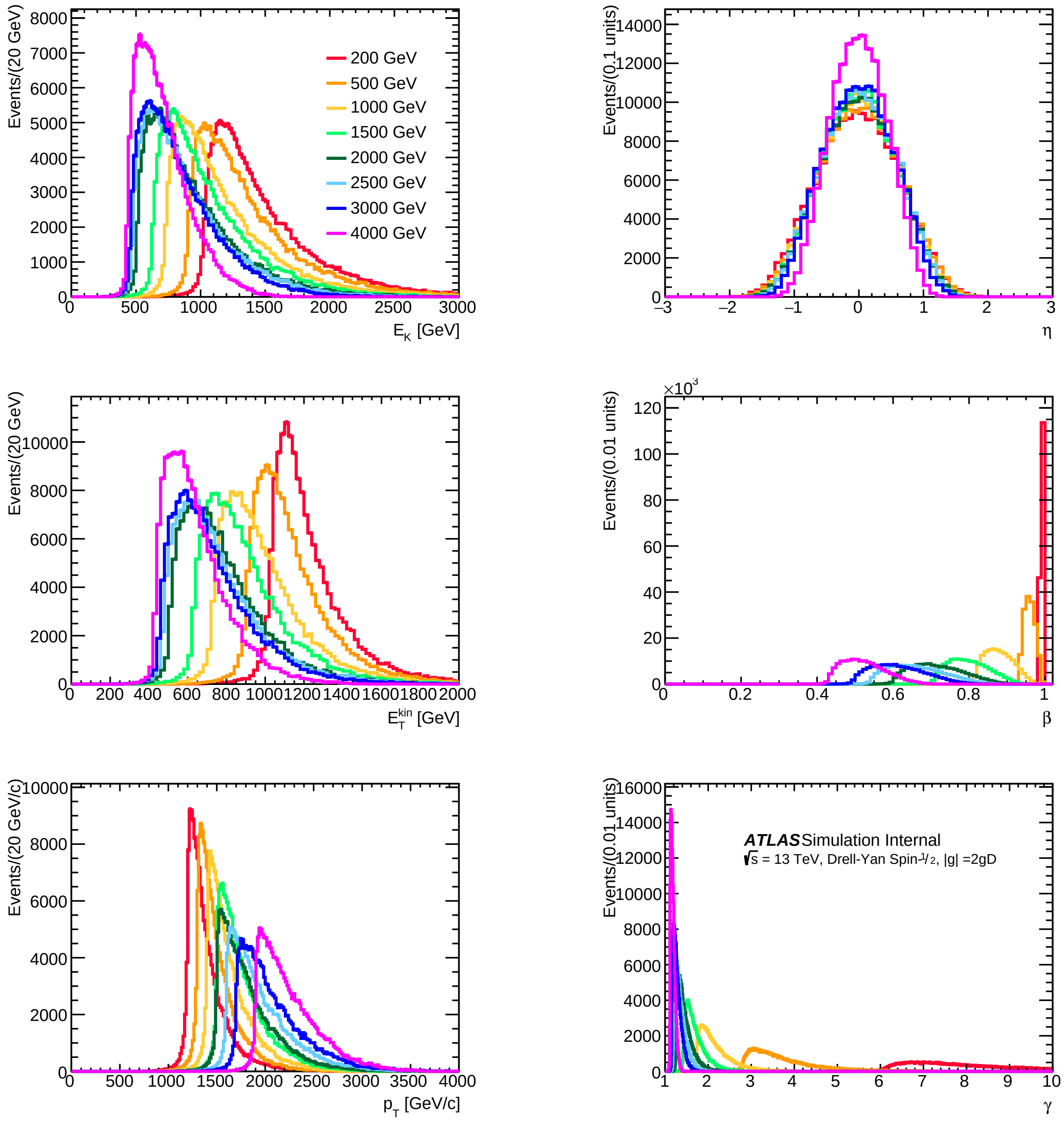

Figure A.14: Generator-level transverse kinetic energy $E_{\mathrm{T}}^{\mathrm{kin}}$, pseudorapidity η, kinetic energy E_{K}, relativistic velocity β, transverse momentum p_{T}, and relativistic γ factor, distributions for Drell-Yan pair-produced charge $2g_{\mathrm{D}}$ spin-½ monopoles with various masses (after a minimum p_{T} cut is applied).

A.3 PF spin-0

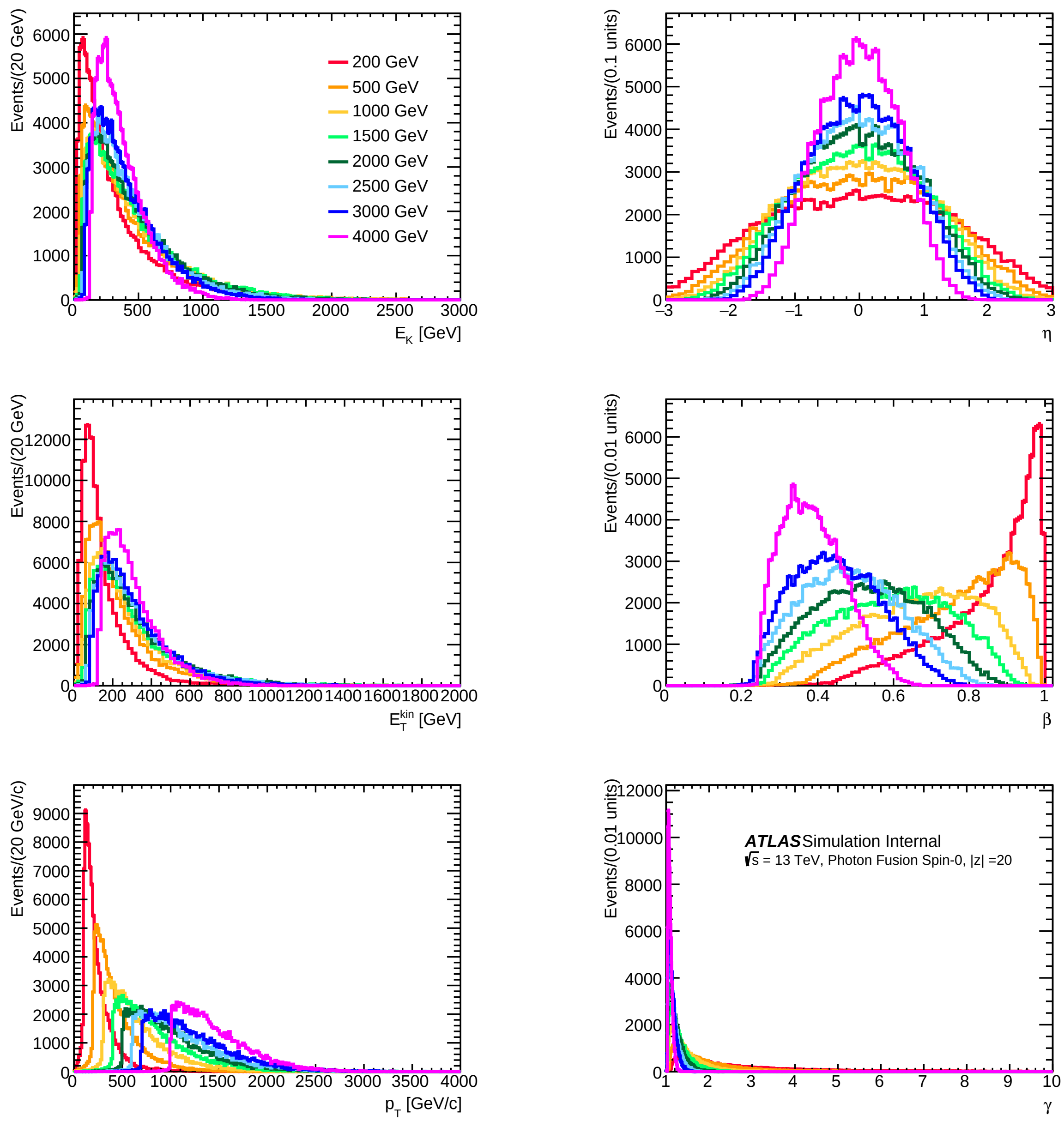

Figure A.15: Generator-level transverse kinetic energy $E_{\mathrm{T}}^{\mathrm{kin}}$, pseudorapidity η, kinetic energy E_{K}, relativistic velocity β, transverse momentum p_{T}, and relativistic γ factor, distributions for Photon Fusion pair-produced charge $|z| = 20$ spin-0 HECOs with various masses (after a minimum p_{T} cut is applied).

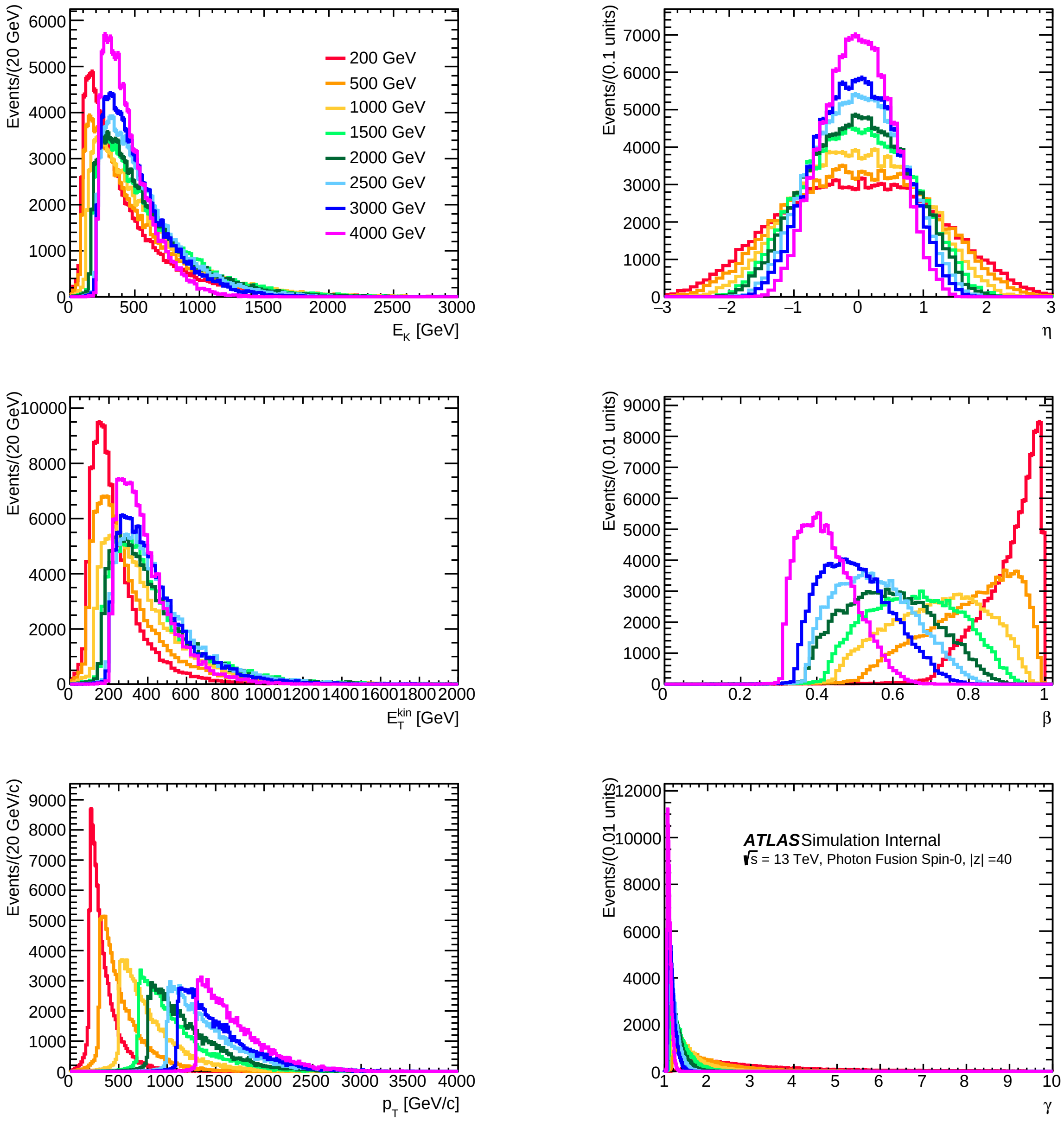

Figure A.16: Generator-level transverse kinetic energy $E_{\mathrm{T}}^{\mathrm{kin}}$, pseudorapidity η, kinetic energy E_{K}, relativistic velocity β, transverse momentum p_{T}, and relativistic γ factor, distributions for Photon Fusion pair-produced charge $|z| = 40$ spin-0 HECOs with various masses (after a minimum p_{T} cut is applied).

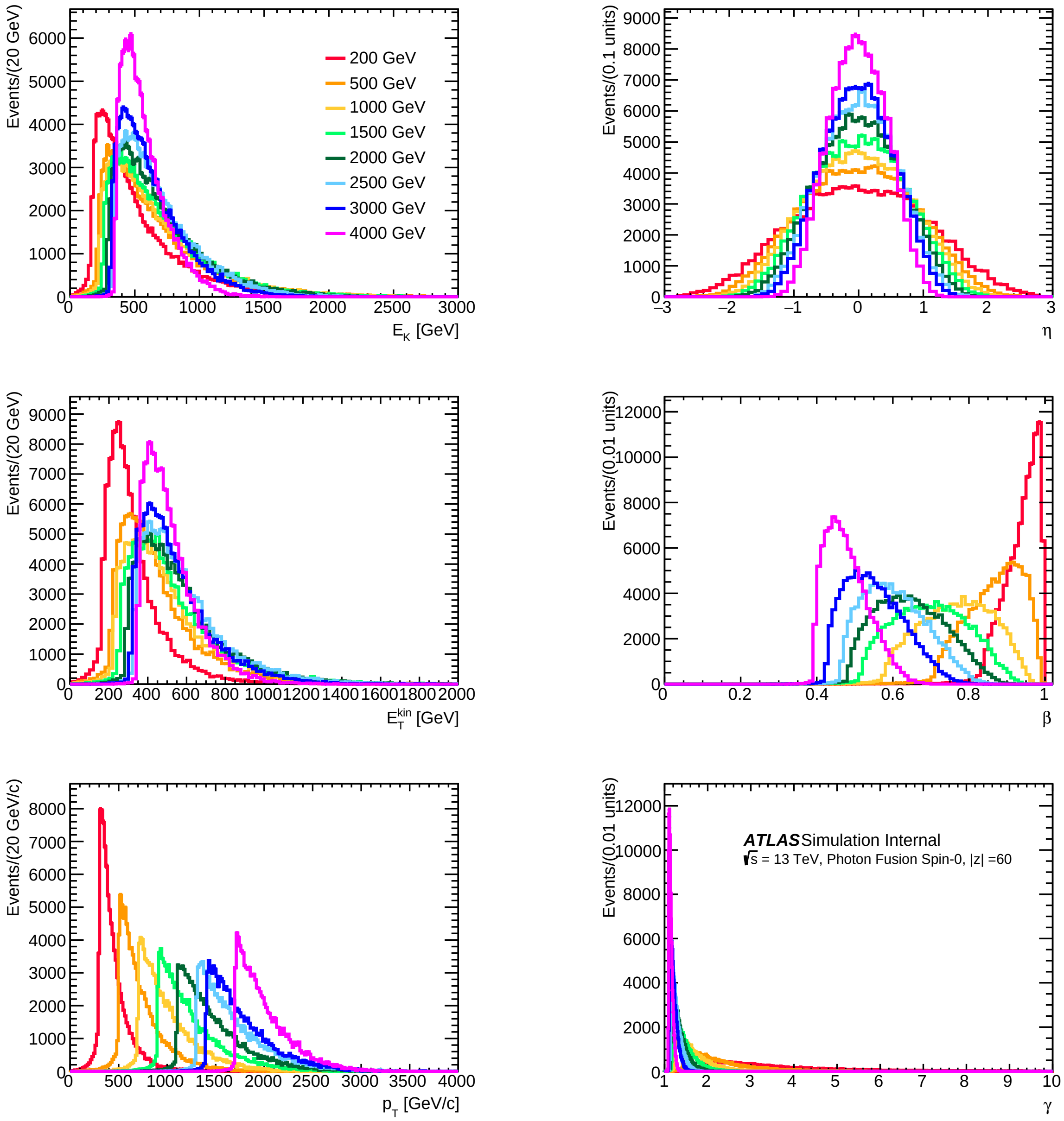

Figure A.17: Generator-level transverse kinetic energy $E_{\mathrm{T}}^{\mathrm{kin}}$, pseudorapidity η, kinetic energy E_{K}, relativistic velocity β, transverse momentum p_{T}, and relativistic γ factor, distributions for Photon Fusion pair-produced charge $|z| = 60$ spin-0 HECOs with various masses (after a minimum p_{T} cut is applied).

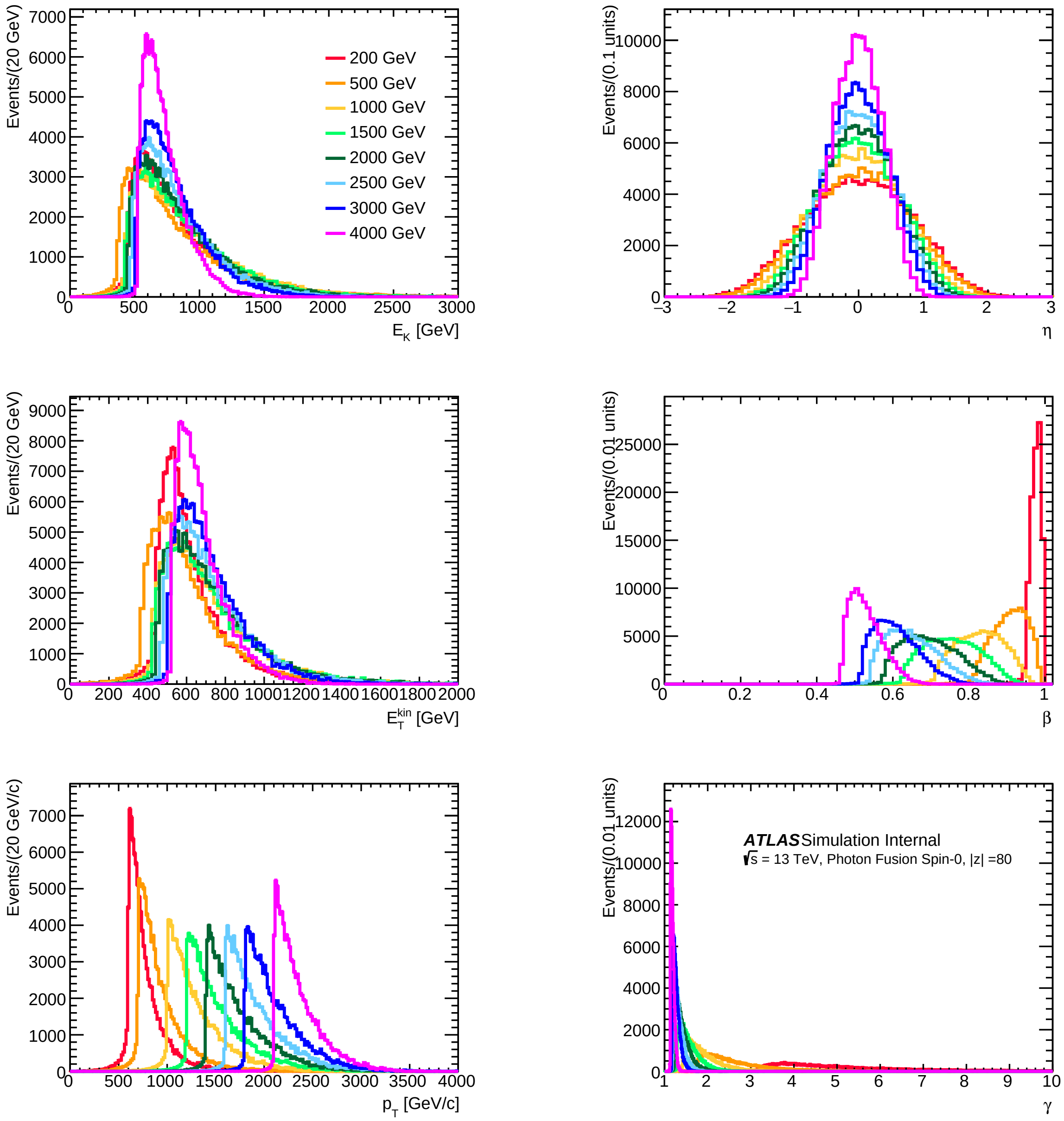

Figure A.18: Generator-level transverse kinetic energy $E_{\mathrm{T}}^{\mathrm{kin}}$, pseudorapidity η, kinetic energy E_{K}, relativistic velocity β, transverse momentum p_{T}, and relativistic γ factor, distributions for Photon Fusion pair-produced charge $|z| = 80$ spin-0 HECOs with various masses (after a minimum p_{T} cut is applied).

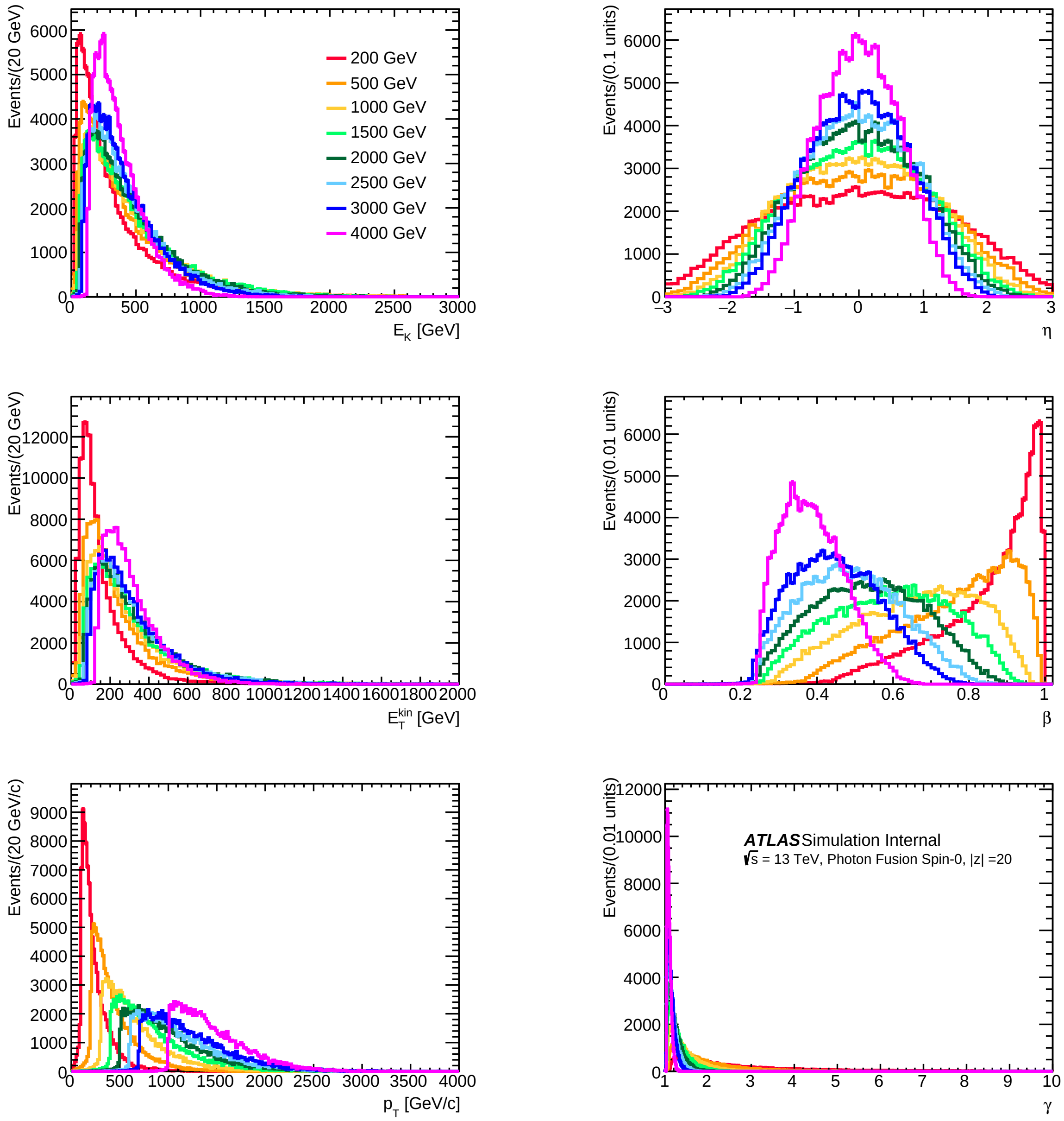

Figure A.19: Generator-level transverse kinetic energy $E_{\mathrm{T}}^{\mathrm{kin}}$, pseudorapidity η, kinetic energy E_{K}, relativistic velocity β, transverse momentum p_{T}, and relativistic γ factor, distributions for Photon Fusion pair-produced charge $|z| = 100$ spin-0 HECOs with various masses (after a minimum p_{T} cut is applied).

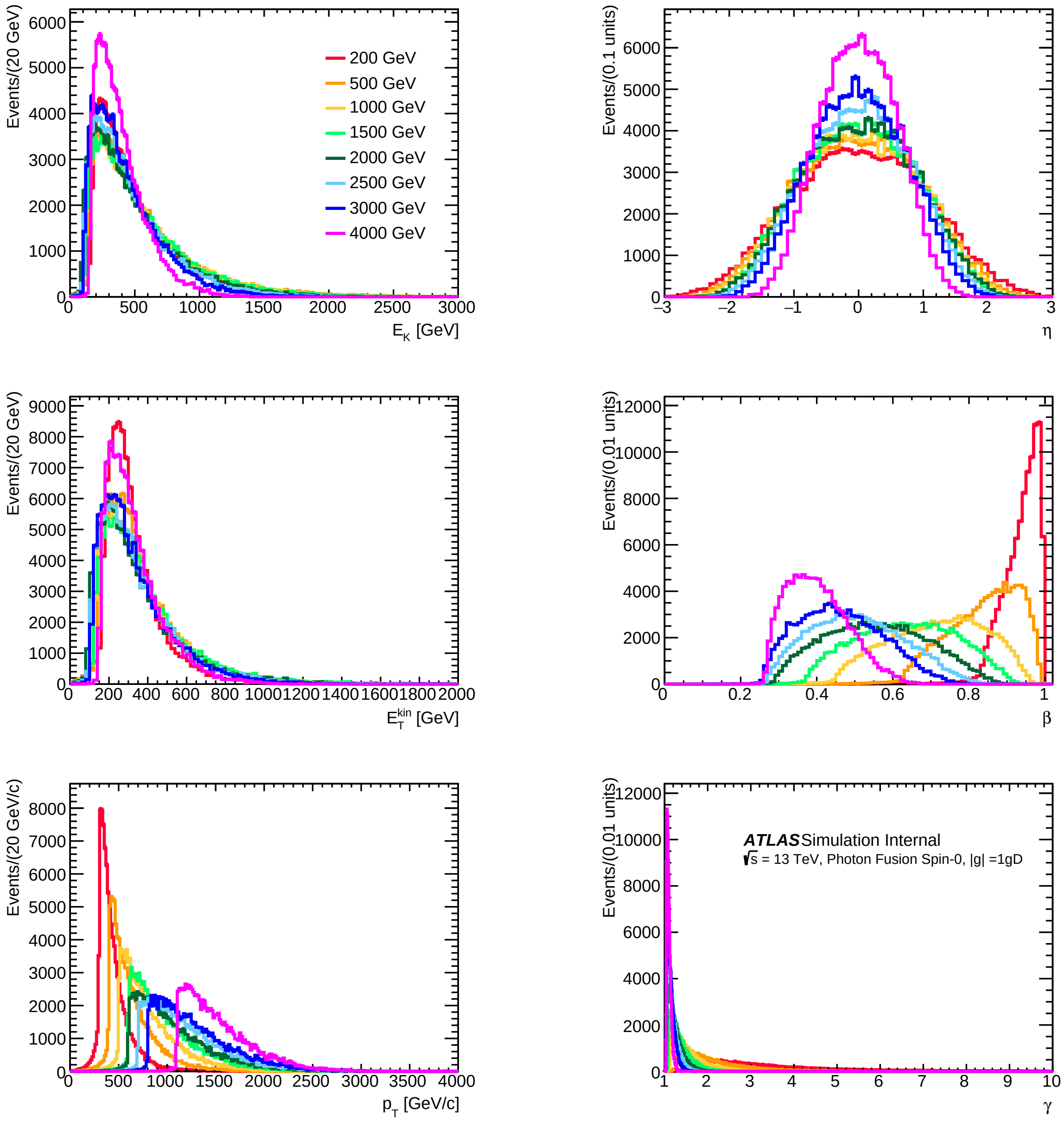

Figure A.20: Generator-level transverse kinetic energy $E_{\mathrm{T}}^{\mathrm{kin}}$, pseudorapidity η, kinetic energy E_{K}, relativistic velocity β, transverse momentum p_{T}, and relativistic γ factor, distributions for Photon Fusion pair-produced charge $1g_{\mathrm{D}}$ spin-0 monopoles with various masses (after a minimum p_{T} cut is applied).

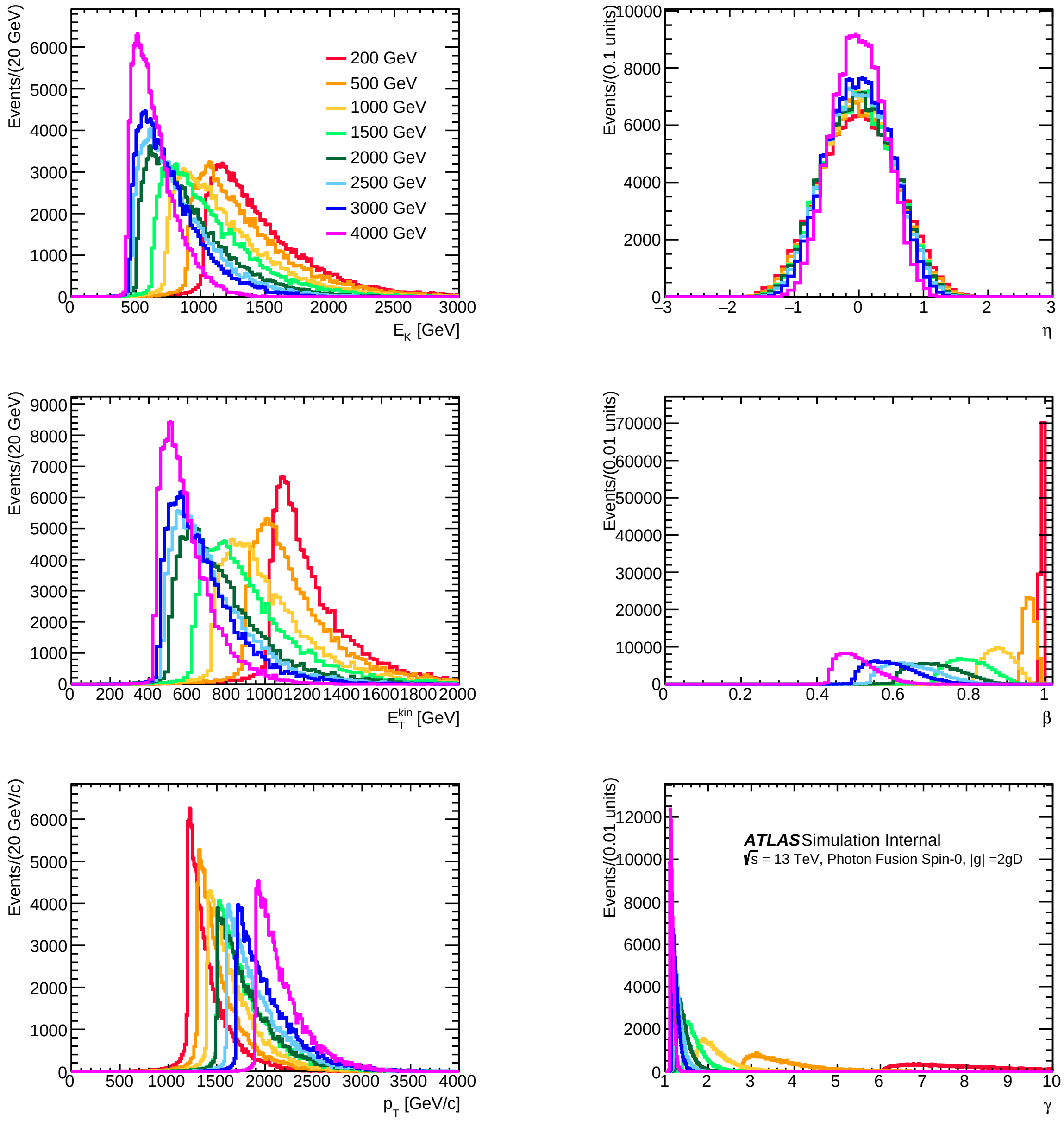

Figure A.21: Generator-level transverse kinetic energy $E_{\mathrm{T}}^{\mathrm{kin}}$, pseudorapidity η, kinetic energy E_{K}, relativistic velocity β, transverse momentum p_{T}, and relativistic γ factor, distributions for Photon Fusion pair-produced charge $2g_{\mathrm{D}}$ spin-0 monopoles with various masses (after a minimum p_{T} cut is applied).

A.4 PF spin-½

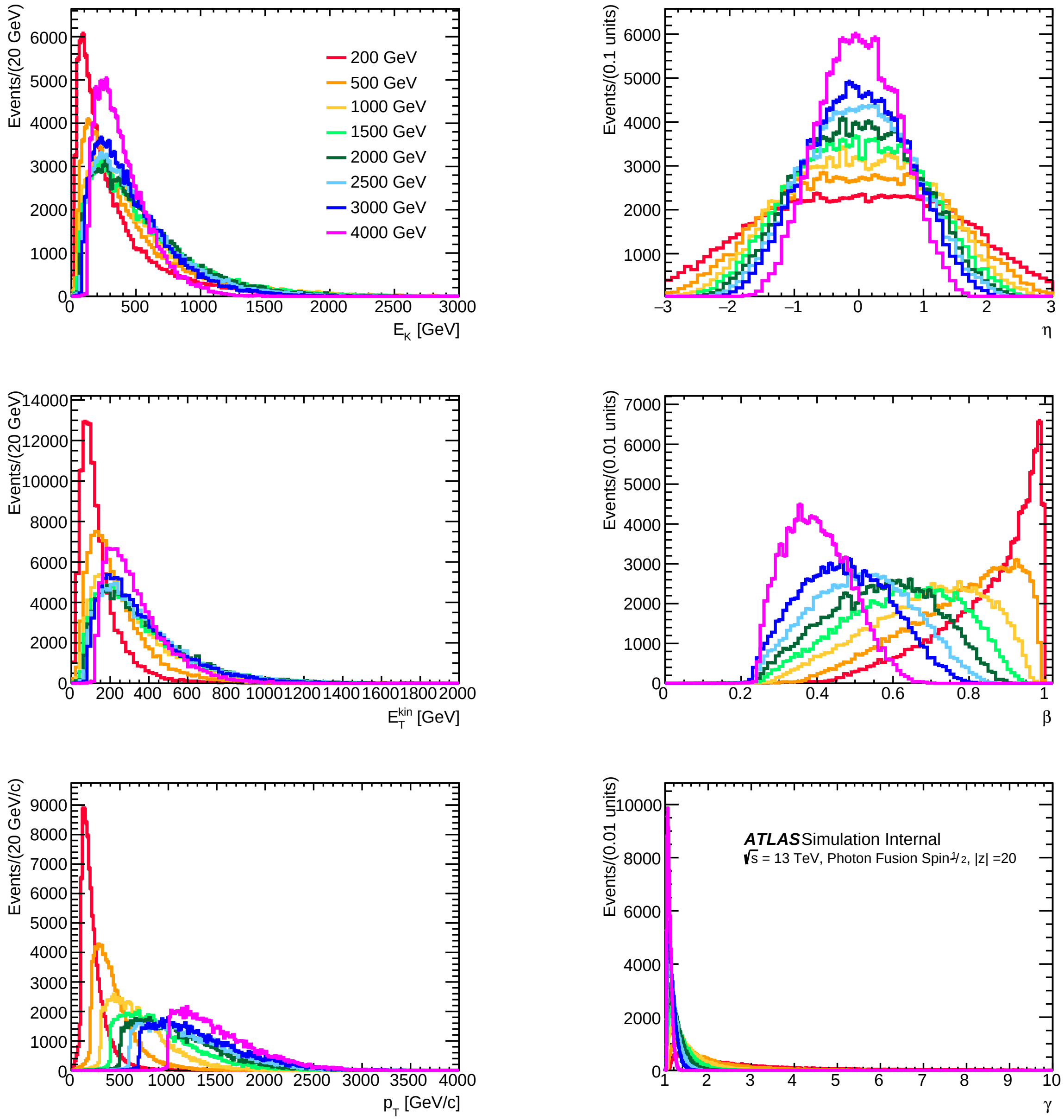

Figure A.22: Generator-level transverse kinetic energy $E_{\mathrm{T}}^{\mathrm{kin}}$, pseudorapidity η, kinetic energy E_{K}, relativistic velocity β, transverse momentum p_{T}, and relativistic γ factor, distributions for Photon Fusion pair-produced charge $|z| = 20$ spin-½ HECOs with various masses (after a minimum p_{T} cut is applied).

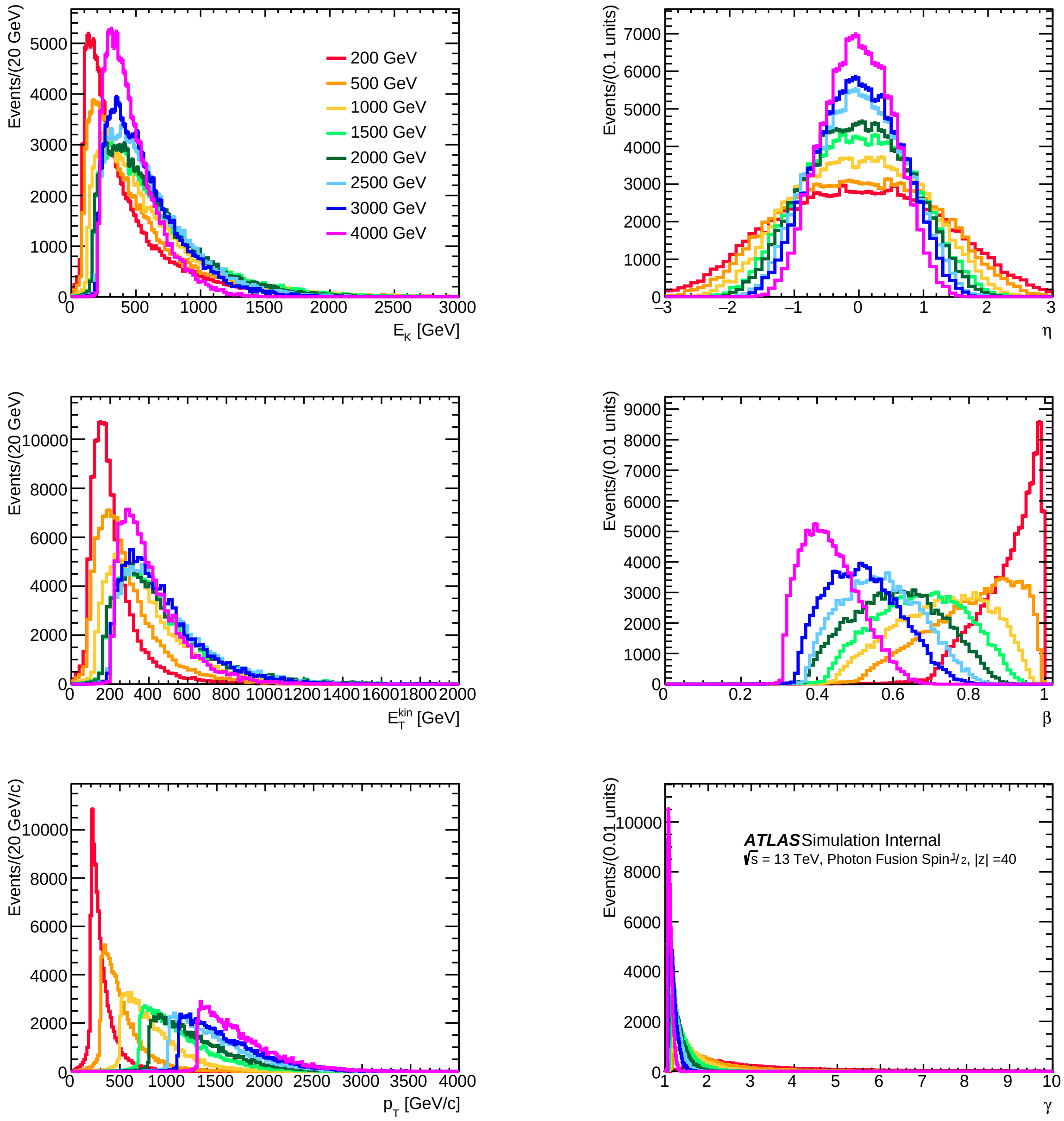

Figure A.23: Generator-level transverse kinetic energy $E_{\mathrm{T}}^{\mathrm{kin}}$, pseudorapidity η, kinetic energy E_{K}, relativistic velocity β, transverse momentum p_{T}, and relativistic γ factor, distributions for Photon Fusion pair-produced charge $|z| = 40$ spin-½ HECOs with various masses (after a minimum p_{T} cut is applied).

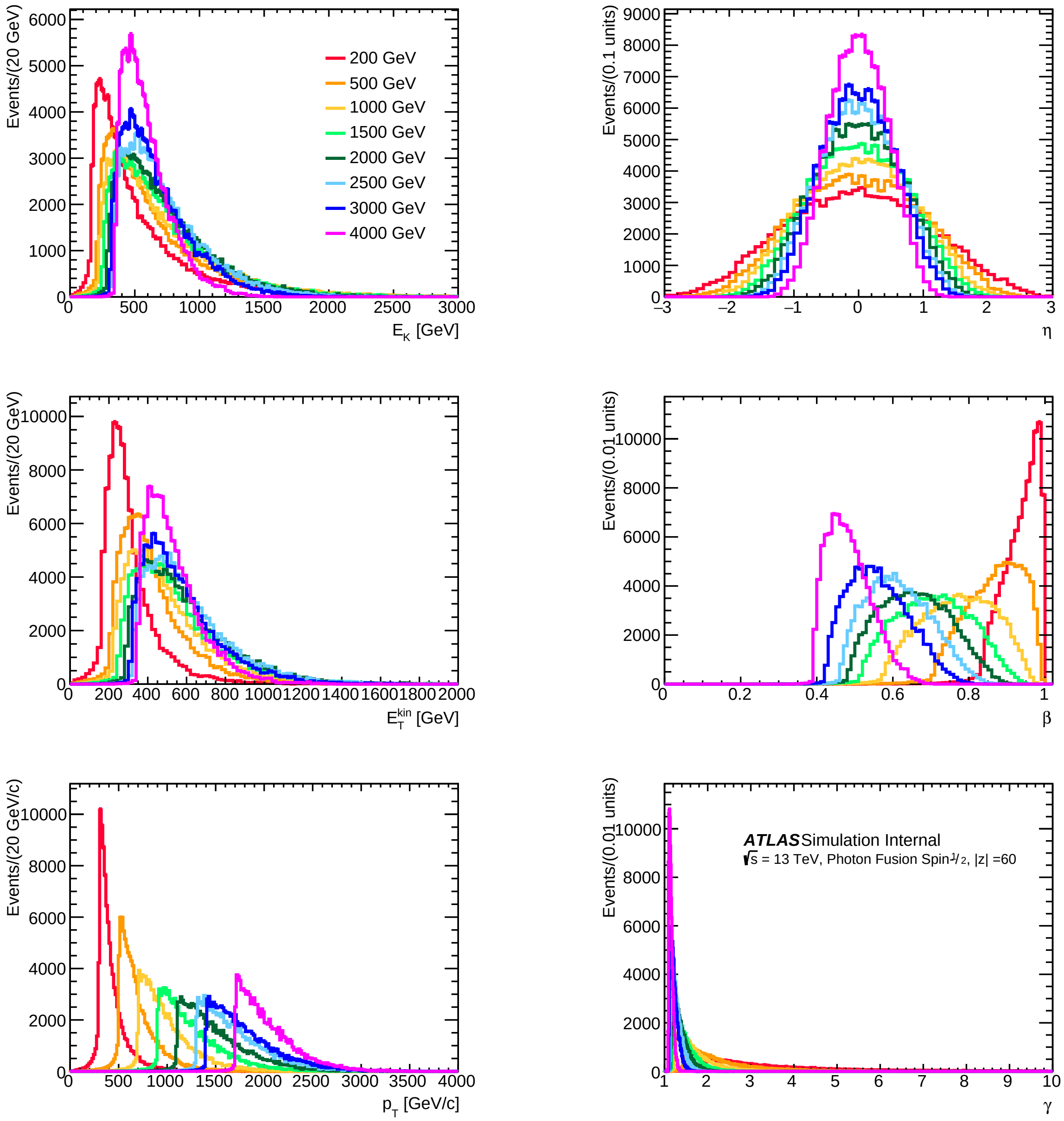

Figure A.24: Generator-level transverse kinetic energy $E_{\mathrm{T}}^{\mathrm{kin}}$, pseudorapidity η, kinetic energy E_{K}, relativistic velocity β, transverse momentum p_{T}, and relativistic γ factor, distributions for Photon Fusion pair-produced charge $|z| = 60$ spin-½ HECOs with various masses (after a minimum p_{T} cut is applied).

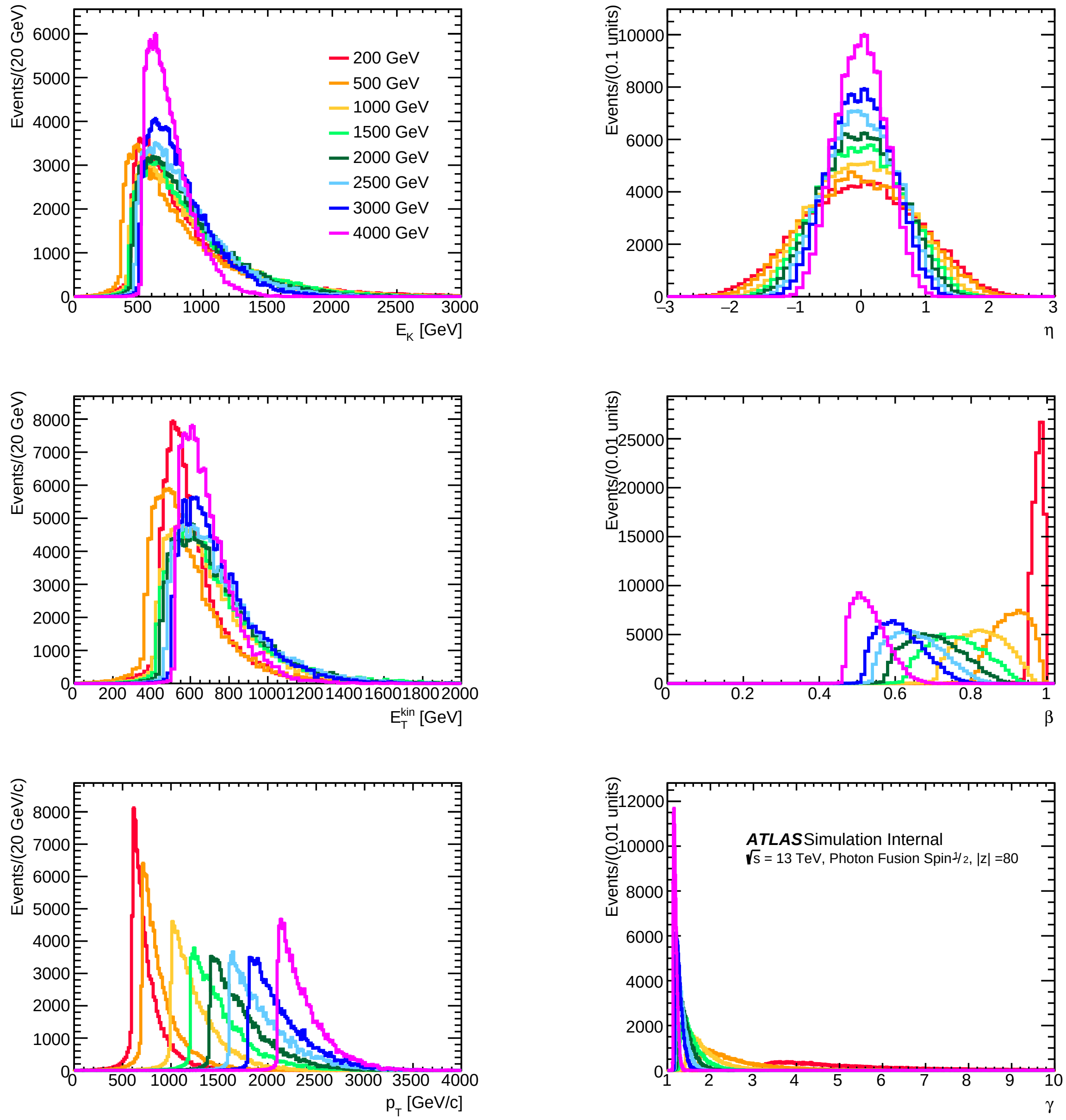

Figure A.25: Generator-level transverse kinetic energy $E_{\mathrm{T}}^{\mathrm{kin}}$, pseudorapidity η, kinetic energy E_{K}, relativistic velocity β, transverse momentum p_{T}, and relativistic γ factor, distributions for Photon Fusion pair-produced charge $|z| = 80$ spin-½ HECOs with various masses (after a minimum p_{T} cut is applied).

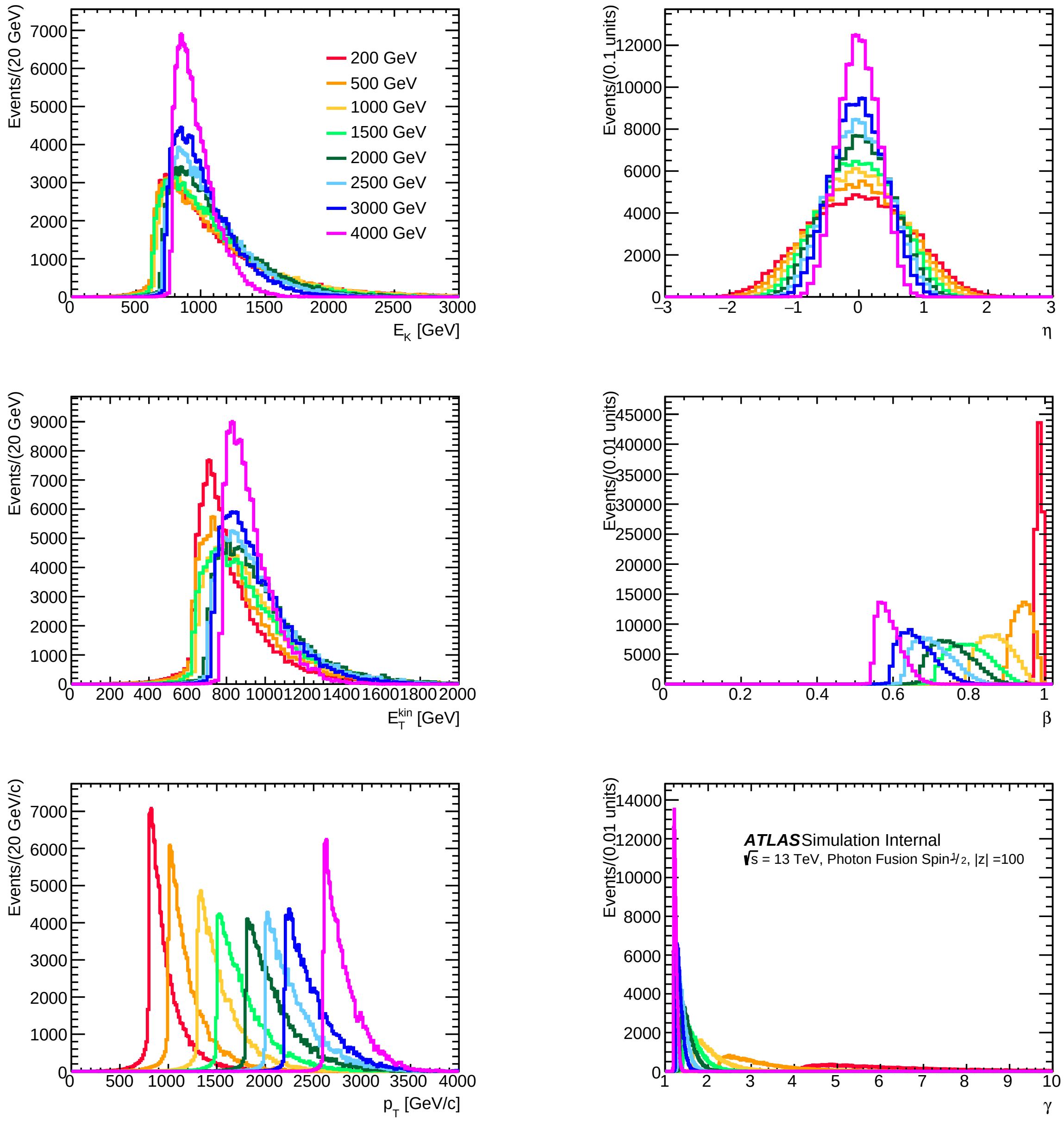

Figure A.26: Generator-level transverse kinetic energy $E_{\mathrm{T}}^{\mathrm{kin}}$, pseudorapidity η, kinetic energy E_{K}, relativistic velocity β, transverse momentum p_{T}, and relativistic γ factor, distributions for Photon Fusion pair-produced charge $|z| = 100$ spin-½ HECOs with various masses (after a minimum p_{T} cut is applied).

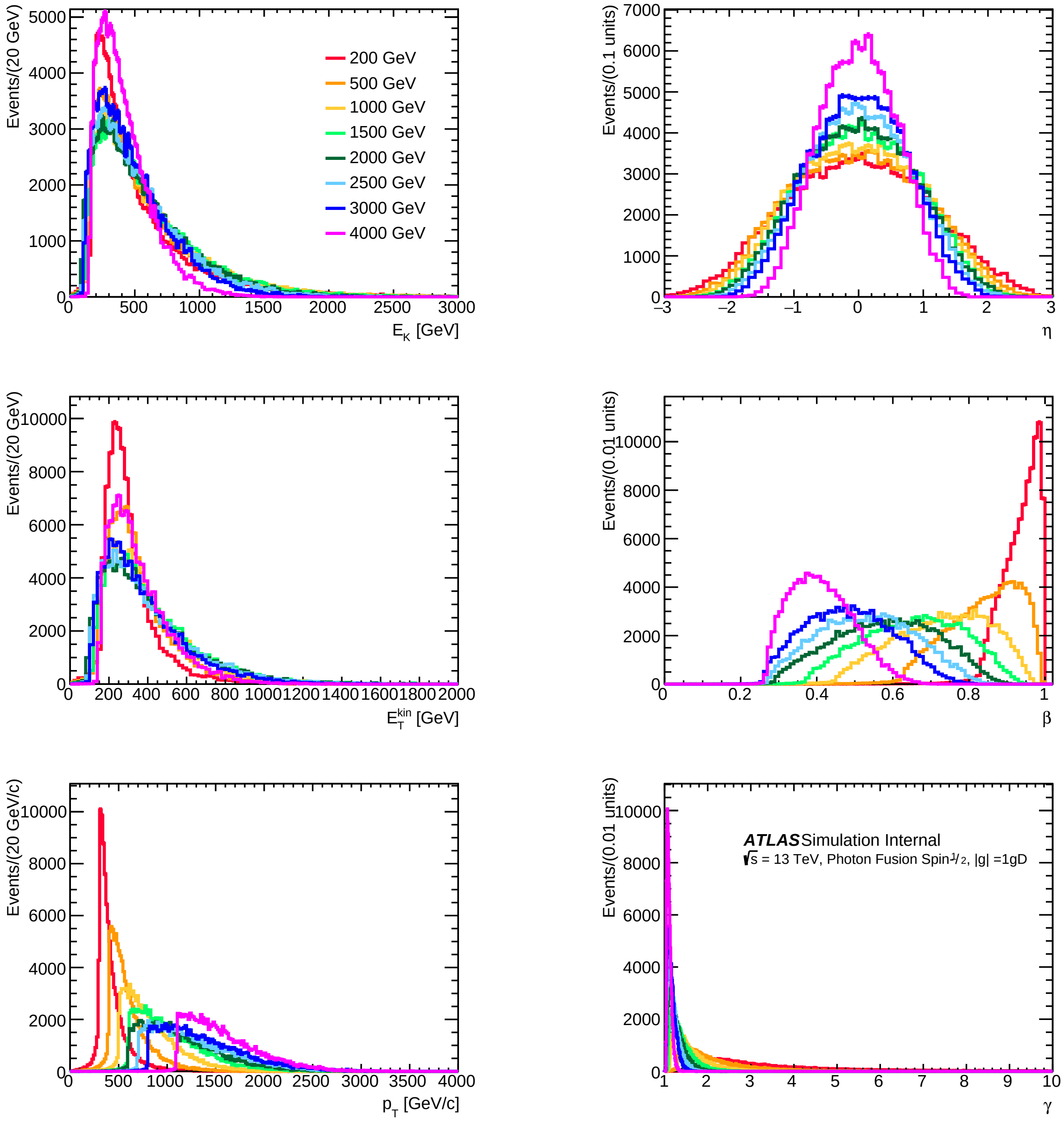

Figure A.27: Generator-level transverse kinetic energy $E_{\mathrm{T}}^{\mathrm{kin}}$, pseudorapidity η, kinetic energy E_{K}, relativistic velocity β, transverse momentum p_{T}, and relativistic γ factor, distributions for Photon Fusion pair-produced charge $1g_{\mathrm{D}}$ spin-½ monopoles with various masses (after a minimum p_{T} cut is applied).

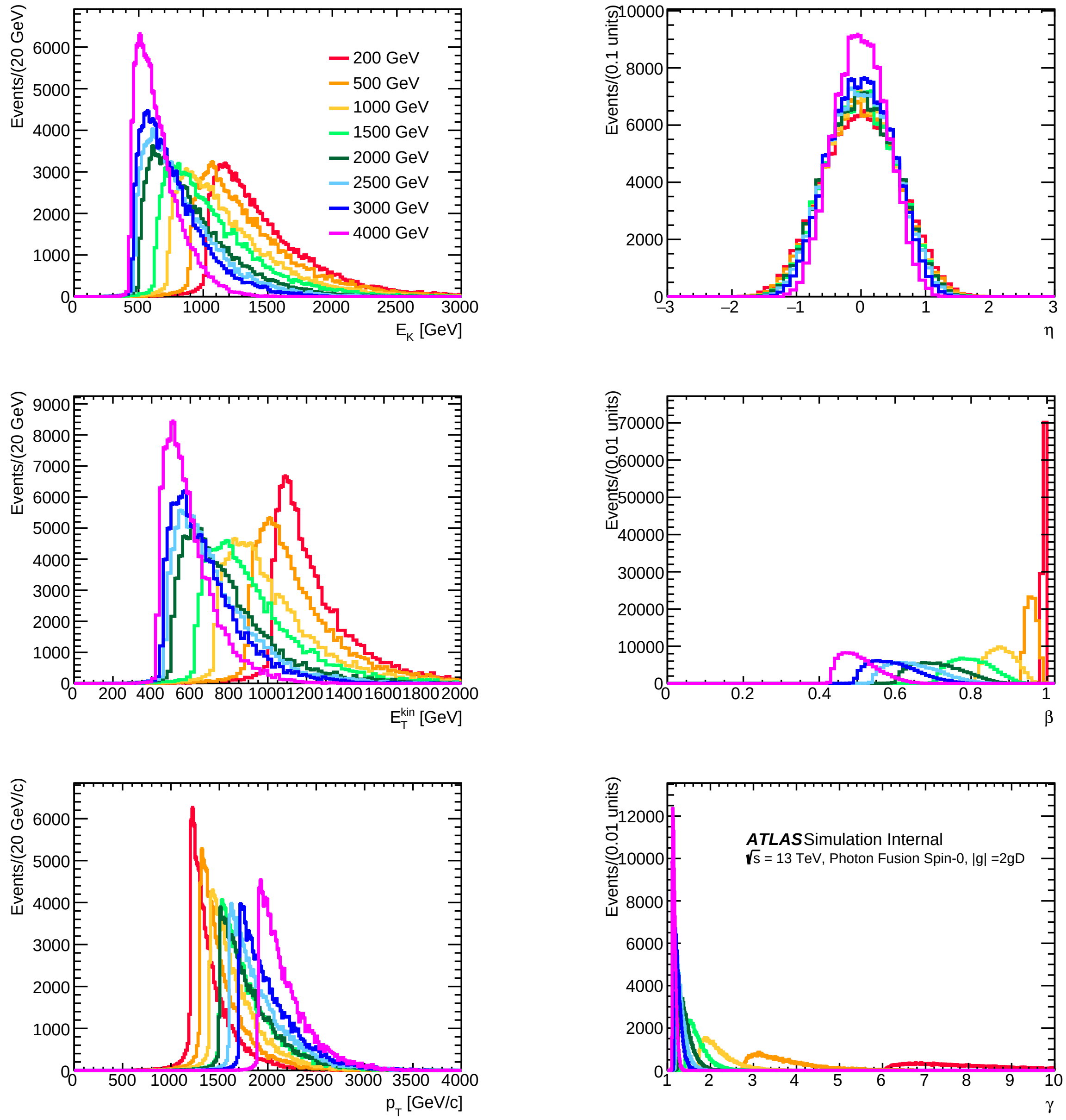

Figure A.28: Generator-level transverse kinetic energy $E_{\mathrm{T}}^{\mathrm{kin}}$, pseudorapidity η, kinetic energy E_{K}, relativistic velocity β, transverse momentum p_{T}, and relativistic γ factor, distributions for Photon Fusion pair-produced charge $2g_{\mathrm{D}}$ spin-½ monopoles with various masses (after a minimum p_{T} cut is applied).

APPENDIX B

Transverse Momentum Cut Efficiency

Table B.1 contains the production cross section before and after applying p_{T} cuts for each mass, charge, spin and production mechanism combination studied. The p_{T} efficiency is defined as the ratio between the production cross section after applying the cut and the production cross section before applying the cut.

Mech.	S	g, z [g_D, e]	Mass [GeV]	pT cut [GeV]	σ_{after} [pb]	σ_{before} [pb]	pT eff.
DY	0	1	200	300	6.9	30	2.3×10^{-1}
DY	0	1	500	400	3.7×10^{-1}	6.2×10^{-1}	5.9×10^{-1}
DY	0	1	1000	500	1.2×10^{-2}	1.5×10^{-2}	8.1×10^{-1}
DY	0	1	1500	600	7.0×10^{-4}	8.1×10^{-4}	8.6×10^{-1}
DY	0	1	2000	600	5.6×10^{-5}	6.1×10^{-5}	9.2×10^{-1}
DY	0	1	2500	700	4.5×10^{-6}	5.0×10^{-6}	9.1×10^{-1}

Continued on next page

Table B.1: Cross sections before and after p_T cuts and resulting p_{T} efficiencies.

Mech.	S	g, z [g_D, e]	Mass [GeV]	pT cut [GeV]	σ_{after} [pb]	σ_{before} [pb]	pT eff.
DY	0	1	3000	800	4.0×10^{-7}	4.4×10^{-7}	9.0×10^{-1}
DY	0	1	4000	1100	3.0×10^{-9}	3.7×10^{-9}	8.2×10^{-1}
DY	0	2	200	1200	7.0×10^{-2}	1.2×10^{2}	5.9×10^{-4}
DY	0	2	500	1300	2.5×10^{-2}	2.5	1.0×10^{-2}
DY	0	2	1000	1400	4.0×10^{-3}	5.8×10^{-2}	6.9×10^{-2}
DY	0	2	1500	1500	4.8×10^{-4}	3.2×10^{-3}	1.5×10^{-1}
DY	0	2	2000	1500	6.4×10^{-5}	2.4×10^{-4}	2.6×10^{-1}
DY	0	2	2500	1600	6.3×10^{-6}	2.0×10^{-5}	3.2×10^{-1}
DY	0	2	3000	1700	6.3×10^{-7}	1.8×10^{-6}	3.6×10^{-1}
DY	0	2	4000	1900	4.9×10^{-9}	1.5×10^{-8}	3.3×10^{-1}
DY	0	20	200	100	2.4	2.7	9.0×10^{-1}
DY	0	20	500	200	5.3×10^{-2}	5.7×10^{-2}	9.4×10^{-1}
DY	0	20	1000	300	1.3×10^{-3}	1.3×10^{-3}	9.6×10^{-1}
DY	0	20	1500	400	7.1×10^{-5}	7.4×10^{-5}	9.6×10^{-1}
DY	0	20	2000	500	5.3×10^{-6}	5.5×10^{-6}	9.6×10^{-1}
DY	0	20	2500	600	4.3×10^{-7}	4.5×10^{-7}	9.5×10^{-1}
DY	0	20	3000	700	3.8×10^{-8}	4.0×10^{-8}	9.4×10^{-1}
DY	0	20	4000	1000	2.9×10^{-10}	3.4×10^{-10}	8.7×10^{-1}
DY	0	40	200	200	5.6	1.1×10^{1}	5.2×10^{-1}
DY	0	40	500	300	1.8×10^{-1}	2.3×10^{-1}	7.9×10^{-1}
DY	0	40	1000	500	4.3×10^{-3}	5.3×10^{-3}	8.1×10^{-1}
DY	0	40	1500	700	2.3×10^{-4}	3.0×10^{-4}	7.8×10^{-1}
DY	0	40	2000	800	1.8×10^{-5}	2.2×10^{-5}	8.0×10^{-1}
DY	0	40	2500	1000	1.4×10^{-6}	1.8×10^{-6}	7.4×10^{-1}
DY	0	40	3000	1100	1.2×10^{-7}	1.6×10^{-7}	7.5×10^{-1}
DY	0	40	4000	1300	9.6×10^{-10}	1.3×10^{-9}	7.1×10^{-1}

Continued on next page

Table B.1: Cross sections before and after p_T cuts and resulting p_{T} efficiencies.

Mech.	S	g, z [g_D, e]	Mass [GeV]	pT cut [GeV]	σ_{after} [pb]	σ_{before} [pb]	pT eff.
DY	0	60	200	300	5.6	2.4×10^{1}	2.3×10^{-1}
DY	0	60	500	500	2.1×10^{-1}	5.1×10^{-1}	4.1×10^{-1}
DY	0	60	1000	700	6.8×10^{-3}	1.2×10^{-2}	5.7×10^{-1}
DY	0	60	1500	900	3.9×10^{-4}	6.7×10^{-4}	5.9×10^{-1}
DY	0	60	2000	1100	2.8×10^{-5}	5.0×10^{-5}	5.6×10^{-1}
DY	0	60	2500	1300	2.1×10^{-6}	4.1×10^{-6}	5.2×10^{-1}
DY	0	60	3000	1400	2.0×10^{-7}	3.6×10^{-7}	5.5×10^{-1}
DY	0	60	4000	1700	$e1.4 \times 10^{-9}$	3.0×10^{-9}	4.6×10^{-1}
DY	0	80	200	600	9.5×10^{-1}	4.3×10^{1}	2.2×10^{-2}
DY	0	80	500	700	1.5×10^{-1}	9.1×10^{-1}	1.7×10^{-1}
DY	0	80	1000	1000	5.5×10^{-3}	2.1×10^{-2}	2.6×10^{-1}
DY	0	80	1500	1200	3.8×10^{-4}	1.2×10^{-3}	3.2×10^{-1}
DY	0	80	2000	1400	2.9×10^{-5}	8.8×10^{-5}	3.3×10^{-1}
DY	0	80	2500	1600	2.3×10^{-6}	7.3×10^{-6}	3.2×10^{-1}
DY	0	80	3000	1800	1.9×10^{-7}	6.5×10^{-7}	3.0×10^{-1}
DY	0	80	4000	2100	1.2×10^{-9}	5.4×10^{-9}	2.3×10^{-1}
DY	0	100	200	800	3.9×10^{-1}	6.8×10^{1}	5.8×10^{-3}
DY	0	100	500	1000	5.9×10^{-2}	1.4	4.1×10^{-2}
DY	0	100	1000	1300	3.3×10^{-3}	3.3×10^{-2}	9.9×10^{-2}
DY	0	100	1500	1500	2.7×10^{-4}	1.8×10^{-3}	1.5×10^{-1}
DY	0	100	2000	1800	1.8×10^{-5}	1.4×10^{-4}	1.3×10^{-1}
DY	0	100	2500	2000	1.5×10^{-6}	1.1×10^{-5}	1.3×10^{-1}
DY	0	100	3000	2200	1.4×10^{-7}	1.0×10^{-6}	1.4×10^{-1}
DY	0	100	4000	2600	5.6×10^{-10}	8.4×10^{-9}	6.6×10^{-2}
DY	½	1	200	300	2.7×10^{1}	3.4×10^{2}	7.7×10^{-2}
DY	½	1	500	400	2.3	8.5	2.7×10^{-1}

Continued on next page

Table B.1: Cross sections before and after p_T cuts and resulting p_{T} efficiencies.

Mech.	S	g, z [g_D, e]	Mass [GeV]	pT cut [GeV]	σ_{after} [pb]	σ_{before} [pb]	pT eff.
DY	½	1	1000	500	1.1×10^{-1}	2.4×10^{-1}	4.7×10^{-1}
DY	½	1	1500	600	8.7×10^{-3}	1.6×10^{-2}	5.3×10^{-1}
DY	½	1	2000	600	9.4×10^{-4}	1.5×10^{-3}	6.4×10^{-1}
DY	½	1	2500	700	8.9×10^{-5}	1.4×10^{-4}	6.2×10^{-1}
DY	½	1	3000	800	8.7×10^{-6}	1.4×10^{-5}	6.0×10^{-1}
DY	½	1	4000	1100	7.9×10^{-8}	1.6×10^{-7}	4.8×10^{-1}
DY	½	2	200	1200	1.8×10^{-1}	1.4×10^{3}	1.3×10^{-4}
DY	½	2	500	1300	7.4×10^{-2}	3.4×10^{1}	2.2×10^{-3}
DY	½	2	1000	1400	1.6×10^{-2}	9.6×10^{-1}	1.7×10^{-2}
DY	½	2	1500	1500	2.6×10^{-3}	6.5×10^{-2}	4.0×10^{-2}
DY	½	2	2000	1500	4.8×10^{-4}	5.9×10^{-3}	8.2×10^{-2}
DY	½	2	2500	1600	5.8×10^{-5}	5.7×10^{-4}	1.0×10^{-1}
DY	½	2	3000	1700	6.9×10^{-6}	5.8×10^{-5}	1.2×10^{-1}
DY	½	2	4000	1900	7.4×10^{-8}	6.6×10^{-7}	1.1×10^{-1}
DY	½	20	200	100	1.8×10^{1}	2.8×10^{1}	6.2×10^{-1}
DY	½	20	500	200	4.7×10^{-1}	7.0×10^{-1}	6.7×10^{-1}
DY	½	20	1000	300	1.5×10^{-2}	2.0×10^{-2}	7.5×10^{-1}
DY	½	20	1500	400	1.0×10^{-3}	1.3×10^{-3}	7.5×10^{-1}
DY	½	20	2000	500	8.7×10^{-5}	1.2×10^{-4}	7.3×10^{-1}
DY	½	20	2500	600	8.1×10^{-6}	1.2×10^{-5}	7.0×10^{-1}
DY	½	20	3000	700	7.9×10^{-7}	1.2×10^{-6}	6.8×10^{-1}
DY	½	20	4000	1000	7.3×10^{-9}	1.3×10^{-8}	5.5×10^{-1}
DY	½	40	200	200	2.5×10^{1}	1.1×10^{2}	2.2×10^{-1}
DY	½	40	500	300	1.2	2.8	4.4×10^{-1}
DY	½	40	1000	500	3.7×10^{-2}	7.9×10^{-2}	4.7×10^{-1}
DY	½	40	1500	700	2.3×10^{-3}	5.3×10^{-3}	4.3×10^{-1}

Continued on next page

Table B.1: Cross sections before and after p_T cuts and resulting p_{T} efficiencies.

Mech.	S	g, z [g_D, e]	Mass [GeV]	pT cut [GeV]	σ_{after} [pb]	σ_{before} [pb]	pT eff.
DY	½	40	2000	800	2.2×10^{-4}	4.8×10^{-4}	4.6×10^{-1}
DY	½	40	2500	1000	1.8×10^{-5}	4.6×10^{-5}	3.9×10^{-1}
DY	½	40	3000	1100	1.8×10^{-6}	4.7×10^{-6}	3.9×10^{-1}
DY	½	40	4000	1300	1.9×10^{-8}	5.3×10^{-8}	3.6×10^{-1}
DY	½	60	200	300	2.0×10^{1}	2.6×10^{2}	7.7×10^{-2}
DY	½	60	500	500	9.7×10^{-1}	6.3	1.5×10^{-1}
DY	½	60	1000	700	4.4×10^{-2}	1.8×10^{-1}	2.5×10^{-1}
DY	½	60	1500	900	3.1×10^{-3}	1.2×10^{-2}	2.6×10^{-1}
DY	½	60	2000	1100	2.6×10^{-4}	1.1×10^{-3}	2.4×10^{-1}
DY	½	60	2500	1300	2.2×10^{-5}	1.0×10^{-4}	2.1×10^{-1}
DY	½	60	3000	1400	2.4×10^{-6}	1.1×10^{-5}	2.3×10^{-1}
DY	½	60	4000	1700	2.1×10^{-8}	1.2×10^{-7}	1.7×10^{-1}
DY	½	80	200	600	2.5	4.6×10^{2}	5.4×10^{-3}
DY	½	80	500	700	5.6×10^{-1}	1.1×10^{1}	5.0×10^{-2}
DY	½	80	1000	1000	2.6×10^{-2}	3.1×10^{-1}	8.4×10^{-2}
DY	½	80	1500	1200	2.3×10^{-3}	2.1×10^{-2}	1.1×10^{-1}
DY	½	80	2000	1400	2.1×10^{-4}	1.9×10^{-3}	1.1×10^{-1}
DY	½	80	2500	1600	1.9×10^{-5}	1.8×10^{-4}	1.0×10^{-1}
DY	½	80	3000	1800	1.8×10^{-6}	1.9×10^{-5}	9.5×10^{-2}
DY	½	80	4000	2100	1.5×10^{-8}	2.1×10^{-7}	6.8×10^{-2}
DY	½	100	200	800	9.5×10^{-1}	7.1×10^{2}	1.3×10^{-3}
DY	½	100	500	1000	1.7×10^{-1}	1.7×10^{1}	9.9×10^{-3}
DY	½	100	1000	1300	1.2×10^{-2}	4.9×10^{-1}	2.5×10^{-2}
DY	½	100	1500	1500	1.3×10^{-3}	3.3×10^{-2}	4.0×10^{-2}
DY	½	100	2000	1800	9.6×10^{-5}	3.0×10^{-3}	3.2×10^{-2}
DY	½	100	2500	2000	9.8×10^{-6}	2.9×10^{-4}	3.4×10^{-2}

Continued on next page

Table B.1: Cross sections before and after p_T cuts and resulting p_{T} efficiencies.

Mech.	S	g, z [g_D, e]	Mass [GeV]	pT cut [GeV]	σ_{after} [pb]	σ_{before} [pb]	pT eff.
DY	½	100	3000	2200	9.9×10^{-7}	2.9×10^{-5}	3.4×10^{-2}
DY	½	100	4000	2600	5.0×10^{-9}	3.3×10^{-7}	1.5×10^{-2}
PF	0	1	200	300	1.2×10^{3}	1.1×10^{4}	1.1×10^{-1}
PF	0	1	500	400	7.9×10^{1}	3.0×10^{2}	2.6×10^{-1}
PF	0	1	1000	500	4.2	1.0×10^{1}	4.2×10^{-1}
PF	0	1	1500	600	3.8×10^{-1}	7.8×10^{-1}	4.9×10^{-1}
PF	0	1	2000	600	5.0×10^{-2}	8.2×10^{-2}	6.0×10^{-1}
PF	0	1	2500	700	5.5×10^{-3}	9.5×10^{-3}	5.8×10^{-1}
PF	0	1	3000	800	5.7×10^{-4}	1.0×10^{-3}	5.5×10^{-1}
PF	0	1	4000	1100	3.0×10^{-6}	6.8×10^{-6}	4.4×10^{-1}
PF	0	2	200	1200	6.8×10^{1}	1.7×10^{5}	3.9×10^{-4}
PF	0	2	500	1300	2.4×10^{1}	4.9×10^{3}	4.9×10^{-3}
PF	0	2	1000	1400	3.8	1.6×10^{2}	2.4×10^{-2}
PF	0	2	1500	1500	5.3×10^{-1}	1.3×10^{1}	4.3×10^{-2}
PF	0	2	2000	1500	1.0×10^{-1}	1.3	7.6×10^{-2}
PF	0	2	2500	1600	1.3×10^{-2}	1.5×10^{-1}	8.5×10^{-2}
PF	0	2	3000	1700	1.4×10^{-3}	1.7×10^{-2}	8.3×10^{-2}
PF	0	2	4000	1900	5.8×10^{-6}	1.1×10^{-4}	5.3×10^{-2}
PF	0	20	200	100	5.3×10^{1}	9.0×10^{1}	5.8×10^{-1}
PF	0	20	500	200	1.6	2.5	6.3×10^{-1}
PF	0	20	1000	300	5.8×10^{-2}	8.3×10^{-2}	7.1×10^{-1}
PF	0	20	1500	400	4.6×10^{-3}	6.5×10^{-3}	7.1×10^{-1}
PF	0	20	2000	500	4.8×10^{-4}	6.9×10^{-4}	7.0×10^{-1}
PF	0	20	2500	600	5.3×10^{-5}	7.9×10^{-5}	6.7×10^{-1}
PF	0	20	3000	700	5.4×10^{-6}	8.6×10^{-6}	6.3×10^{-1}
PF	0	20	4000	1000	2.5×10^{-8}	5.7×10^{-8}	4.4×10^{-1}

Continued on next page

Table B.1: Cross sections before and after p_T cuts and resulting p_{T} efficiencies.

Mech.	S	g, z [g_D, e]	Mass [GeV]	pT cut [GeV]	σ_{after} [pb]	σ_{before} [pb]	pT eff.
PF	0	40	200	200	3.6×10^{2}	1.4×10^{3}	2.5×10^{-1}
PF	0	40	500	300	1.7×10^{1}	4.0×10^{1}	4.1×10^{-1}
PF	0	40	1000	500	5.6×10^{-1}	1.3	4.2×10^{-1}
PF	0	40	1500	700	4.0×10^{-2}	1.0×10^{-1}	3.9×10^{-1}
PF	0	40	2000	800	4.6×10^{-3}	1.1×10^{-2}	4.2×10^{-1}
PF	0	40	2500	1000	5.3×10^{-4}	1.3×10^{-3}	4.2×10^{-1}
PF	0	40	3000	1100	4.6×10^{-5}	1.4×10^{-4}	3.3×10^{-1}
PF	0	40	4000	1300	2.3×10^{-7}	9.1×10^{-7}	2.5×10^{-1}
PF	0	60	200	300	8.2×10^{2}	7.3×10^{3}	1.1×10^{-1}
PF	0	60	500	500	3.4×10^{1}	2.0×10^{2}	1.7×10^{-1}
PF	0	60	1000	700	1.5	6.7	2.3×10^{-1}
PF	0	60	1500	900	1.2×10^{-1}	5.2×10^{-1}	2.3×10^{-1}
PF	0	60	2000	1100	1.2×10^{-2}	5.5×10^{-2}	2.1×10^{-1}
PF	0	60	2500	1300	1.1×10^{-3}	6.4×10^{-3}	1.8×10^{-1}
PF	0	60	3000	1400	1.2×10^{-4}	6.9×10^{-4}	1.8×10^{-1}
PF	0	60	4000	1700	4.3×10^{-7}	4.6×10^{-6}	9.5×10^{-2}
PF	0	80	200	600	2.8×10^{2}	2.3×10^{4}	1.2×10^{-2}
PF	0	80	500	700	4.4×10^{1}	6.5×10^{2}	6.9×10^{-2}
PF	0	80	1000	1000	1.9	2.1×10^{1}	8.8×10^{-2}
PF	0	80	1500	1200	1.7×10^{-1}	1.7	1.0×10^{-1}
PF	0	80	2000	1400	1.7×10^{-2}	1.8×10^{-1}	9.9×10^{-2}
PF	0	80	2500	1600	1.7×10^{-3}	2.0×10^{-2}	8.4×10^{-2}
PF	0	80	3000	1800	1.4×10^{-4}	2.2×10^{-3}	6.3×10^{-2}
PF	0	80	4000	2100	4.0×10^{-7}	1.5×10^{-5}	2.7×10^{-2}
PF	0	100	200	800	2.0×10^{2}	5.6×10^{4}	3.5×10^{-3}
PF	0	100	500	1000	2.9×10^{1}	1.6×10^{3}	1.8×10^{-2}

Continued on next page

Table B.1: Cross sections before and after p_T cuts and resulting p_{T} efficiencies.

Mech.	S	g, z [g_D, e]	Mass [GeV]	pT cut [GeV]	σ_{after} [pb]	σ_{before} [pb]	pT eff.
PF	0	100	1000	1300	1.7	5.2×10^{1}	3.3×10^{-2}
PF	0	100	1500	1500	1.7×10^{-1}	4.1	4.3×10^{-2}
PF	0	100	2000	1800	1.4×10^{-2}	4.3×10^{-1}	3.2×10^{-2}
PF	0	100	2500	2000	1.3×10^{-3}	4.9×10^{-2}	2.7×10^{-2}
PF	0	100	3000	2200	1.0×10^{-4}	5.4×10^{-3}	1.9×10^{-2}
PF	0	100	4000	2600	1.4×10^{-7}	3.5×10^{-5}	3.9×10^{-3}
PF	½	1	200	300	6.4×10^{3}	6.1×10^{4}	1.0×10^{-1}
PF	½	1	500	400	5.4×10^{2}	1.6×10^{3}	3.4×10^{-1}
PF	½	1	1000	500	2.6×10^{1}	4.6×10^{1}	5.6×10^{-1}
PF	½	1	1500	600	2.0	3.3	6.2×10^{-1}
PF	½	1	2000	600	2.3×10^{-1}	3.2×10^{-1}	7.1×10^{-1}
PF	½	1	2500	700	2.3×10^{-2}	3.3×10^{-2}	6.9×10^{-1}
PF	½	1	3000	800	2.2×10^{-3}	3.4×10^{-3}	6.5×10^{-1}
PF	½	1	4000	1100	9.8×10^{-6}	1.9×10^{-5}	5.1×10^{-1}
PF	½	2	200	1200	1.9×10^{2}	9.8×10^{5}	1.9×10^{-4}
PF	½	2	500	1300	8.4×10^{1}	2.5×10^{4}	3.3×10^{-3}
PF	½	2	1000	1400	2.0×10^{1}	7.4×10^{2}	2.7×10^{-2}
PF	½	2	1500	1500	3.4	5.3×10^{1}	6.5×10^{-2}
PF	½	2	2000	1500	6.4×10^{-1}	5.1	1.3×10^{-1}
PF	½	2	2500	1600	7.5×10^{-2}	5.4×10^{-1}	1.4×10^{-1}
PF	½	2	3000	1700	7.3×10^{-3}	5.4×10^{-2}	1.4×10^{-1}
PF	½	2	4000	1900	2.5×10^{-5}	3.0×10^{-4}	8.3×10^{-2}
PF	½	20	200	100	3.6×10^{2}	5.1×10^{2}	7.0×10^{-1}
PF	½	20	500	200	9.8	1.3×10^{1}	7.5×10^{-1}
PF	½	20	1000	300	3.1×10^{-1}	3.9×10^{-1}	8.1×10^{-1}
PF	½	20	1500	400	2.2×10^{-2}	2.7×10^{-2}	8.1×10^{-1}

Continued on next page

Table B.1: Cross sections before and after p_T cuts and resulting p_{T} efficiencies.

Mech.	S	g, z [g_D, e]	Mass [GeV]	pT cut [GeV]	σ_{after} [pb]	σ_{before} [pb]	pT eff.
PF	½	20	2000	500	2.1×10^{-3}	2.6×10^{-3}	7.9×10^{-1}
PF	½	20	2500	600	2.1×10^{-4}	2.8×10^{-4}	7.6×10^{-1}
PF	½	20	3000	700	2.0×10^{-5}	2.8×10^{-5}	7.2×10^{-1}
PF	½	20	4000	1000	8.1×10^{-8}	1.6×10^{-7}	5.1×10^{-1}
PF	½	40	200	200	2.3×10^{3}	8.1×10^{3}	2.9×10^{-1}
PF	½	40	500	300	1.1×10^{2}	2.1×10^{2}	5.3×10^{-1}
PF	½	40	1000	500	3.4	6.2	5.6×10^{-1}
PF	½	40	1500	700	2.3×10^{-1}	4.4×10^{-1}	5.2×10^{-1}
PF	½	40	2000	800	2.3×10^{-2}	4.2×10^{-2}	5.5×10^{-1}
PF	½	40	2500	1000	2.4×10^{-3}	4.4×10^{-3}	5.4×10^{-1}
PF	½	40	3000	1100	2.0×10^{-4}	4.5×10^{-4}	4.4×10^{-1}
PF	½	40	4000	1300	8.1×10^{-7}	2.5×10^{-6}	3.2×10^{-1}
PF	½	60	200	300	4.3×10^{3}	4.1×10^{4}	1.0×10^{-1}
PF	½	60	500	500	2.2×10^{2}	1.1×10^{3}	2.1×10^{-1}
PF	½	60	1000	700	1.0×10^{1}	3.1×10^{1}	3.3×10^{-1}
PF	½	60	1500	900	7.7×10^{-1}	2.2	3.5×10^{-1}
PF	½	60	2000	1100	6.9×10^{-2}	2.1×10^{-1}	3.2×10^{-1}
PF	½	60	2500	1300	6.1×10^{-3}	2.2×10^{-2}	2.7×10^{-1}
PF	½	60	3000	1400	5.9×10^{-4}	2.3×10^{-3}	2.6×10^{-1}
PF	½	60	4000	1700	1.8×10^{-6}	1.3×10^{-5}	1.4×10^{-1}
PF	½	80	200	600	1.0×10^{3}	1.3×10^{5}	7.6×10^{-3}
PF	½	80	500	700	2.4×10^{2}	3.4×10^{3}	7.1×10^{-2}
PF	½	80	1000	1000	1.2×10^{1}	9.9×10^{1}	1.2×10^{-1}
PF	½	80	1500	1200	1.1	7.0	1.6×10^{-1}
PF	½	80	2000	1400	1.1×10^{-1}	6.8×10^{-1}	1.6×10^{-1}
PF	½	80	2500	1600	1.0×10^{-2}	7.1×10^{-2}	1.4×10^{-1}

Continued on next page

Table B.1: Cross sections before and after p_T cuts and resulting p_{T} efficiencies.

Mech.	S	g, z [g_D, e]	Mass [GeV]	pT cut [GeV]	σ_{after} [pb]	σ_{before} [pb]	pT eff.
PF	½	80	3000	1800	7.6×10^{-4}	7.1×10^{-3}	1.1×10^{-1}
PF	½	80	4000	2100	1.9×10^{-6}	4.0×10^{-5}	4.6×10^{-2}
PF	½	100	200	800	6.1×10^{2}	3.2×10^{5}	1.9×10^{-3}
PF	½	100	500	1000	1.2×10^{2}	8.2×10^{3}	1.5×10^{-2}
PF	½	100	1000	1300	9.6	2.4×10^{2}	4.0×10^{-2}
PF	½	100	1500	1500	1.1	1.7×10^{1}	6.5×10^{-2}
PF	½	100	2000	1800	8.8×10^{-2}	1.7	5.3×10^{-2}
PF	½	100	2500	2000	8.3×10^{-3}	1.7×10^{-1}	4.8×10^{-2}
PF	½	100	3000	2200	6.0×10^{-4}	1.7×10^{-2}	3.4×10^{-2}
PF	½	100	4000	2600	7.4×10^{-7}	9.8×10^{-5}	7.5×10^{-3}

Table B.1: Cross sections before and after p_T cuts and resulting p_{T} efficiencies.

APPENDIX C

Efficiency maps

The efficiency maps indicate the signal selection efficiency for particles as a function of transverse kinetic energy and pseudorapidity. The maps were made using the fully simulated Monte Carlo model-independent single particle samples described in Section 4.2.1, for all masses and each of the monopole and HECO charges studied. Selection cuts were applied with the criteria described in Section 5.2.

C.1 Monopole $1g_{\mathrm{D}}$

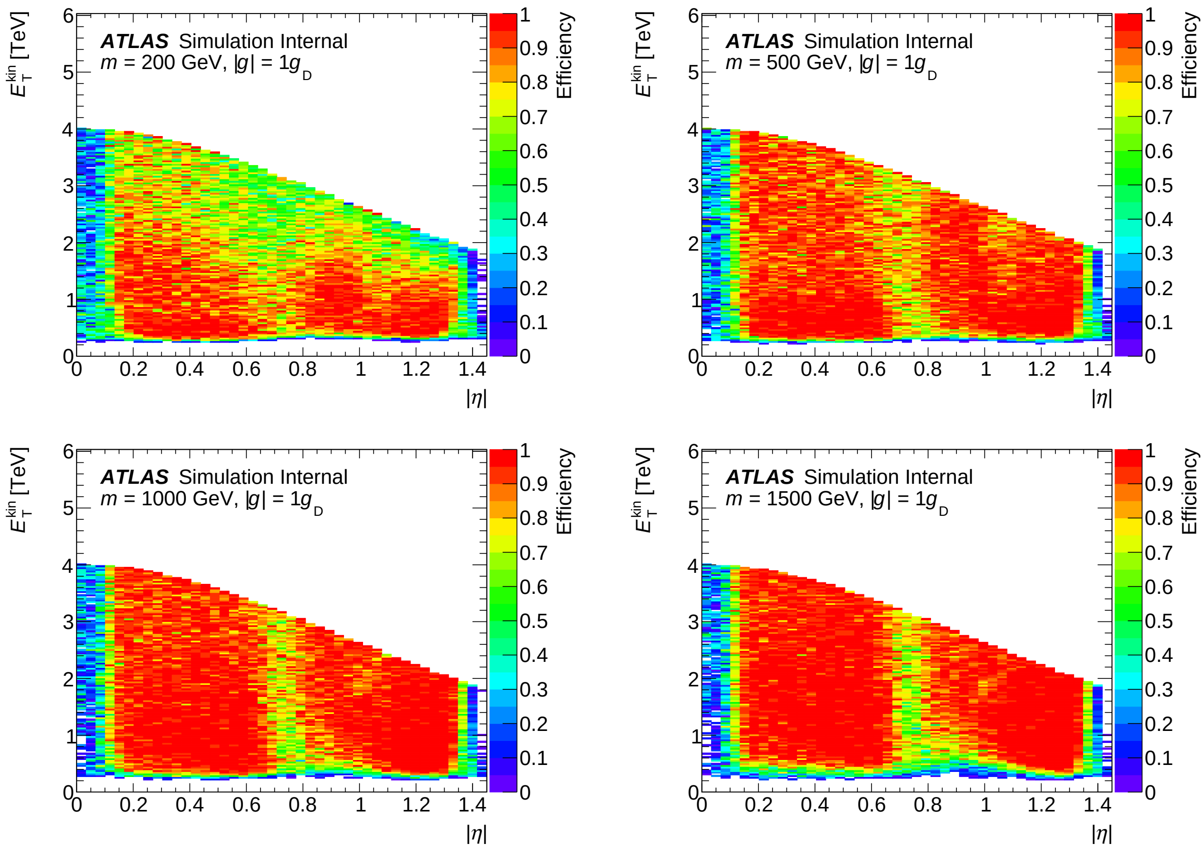

Figure C.1: Selection efficiency as a function of transverse kinetic energy $E_{\mathrm{T}}^{\mathrm{kin}}$ and pseudorapidity η for $1g_{\mathrm{D}}$ monopoles.

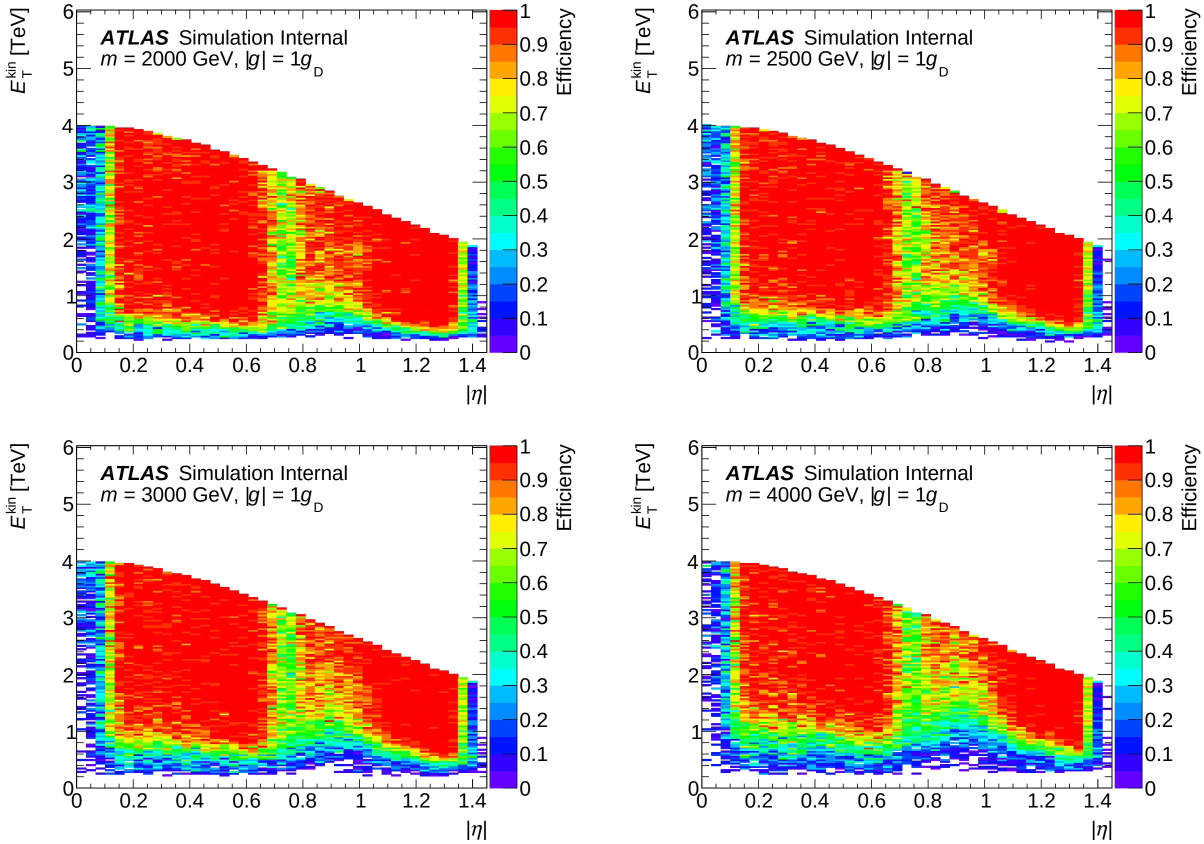

Figure C.1 continued.

C.2 Monopole $2g_\mathrm{D}$

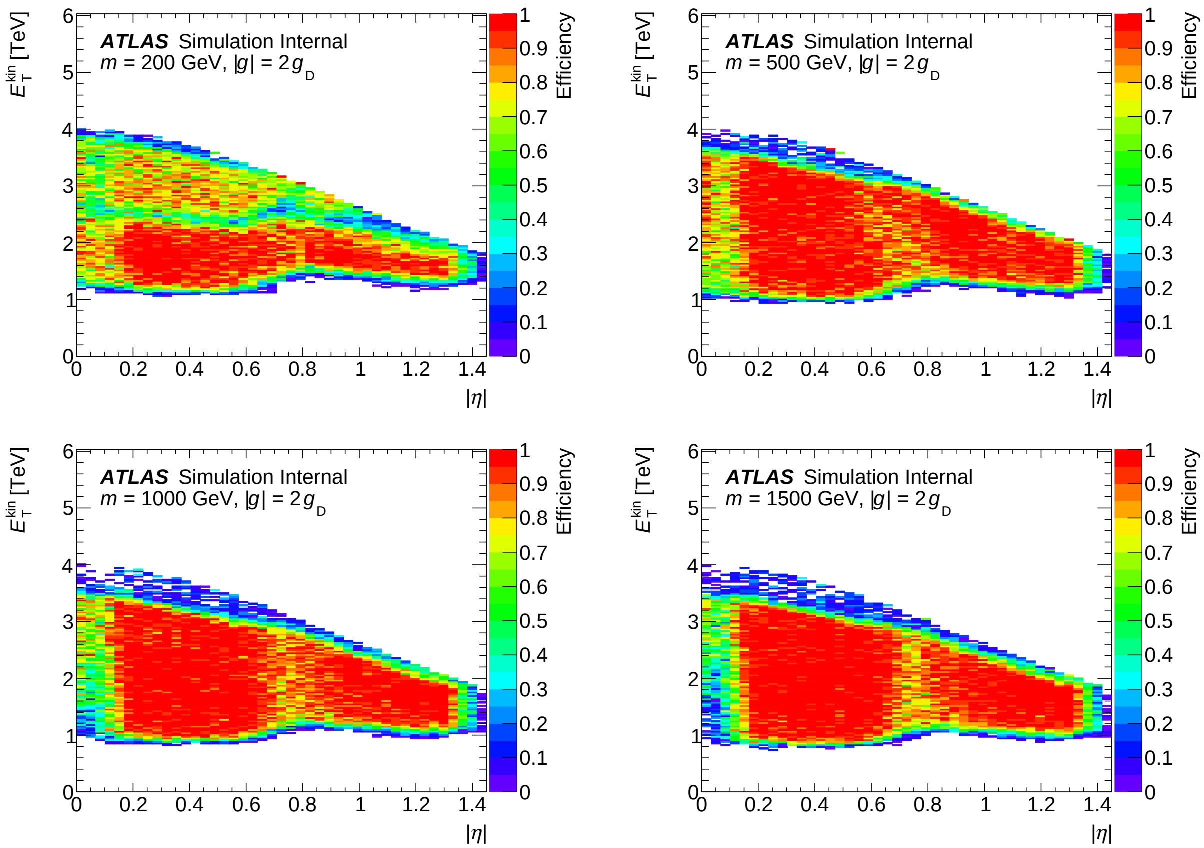

Figure C.3: Selection efficiency as a function of transverse kinetic energy $E_\mathrm{T}^\mathrm{kin}$ and pseudorapidity η for $2g_\mathrm{D}$ monopoles.

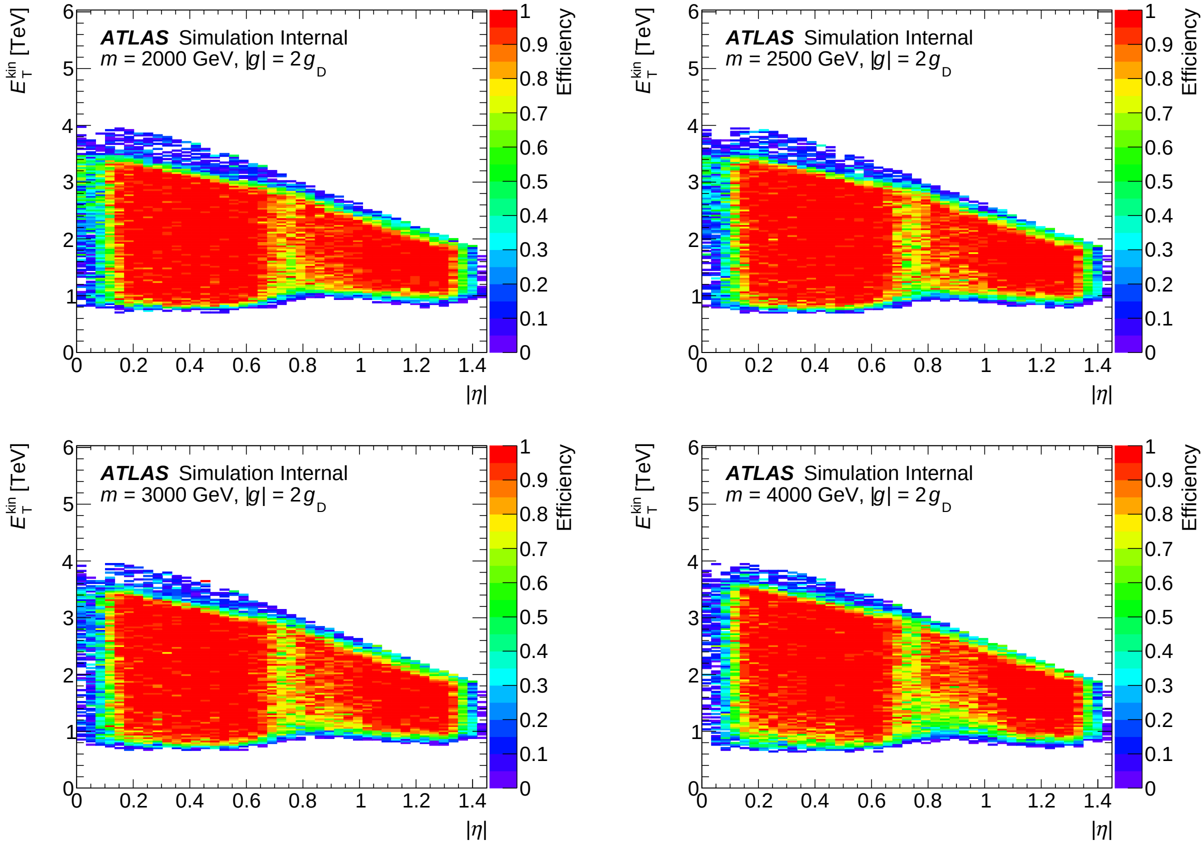

Figure C.3 continued.

C.3 HECO $|z|$=20

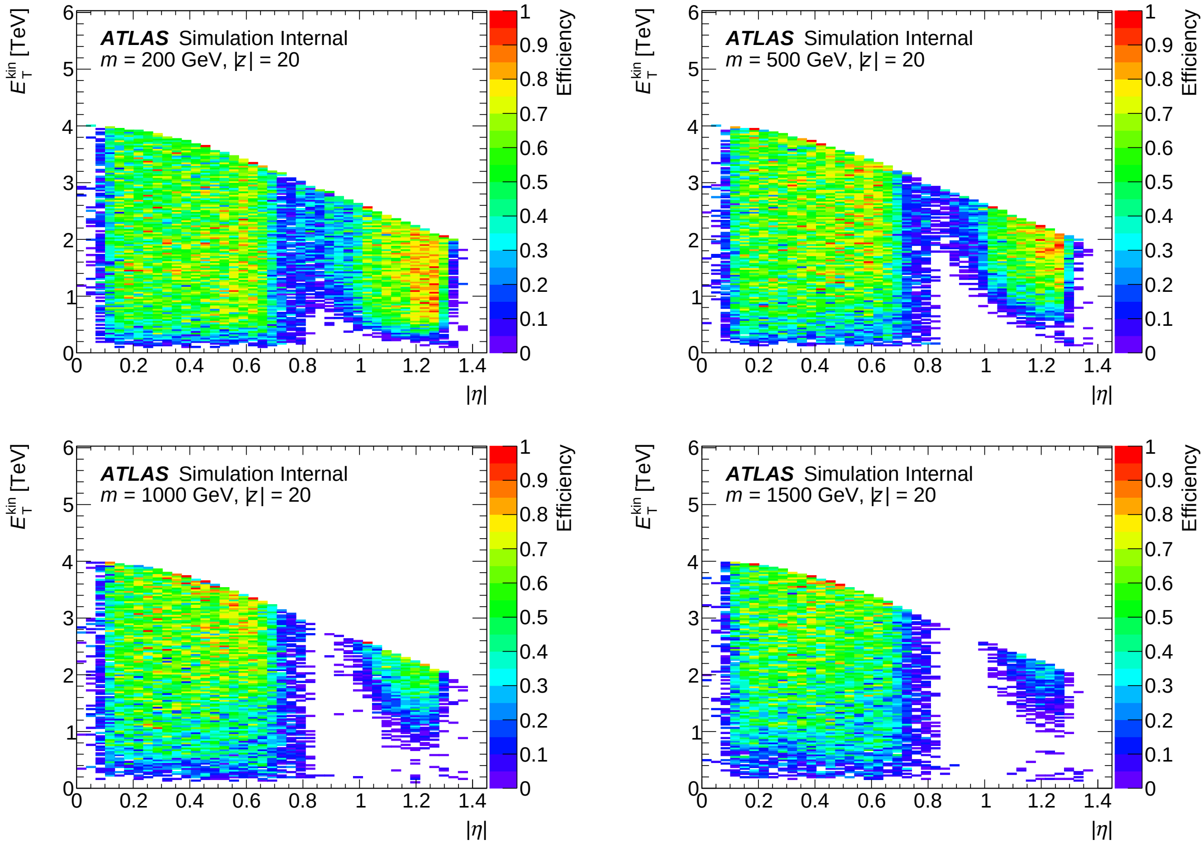

Figure C.5: Selection efficiency as a function of transverse kinetic energy $E_{\mathrm{T}}^{\mathrm{kin}}$ and pseudorapidity η for HECOs of charge $|z| = 20$.

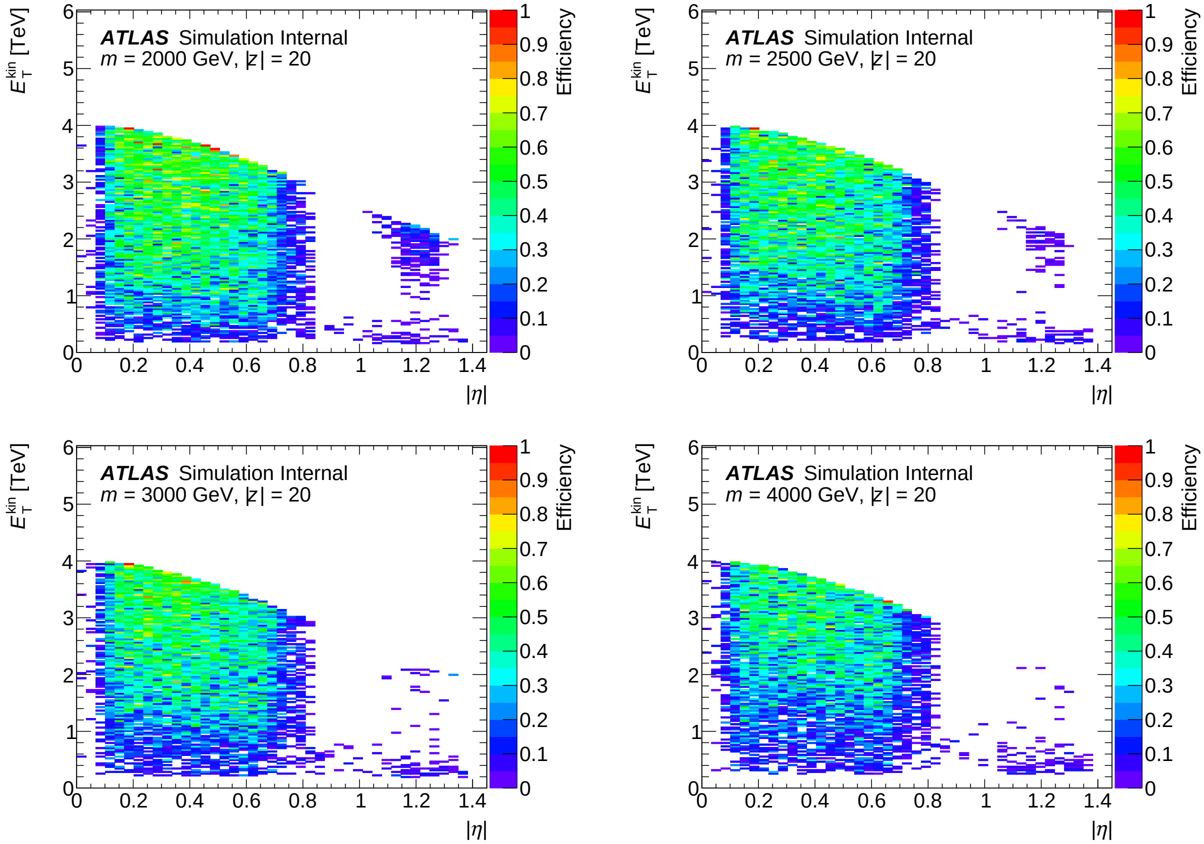

Figure C.5 continued.

C.4 HECO |z|=40

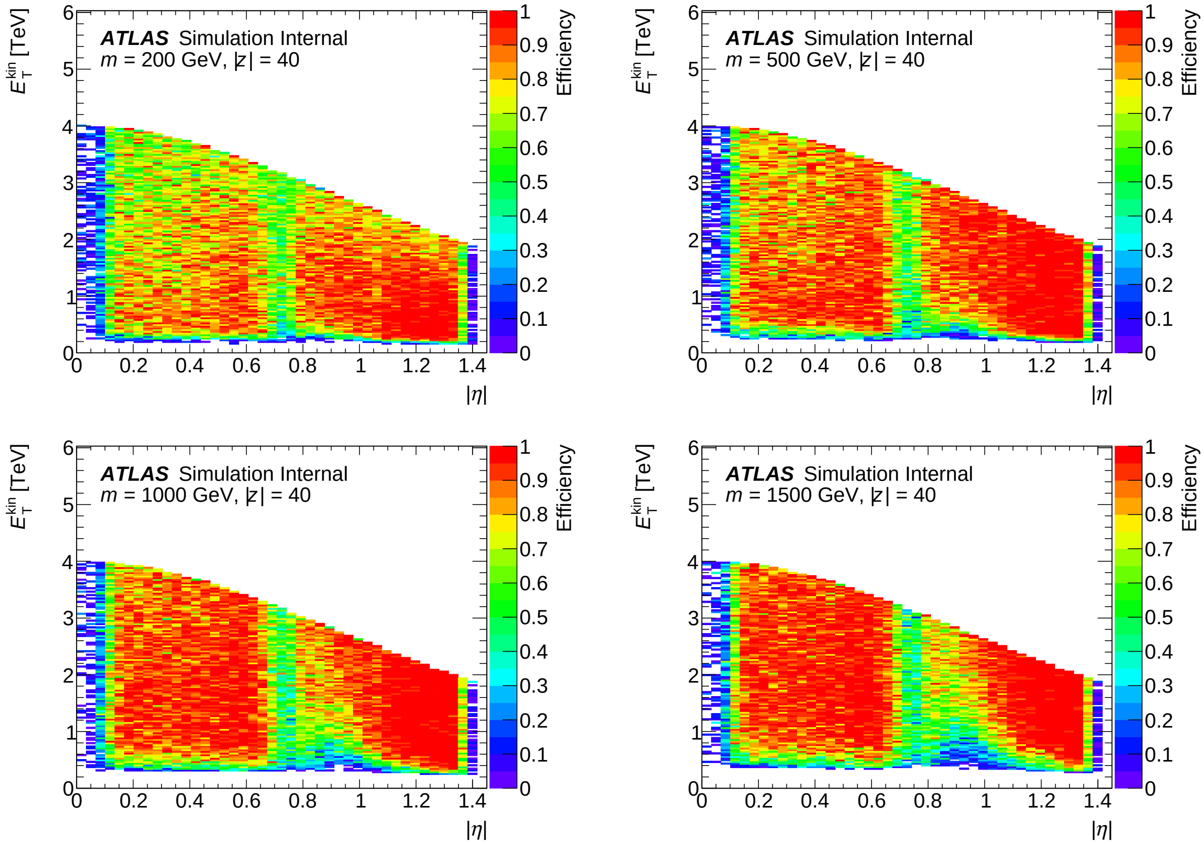

Figure C.7: Selection efficiency as a function of transverse kinetic energy $E_{\mathrm{T}}^{\mathrm{kin}}$ and pseudorapidity η for HECOs of charge $|z| = 40$.

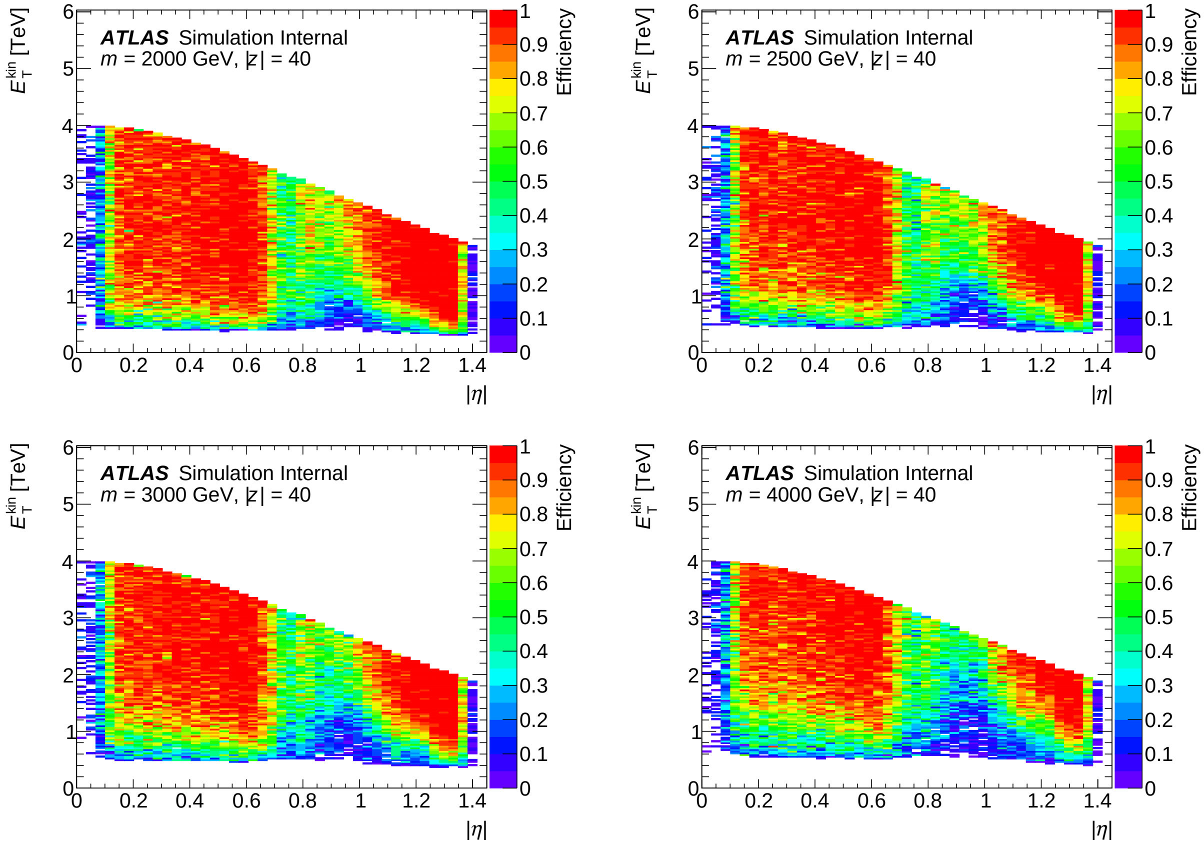

Figure C.7 continued.

C.5 HECO |z|=60

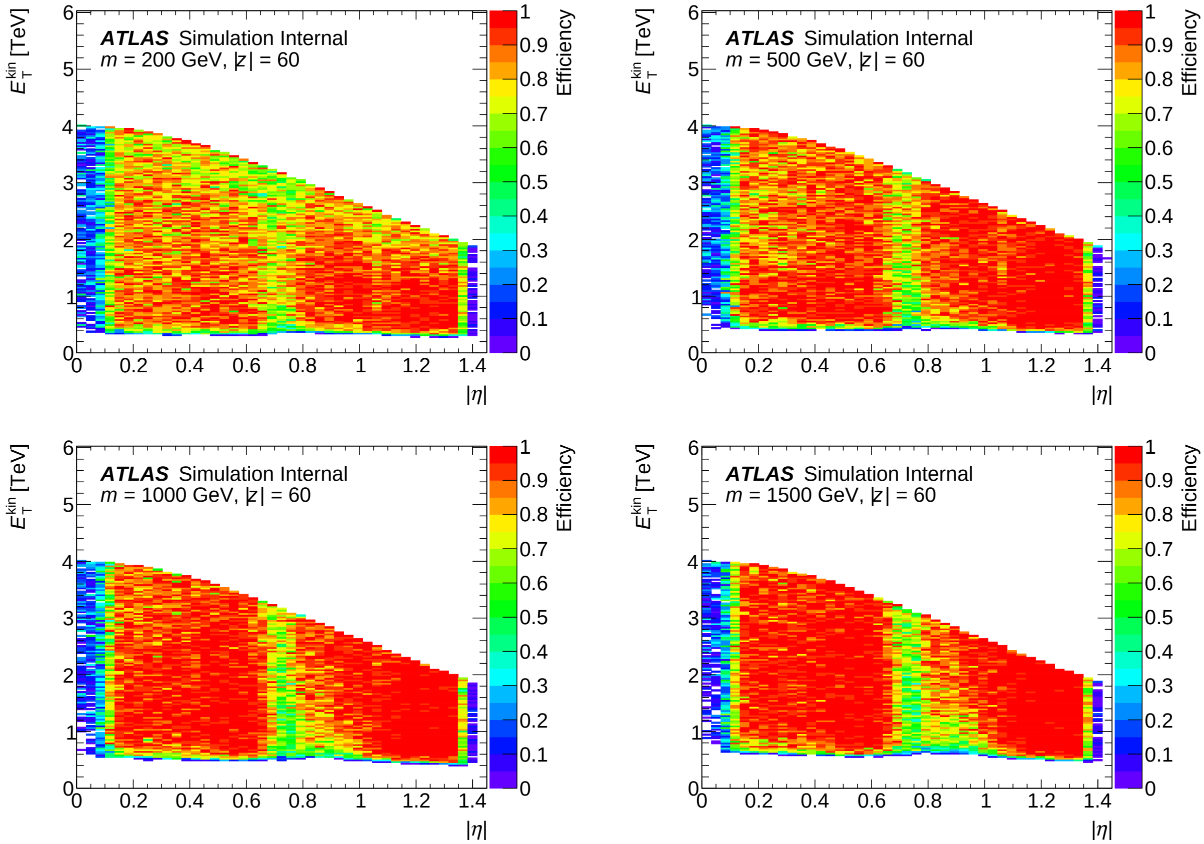

Figure C.9: Selection efficiency as a function of transverse kinetic energy $E_{\mathrm{T}}^{\mathrm{kin}}$ and pseudorapidity η for HECOs of charge $|z| = 60$.

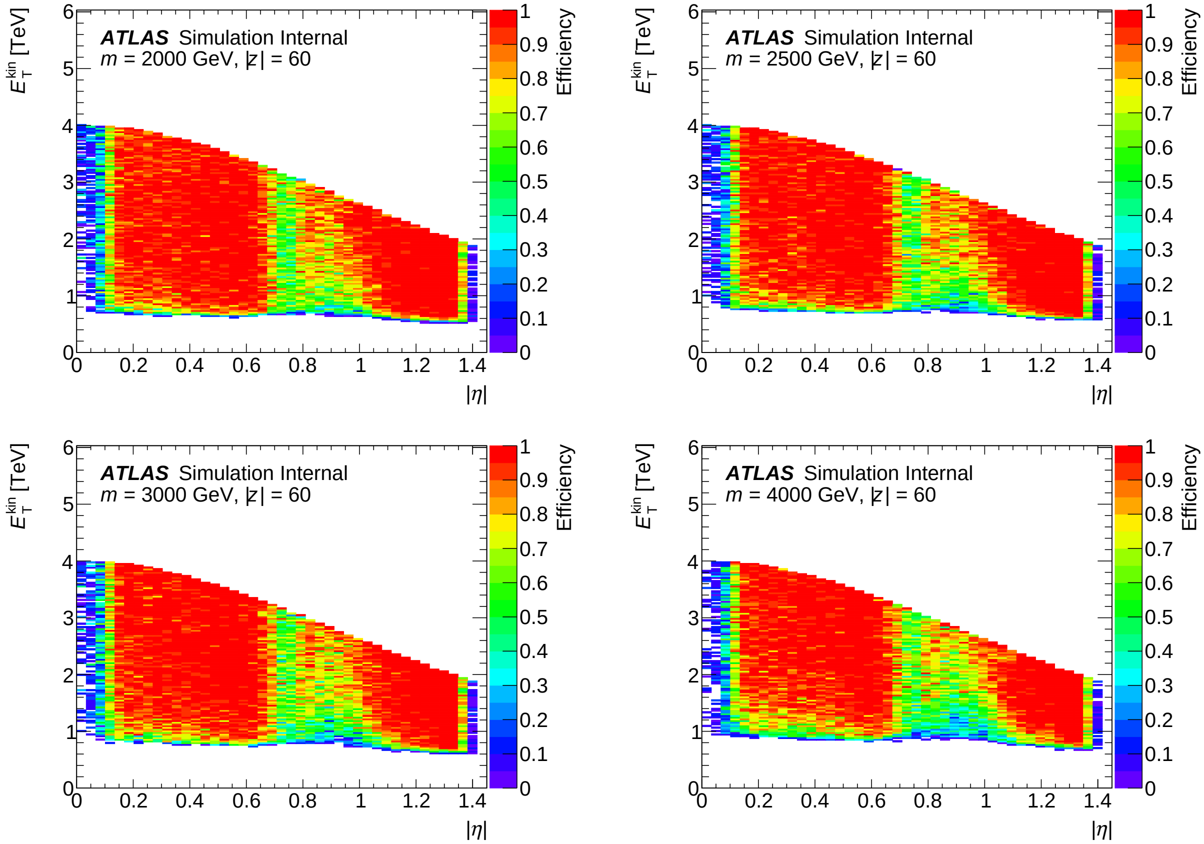

Figure C.9 continued.

C.6 HECO |z|=80

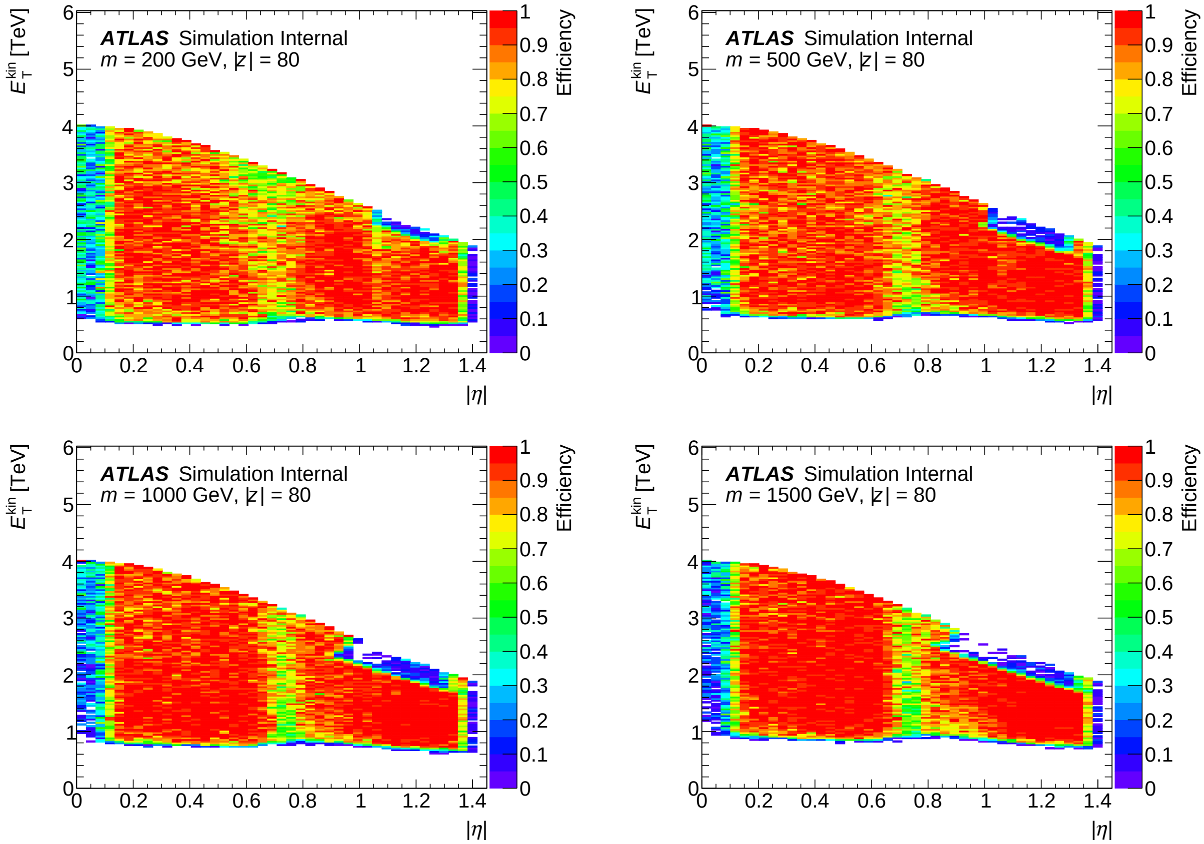

Figure C.11: Selection efficiency as a function of transverse kinetic energy $E_{\mathrm{T}}^{\mathrm{kin}}$ and pseudorapidity η for HECOs of charge $|z| = 80$.

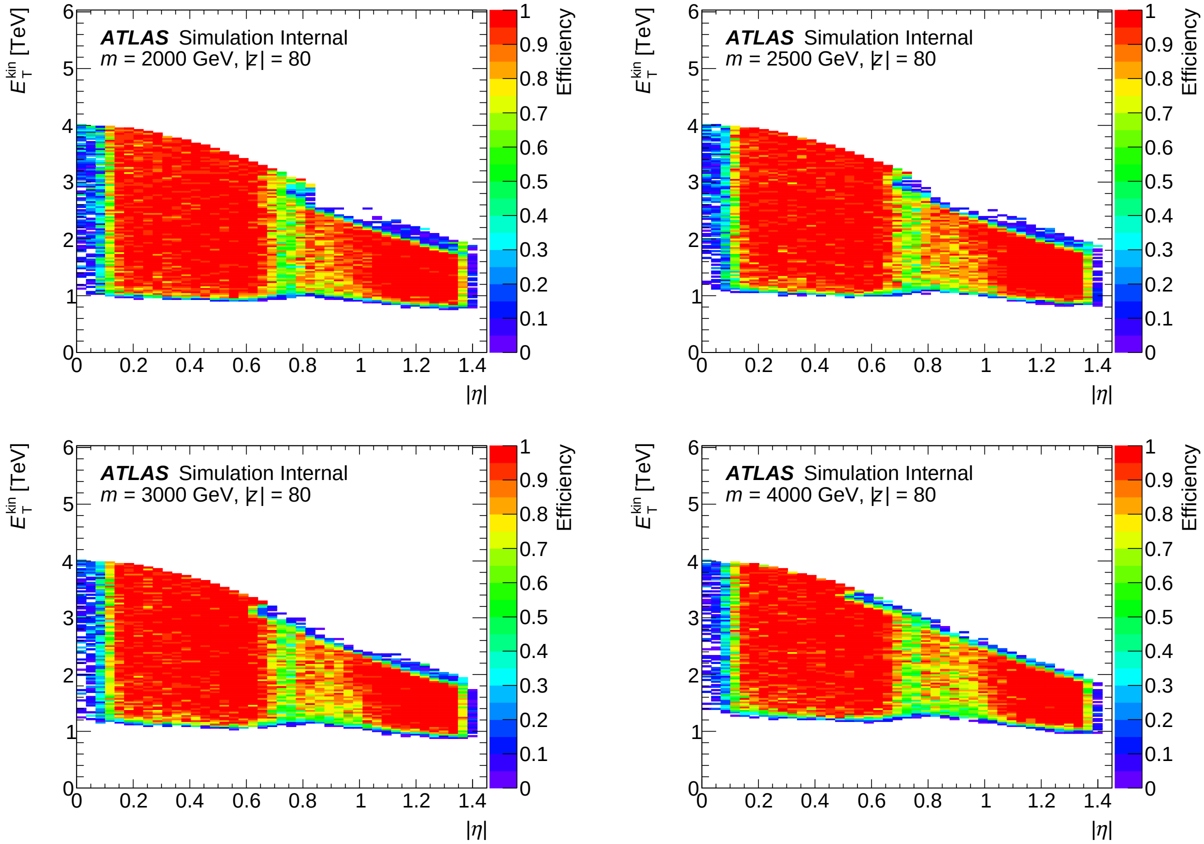

Figure C.11 continued.

C.7 HECO |z|=100

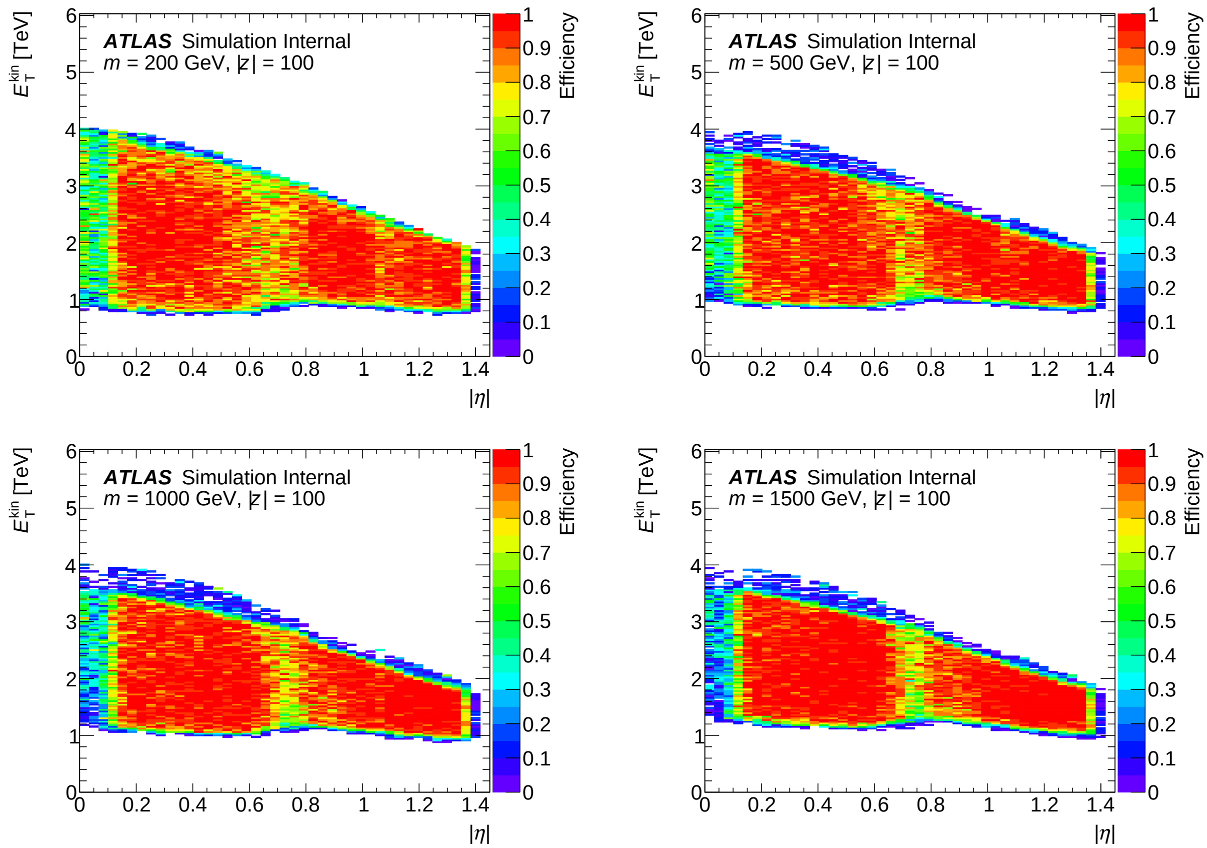

Figure C.13: Selection efficiency as a function of transverse kinetic energy $E_{\mathrm{T}}^{\mathrm{kin}}$ and pseudorapidity η for HECOs of charge $|z| = 100$.

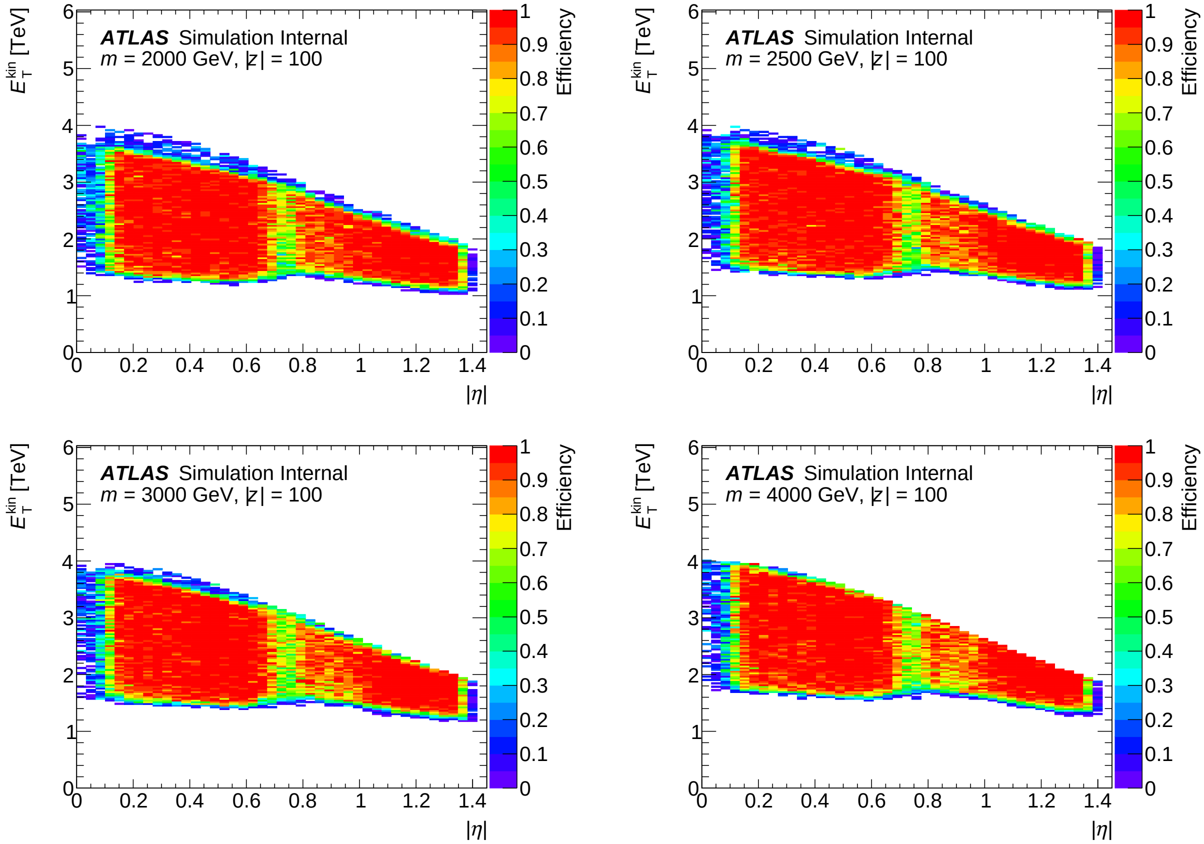

Figure C.13 continued.

APPENDIX D

Receiver operating characteristic curves for f_{HT} and w

Figures D.1–D.2 illustrate ROC curves for the f_{HT} and w variables for a pseudodata background sample and the Drell-Yan spin-½ for all mass and charge combinations signal samples. Further details can be found in Section 5.2.3.

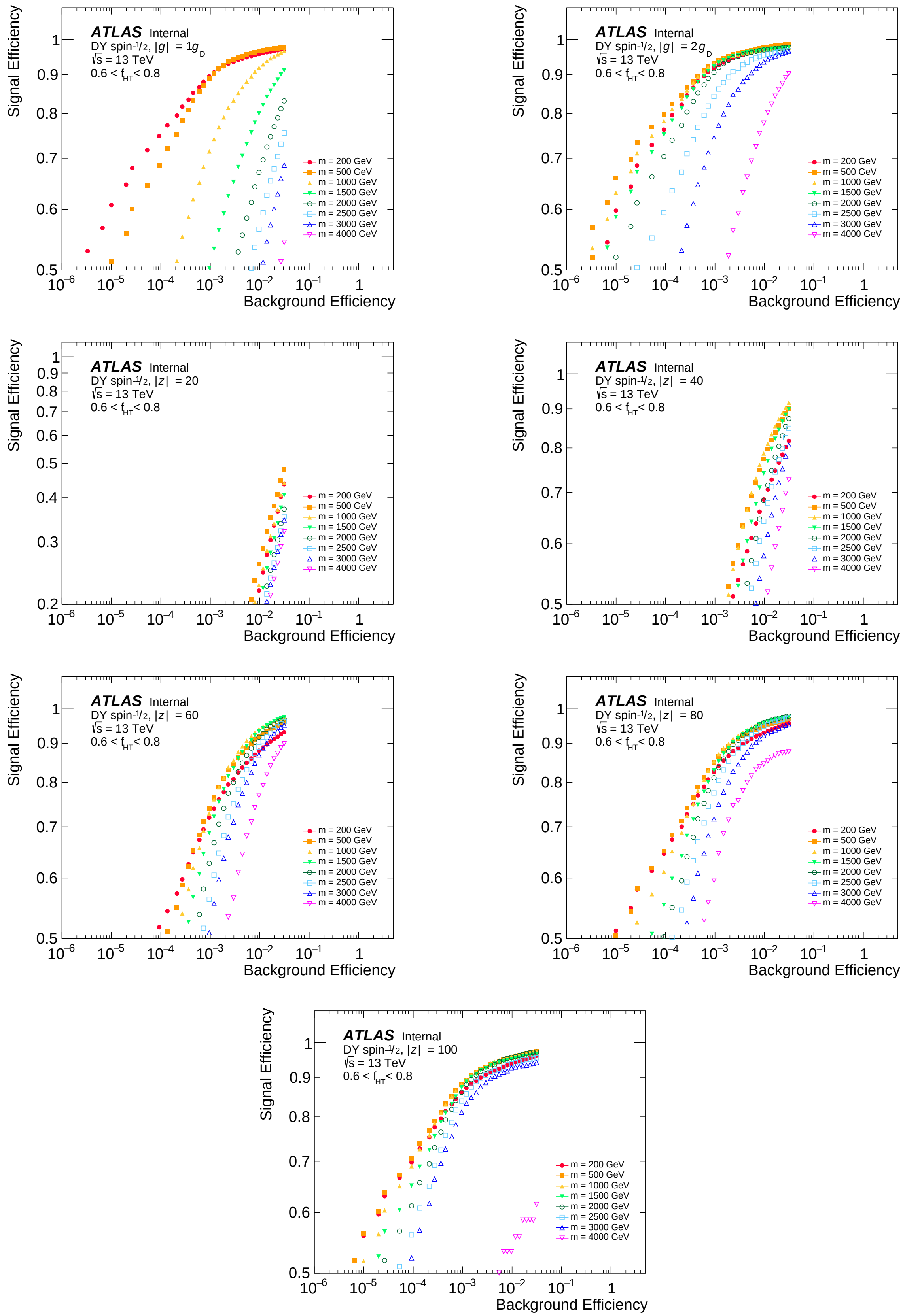

Figure D.1: ROC curves of f_{HT} for cuts in $0.6 < f_{\mathrm{HT}} < 0.8$ DY spin-½ $1g_{\mathrm{D}}$ and $2g_{\mathrm{D}}$ magnetic monopoles (top) and $|z|$= 20, 40, 60, 80 and 100 HECOs for all masses.

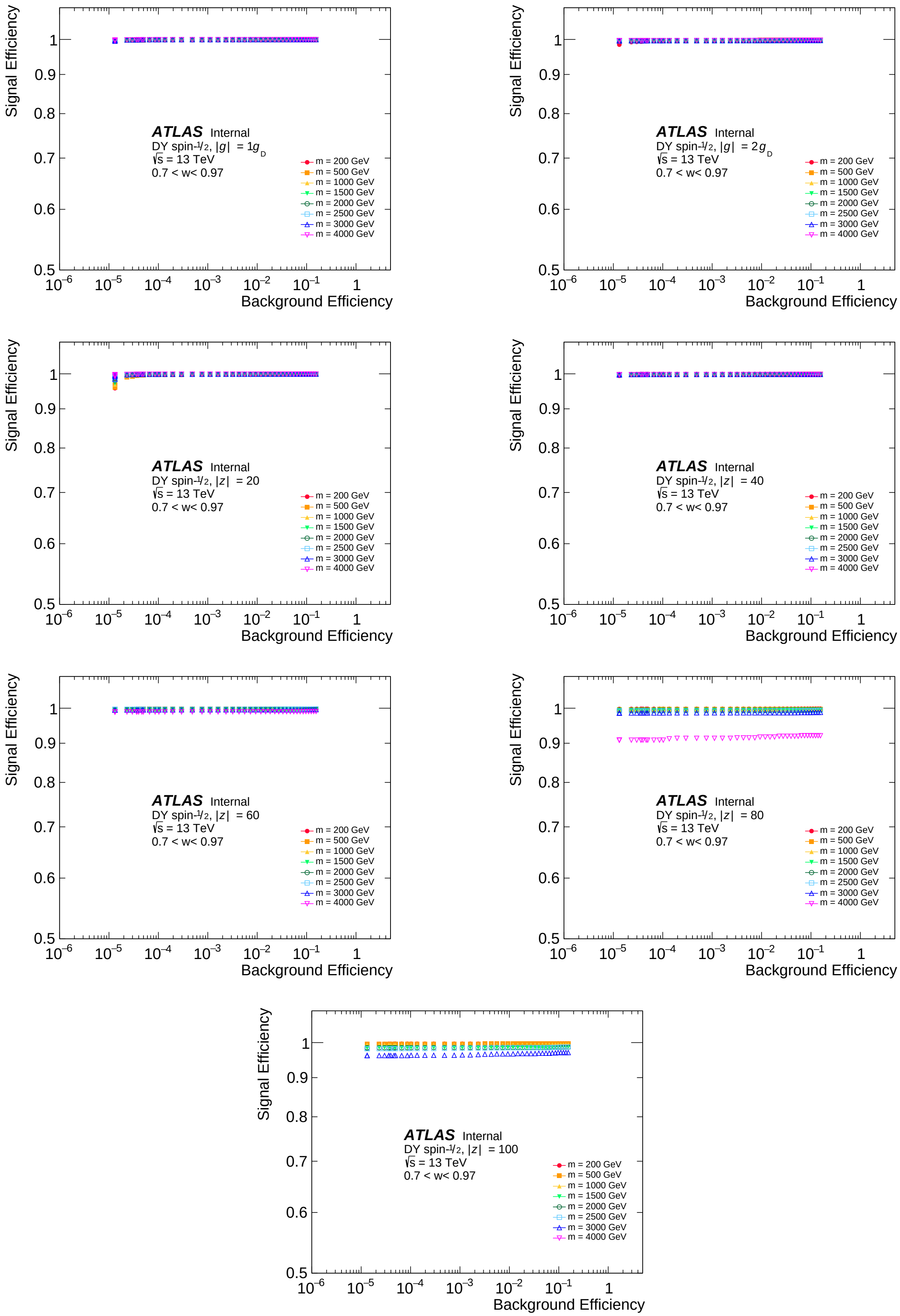

Figure D.2: ROC curves of w for cuts in $0.7 < w < 0.97$ for DY spin-½ $1g_{\mathrm{D}}$ and $2g_{\mathrm{D}}$ magnetic monopoles (top) and $|z|$= 20, 40, 60, 80 and 100 HECOs for all masses.

APPENDIX E

Total signal selection efficiencies

Table E.1 contains the signal selection efficiencies for all signal samples considered in this thesis. The statistical uncertainty is the binomial error. Efficiencies for alternative production mechanisms, DY spin-0 and PF spin-0 and spin-½, are computed through extrapolation. The rightmost column has a count of the events in the sample used to compute the efficiencies.

Mech.	**S**	$\|g\|$, $\|z\|$ [g_D, e]	**Mass [GeV]**	**efficiency %**	**± uncertainty %**	**event counts**
DY	0	1	200	7.94	0.06	50000
DY	0	1	500	33.0	0.2	50000
DY	0	1	1000	52.3	0.2	50000
DY	0	1	1500	54.0	0.2	50000
DY	0	1	2000	49.1	0.2	50000

Continued on next page

Table E.1: Signal selection efficiency for Drell-Yan (DY) and Photon Fusion (PF) production mechanisms. The *event count* column indicates the number of events used in the fully simulated or generator level pair production signal samples.

Mech.	S	$\|g\|$, $\|z\|$ [$g_{\mathbf{D}}$, e]	Mass [GeV]	efficiency %	$\pm$ uncertainty %	event counts
DY	0	1	2500	43.1	0.2	50000
DY	0	1	3000	37.8	0.2	50000
DY	0	1	4000	22.9	0.2	50000
DY	0	2	200	0.0281	0.0002	50000
DY	0	2	500	0.591	0.003	50000
DY	0	2	1000	3.47	0.02	50000
DY	0	2	1500	7.09	0.04	50000
DY	0	2	2000	9.93	0.07	50000
DY	0	2	2500	12.38	0.08	50000
DY	0	2	3000	14.32	0.09	50000
DY	0	2	4000	9.02	0.07	50000
DY	0	20	200	6.4	0.1	50000
DY	0	20	500	13.2	0.1	50000
DY	0	20	1000	16.6	0.2	50000
DY	0	20	1500	15.4	0.2	50000
DY	0	20	2000	13.9	0.2	50000
DY	0	20	2500	11.7	0.1	50000
DY	0	20	3000	11.1	0.1	50000
DY	0	20	4000	7.8	0.1	50000
DY	0	40	200	14.1	0.1	50000
DY	0	40	500	32.1	0.2	50000
DY	0	40	1000	39.8	0.2	50000
DY	0	40	1500	38.0	0.2	50000
DY	0	40	2000	33.8	0.2	50000
DY	0	40	2500	28.3	0.2	50000

Continued on next page

Table E.1: Signal selection efficiency for Drell-Yan (DY) and Photon Fusion (PF) production mechanisms. The *event count* column indicates the number of events used in the fully simulated or generator level pair production signal samples.

Mech.	**S**	$\|g\|$, $\|z\|$ [$g_{\mathbf{D}}$, **e**]	**Mass** [**GeV**]	**efficiency %**	**± uncertainty %**	**event counts**
DY	0	40	3000	24.7	0.2	50000
DY	0	40	4000	12.9	0.1	50000
DY	0	60	200	5.74	0.05	50000
DY	0	60	500	17.4	0.1	50000
DY	0	60	1000	24.3	0.1	50000
DY	0	60	1500	23.2	0.1	50000
DY	0	60	2000	20.4	0.1	50000
DY	0	60	2500	17.0	0.1	50000
DY	0	60	3000	13.7	0.1	50000
DY	0	60	4000	3.77	0.06	50000
DY	0	80	200	1.213	0.007	50000
DY	0	80	500	5.78	0.04	50000
DY	0	80	1000	9.11	0.07	50000
DY	0	80	1500	8.57	0.07	50000
DY	0	80	2000	7.01	0.07	50000
DY	0	80	2500	5.69	0.06	50000
DY	0	80	3000	3.96	0.05	50000
DY	0	80	4000	0.3	0.01	50000
DY	0	100	200	0.224	0.002	50000
DY	0	100	500	1.38	0.01	50000
DY	0	100	1000	2.48	0.02	50000
DY	0	100	1500	2.31	0.03	50000
DY	0	100	2000	1.7	0.02	50000
DY	0	100	2500	1.25	0.02	50000
DY	0	100	3000	0.69	0.01	50000

Continued on next page

Table E.1: Signal selection efficiency for Drell-Yan (DY) and Photon Fusion (PF) production mechanisms. The *event count* column indicates the number of events used in the fully simulated or generator level pair production signal samples.

Mech.	**S**	$\|g\|$, $\|z\|$ $[g_\mathbf{D}$, **e**]	**Mass** [**GeV**]	**efficiency %**	**± uncertainty %**	**event counts**
DY	0	100	4000	0.0026	0.0006	50000
DY	½	1	200	2.3	0.01	79999
DY	½	1	500	12.38	0.06	79999
DY	½	1	1000	23.7	0.1	79999
DY	½	1	1500	25.1	0.1	79999
DY	½	1	2000	22.1	0.1	79999
DY	½	1	2500	18.6	0.1	79999
DY	½	1	3000	15.9	0.1	79999
DY	½	1	4000	7.86	0.07	79999
DY	½	2	200	0.00585	3×10^{-5}	79799
DY	½	2	500	0.1218	0.0006	79899
DY	½	2	1000	0.776	0.004	79999
DY	½	2	1500	1.668	0.009	79999
DY	½	2	2000	2.49	0.02	80143
DY	½	2	2500	3.15	0.02	80143
DY	½	2	3000	3.67	0.02	79999
DY	½	2	4000	2.29	0.02	79999
DY	½	20	200	2.24	0.04	79999
DY	½	20	500	5.51	0.07	80143
DY	½	20	1000	6.67	0.08	79999
DY	½	20	1500	6.35	0.07	79999
DY	½	20	2000	5.46	0.07	79999
DY	½	20	2500	4.89	0.06	79999
DY	½	20	3000	4.46	0.06	79999
DY	½	20	4000	3.25	0.05	79999

Continued on next page

Table E.1: Signal selection efficiency for Drell-Yan (DY) and Photon Fusion (PF) production mechanisms. The *event count* column indicates the number of events used in the fully simulated or generator level pair production signal samples.

Mech.	**S**	$\lvert g \rvert$, $\lvert z \rvert$ [$g_{\mathbf{D}}$, **e**]	**Mass [GeV]**	**efficiency %**	**± uncertainty %**	**event counts**
DY	½	40	200	4.68	0.04	79999
DY	½	40	500	12.93	0.08	79999
DY	½	40	1000	17.16	0.09	79999
DY	½	40	1500	15.86	0.08	79999
DY	½	40	2000	12.9	0.08	79999
DY	½	40	2500	9.09	0.06	79999
DY	½	40	3000	8.41	0.06	79999
DY	½	40	4000	3.71	0.04	79999
DY	½	60	200	1.61	0.01	80143
DY	½	60	500	5.32	0.03	79999
DY	½	60	1000	8.36	0.05	79999
DY	½	60	1500	7.81	0.05	79999
DY	½	60	2000	6.51	0.04	79999
DY	½	60	2500	5.16	0.04	79999
DY	½	60	3000	4.0	0.03	79999
DY	½	60	4000	0.8	0.01	79999
DY	½	80	200	0.288	0.001	79999
DY	½	80	500	1.44	0.009	79999
DY	½	80	1000	2.48	0.02	80143
DY	½	80	1500	2.29	0.02	79999
DY	½	80	2000	1.81	0.02	79999
DY	½	80	2500	1.29	0.01	79999
DY	½	80	3000	0.88	0.01	79999
DY	½	80	4000	0.048	0.002	79999
DY	½	100	200	0.0513	0.0005	29999

Continued on next page

Table E.1: Signal selection efficiency for Drell-Yan (DY) and Photon Fusion (PF) production mechanisms. The *event count* column indicates the number of events used in the fully simulated or generator level pair production signal samples.

Mech.	**S**	**$\|g\|$, $\|z\|$ [$g_{\mathbf{D}}$, e]**	**Mass [GeV]**	**efficiency %**	**± uncertainty %**	**event counts**
DY	½	100	500	0.309	0.003	29999
DY	½	100	1000	0.577	0.007	29999
DY	½	100	1500	0.505	0.008	29999
DY	½	100	2000	0.352	0.006	29999
DY	½	100	2500	0.247	0.005	29999
DY	½	100	3000	0.119	0.004	29999
DY	½	100	4000	0.0006	0.0002	29999
PF	0	1	200	4.63	0.0315	50000
PF	0	1	500	14.18	0.0794	50000
PF	0	1	1000	21.99	0.1205	50000
PF	0	1	1500	22.58	0.1309	50000
PF	0	1	2000	19.96	0.1386	50000
PF	0	1	2500	15.81	0.1247	50000
PF	0	1	3000	11.92	0.1078	50000
PF	0	1	4000	6.01	0.0703	50000
PF	0	2	200	0.02	0.0001	50000
PF	0	2	500	0.3	0.0017	50000
PF	0	2	1000	1.22	0.0076	50000
PF	0	2	1500	1.98	0.0129	50000
PF	0	2	2000	2.34	0.0186	50000
PF	0	2	2500	2.33	0.0196	50000
PF	0	2	3000	1.99	0.018	50000
PF	0	2	4000	0.67	0.0084	50000
PF	0	20	200	4.3	0.0693	50000
PF	0	20	500	6.83	0.0897	50000

Continued on next page

Table E.1: Signal selection efficiency for Drell-Yan (DY) and Photon Fusion (PF) production mechanisms. The *event count* column indicates the number of events used in the fully simulated or generator level pair production signal samples.

Mech.	**S**	$\|g\|$, $\|z\|$ [$g_\mathbf{D}$, **e**]	**Mass [GeV]**	**efficiency %**	**± uncertainty %**	**event counts**
PF	0	20	1000	7.26	0.0975	50000
PF	0	20	1500	6.36	0.0922	50000
PF	0	20	2000	5.5	0.0852	50000
PF	0	20	2500	4.45	0.0756	50000
PF	0	20	3000	4.09	0.0705	50000
PF	0	20	4000	2.13	0.0427	50000
PF	0	40	200	7.84	0.0599	50000
PF	0	40	500	14.15	0.0997	50000
PF	0	40	1000	16.02	0.1067	50000
PF	0	40	1500	14.3	0.0976	50000
PF	0	40	2000	11.74	0.0933	50000
PF	0	40	2500	9.92	0.0866	50000
PF	0	40	3000	5.51	0.059	50000
PF	0	40	4000	1.48	0.027	50000
PF	0	60	200	3.35	0.027	50000
PF	0	60	500	7.05	0.0466	50000
PF	0	60	1000	8.27	0.059	50000
PF	0	60	1500	7.23	0.0561	50000
PF	0	60	2000	5.63	0.0478	50000
PF	0	60	2500	3.77	0.0361	50000
PF	0	60	3000	1.9	0.0256	50000
PF	0	60	4000	0.18	0.0058	50000
PF	0	80	200	0.72	0.0042	50000
PF	0	80	500	2.43	0.018	50000
PF	0	80	1000	3.15	0.0232	50000

Continued on next page

Table E.1: Signal selection efficiency for Drell-Yan (DY) and Photon Fusion (PF) production mechanisms. The *event count* column indicates the number of events used in the fully simulated or generator level pair production signal samples.

Mech.	**S**	$\|g\|$, $\|z\|$ [g_D, e]	**Mass** [GeV]	**efficiency %**	**± uncertainty %**	**event counts**
PF	0	80	1500	2.53	0.0225	50000
PF	0	80	2000	1.59	0.0176	50000
PF	0	80	2500	0.76	0.0113	50000
PF	0	80	3000	0.28	0.0059	50000
PF	0	80	4000	0.01	0.0006	50000
PF	0	100	200	0.14	0.001	50000
PF	0	100	500	0.65	0.0049	50000
PF	0	100	1000	0.89	0.0076	50000
PF	0	100	1500	0.65	0.0074	50000
PF	0	100	2000	0.32	0.0045	50000
PF	0	100	2500	0.12	0.0025	50000
PF	0	100	3000	0.03	0.001	50000
PF	0	100	4000	0	0	50000
PF	½	1	200	3.54	0.0266	50000
PF	½	1	500	17.16	0.0985	50000
PF	½	1	1000	30.6	0.1541	50000
PF	½	1	1500	31.93	0.1642	50000
PF	½	1	2000	29.1	0.1714	50000
PF	½	1	2500	23.43	0.1572	50000
PF	½	1	3000	17.2	0.1357	50000
PF	½	1	4000	8.39	0.0889	50000
PF	½	2	200	0.01	0.0001	50000
PF	½	2	500	0.19	0.0011	50000
PF	½	2	1000	1.29	0.0083	50000
PF	½	2	1500	2.91	0.0191	50000

Continued on next page

Table E.1: Signal selection efficiency for Drell-Yan (DY) and Photon Fusion (PF) production mechanisms. The *event count* column indicates the number of events used in the fully simulated or generator level pair production signal samples.

Mech.	**S**	$\lvert g \rvert$, $\lvert z \rvert$ [g_D, e]	**Mass** [GeV]	**efficiency %**	**± uncertainty %**	**event counts**
PF	½	2	2000	3.97	0.0309	50000
PF	½	2	2500	4.29	0.034	50000
PF	½	2	3000	3.66	0.0309	50000
PF	½	2	4000	1.22	0.0142	50000
PF	½	40	4000	2.49	0.0396	50000
PF	½	60	200	2.5	0.0225	50000
PF	½	60	500	7.72	0.0543	50000
PF	½	60	1000	11.73	0.0825	50000
PF	½	60	1500	11.59	0.0842	50000
PF	½	60	2000	9.74	0.0751	50000
PF	½	60	2500	6.6	0.058	50000
PF	½	60	3000	3.52	0.042	50000
PF	½	60	4000	0.34	0.0097	50000
PF	½	80	200	0.42	0.0025	50000
PF	½	80	500	2.18	0.0174	50000
PF	½	80	1000	3.95	0.0304	50000
PF	½	80	1500	3.97	0.035	50000
PF	½	80	2000	2.69	0.0291	50000
PF	½	80	2500	1.56	0.0208	50000
PF	½	80	3000	0.62	0.0114	50000
PF	½	80	4000	0.02	0.0012	50000
PF	½	100	200	0.08	0.0005	50000
PF	½	100	500	0.49	0.0038	50000
PF	½	100	1000	0.98	0.0088	50000
PF	½	100	1500	0.9	0.0107	50000

Continued on next page

Table E.1: Signal selection efficiency for Drell-Yan (DY) and Photon Fusion (PF) production mechanisms. The *event count* column indicates the number of events used in the fully simulated or generator level pair production signal samples.

Mech.	**S**	$\|g\|$, $\|z\|$ [$g_\mathbf{D}$, **e**]	**Mass** [**GeV**]	**efficiency %**	**± uncertainty %**	**event counts**
PF	½	100	2000	0.53	0.0075	50000
PF	½	100	2500	0.21	0.0045	50000
PF	½	100	3000	0.05	0.0019	50000
PF	½	100	4000	0	0	50000

Table E.1: Signal selection efficiency for Drell-Yan (DY) and Photon Fusion (PF) production mechanisms. The *event count* column indicates the number of events used in the fully simulated or generator level pair production signal samples.

APPENDIX F

Signal Selection Efficiency Cut Flow

Table F.1 contains the values, in percentages, for the signal selection efficiency as the criteria for selection is applied on the Drell-Yan spin-½ MC signal samples for all mass and charge combinations considered.

$\lvert g\rvert$, $\lvert z\rvert$ [g_{D}, e]	Mass [GeV]	p_{T} eff.	L1	HLT	Pres.	w	f_{HT}
1	200	7.74	4.55	3.02	2.41	2.41	2.3
1	500	26.6	19.3	15.7	12.9	12.9	12.4
1	1000	46.8	36.1	30.9	26.5	26.4	23.7
1	1500	53.4	42.5	37.5	33.0	33.0	25.1
1	2000	63.9	47.9	40.7	35.9	35.8	22.1
1	2500	62.3	47.6	40.8	36.8	36.7	18.6

Continued on next page

Table F.1: Cut flow of the selection efficiency (in percentages) for fully simulated Drell-Yan spin-½ samples of all considered masses and charges.

$\lvert g \rvert$, $\lvert z \rvert$ [g_{D}, e]	Mass [GeV]	p_{T} eff.	L1	HLT	Pres.	w	f_{HT}
1	3000	60.3	47.4	40.7	37.3	37.2	15.9
1	4000	48.26	35.7	28.83	27.85	27.82	7.86
2	200	0.013	0.007	0.006	0.006	0.006	0.006
2	500	0.22	0.14	0.13	0.13	0.13	0.12
2	1000	1.68	0.93	0.82	0.81	0.8	0.78
2	1500	4.0	2.06	1.76	1.73	1.72	1.67
2	2000	8.2	3.4	2.64	2.58	2.57	2.49
2	2500	10.19	4.35	3.4	3.34	3.32	3.15
2	3000	11.98	5.18	4.06	4.0	3.99	3.67
2	4000	11.25	4.2	3.19	3.15	3.14	2.29
20	200	61.59	24.86	17.35	12.91	12.82	2.24
20	500	67.38	42.88	32.72	26.44	26.24	5.51
20	1000	74.79	54.87	42.55	36.66	36.47	6.67
20	1500	75.11	58.85	46.1	40.84	40.65	6.35
20	2000	73.11	57.67	44.61	40.08	39.93	5.46
20	2500	70.42	54.99	42.1	38.48	38.37	4.89
20	3000	67.86	52.71	39.9	36.61	36.52	4.46
20	4000	54.88	42.41	30.63	29.13	29.08	3.25
40	200	22.21	15.6	10.67	7.32	7.31	4.68
40	500	44.3	31.6	23.9	17.9	17.8	12.9
40	1000	46.8	34.8	29.0	23.4	23.3	17.2
40	1500	43.0	31.7	27.3	23.3	23.3	15.9
40	2000	45.7	30.0	24.7	21.0	21.0	12.9
40	2500	38.7	23.1	18.5	15.9	15.9	9.1
40	3000	39.11	23.24	18.44	16.58	16.54	8.41

Continued on next page

Table F.1: Cut flow of the selection efficiency (in percentages) for fully simulated Drell-Yan spin-½ samples of all considered masses and charges.

$\lvert g\rvert$, $\lvert z\rvert$ [g_{D}, e]	Mass [GeV]	p_{T} eff.	L1	HLT	Pres.	w	f_{HT}
40	4000	36.27	13.89	9.37	9.05	9.03	3.71
60	200	7.66	4.36	2.71	1.87	1.87	1.61
60	500	15.48	9.72	7.81	5.92	5.9	5.32
60	1000	25.13	14.05	11.25	9.09	9.07	8.36
60	1500	26.2	13.07	10.19	8.59	8.57	7.81
60	2000	23.99	10.98	8.25	7.33	7.31	6.51
60	2500	21.02	9.03	6.57	6.02	6.0	5.16
60	3000	22.81	8.06	5.13	4.84	4.81	4.0
60	4000	17.47	3.21	1.15	1.12	1.11	0.8
80	200	0.54	0.39	0.36	0.31	0.31	0.29
80	500	5.05	2.43	1.92	1.53	1.53	1.44
80	1000	8.4	3.84	3.03	2.62	2.61	2.48
80	1500	10.85	4.0	2.72	2.42	2.41	2.29
80	2000	10.92	3.43	2.07	1.91	1.9	1.81
80	2500	10.18	2.81	1.45	1.38	1.37	1.29
80	3000	9.47	2.3	1.01	0.97	0.96	0.88
80	4000	6.833	0.831	0.062	0.058	0.053	0.048
100	200	0.13	0.07	0.06	0.06	0.06	0.05
100	500	0.99	0.45	0.37	0.33	0.33	0.31
100	1000	2.54	0.93	0.66	0.61	0.6	0.58
100	1500	3.98	1.09	0.58	0.54	0.53	0.5
100	2000	3.23	0.82	0.39	0.37	0.37	0.35
100	2500	3.38	0.76	0.28	0.27	0.26	0.25
100	3000	3.39	0.62	0.14	0.13	0.13	0.12

100	4000	1.505	0.15	0.003	0.002	0.001	0.001

Table F.1: Cut flow of the selection efficiency (in percentages) for fully simulated Drell-Yan spin-½ samples of all considered masses and charges.

APPENDIX G

Total signal selection systematic uncertainties

Values for all sources of systematic uncertainties are consigned in Tables G.1–G.28 as relative percentages of the signal selection efficiency, for all production modes, masses and charges considered.

G.0.1 Drell-Yan spin-1/2

G.0.2 Photon fusion spin-0

G.0.3 Photon fusion spin-1/2

Drell-Yan Spin-0 $1g_{\mathrm{D}}$	eff.	Material	Birks Law	δ-ray prod.	TRT Occ.	Calo Arrival	Extrap	Pileup w. Up	Pileup w. Down	Total Up	Total Down
200 GeV	8	-3 ± 1	12 ± 0	5 ± 0	-2 ± 0	0 ± 0	-1 ± 0	0 ± 0	0 ± 0	13	11
500 GeV	33	-3 ± 1	6 ± 0	0 ± 0	-2 ± 0	0 ± 0	-2 ± 0	0 ± 0	0 ± 0	7	5
1000 GeV	52	-3 ± 1	5 ± 0	-1 ± 0	-1 ± 0	0 ± 0	-1 ± 0	-1 ± 0	1 ± 0	6	3
1500 GeV	54	-3 ± 1	5 ± 0	1 ± 0	0 ± 0	-2 ± 0	0 ± 0	-1 ± 0	1 ± 0	6	3
2000 GeV	49	-3 ± 1	5 ± 0	-1 ± 0	1 ± 0	-4 ± 0	1 ± 0	-2 ± 0	2 ± 0	5	0
2500 GeV	43	-3 ± 1	5 ± 0	1 ± 0	2 ± 0	-5 ± 0	0 ± 0	-2 ± 0	2 ± 0	4	-3
3000 GeV	38	-3 ± 1	5 ± 0	4 ± 0	2 ± 0	-8 ± 0	2 ± 0	-3 ± 0	2 ± 0	1	-8
4000 GeV	23	-3 ± 1	10 ± 0	0 ± 0	4 ± 0	-12 ± 0	3 ± 0	-4 ± 0	5 ± 0	-2	-8

Table G.1: Relative uncertainties (sys ± stat) on the signal efficiencies in percentages for Drell-Yan spin-0 monopoles of charge $|g| = 1g_{\mathrm{D}}$. The total relative uncertainties are calculated as quadratic sums of the individual relative uncertainties, where the detector-material uncertainty and δ-ray uncertainty are taken as symmetric, as described in the text.

Drell-Yan Spin-0 $2g_D$	eff.	Material	Birks Law	δ-ray prod.	TRT Occ.	Calo Arrival	Extrap	Pileup w. Up	Pileup w. Down	Total Up	Total Down
200 GeV	0	-16 ± 6	5 ± 0	1 ± 0	-2 ± 0	0 ± 0	2 ± 0	0 ± 0	0 ± 0	16	-15
500 GeV	1	-16 ± 6	6 ± 0	-4 ± 0	-2 ± 0	0 ± 0	2 ± 0	0 ± 0	0 ± 0	17	-15
1000 GeV	3	-16 ± 6	5 ± 0	0 ± 0	-2 ± 0	0 ± 0	1 ± 0	0 ± 0	0 ± 0	16	-15
1500 GeV	7	-16 ± 6	5 ± 0	-1 ± 0	-2 ± 0	0 ± 0	2 ± 0	0 ± 0	0 ± 0	16	-15
2000 GeV	10	-16 ± 6	5 ± 0	1 ± 0	-2 ± 0	0 ± 0	1 ± 0	0 ± 0	0 ± 0	16	-15
2500 GeV	12	-16 ± 6	5 ± 0	4 ± 0	-1 ± 0	0 ± 0	0 ± 0	0 ± 0	0 ± 0	17	-15
3000 GeV	14	-16 ± 6	5 ± 0	3 ± 0	-1 ± 0	0 ± 0	0 ± 0	-1 ± 0	1 ± 0	17	-15
4000 GeV	9	-16 ± 6	11 ± 0	2 ± 0	0 ± 0	0 ± 0	2 ± 0	-2 ± 0	1 ± 0	19	-11

Table G.2: Relative uncertainties (sys ± stat) on the signal efficiencies in percentages for Drell-Yan spin-0 monopoles of charge $|g| = 2g_D$. The total relative uncertainties are calculated as quadratic sums of the individual relative uncertainties, where the detector-material uncertainty and the δ-ray uncertainty are taken as symmetric, as described in the text.

Drell-Yan Spin-0 $\lvert z \rvert = 20$	eff.	Material	Birks High	δ-ray prod.	TRT Occ.	Calo Arrival	Extrap	Pileup w. Up	Pileup w. Down	Total Up	Total Down
200 GeV	6	-5 ± 2	11 ± 0	5 ± 0	7 ± 0	0 ± 0	2 ± 0	-4 ± 0	4 ± 0	15	11
500 GeV	13	-5 ± 2	15 ± 0	0 ± 0	6 ± 0	0 ± 0	1 ± 0	-4 ± 0	4 ± 0	17	15
1000 GeV	17	-5 ± 2	7 ± 0	-1 ± 0	8 ± 0	0 ± 0	7 ± 0	-5 ± 0	4 ± 0	14	11
1500 GeV	15	-5 ± 2	25 ± 0	1 ± 0	7 ± 0	0 ± 0	5 ± 0	-5 ± 0	5 ± 0	28	26
2000 GeV	14	-5 ± 2	24 ± 0	-1 ± 0	8 ± 0	-2 ± 0	5 ± 0	-6 ± 0	6 ± 0	27	25
2500 GeV	12	-5 ± 2	11 ± 0	1 ± 0	10 ± 0	-4 ± 0	0 ± 0	-7 ± 0	6 ± 0	16	11
3000 GeV	11	-5 ± 2	22 ± 0	4 ± 0	11 ± 0	-6 ± 0	9 ± 0	-7 ± 0	7 ± 0	27	24
4000 GeV	8	-5 ± 2	5 ± 0	0 ± 0	11 ± 0	-17 ± 0	2 ± 0	-8 ± 0	8 ± 0	-6	-15

Table G.3: Relative uncertainties (sys ± stat) on the signal efficiencies in percentages for Drell-Yan spin-0 HECOs of charge $\lvert z \rvert = 20$. The total relative uncertainties are calculated as quadratic sums of the individual relative uncertainties, where the detector-material uncertainty and the δ-ray uncertainty are taken as symmetric, as described in the text.

Drell-Yan Spin-0 $\lvert z \rvert = 40$	eff.	Material	Birks High	δ-ray prod.	TRT Occ.	Calo Arrival	Extrap	Pileup w. Up	Pileup w. Down	Total Up	Total Down
200 GeV	14	-3 ± 1	5 ± 0	5 ± 0	0 ± 0	0 ± 0	0 ± 0	-1 ± 0	1 ± 0	7	-2
500 GeV	32	-3 ± 1	5 ± 0	0 ± 0	0 ± 0	0 ± 0	-1 ± 0	-1 ± 0	1 ± 0	6	4
1000 GeV	40	-3 ± 1	5 ± 0	-1 ± 0	0 ± 0	0 ± 0	-1 ± 0	-1 ± 0	1 ± 0	6	4
1500 GeV	38	-3 ± 1	5 ± 0	1 ± 0	1 ± 0	-1 ± 0	1 ± 0	-2 ± 0	2 ± 0	6	4
2000 GeV	34	-3 ± 1	6 ± 0	-1 ± 0	2 ± 0	-3 ± 0	2 ± 0	-2 ± 0	2 ± 0	6	4
2500 GeV	28	-3 ± 1	7 ± 0	1 ± 0	3 ± 0	-4 ± 0	-2 ± 0	-2 ± 0	2 ± 0	6	4
3000 GeV	25	-3 ± 1	6 ± 0	4 ± 0	3 ± 0	-5 ± 0	2 ± 0	-3 ± 0	3 ± 0	7	-2
4000 GeV	13	-3 ± 1	5 ± 0	0 ± 0	4 ± 0	-4 ± 0	4 ± 0	-3 ± 0	3 ± 0	8	5

Table G.4: Relative uncertainties (sys ± stat) on the signal efficiencies in percentages for Drell-Yan spin-0 HECOs of charge $\lvert z \rvert = 40$. The total relative uncertainties are calculated as quadratic sums of the individual relative uncertainties, where the detector-material uncertainty and the δ-ray uncertainty are taken as symmetric, as described in the text.

Drell-Yan Spin-0 $\lvert z \rvert = 60$	eff.	Material	Birks High	δ-ray prod.	TRT Occ.	Calo Arrival	Extrap	Pileup w. Up	Pileup w. Down	Total Up	Total Down
200 GeV	6	-3 $\pm$ 1	5 $\pm$ 0	5 $\pm$ 0	-2 $\pm$ 0	0 $\pm$ 0	0 $\pm$ 0	0 $\pm$ 0	0 $\pm$ 0	7	-3
500 GeV	17	-3 $\pm$ 1	5 $\pm$ 0	0 $\pm$ 0	-2 $\pm$ 0	0 $\pm$ 0	0 $\pm$ 0	0 $\pm$ 0	0 $\pm$ 0	5	4
1000 GeV	24	-3 $\pm$ 1	5 $\pm$ 0	-1 $\pm$ 0	-2 $\pm$ 0	0 $\pm$ 0	-1 $\pm$ 0	0 $\pm$ 0	1 $\pm$ 0	5	4
1500 GeV	23	-3 $\pm$ 1	5 $\pm$ 0	1 $\pm$ 0	-1 $\pm$ 0	0 $\pm$ 0	-1 $\pm$ 0	-1 $\pm$ 0	1 $\pm$ 0	6	4
2000 GeV	20	-3 $\pm$ 1	5 $\pm$ 0	-1 $\pm$ 0	-1 $\pm$ 0	0 $\pm$ 0	1 $\pm$ 0	-1 $\pm$ 0	1 $\pm$ 0	6	4
2500 GeV	17	-3 $\pm$ 1	5 $\pm$ 0	1 $\pm$ 0	-1 $\pm$ 0	-1 $\pm$ 0	1 $\pm$ 0	-1 $\pm$ 0	1 $\pm$ 0	6	4
3000 GeV	14	-3 $\pm$ 1	5 $\pm$ 0	4 $\pm$ 0	0 $\pm$ 0	-1 $\pm$ 0	0 $\pm$ 0	-1 $\pm$ 0	1 $\pm$ 0	7	1
4000 GeV	4	-3 $\pm$ 1	5 $\pm$ 0	0 $\pm$ 0	1 $\pm$ 0	-1 $\pm$ 0	1 $\pm$ 0	-1 $\pm$ 0	2 $\pm$ 0	6	4

Table G.5: Relative uncertainties (sys $\pm$ stat) on the signal efficiencies in percentages for Drell-Yan spin-0 HECOs of charge $\lvert z \rvert = 60$. The total relative uncertainties are calculated as quadratic sums of the individual relative uncertainties, where the detector-material uncertainty and the δ-ray uncertainty are taken as symmetric, as described in the text.

Drell-Yan Spin-0 $\lvert z\rvert = 80$	eff.	Material	Birks High	δ-ray prod.	TRT Occ.	Calo Arrival	Extrap	Pileup w. Up	Pileup w. Down	Total Up	Total Down
200 GeV	1	-6 ± 3	10 ± 0	1 ± 0	-2 ± 0	0 ± 0	1 ± 0	0 ± 0	0 ± 0	12	8
500 GeV	6	-6 ± 3	5 ± 0	-4 ± 0	-2 ± 0	0 ± 0	0 ± 0	0 ± 0	0 ± 0	9	-6
1000 GeV	9	-6 ± 3	5 ± 0	0 ± 0	-2 ± 0	0 ± 0	1 ± 0	0 ± 0	0 ± 0	8	-5
1500 GeV	9	-6 ± 3	5 ± 0	-1 ± 0	-2 ± 0	0 ± 0	0 ± 0	0 ± 0	0 ± 0	8	-5
2000 GeV	7	-6 ± 3	5 ± 0	1 ± 0	-2 ± 0	0 ± 0	0 ± 0	-1 ± 0	0 ± 0	8	-5
2500 GeV	6	-6 ± 3	5 ± 0	4 ± 0	-2 ± 0	0 ± 0	0 ± 0	0 ± 0	0 ± 0	9	-6
3000 GeV	4	-6 ± 3	5 ± 0	3 ± 0	-2 ± 0	0 ± 0	1 ± 0	0 ± 0	0 ± 0	9	-5
4000 GeV	0	-6 ± 3	12 ± 1	2 ± 0	-2 ± 0	0 ± 0	-4 ± 0	-1 ± 0	0 ± 0	13	9

Table G.6: Relative uncertainties (sys ± stat) on the signal efficiencies in percentages for Drell-Yan spin-0 HECOs of charge $\lvert z\rvert = 80$. The total relative uncertainties are calculated as quadratic sums of the individual relative uncertainties, where the detector-material uncertainty and the δ-ray uncertainty are taken as symmetric, as described in the text.

Drell-Yan Spin-0 $\lvert z\rvert = 100$	eff.	Material	Birks High	δ-ray prod.	TRT Occ.	Calo Arrival	Extrap	Pileup w. Up	Pileup w. Down	Total Up	Total Down
200 GeV	0	-14 ± 8	5 ± 0	1 ± 0	-2 ± 0	0 ± 0	-1 ± 0	0 ± 0	0 ± 0	14	-13
500 GeV	1	-14 ± 8	5 ± 0	-4 ± 0	-2 ± 0	0 ± 0	0 ± 0	0 ± 0	0 ± 0	15	-13
1000 GeV	2	-14 ± 8	5 ± 0	0 ± 0	-2 ± 0	0 ± 0	0 ± 0	0 ± 0	0 ± 0	14	-13
1500 GeV	2	-14 ± 8	5 ± 0	-1 ± 0	-3 ± 0	0 ± 0	1 ± 0	0 ± 0	0 ± 0	14	-13
2000 GeV	2	-14 ± 8	5 ± 0	1 ± 0	-2 ± 0	0 ± 0	1 ± 0	0 ± 0	0 ± 0	14	-13
2500 GeV	1	-14 ± 8	5 ± 0	4 ± 0	-3 ± 0	0 ± 0	1 ± 0	0 ± 0	1 ± 0	15	-13
3000 GeV	1	-14 ± 8	5 ± 0	3 ± 0	-2 ± 0	0 ± 0	0 ± 0	0 ± 0	0 ± 0	15	-13
4000 GeV	0	-14 ± 8	20 ± 7	2 ± 0	0 ± 0	0 ± 0	1 ± 0	0 ± 0	0 ± 0	24	15

Table G.7: Relative uncertainties (sys ± stat) on the signal efficiencies in percentages for Drell-Yan spin-0 HECOs of charge $\lvert z\rvert = 100$. The total relative uncertainties are calculated as quadratic sums of the individual relative uncertainties, where the detector-material uncertainty and the δ-ray uncertainty are taken as symmetric, as described in the text.

Drell-Yan Spin-½ $1g_{\mathrm{D}}$	eff.	Material	Birks High	δ-ray prod.	TRT Occ.	Calo Arrival	Pileup w. Up	Pileup w. Down	Total Up	Total Down
200 GeV	3	-4 ± 1	14 ± 0	6 ± 0	0 ± 0	0 ± 0	0 ± 0	0 ± 0	16	13
500 GeV	12	-4 ± 1	9 ± 0	-1 ± 0	0 ± 0	0 ± 0	0 ± 0	0 ± 0	10	8
1000 GeV	24	-4 ± 1	5 ± 0	-1 ± 0	1 ± 0	0 ± 0	-1 ± 0	0 ± 0	6	3
1500 GeV	25	-4 ± 1	5 ± 0	2 ± 0	2 ± 0	-2 ± 0	-1 ± 0	1 ± 0	7	3
2000 GeV	22	-4 ± 1	5 ± 0	0 ± 0	5 ± 0	-3 ± 0	-2 ± 0	2 ± 0	8	5
2500 GeV	19	-4 ± 1	5 ± 0	0 ± 0	7 ± 0	-5 ± 0	-3 ± 0	3 ± 0	8	5
3000 GeV	16	-4 ± 1	5 ± 0	2 ± 0	8 ± 0	-9 ± 0	-4 ± 0	4 ± 0	7	-4
4000 GeV	8	-4 ± 1	10 ± 0	-2 ± 0	13 ± 0	-20 ± 0	-6 ± 0	6 ± 0	-10	-14

Table G.8: Relative uncertainties (sys ± stat) on the signal efficiencies in percentages for Drell-Yan spin-½ monopoles of charge $|g| = 1g_{\mathrm{D}}$. The total relative uncertainties are calculated as quadratic sums of the individual relative uncertainties, where the detector-material uncertainty and the δ-ray uncertainty are taken as symmetric, as described in the text.

Drell-Yan Spin-½ $2g_D$	eff.	Material	Birks High	δ-ray prod.	TRT Occ.	Calo Arrival	Pileup w. Up	Pileup w. Down	Total Up	Total Down
200 GeV	0	-18 ± 5	5 ± 0	1 ± 0	0 ± 0	0 ± 0	0 ± 0	0 ± 0	19	-17
500 GeV	0	-18 ± 5	6 ± 0	-4 ± 0	0 ± 0	0 ± 0	0 ± 0	0 ± 0	19	-17
1000 GeV	1	-18 ± 5	5 ± 0	0 ± 0	0 ± 0	0 ± 0	0 ± 0	0 ± 0	19	-17
1500 GeV	2	-18 ± 5	6 ± 0	-1 ± 0	0 ± 0	0 ± 0	0 ± 0	0 ± 0	19	-17
2000 GeV	2	-18 ± 5	5 ± 0	1 ± 0	0 ± 0	0 ± 0	0 ± 0	0 ± 0	19	-17
2500 GeV	3	-18 ± 5	5 ± 0	4 ± 0	0 ± 0	0 ± 0	0 ± 0	0 ± 0	19	-18
3000 GeV	4	-18 ± 5	5 ± 0	3 ± 0	0 ± 0	0 ± 0	-1 ± 0	0 ± 0	19	-18
4000 GeV	2	-18 ± 5	12 ± 0	2 ± 0	2 ± 0	0 ± 0	-2 ± 0	2 ± 0	22	-14

Table G.9: Relative uncertainties (sys ± stat) on the signal efficiencies in percentages for Drell-Yan spin-½ monopoles of charge $|g| = 2g_D$. The total relative uncertainties are calculated as quadratic sums of the individual relative uncertainties, where the detector-material uncertainty and the δ-ray uncertainty are taken as symmetric, as described in the text.

Drell-Yan Spin-½ $\lvert z\rvert = 20$	eff.	Material	Birks High	δ-ray prod.	TRT Occ.	Calo Arrival	Pileup w. Up	Pileup w. Down	Total Up	Total Down
200 GeV	2	-9 ± 4	21 ± 1	6 ± 0	17 ± 1	0 ± 0	-4 ± 0	4 ± 0	30	25
500 GeV	6	-9 ± 4	18 ± 0	-1 ± 0	15 ± 0	0 ± 0	-5 ± 0	5 ± 0	26	21
1000 GeV	7	-9 ± 4	14 ± 0	-1 ± 0	16 ± 0	0 ± 0	-6 ± 0	5 ± 0	24	19
1500 GeV	6	-9 ± 4	31 ± 0	2 ± 0	19 ± 0	-2 ± 0	-6 ± 0	6 ± 0	38	34
2000 GeV	5	-9 ± 4	25 ± 1	0 ± 0	20 ± 0	-4 ± 0	-7 ± 0	7 ± 0	34	30
2500 GeV	5	-9 ± 4	12 ± 0	0 ± 0	22 ± 0	-8 ± 0	-7 ± 0	8 ± 0	27	21
3000 GeV	4	-9 ± 4	28 ± 0	2 ± 0	22 ± 0	-14 ± 0	-8 ± 0	9 ± 0	35	30
4000 GeV	3	-9 ± 4	15 ± 0	-2 ± 0	24 ± 1	-27 ± 0	-9 ± 0	9 ± 0	15	-11

Table G.10: Relative uncertainties (sys ± stat) on the signal efficiencies in percentages for Drell-Yan spin-½ HECOs of charge $\lvert z\rvert = 20$. The total relative uncertainties are calculated as quadratic sums of the individual relative uncertainties, where the detector-material uncertainty and the δ-ray uncertainty are taken as symmetric, as described in the text.

Drell-Yan Spin-½ $\lvert z \rvert = 40$	eff.	Material	Birks High	δ-ray prod.	TRT Occ.	Calo Arrival	Pileup w. Up	Pileup w. Down	Total Up	Total Down
200 GeV	5	-4 ± 1	5 ± 0	6 ± 0	4 ± 0	0 ± 0	-1 ± 0	1 ± 0	9	-3
500 GeV	13	-4 ± 1	5 ± 0	-1 ± 0	3 ± 0	0 ± 0	-1 ± 0	1 ± 0	7	4
1000 GeV	17	-4 ± 1	6 ± 0	-1 ± 0	3 ± 0	0 ± 0	-1 ± 0	1 ± 0	8	5
1500 GeV	16	-4 ± 1	5 ± 0	2 ± 0	4 ± 0	-1 ± 0	-2 ± 0	2 ± 0	8	4
2000 GeV	13	-4 ± 1	5 ± 0	0 ± 0	5 ± 0	-2 ± 0	-2 ± 0	2 ± 0	8	5
2500 GeV	9	-4 ± 1	9 ± 0	0 ± 0	6 ± 0	-2 ± 0	-3 ± 0	3 ± 0	11	9
3000 GeV	8	-4 ± 1	8 ± 0	2 ± 0	7 ± 0	-3 ± 0	-3 ± 0	3 ± 0	11	8
4000 GeV	4	-4 ± 1	6 ± 0	-2 ± 0	10 ± 0	-5 ± 0	-5 ± 0	5 ± 0	13	8

Table G.11: Relative uncertainties (sys ± stat) on the signal efficiencies in percentages for Drell-Yan spin-½ HECOs of charge $\lvert z \rvert = 40$. The total relative uncertainties are calculated as quadratic sums of the individual relative uncertainties, where the detector-material uncertainty and the δ-ray uncertainty are taken as symmetric, as described in the text.

Drell-Yan Spin-½ $\lvert z \rvert = 60$	eff.	Material	Birks High	δ-ray prod.	TRT Occ.	Calo Arrival	Pileup w. Up	Pileup w. Down	Total Up	Total Down
200 GeV	2	-3 ± 1	5 ± 0	6 ± 0	1 ± 0	0 ± 0	-1 ± 0	1 ± 0	8	-4
500 GeV	5	-3 ± 1	5 ± 0	-1 ± 0	1 ± 0	0 ± 0	0 ± 0	0 ± 0	6	4
1000 GeV	8	-3 ± 1	5 ± 0	-1 ± 0	0 ± 0	0 ± 0	-1 ± 0	1 ± 0	6	3
1500 GeV	8	-3 ± 1	5 ± 0	2 ± 0	1 ± 0	0 ± 0	-1 ± 0	1 ± 0	6	3
2000 GeV	7	-3 ± 1	5 ± 0	0 ± 0	1 ± 0	0 ± 0	-1 ± 0	1 ± 0	6	4
2500 GeV	5	-3 ± 1	5 ± 0	0 ± 0	1 ± 0	0 ± 0	-1 ± 0	1 ± 0	6	4
3000 GeV	4	-3 ± 1	5 ± 0	2 ± 0	2 ± 0	0 ± 0	-1 ± 0	1 ± 0	7	3
4000 GeV	1	-3 ± 1	5 ± 0	-2 ± 0	3 ± 0	0 ± 0	-2 ± 0	2 ± 0	7	3

Table G.12: Relative uncertainties (sys ± stat) on the signal efficiencies in percentages for Drell-Yan spin-½ HECOs of charge $\lvert z \rvert = 60$. The total relative uncertainties are calculated as quadratic sums of the individual relative uncertainties, where the detector-material uncertainty and the δ-ray uncertainty are taken as symmetric, as described in the text.

Drell-Yan Spin-½ $\lvert z\rvert = 80$	eff.	Material	Birks High	δ-ray prod.	TRT Occ.	Calo Arrival	Pileup w. Up	Pileup w. Down	Total Up	Total Down
200 GeV	0	-8 ± 3	11 ± 0	1 ± 0	0 ± 0	0 ± 0	0 ± 0	0 ± 0	14	7
500 GeV	1	-8 ± 3	5 ± 0	-4 ± 0	0 ± 0	0 ± 0	0 ± 0	0 ± 0	10	-8
1000 GeV	2	-8 ± 3	5 ± 0	0 ± 0	0 ± 0	0 ± 0	0 ± 0	0 ± 0	10	-7
1500 GeV	2	-8 ± 3	5 ± 0	-1 ± 0	0 ± 0	0 ± 0	0 ± 0	0 ± 0	10	-7
2000 GeV	2	-8 ± 3	5 ± 0	1 ± 0	0 ± 0	0 ± 0	0 ± 0	0 ± 0	10	-7
2500 GeV	1	-8 ± 3	5 ± 0	4 ± 0	0 ± 0	0 ± 0	-1 ± 0	0 ± 0	11	-8
3000 GeV	1	-8 ± 3	5 ± 0	3 ± 0	0 ± 0	0 ± 0	0 ± 0	0 ± 0	10	-7
4000 GeV	0	-8 ± 3	15 ± 1	2 ± 0	0 ± 0	0 ± 0	-1 ± 0	1 ± 0	17	12

Table G.13: Relative uncertainties (sys ± stat) on the signal efficiencies in percentages for Drell-Yan spin-½ HECOs of charge $|z| = 80$. The total relative uncertainties are calculated as quadratic sums of the individual relative uncertainties, where the detector-material uncertainty and the δ-ray uncertainty are taken as symmetric, as described in the text.

Drell-Yan Spin-½ $\lvert z\rvert = 100$	eff.	Material	Birks High	δ-ray prod.	TRT Occ.	Calo Arrival	Pileup w. Up	Pileup w. Down	Total Up	Total Down
200 GeV	0	-16 ± 13	5 ± 0	1 ± 0	0 ± 0	0 ± 0	0 ± 0	0 ± 0	17	-15
500 GeV	0	-16 ± 13	5 ± 0	-4 ± 0	0 ± 0	0 ± 0	0 ± 0	0 ± 0	17	-15
1000 GeV	1	-16 ± 13	5 ± 0	0 ± 0	0 ± 0	0 ± 0	0 ± 0	0 ± 0	17	-15
1500 GeV	1	-16 ± 13	5 ± 0	-1 ± 0	0 ± 0	0 ± 0	0 ± 0	0 ± 0	17	-15
2000 GeV	0	-16 ± 13	5 ± 0	1 ± 0	0 ± 0	0 ± 0	0 ± 0	0 ± 0	17	-15
2500 GeV	0	-16 ± 13	5 ± 0	4 ± 0	0 ± 0	0 ± 0	-1 ± 0	1 ± 0	17	-16
3000 GeV	0	-16 ± 13	5 ± 0	3 ± 0	0 ± 0	0 ± 0	-1 ± 0	1 ± 0	17	-15
4000 GeV	0	-16 ± 13	5 ± 0	2 ± 0	0 ± 0	0 ± 0	-3 ± 0	4 ± 0	17	-15

Table G.14: Relative uncertainties (sys ± stat) on the signal efficiencies in percentages for Drell-Yan spin-½ HECOs of charge $\lvert z\rvert = 100$. The total relative uncertainties are calculated as quadratic sums of the individual relative uncertainties, where the detector-material uncertainty and the δ-ray uncertainty are taken as symmetric, as described in the text.

Photon Fusion Spin-0 $1g_{\mathrm{D}}$	eff.	Material	Birks High	δ-ray prod.	TRT Occ.	Calo Arrival	Extrap	Pileup w. Up	Pileup w. Down	Total Up	Total Down
200 GeV	5	-3 ± 1	11 ± 0	5 ± 0	-2 ± 0	0 ± 0	-1 ± 0	0 ± 0	0 ± 0	12	9
500 GeV	14	-3 ± 1	7 ± 0	0 ± 0	-2 ± 0	0 ± 0	-2 ± 0	0 ± 0	0 ± 0	7	6
1000 GeV	22	-3 ± 1	5 ± 0	-1 ± 0	-1 ± 0	0 ± 0	-1 ± 0	-1 ± 0	1 ± 0	6	3
1500 GeV	23	-3 ± 1	5 ± 0	2 ± 0	0 ± 0	-4 ± 0	0 ± 0	-1 ± 0	1 ± 0	6	-2
2000 GeV	20	-3 ± 1	6 ± 0	1 ± 0	2 ± 0	-8 ± 0	1 ± 0	-2 ± 0	2 ± 0	-4	-7
2500 GeV	16	-3 ± 1	6 ± 0	0 ± 0	4 ± 0	-10 ± 0	0 ± 0	-3 ± 0	3 ± 0	-6	-9
3000 GeV	12	-3 ± 1	6 ± 0	3 ± 0	5 ± 0	-16 ± 0	2 ± 0	-4 ± 0	4 ± 0	-12	-15
4000 GeV	6	-3 ± 1	14 ± 0	-7 ± 0	5 ± 0	-30 ± 0	3 ± 0	-6 ± 0	6 ± 0	-24	-28

Table G.15: Relative uncertainties (sys ± stat) on the signal efficiencies in percentages for photon fusion spin-0 monopoles of charge $|g| = 1g_{\mathrm{D}}$. The total relative uncertainties are calculated as quadratic sums of the individual relative uncertainties, where the detector-material uncertainty and the δ-ray uncertainty are taken as symmetric, as described in the text.

Photon Fusion Spin-0 $2g_D$	eff.	Material	Birks High	δ-ray prod.	TRT Occ.	Calo Arrival	Extrap	Pileup w. Up	Pileup w. Down	Total Up	Total Down
200 GeV	0	-15 ± 6	5 ± 0	1 ± 0	-2 ± 0	0 ± 0	2 ± 0	0 ± 0	0 ± 0	16	-14
500 GeV	0	-15 ± 6	6 ± 0	-4 ± 0	-2 ± 0	0 ± 0	2 ± 0	0 ± 0	0 ± 0	16	-14
1000 GeV	1	-15 ± 6	5 ± 0	0 ± 0	-2 ± 0	0 ± 0	1 ± 0	0 ± 0	0 ± 0	16	-14
1500 GeV	2	-15 ± 6	5 ± 0	-1 ± 0	-2 ± 0	0 ± 0	2 ± 0	0 ± 0	0 ± 0	16	-14
2000 GeV	2	-15 ± 6	5 ± 0	1 ± 0	-2 ± 0	0 ± 0	1 ± 0	0 ± 0	0 ± 0	16	-14
2500 GeV	2	-15 ± 6	5 ± 0	4 ± 0	-1 ± 0	0 ± 0	0 ± 0	0 ± 0	0 ± 0	16	-15
3000 GeV	2	-15 ± 6	5 ± 0	5 ± 0	-2 ± 0	0 ± 0	0 ± 0	-1 ± 0	1 ± 0	16	-15
4000 GeV	1	-15 ± 6	16 ± 0	2 ± 0	0 ± 0	0 ± 0	2 ± 0	-2 ± 0	2 ± 0	22	5

Table G.16: Relative uncertainties (sys ± stat) on the signal efficiencies in percentages for photon fusion spin-0 monopoles of charge $|g| = 2g_D$. The total relative uncertainties are calculated as quadratic sums of the individual relative uncertainties, where the detector-material uncertainty and the δ-ray uncertainty are taken as symmetric, as described in the text.

Photon Fusion Spin-0 $\lvert z \rvert = 20$	eff.	Material	Birks High	δ-ray prod.	TRT Occ.	Calo Arrival	Extrap	Pileup w. Up	Pileup w. Down	Total Up	Total Down
200 GeV	4	-10 ± 5	10 ± 0	5 ± 0	7 ± 0	0 ± 0	2 ± 0	-4 ± 0	4 ± 0	17	4
500 GeV	7	-10 ± 5	16 ± 0	0 ± 0	6 ± 0	0 ± 0	1 ± 0	-4 ± 0	4 ± 0	20	14
1000 GeV	7	-10 ± 5	12 ± 0	-1 ± 0	9 ± 0	-1 ± 0	7 ± 0	-5 ± 0	5 ± 0	20	12
1500 GeV	6	-10 ± 5	29 ± 1	2 ± 0	7 ± 0	-2 ± 0	5 ± 0	-6 ± 0	6 ± 0	32	28
2000 GeV	6	-10 ± 5	25 ± 1	1 ± 0	8 ± 0	-7 ± 0	5 ± 0	-7 ± 0	7 ± 0	29	23
2500 GeV	4	-10 ± 5	12 ± 0	0 ± 0	11 ± 0	-12 ± 0	0 ± 0	-8 ± 0	7 ± 0	16	-6
3000 GeV	4	-10 ± 5	29 ± 1	3 ± 0	11 ± 0	-19 ± 0	9 ± 0	-8 ± 0	9 ± 0	29	23
4000 GeV	2	-10 ± 5	39 ± 2	-7 ± 0	14 ± 0	-40 ± 1	2 ± 0	-9 ± 0	9 ± 0	20	-5

Table G.17: Relative uncertainties (sys ± stat) on the signal efficiencies in percentages for photon fusion spin-0 HECOs of charge $|z| = 20$. The total relative uncertainties are calculated as quadratic sums of the individual relative uncertainties, where the detector-material uncertainty and the δ-ray uncertainty are taken as symmetric, as described in the text.

Photon Fusion Spin-0 $\|z\| = 40$	eff.	Material	Birks High	δ-ray prod.	TRT Occ.	Calo Arrival	Extrap	Pileup w. Up	Pileup w. Down	Total Up	Total Down
200 GeV	8	-4 ± 1	5 ± 0	5 ± 0	0 ± 0	0 ± 0	0 ± 0	-1 ± 0	1 ± 0	8	-4
500 GeV	14	-4 ± 1	5 ± 0	0 ± 0	0 ± 0	0 ± 0	-1 ± 0	-1 ± 0	1 ± 0	7	2
1000 GeV	16	-4 ± 1	5 ± 0	-1 ± 0	0 ± 0	0 ± 0	-1 ± 0	-1 ± 0	1 ± 0	7	2
1500 GeV	14	-4 ± 1	5 ± 0	2 ± 0	1 ± 0	-3 ± 0	1 ± 0	-2 ± 0	2 ± 0	7	-3
2000 GeV	12	-4 ± 1	5 ± 0	1 ± 0	2 ± 0	-7 ± 0	2 ± 0	-2 ± 0	2 ± 0	4	-6
2500 GeV	10	-4 ± 1	10 ± 0	0 ± 0	4 ± 0	-9 ± 0	-2 ± 0	-2 ± 0	2 ± 0	8	3
3000 GeV	6	-4 ± 1	8 ± 0	3 ± 0	4 ± 0	-10 ± 0	2 ± 0	-3 ± 0	3 ± 0	5	-7
4000 GeV	1	-4 ± 1	9 ± 0	-7 ± 0	5 ± 0	-7 ± 0	4 ± 0	-3 ± 0	4 ± 0	12	-4

Table G.18: Relative uncertainties (sys ± stat) on the signal efficiencies in percentages for photon fusion spin-0 HECOs of charge $|z| = 40$. The total relative uncertainties are calculated as quadratic sums of the individual relative uncertainties. Note that the detector-material uncertainty and the δ-ray uncertainty are taken as symmetric, as described in the text.

Photon Fusion Spin-0 $\lvert z\rvert = 60$	eff.	Material	Birks High	δ-ray prod.	TRT Occ.	Calo Arrival	Extrap	Pileup w. Up	Pileup w. Down	Total Up	Total Down
200 GeV	3	-3 ± 1	5 ± 0	5 ± 0	-2 ± 0	0 ± 0	0 ± 0	0 ± 0	0 ± 0	7	-3
500 GeV	7	-3 ± 1	5 ± 0	0 ± 0	-2 ± 0	0 ± 0	0 ± 0	0 ± 0	1 ± 0	6	3
1000 GeV	8	-3 ± 1	5 ± 0	-1 ± 0	-2 ± 0	0 ± 0	-1 ± 0	-1 ± 0	1 ± 0	6	3
1500 GeV	7	-3 ± 1	5 ± 0	2 ± 0	-2 ± 0	0 ± 0	-1 ± 0	-1 ± 0	1 ± 0	6	2
2000 GeV	6	-3 ± 1	5 ± 0	1 ± 0	-1 ± 0	0 ± 0	1 ± 0	-1 ± 0	1 ± 0	6	3
2500 GeV	4	-3 ± 1	5 ± 0	0 ± 0	-1 ± 0	-1 ± 0	1 ± 0	-1 ± 0	1 ± 0	6	3
3000 GeV	2	-3 ± 1	5 ± 0	3 ± 0	0 ± 0	-2 ± 0	0 ± 0	-1 ± 0	1 ± 0	7	-2
4000 GeV	0	-3 ± 1	5 ± 0	-7 ± 0	3 ± 0	-2 ± 0	1 ± 0	-1 ± 0	2 ± 0	10	-6

Table G.19: Relative uncertainties (sys ± stat) on the signal efficiencies in percentages for photon fusion spin-0 HECOs of charge $\lvert z\rvert = 60$. The total relative uncertainties are calculated as quadratic sums of the individual relative uncertainties. Note that the detector-material uncertainty and the δ-ray uncertainty are taken as symmetric, as described in the text.

Photon Fusion Spin-0 $\lvert z \rvert = 80$	eff.	Material	Birks High	δ-ray prod.	TRT Occ.	Calo Arrival	Extrap	Pileup w. Up	Pileup w. Down	Total Up	Total Down
200 GeV	1	-7 ± 4	10 ± 0	1 ± 0	-2 ± 0	0 ± 0	1 ± 0	0 ± 0	0 ± 0	12	6
500 GeV	2	-7 ± 4	5 ± 0	-4 ± 0	-2 ± 0	0 ± 0	0 ± 0	0 ± 0	0 ± 0	9	-7
1000 GeV	3	-7 ± 4	5 ± 0	0 ± 0	-2 ± 0	0 ± 0	1 ± 0	0 ± 0	0 ± 0	9	-6
1500 GeV	3	-7 ± 4	5 ± 0	-1 ± 0	-2 ± 0	0 ± 0	0 ± 0	0 ± 0	0 ± 0	9	-6
2000 GeV	2	-7 ± 4	5 ± 0	1 ± 0	-2 ± 0	0 ± 0	0 ± 0	0 ± 0	0 ± 0	9	-6
2500 GeV	1	-7 ± 4	5 ± 0	4 ± 0	-2 ± 0	0 ± 0	0 ± 0	0 ± 0	0 ± 0	10	-7
3000 GeV	0	-7 ± 4	5 ± 0	5 ± 0	-3 ± 0	0 ± 0	1 ± 0	0 ± 0	1 ± 0	10	-7
4000 GeV	0	-7 ± 4	17 ± 2	2 ± 0	-5 ± 1	0 ± 0	-4 ± 0	-5 ± 1	0 ± 0	18	14

Table G.20: Relative uncertainties (sys ± stat) on the signal efficiencies in percentages for photon fusion spin-0 HECOs of charge $\lvert z \rvert = 80$. The total relative uncertainties are calculated as quadratic sums of the individual relative uncertainties, where the detector-material uncertainty and the δ-ray uncertainty are taken as symmetric, as described in the text.

Photon Fusion Spin-0 $\lvert z \rvert = 100$	eff.	Material	Birks High	δ-ray prod.	TRT Occ.	Calo Arrival	Extrap	Pileup w. Up	Pileup w. Down	Total Up	Total Down
200 GeV	0	-14 ± 9	5 ± 0	1 ± 0	-2 ± 0	0 ± 0	-1 ± 0	0 ± 0	0 ± 0	14	-13
500 GeV	1	-14 ± 9	5 ± 0	-4 ± 0	-2 ± 0	0 ± 0	0 ± 0	0 ± 0	0 ± 0	15	-13
1000 GeV	1	-14 ± 9	5 ± 0	0 ± 0	-2 ± 0	0 ± 0	0 ± 0	0 ± 0	0 ± 0	14	-13
1500 GeV	1	-14 ± 9	5 ± 0	-1 ± 0	-3 ± 0	0 ± 0	1 ± 0	0 ± 0	0 ± 0	14	-13
2000 GeV	0	-14 ± 9	5 ± 0	1 ± 0	-2 ± 0	0 ± 0	1 ± 0	0 ± 0	0 ± 0	14	-13
2500 GeV	0	-14 ± 9	7 ± 0	4 ± 0	-2 ± 0	0 ± 0	1 ± 0	0 ± 0	0 ± 0	16	-13
3000 GeV	0	-14 ± 9	5 ± 0	5 ± 0	-1 ± 0	-1 ± 0	0 ± 0	-1 ± 0	-1 ± 0	15	-14
4000 GeV	0	-14 ± 9	5 ± 0	2 ± 0	0 ± 0	0 ± 0	1 ± 0	0 ± 0	0 ± 0	15	-13

Table G.21: Relative uncertainties (sys ± stat) on the signal efficiencies in percentages for photon fusion spin-0 HECOs of charge $\lvert z \rvert = 100$. The total relative uncertainties are calculated as quadratic sums of the individual relative uncertainties, where the detector-material uncertainty and the δ-ray uncertainty are taken as symmetric, as described in the text.

Photon Fusion Spin-½ $1g_{\mathrm{D}}$	eff.	Material	Birks High	δ-ray prod.	TRT Occ.	Calo Arrival	Extrap	Pileup w. Up	Pileup w. Down	Total Up	Total Down
200 GeV	4	-4 ± 1	14 ± 0	6 ± 0	-2 ± 0	0 ± 0	-1 ± 0	0 ± 0	0 ± 0	15	12
500 GeV	17	-4 ± 1	8 ± 0	0 ± 0	-2 ± 0	0 ± 0	-2 ± 0	0 ± 0	0 ± 0	8	7
1000 GeV	31	-4 ± 1	5 ± 0	-1 ± 0	-1 ± 0	0 ± 0	-1 ± 0	-1 ± 0	1 ± 0	6	3
1500 GeV	32	-4 ± 1	5 ± 0	2 ± 0	0 ± 0	-3 ± 0	0 ± 0	-1 ± 0	1 ± 0	6	-1
2000 GeV	29	-4 ± 1	5 ± 0	0 ± 0	1 ± 0	-7 ± 0	1 ± 0	-2 ± 0	2 ± 0	-2	-6
2500 GeV	23	-4 ± 1	5 ± 0	0 ± 0	3 ± 0	-9 ± 0	0 ± 0	-3 ± 0	2 ± 0	-5	-8
3000 GeV	17	-4 ± 1	5 ± 0	4 ± 0	4 ± 0	-13 ± 0	2 ± 0	-4 ± 0	3 ± 0	-10	-13
4000 GeV	8	-4 ± 1	14 ± 0	-6 ± 0	5 ± 0	-27 ± 0	3 ± 0	-6 ± 0	6 ± 0	-21	-25

Table G.22: Relative uncertainties (sys ± stat) on the signal efficiencies in percentages for photon fusion spin-½ monopoles of charge $|g| = 1g_{\mathrm{D}}$. The total relative uncertainties are calculated as quadratic sums of the individual relative uncertainties, where the detector-material uncertainty and the δ-ray uncertainty are taken as symmetric, as described in the text.

Photon Fusion Spin-½ $2g_{\mathrm{D}}$	eff.	Material	Birks High	δ-ray prod.	TRT Occ.	Calo Arrival	Extrap	Pileup w. Up	Pileup w. Down	Total Up	Total Down
200 GeV	0	-17 $\pm$ 6	5 $\pm$ 0	0 $\pm$ 0	-2 $\pm$ 0	0 $\pm$ 0	2 $\pm$ 0	0 $\pm$ 0	0 $\pm$ 0	18	-16
500 GeV	0	-17 $\pm$ 6	6 $\pm$ 0	-4 $\pm$ 0	-2 $\pm$ 0	0 $\pm$ 0	2 $\pm$ 0	0 $\pm$ 0	0 $\pm$ 0	18	-17
1000 GeV	1	-17 $\pm$ 6	5 $\pm$ 0	0 $\pm$ 0	-2 $\pm$ 0	0 $\pm$ 0	1 $\pm$ 0	0 $\pm$ 0	0 $\pm$ 0	18	-16
1500 GeV	3	-17 $\pm$ 6	5 $\pm$ 0	-1 $\pm$ 0	-2 $\pm$ 0	0 $\pm$ 0	2 $\pm$ 0	0 $\pm$ 0	0 $\pm$ 0	18	-16
2000 GeV	4	-17 $\pm$ 6	5 $\pm$ 0	1 $\pm$ 0	-2 $\pm$ 0	0 $\pm$ 0	1 $\pm$ 0	0 $\pm$ 0	0 $\pm$ 0	18	-17
2500 GeV	4	-17 $\pm$ 6	5 $\pm$ 0	4 $\pm$ 0	-1 $\pm$ 0	0 $\pm$ 0	0 $\pm$ 0	0 $\pm$ 0	0 $\pm$ 0	18	-17
3000 GeV	4	-17 $\pm$ 6	5 $\pm$ 0	4 $\pm$ 0	-1 $\pm$ 0	0 $\pm$ 0	0 $\pm$ 0	-1 $\pm$ 0	1 $\pm$ 0	18	-17
4000 GeV	1	-17 $\pm$ 6	14 $\pm$ 0	3 $\pm$ 0	0 $\pm$ 0	0 $\pm$ 0	2 $\pm$ 0	-2 $\pm$ 0	2 $\pm$ 0	23	-10

Table G.23: Relative uncertainties (sys $\pm$ stat) on the signal efficiencies in percentages for photon fusion spin-½ monopoles of charge $|g| = 2g_{\mathrm{D}}$. The total relative uncertainties are calculated as quadratic sums of the individual relative uncertainties, where the detector-material uncertainty and the δ-ray uncertainty are taken as symmetric, as described in the text.

Photon Fusion Spin-½ $\lvert z \rvert = 20$	eff.	Material	Birks High	δ-ray prod.	TRT Occ.	Calo Arrival	Extrap	Pileup w. Up	Pileup w. Down	Total Up	Total Down
200 GeV	4	-8 ± 4	12 ± 0	6 ± 0	8 ± 0	0 ± 0	2 ± 0	-4 ± 0	4 ± 0	18	9
500 GeV	8	-8 ± 4	16 ± 0	0 ± 0	6 ± 0	0 ± 0	1 ± 0	-4 ± 0	4 ± 0	20	15
1000 GeV	9	-8 ± 4	14 ± 0	-1 ± 0	8 ± 0	0 ± 0	7 ± 0	-5 ± 0	5 ± 0	20	15
1500 GeV	9	-8 ± 4	26 ± 0	2 ± 0	8 ± 0	-2 ± 0	5 ± 0	-5 ± 0	5 ± 0	30	26
2000 GeV	8	-8 ± 4	22 ± 0	0 ± 0	9 ± 0	-5 ± 0	5 ± 0	-7 ± 0	6 ± 0	25	21
2500 GeV	6	-8 ± 4	8 ± 0	0 ± 0	10 ± 0	-8 ± 0	0 ± 0	-7 ± 0	7 ± 0	15	-5
3000 GeV	6	-8 ± 4	26 ± 1	4 ± 0	11 ± 0	-14 ± 0	9 ± 0	-7 ± 0	9 ± 0	29	24
4000 GeV	3	-8 ± 4	26 ± 1	-6 ± 0	14 ± 0	-34 ± 1	2 ± 0	-8 ± 0	9 ± 0	-9	-21

Table G.24: Relative uncertainties (sys ± stat) on the signal efficiencies in percentages for photon fusion spin-½ HECOs of charge $\lvert z \rvert = 20$. The total relative uncertainties are calculated as quadratic sums of the individual relative uncertainties, where the detector-material uncertainty and the δ-ray uncertainty are taken as symmetric, as described in the text.

Photon Fusion Spin-½ $\lvert z\rvert = 40$	eff.	Material	Birks High	δ-ray prod.	TRT Occ.	Calo Arrival	Extrap	Pileup w. Up	Pileup w. Down	Total Up	Total Down
200 GeV	7	-4 ± 1	5 ± 0	6 ± 0	0 ± 0	0 ± 0	0 ± 0	-1 ± 0	1 ± 0	9	-5
500 GeV	17	-4 ± 1	5 ± 0	0 ± 0	0 ± 0	0 ± 0	-1 ± 0	-1 ± 0	1 ± 0	6	3
1000 GeV	22	-4 ± 1	5 ± 0	-1 ± 0	0 ± 0	0 ± 0	-1 ± 0	-1 ± 0	1 ± 0	6	3
1500 GeV	22	-4 ± 1	5 ± 0	2 ± 0	1 ± 0	-2 ± 0	1 ± 0	-2 ± 0	2 ± 0	7	1
2000 GeV	18	-4 ± 1	5 ± 0	0 ± 0	2 ± 0	-5 ± 0	2 ± 0	-2 ± 0	2 ± 0	5	-4
2500 GeV	15	-4 ± 1	8 ± 0	0 ± 0	4 ± 0	-9 ± 0	-2 ± 0	-2 ± 0	2 ± 0	5	-4
3000 GeV	9	-4 ± 1	9 ± 0	4 ± 0	4 ± 0	-8 ± 0	2 ± 0	-3 ± 0	3 ± 0	8	-4
4000 GeV	2	-4 ± 1	9 ± 0	-6 ± 0	4 ± 0	-7 ± 0	4 ± 0	-4 ± 0	4 ± 0	11	1

Table G.25: Relative uncertainties (sys ± stat) on the signal efficiencies in percentages for photon fusion spin-½ HECOs of charge $\lvert z\rvert = 40$. The total relative uncertainties are calculated as quadratic sums of the individual relative uncertainties, where the detector-material uncertainty and the δ-ray uncertainty are taken as symmetric, as described in the text.

Photon Fusion Spin-½ $\lvert z\rvert = 60$	eff.	Material	Birks High	δ-ray prod.	TRT Occ.	Calo Arrival	Extrap	Pileup w. Up	Pileup w. Down	Total Up	Total Down
200 GeV	3	-4 ± 1	5 ± 0	6 ± 0	-2 ± 0	0 ± 0	0 ± 0	0 ± 0	0 ± 0	8	-5
500 GeV	8	-4 ± 1	5 ± 0	0 ± 0	-2 ± 0	0 ± 0	0 ± 0	-1 ± 0	0 ± 0	6	3
1000 GeV	12	-4 ± 1	5 ± 0	-1 ± 0	-2 ± 0	0 ± 0	-1 ± 0	-1 ± 0	1 ± 0	6	3
1500 GeV	12	-4 ± 1	5 ± 0	2 ± 0	-2 ± 0	0 ± 0	-1 ± 0	-1 ± 0	1 ± 0	6	2
2000 GeV	10	-4 ± 1	5 ± 0	0 ± 0	-1 ± 0	0 ± 0	1 ± 0	-1 ± 0	1 ± 0	6	3
2500 GeV	7	-4 ± 1	5 ± 0	0 ± 0	-1 ± 0	-1 ± 0	1 ± 0	-1 ± 0	1 ± 0	6	3
3000 GeV	4	-4 ± 1	5 ± 0	4 ± 0	0 ± 0	-2 ± 0	0 ± 0	-1 ± 0	1 ± 0	7	-2
4000 GeV	0	-4 ± 1	5 ± 0	-6 ± 0	1 ± 0	-1 ± 0	1 ± 0	-2 ± 0	1 ± 0	9	-4

Table G.26: Relative uncertainties (sys ± stat) on the signal efficiencies in percentages for photon fusion spin-½ HECOs of charge $\lvert z\rvert = 60$. The total relative uncertainties are calculated as quadratic sums of the individual relative uncertainties. Note that the detector-material uncertainty and the δ-ray uncertainty are taken as symmetric, as described in the text.

Photon Fusion Spin-½ $\lvert z \rvert = 80$	eff.	Material	Birks High	δ-ray prod.	TRT Occ.	Calo Arrival	Extrap	Pileup w. Up	Pileup w. Down	Total Up	Total Down
200 GeV	0	-8 ± 4	10 ± 0	0 ± 0	-2 ± 0	0 ± 0	1 ± 0	0 ± 0	0 ± 0	13	6
500 GeV	2	-8 ± 4	5 ± 0	-4 ± 0	-2 ± 0	0 ± 0	0 ± 0	0 ± 0	0 ± 0	10	-7
1000 GeV	4	-8 ± 4	5 ± 0	0 ± 0	-2 ± 0	0 ± 0	1 ± 0	0 ± 0	0 ± 0	9	-6
1500 GeV	4	-8 ± 4	5 ± 0	-1 ± 0	-2 ± 0	0 ± 0	0 ± 0	0 ± 0	0 ± 0	9	-6
2000 GeV	3	-8 ± 4	5 ± 0	1 ± 0	-2 ± 0	0 ± 0	0 ± 0	0 ± 0	0 ± 0	9	-6
2500 GeV	2	-8 ± 4	5 ± 0	4 ± 0	-2 ± 0	0 ± 0	0 ± 0	-1 ± 0	0 ± 0	10	-7
3000 GeV	1	-8 ± 4	5 ± 0	4 ± 0	-2 ± 0	0 ± 0	1 ± 0	-1 ± 0	0 ± 0	10	-7
4000 GeV	0	-8 ± 4	11 ± 1	3 ± 0	-3 ± 0	0 ± 0	-4 ± 0	0 ± 0	0 ± 0	13	6

Table G.27: Relative uncertainties (sys ± stat) on the signal efficiencies in percentages for photon fusion spin-½ HECOs of charge $\lvert z \rvert = 80$. The total relative uncertainties are calculated as quadratic sums of the individual relative uncertainties, where the detector-material uncertainty and the δ-ray uncertainty are taken as symmetric, as described in the text.

Photon Fusion Spin-½ $\lvert z \rvert = 100$	eff.	Material	Birks High	δ-ray prod.	TRT Occ.	Calo Arrival	Extrap	Pileup w. Up	Pileup w. Down	Total Up	Total Down
200 GeV	0	-14 ± 9	5 ± 0	0 ± 0	-2 ± 0	0 ± 0	-1 ± 0	0 ± 0	0 ± 0	15	-13
500 GeV	0	-14 ± 9	5 ± 0	-4 ± 0	-2 ± 0	0 ± 0	0 ± 0	0 ± 0	0 ± 0	15	-14
1000 GeV	1	-14 ± 9	5 ± 0	0 ± 0	-2 ± 0	0 ± 0	0 ± 0	0 ± 0	0 ± 0	15	-13
1500 GeV	1	-14 ± 9	5 ± 0	-1 ± 0	-3 ± 0	0 ± 0	1 ± 0	0 ± 0	0 ± 0	15	-13
2000 GeV	1	-14 ± 9	5 ± 0	1 ± 0	-3 ± 0	0 ± 0	1 ± 0	0 ± 0	0 ± 0	15	-13
2500 GeV	0	-14 ± 9	8 ± 0	4 ± 0	-3 ± 0	0 ± 0	1 ± 0	-1 ± 0	0 ± 0	16	-13
3000 GeV	0	-14 ± 9	5 ± 0	4 ± 0	-2 ± 0	1 ± 0	0 ± 0	0 ± 0	1 ± 0	15	-14
4000 GeV	0	-14 ± 9	5 ± 0	3 ± 0	0 ± 0	0 ± 0	1 ± 0	0 ± 0	0 ± 0	15	-13

Table G.28: Relative uncertainties (sys ± stat) on the signal efficiencies in percentages for photon fusion spin-½ HECOs of charge $\lvert z \rvert = 100$. The total relative uncertainties are calculated as quadratic sums of the individual relative uncertainties, where the detector-material uncertainty and the δ-ray uncertainty are taken as symmetric, as described in the text.

APPENDIX H

Signal sample ABCD plane distribution

Table H.1 contains the signal sample yields for each SR and CR in the ABCD plane, for all DY spin-½ samples. Column three indicates the number of preselected HIP candidates, column eight indicates the fraction of preselected candidates that are contained in the ABCD plane and finally column nine indicates the fraction of HIP candidates in the ABCD plane that are actually SR yields.

$\|g\|$, $\|z\|$ [g_D, e]	m [GeV]	PC	A	B	C	D	$\frac{A+B+C+D}{PC}$	$\frac{A}{A+B+C+D}$
1	200	24966	23731	22	1170	9	1.0	0.95
1	500	38807	37198	59	1481	12	1.0	0.96
1	1000	45277	40587	25	4541	15	1.0	0.9
1	1500	49512	37556	30	11696	23	1.0	0.76
1	2000	44921	27691	18	16902	38	0.99	0.62

Continued on next page

Table H.1: Drell-Yan spin-½ signal sample yields in the ABCD plane. PC stands for Preselected Candidates and A, B, C, D stand for data yields in each region. Yields have been rounded to nearest integer.

$\lvert g \rvert$, $\lvert z \rvert$ [$g_{\mathbf{D}}$, e]	m [GeV]	PC	A	B	C	D	$\frac{A+B+C+D}{PC}$	$\frac{A}{A+B+C+D}$
1	2500	47190	23923	10	22862	44	0.99	0.51
1	3000	49430	21041	10	27942	50	0.99	0.43
1	4000	46172	13025	4	32594	37	0.99	0.29
2	200	37869	36318	243	1264	28	1.0	0.96
2	500	46032	44618	88	1296	14	1.0	0.97
2	1000	38275	36893	59	1272	16	1.0	0.96
2	1500	34613	33372	67	1130	28	1.0	0.96
2	2000	25258	24336	46	817	32	1.0	0.96
2	2500	26274	24815	45	1311	53	1.0	0.95
2	3000	26724	24484	34	2096	44	1.0	0.92
2	4000	22378	16306	16	5872	39	0.99	0.73
20	200	16769	2915	18	13404	88	0.98	0.18
20	500	31451	6557	40	24057	167	0.98	0.21
20	1000	39215	7137	31	31222	149	0.98	0.19
20	1500	43498	6767	24	35768	148	0.98	0.16
20	2000	43854	5972	15	37050	122	0.98	0.14
20	2500	43717	5556	6	37290	96	0.98	0.13
20	3000	43155	5263	2	37166	80	0.99	0.12
20	4000	42463	4731	3	36953	49	0.98	0.11
40	200	26362	16859	9	9237	4	0.99	0.65
40	500	32227	23348	4	8678	10	0.99	0.73
40	1000	39917	29322	16	10396	26	1.0	0.74
40	1500	43387	29507	22	13677	25	1.0	0.68
40	2000	36808	22607	10	14059	32	1.0	0.62
40	2500	32966	18804	7	14006	40	1.0	0.57

Continued on next page

Table H.1: Drell-Yan spin-½ signal sample yields in the ABCD plane. PC stands for Preselected Candidates and A, B, C, D stand for data yields in each region. Yields have been rounded to nearest integer.

$\|g\|$, $\|z\|$ [$g_{\mathbf{D}}$, e]	m [GeV]	PC	A	B	C	D	$\frac{A+B+C+D}{PC}$	$\frac{A}{A+B+C+D}$
40	3000	33905	17210	9	16497	42	1.0	0.51
40	4000	19953	8175	5	11609	27	0.99	0.41
60	200	19603	16871	11	2622	12	1.0	0.86
60	500	30580	27517	20	2938	27	1.0	0.9
60	1000	28942	26615	13	2209	39	1.0	0.92
60	1500	26237	23855	16	2263	38	1.0	0.91
60	2000	24449	21706	19	2646	33	1.0	0.89
60	2500	22925	19638	18	3184	35	1.0	0.86
60	3000	16978	14040	14	2831	61	1.0	0.83
60	4000	5141	3672	4	1391	37	0.99	0.72
80	200	46153	42379	43	3615	16	1.0	0.92
80	500	24331	22832	24	1385	34	1.0	0.94
80	1000	24976	23680	34	1190	33	1.0	0.95
80	1500	17841	16866	22	876	41	1.0	0.95
80	2000	14011	13229	15	684	51	1.0	0.95
80	2500	10854	10120	20	641	47	1.0	0.93
80	3000	8220	7412	19	681	75	1.0	0.91
80	4000	679	559	5	56	44	0.98	0.84
100	200	12355	11465	24	835	9	1.0	0.93
100	500	9878	9360	17	471	13	1.0	0.95
100	1000	7192	6831	18	308	20	1.0	0.95
100	1500	4033	3805	5	167	34	1.0	0.95
100	2000	3449	3265	8	130	32	1.0	0.95
100	2500	2373	2197	9	131	24	1.0	0.93
100	3000	1163	1056	8	59	27	0.99	0.92

Continued on next page

Table H.1: Drell-Yan spin-½ signal sample yields in the ABCD plane. PC stands for Preselected Candidates and A, B, C, D stand for data yields in each region. Yields have been rounded to nearest integer.

$\|g\|$, $\|z\|$ $[g_D$, e]	m [GeV]	PC	A	B	C	D	$\frac{A+B+C+D}{PC}$	$\frac{A}{A+B+C+D}$
100	4000	35	11	7	0	12	0.89	0.37

Table H.1: Drell-Yan spin-½ signal sample yields in the ABCD plane. PC stands for Preselected Candidates and A, B, C, D stand for data yields in each region. Yields have been rounded to nearest integer.

APPENDIX I

Contributions to Run 2 partial and full HIP analysis.

1. ATLAS Collaboration, Search for magnetic monopoles and stable particles with high electric charges in $\sqrt{s}$=13 TeV pp collisions with the ATLAS detector, Submitted to JHEP, arXiv: 2308.04835

2. Song, Wen Yi and Rodriguez Vera, Ana Maria and Taylor, Wendy and Levchenko, Mikhail, Search for magnetic monopoles and stable high-electric-charge objects in 13 TeV proton-proton collisions with the ATLAS detector, Internal Note (ATL-COM-PHYS-2020-187), https://cds.cern.ch/record/2712308

   For our most recent Highly Ionizing Particle search, documented in this thesis, I was the main responsible for the analysis code. I ran studies to optimize our signal selection variables and attempted the implementation of a random forest classifier to improve our signal selection efficiency at high occupancy rates. I developed the HIP framework through which we computed signal selection efficiencies both through cut-and-count method as well as an extrapolation method. These are documented in Chapters 5 and 6. The framework also included the data-driven *background estimation (Chapter 8) and the cross-section limit setting procedure (Chapter 9). For the latter, I received major support from UEH convener at the time Louie Corpe. Additionally, I was responsible for producing the plots and illustrations available in the paper. I wrote the first draft of the paper and contributed heavily to the internal note.*

3. ATLAS Collaboration, Search for magnetic monopoles and stable high-electric-charge objects in 13 TeV protonproton collisions with the ATLAS detector, Phys. Rev. Lett. 124 (2020) 031802, arXiv: 1905.10130

4. Mermod, Philippe and Lionti, Anthony Eric and Taylor, Wendy and Rodriguez Vera, Ana Maria, Search for magnetic monopoles and stable high-electric-charge objects in 13 TeV proton-proton collision with the ATLAS detector, Internal Note (ATL-COM-PHYS-2017-702), https://cds.cern.ch/record/2267571

   For the first HIP analysis using Run 2 data (covering the years of 2015 and 2016) I was responsible for the computation of the systematic uncertainties, among other responsibilities. Some of that work was used in the search documented in Chapter 7 of this thesis. This included the modification of the Geant4 simulation code to produce alternative signal samples, for the computation of the Birks' Law and the δ-ray production systematic uncertainties. Additionally, I produced the code that computed the TRT occupancy and the Calorimeter cross-talk systematic uncertainties. Finally, I computed the extrapolation systematic uncertainty. The use of the code created for the 2015-2016 computation of the systematic uncertainties, along with additional studies and final computation of the total systematic uncertainties was carried out by other members of the HIP analysis.

APPENDIX J

ATLAS Fact Sheets

The ATLAS Education and Outreach group is the main body in the ATLAS Collaboration responsible for science outreach. Outreach combines communication, education and policy-making. The ATLAS Education and Outreach group supports institutes belonging to the ATLAS Collaboration in their Outreach efforts, coordinates visits to the ATLAS detector and creates all the material sanctioned by the ATLAS Collaboration for education and outreach purposes.

One of these materials is the ATLAS Fact Sheets [107]. These are a set of single-page documents, aimed at a non-expert audience, which contains basic information about the ATLAS Collaboration, the ATLAS detector and the science program at ATLAS. Because these fact sheets are directed to a wider audience, they have been designed as stand-alone documents that require no previous knowledge of particle physics.

Currently, there are ten fact sheets available:

- The ATLAS Collaboration: Describes the group of people that support the functioning and carry out research at the ATLAS experiment.

- Detector Overview: Talks about the main systems that make up the ATLAS detector. It is an introduction to the next four fact sheets that go into detail on each sub-system.
- The Inner Detector: Describes the three layers of the tracking detector in ATLAS.
- Calorimeters: Talks about the two sub-detectors that measure energy deposits of particles.
- Muon Spectrometer: Discusses the outermost sub-detector of ATLAS, responsible for the measurement of the properties of muons.
- Magnet System: Describes the two-part magnet system.
- Trigger and Data Acquisition: Refers to the systems in ATLAS that deal with choosing interesting events and storing them.
- Software and Computing Infrastructure: Describes the software and computing resources used by the detector during data collection, by the different research groups during the analysis stage and finally the open resources available to the wider public.
- Technology Transfer: Gives some examples of technology development made by the ATLAS Collaboration, which has applications outside of particle physics.
- Higgs Boson: Explains the importance of the discovery of the Higgs Boson, the properties measured and the next steps of the physics program related to it.

In order to better support outreach and education in institutes around the world that participate in the ATLAS Collaboration, translations of the ATLAS Fact Sheets are available in French, Spanish, Italian, German and Portuguese. A translation to simplified Chinese is in the works.

Acronyms

ATLAS	A Toroidal LHC ApparatuS.
BSM	Beyond Standard Model.
CERN	Centre Europeen de Recherche Nucléaire.
DY	Drell-Yan.
EM	Electromagnetic.
GUTs	Grand Unified Theories.
HCal	Hadronic Calorimeter.
HECOs	High Electric Charge Objects.
HIPs	Highly Ionizing Particles.
HT	High Threshold.
IBL	Insertable B-Layer.
ID	Inner Detector.
LAr	Liquid Argon calorimeter.
LHC	Large Hadron Collider.
LT	Low Threshold.

MC	Monte Carlo.
ML	Machine Learning.
MoEDAL	Monopole and Exotics Detector at the LHC.
NMC	Ntuple Maker Code.
PDFs	Parton Distribution Functions.
PF	Photon Fusion.
RFC	Random Forest Classifier.
SCT	Semi-Conductor Tracker.
SM	Standard Model.
SQM	Strange Quark Matter.
TRT	Transition Radiation Tracker.